

Squeezed Light and Laser Interferometric Gravitational Wave Detectors

Von der Fakultät für Mathematik und Physik
der Gottfried Wilhelm Leibniz Universität Hannover
zur Erlangung des Grades

Doktor der Naturwissenschaften
– **Dr. rer. nat.** –

genehmigte Dissertation
von

Dipl.-Phys. Simon Chelkowski

geboren am 28. September 1976 in Hannover

2007

Referent: Juniorprof. R. Schnabel
Korreferent: Prof. K. Danzmann
Tag der Promotion: 25. Juni 2007

Summary

Based on the General Theory of Relativity Albert Einstein predicted the existence of gravitational waves as early as 1916. It took until now to develop large-scale interferometric gravitational wave (GW) detectors with sensitivities which would allow a direct measurement of a GW caused by an astrophysical event, such as a nearby supernova explosion. GW detectors have steadily improved over recent years and are currently producing a continuous stream of scientifically relevant data.

The limiting noise in the higher frequency range of the GW detection band is shot noise, which is caused by vacuum fluctuations entering the detector through its dark port. Current GW detectors use high-power lasers to reduce shot noise. In addition, techniques such as power recycling and signal recycling have been developed. These techniques increase the laser power in the interferometer arms and amplify the GW induced signal sidebands respectively, to increase the shot noise limited sensitivity even further. In 1981 Caves proposed using squeezed light to reduce the vacuum fluctuations, thereby increasing the signal-to-noise ratio of the GW detector.

The generation of squeezed states was first experimentally demonstrated by Slusher *et al.* in 1985. Since then, the technique of squeezing has evolved and today it can be used as a tool in real applications such as GW detection. It is planned to use squeezed light in future generations of GW detectors to enhance their sensitivity beyond quantum noise. This thesis analyzes and demonstrates the compatibility of squeezed light and advanced techniques of high-precision laser interferometry for GW detection.

Initially, an optical parametric amplifier (OPA) is set up to produce the desired squeezed states of light (Chapter 3). This source is characterized—and consequently optimized—to deliver a maximum squeezing strength of up to 5.7 dB.

The detuned signal-recycling cavity of GEO 600 and future GW detectors inevitably requires study of the effects caused by reflection of an initially frequency-independent squeezed state of light at such a cavity. The squeezing ellipse orientation of the reflected light is frequency-dependent; consequently, the sensitivity of the GW detector is only enhanced in a small frequency range. In Chapter 4 such frequency-dependent squeezed states are generated and characterized.

The demonstration of a squeezed-light-enhanced dual-recycled Michelson interferometer with a broadband improved sensitivity is presented in Chapter 5. Here, a smaller version of GEO 600, downsized by a factor of 1000, is set up as a tabletop experiment. A detuned filter cavity is used to compensate the effects of the signal-recycling cavity, which results in a non-classical sensitivity improvement in the entire frequency band of interest.

The enhancement of a large scale GW detector demands the availability of squeezed light in the GW detection band from 10 Hz–10 kHz. Chapter 6 describes the newly developed locking scheme required for the generation of such low-frequency squeezing, along with the results obtained.

Finally, an outlook is given in Chapter 7 of the possible performance increase of the next generation GW detector, GEO-HF, due to squeezed-light injection. Different options for filter cavities and their implementation in the current vacuum system are discussed, as well as a detuned twin-signal-recycling option.

Keywords: gravitational wave detector, OPA, frequency-dependent squeezed light, squeezed-light-enhanced dual-recycled Michelson interferometer, low-frequency squeezing, GEO-HF

Zusammenfassung

Im Jahr 1916 hat Albert Einstein basierend auf der Allgemeinen Relativitätstheorie die Existenz von Gravitationswellen vorausgesagt. Erst heutige große interferometrische Gravitationswellendetektoren (GWD) erreichen Sensitivitäten, die eine direkte Detektion einer Gravitationswelle (GW) astrophysikalischen Ursprungs, wie etwa einer nahen Supernova, erlauben würden. GWD sind über die letzten Jahre stetig verbessert worden, so dass zum aktuellen Zeitpunkt eine kontinuierliche Aufnahme wissenschaftlicher Daten gewährleistet ist.

Die limitierende Rauschquelle im oberen Bereich des GW Detektionsbandes ist das Schrotrauschen, welches durch Vakuumfluktuationen verursacht wird. Diese koppeln über den dunklen Ausgang des Interferometers ein. Derzeitige GWD benutzen Hochleistungslaser, um das Schrotrauschen abzusenken. Zusätzlich sind Techniken wie etwa Power-Recycling und Signal-Recycling entwickelt worden. Diese Techniken erhöhen einerseits die Laserleistung in den Interferometerarmen und andererseits werden die durch die GW verursachten Signalseitenbänder verstärkt, was die schrotrauschlimitierte Sensitivität weiter verbessert. 1981 hat Caves vorgeschlagen, gequetschtes Licht zu benutzen, um die Vakuumfluktuationen zu verringern. Dies hat einen Anstieg des Signal-zu-Rausch-Verhältnisses des Gravitationswellendetektors zur Folge.

Slusher *et al.* haben 1985 erstmals gequetschtes Licht hergestellt. Seitdem hat sich die Technik zur Herstellung gequetschten Lichtes weiterentwickelt, so dass es heutzutage als Werkzeug in realen Anwendungen, wie etwa der GW Detektion angewendet werden kann. Gequetschtes Licht wird in zukünftigen GWD benutzt werden, um deren Sensitivität über das Quantenrauschen hinaus zu verbessern. Die vorliegende Arbeit analysiert und demonstriert die Kompatibilität von gequetschtem Licht und Techniken der Präzisions-Laser-Interferometrie für die GW Detektion.

Als erstes wird ein optisch-parametrischer Verstärker (OPA) aufgebaut, der das gewünschte gequetschte Licht produziert (Kapitel 3). Diese Quelle wird charakterisiert und ist über den gesamten Zeitraum dieser Arbeit optimiert worden, so dass eine maximale Rauschunterdrückung des gequetschten Lichtes von 5.7 dB erreicht worden ist.

Die verstimmten Signal-Recycling Resonatoren von GEO 600 und zukünftigen GWD machen eine Untersuchung der Effekte bei Reflektion von anfänglich frequenzunabhängig gequetschtem Licht an diesem verstimmten Resonator unabdingbar. Es stellt sich heraus, dass die Orientierung der Squeezing Ellipse des reflektierten Lichtes frequenzabhängig ist. Deshalb ist die Steigerung der Sensitivität auf einen kleinen Frequenzbereich eingeschränkt. In Kapitel 4 werden solche frequenzabhängig gequetschte Zustände hergestellt und charakterisiert.

Ein squeezed-light-enhanced Dual-Recycled Michelson Interferometer mit einer breitbandigen Verbesserung der Sensitivität wird in Kapitel 5 präsentiert. Eine um den Faktor 1000 verkleinerte Version des GWDs GEO 600 ist auf einem optischen Tisch aufgebaut worden. Ein verstimmter Filter-Resonator wird benutzt, um die Auswirkungen des verstimmten Signal-Recycling-Resonators zu kompensieren und so eine nicht-klassische Steigerung der Sensitivität über die gesamte relevante Bandbreite zu erhalten.

Die Verbesserung eines großen GWD verlangt nach gequetschtem Licht im GW Detektionsband von 10 Hz–10 kHz. Kapitel 6 beschreibt das für die Herstellung tieffrequenten gequetschten Lichtes erforderliche und neu entwickelte Kontrollschema des OPA und präsentiert die daraus resultierenden Ergebnisse.

Zum Abschluss wird in Kapitel 7 ein Ausblick auf die mittels gequetschten Lichtes mögliche Steigerung der Sensitivität von GEO-HF – einem GWD der nächsten Generation – gegeben. Verschiedene Filter-Resonator Topologien und ihre Integration in das bestehende Vakuumsystem werden ebenso diskutiert wie die mögliche Verwendung von verstimmtem Twin-Signal-Recycling.

Stichworte: Gravitationswellendetektor, OPA, frequenzabhängiges gequetschtes Licht, squeezed-light-enhanced Dual-Recycled Michelson Interferometer, tieffrequentes gequetschtes Licht, GEO-HF

Contents

Summary	i
Zusammenfassung	iii
Contents	v
List of figures	ix
List of tables	xvii
Glossary	xix
1 Introduction	1
1.1 Historical overview	1
1.2 The first gravitational wave detector	2
1.3 Gravitational wave detection with laser interferometers	3
1.4 Noise sources in interferometric gravitational wave detectors	7
1.5 Advanced techniques to enhance the quantum noise limited sensitivity of a gravitational wave detector	8
1.6 Structure of the thesis	11
2 Quantum nature of light	13
2.1 The quantization of the electric field	13
2.2 Fock states	14
2.3 Coherent states	15
2.4 Quadrature operators	17
2.5 The Heisenberg uncertainty principle	18
2.6 Squeezed states	20
2.7 The quantum phasor picture	22
2.8 Linearization	22
2.9 Detection schemes	24
2.9.1 Direct detection	24
2.9.2 Shot noise	26
2.9.3 Calculation of the shot noise level	26
2.9.4 Optical losses and detection efficiencies	28
2.9.5 Balanced homodyne detection	30

2.9.6	Homodyne mode mismatch	34
2.10	Squeezing in the sideband picture	35
2.10.1	The classical sideband picture	35
2.10.2	Quantum noise in the sideband picture	37
2.10.2.1	The quantum sideband picture	38
2.10.2.2	Vacuum noise in the quantum sideband picture	38
2.10.2.3	A coherent state in the quantum sideband picture	41
2.10.2.4	Amplitude modulation in the quantum sideband picture	41
2.10.2.5	Phase modulation in the quantum sideband picture	42
2.10.2.6	Squeezed states in the quantum sideband picture	44
2.11	Calculation of squeezing from an OPO cavity	46
2.11.1	Simulations	47
2.11.2	Estimation of the intra-cavity losses	48
2.11.3	An example of a typical OPO	52
2.11.4	Phase fluctuation	52
3	A typical squeezing experiment	57
3.1	Optical components and layout	57
3.2	Laser preparation	58
3.2.1	Laser	58
3.2.2	Modecleaner	61
3.2.3	Frequency stabilization	62
3.3	Nonlinear experimental stage	64
3.3.1	Theory of <u>second harmonic generation</u> —SHG	64
3.3.1.1	Requirements for a SHG	65
3.3.2	Theory of <u>optical parametric amplification/oscillation</u> —OPA/OPO	68
3.3.2.1	Classical properties of parametric amplification	70
3.3.2.2	Quantum properties of parametric amplification	71
3.3.3	Nonlinear cavities	73
3.3.3.1	Optical layout	73
3.3.3.2	Mechanical setup	77
3.3.3.3	Temperature stabilization	82
3.3.4	SHG cavity	83
3.3.4.1	Cavity length locking scheme	84
3.3.5	OPA cavity	85
3.3.5.1	Cavity length locking scheme	85
3.3.5.2	Control of the squeezing angle	86
3.4	Experimental area and detection	88
3.4.1	Homodyne detection	88
3.5	Experimental results	89
3.5.1	Dark noise correction	91
4	Frequency-dependent squeezed light	93
4.1	Squeezed light reflected at a detuned cavity	93
4.1.1	Quantum noise inside gravitational wave interferometers	94

4.1.2	GW detector enhancement with squeezed light	96
4.1.3	Theoretical description of frequency-dependent light	101
4.1.4	Frequency-dependent light in the sideband picture	103
4.2	Optical layout	105
4.2.1	Filter cavity	108
4.2.2	Homodyne detector	109
4.3	Tomography of quantum states	109
4.3.1	The Wigner function	109
4.3.2	Data acquisition	111
4.3.3	Inverse Radon transformation	112
4.3.4	Locking a homodyne detector to an arbitrary quadrature angle . .	114
4.4	Experimental results	115
4.4.1	Frequency-dependent squeezing spectra	116
4.4.2	Tomography of frequency-dependent light	119
4.4.3	Compensation of the rotation of the squeezing ellipse	120
5	Squeezed-light-enhanced dual-recycled Michelson interferometer	125
5.1	Optical layout	127
5.1.1	OPA	129
5.1.2	Filter cavity	131
5.1.3	Homodyne detector	133
5.2	The dual-recycled Michelson interferometer	134
5.2.1	The alignment of the squeezed field into the filter cavity and Michelson interferometer	138
5.2.2	Generation of error signals for the dual-recycled Michelson interferometer	140
5.2.3	Lock acquisition of the dual-recycled Michelson interferometer . .	147
5.3	Injecting signals into the interferometer	149
5.4	Experimental results	151
5.4.1	Loss estimation	156
6	Coherent control of broadband vacuum squeezing	161
6.1	Abstract	161
6.2	Introduction	161
6.3	Control scheme	163
6.4	Experimental setup and results	169
6.5	Application to gravitational wave detectors	172
6.6	Conclusion	175
7	The potential of a squeezed-vacuum-enhanced GEO-HF	177
7.1	The upgrade: From GEO to GEO-HF	178
7.2	Possible increase in GEO-HF's sensitivity due to squeezed vacuum	181
7.3	Parameters and implementation of the required additional optics	187
7.3.1	A short filter cavity	190
7.3.2	A long filter cavity	191

7.3.3	Twin-signal-recycling cavity	191
7.4	Conclusion	193
A	Matlab scripts	195
A.1	The reconstruction of the Wigner function from the measured data	195
A.2	Calculation of GEO-HF's quantum noise limited sensitivity	197
B	Control loop basics and optimizations	203
B.1	Optimizing a servo controller	203
B.2	Measuring an open-loop transfer function	210
C	Electronics	213
C.1	Temperature controller	213
C.2	HV amplifier	213
C.3	Modecleaner servo	213
C.4	Homodyne photodiode	213
C.5	Resonant photodiode	213
D	Origin of technical noise in the squeezed field	225
E	Transfer function of Fabry-Perot cavity	229
	Bibliography	231
	Acknowledgements	245
	Curriculum vitae	247
	Publications	249

List of figures

1.1	The effect of a gravitational wave on a Michelson interferometer as time evolves. The direction of propagation of the gravitational wave is perpendicular to the image plane.	3
1.2	Schematic of three different optical layouts of laser interferometric based gravitational wave detectors	4
1.3	Quantum noise limited strain sensitivities of a simple Michelson interferometer plotted for two different circulating light powers and for a squeezed-light-enhanced simple Michelson interferometer.	6
1.4	Schematic of the layout of a simple Michelson interferometer based gravitational wave detector. The left figure shows how the vacuum noise enters through the dark port while the right figure displays how this vacuum can be replaced with squeezed vacuum using a Faraday rotator.	7
1.5	Schematic of the optical layout of GEO 600 and its quantum noise limited sensitivity, simulated with the design parameters.	9
1.6	Representation of a vacuum and a squeezed vacuum state in quadrature phase space	10
2.1	A bright squeezed state in the quantum phasor picture	21
2.2	Illustrative figure to explain the quantum phasor picture.	23
2.3	The representation of four different quantum states of light in the quantum phasor picture	23
2.4	Three different detection schemes: an ideal direct measurement, a realistic direct measurement and an ideal homodyne measurement	25
2.5	Schematic of the detection schemes for measuring the fluctuations of a light field that are used throughout this thesis.	27
2.6	Resulting variance for different input variances and losses	30
2.7	Schematic of the two balanced homodyne detection schemes, self-homodyne detection and homodyne detection with an external local oscillator	33
2.8	Phasor representing the field given in Equation 2.90.	35
2.9	Amplitude modulated field from Equation 2.91 in the sideband picture for different times within one modulation period	36
2.10	Phase modulated field from Equation 2.92 in the sideband picture for different times within one modulation period	37
2.11	Representation of vacuum noise in the sideband picture and its transition into the quantum sideband picture	39

2.12	Representation of vacuum state in different physical pictures	40
2.13	Representation of coherent state in different physical pictures	41
2.14	Amplitude modulated field in different physical pictures	42
2.15	Phase modulated field in different physical pictures	43
2.16	Amplitude squeezed vacuum field in different physical pictures	45
2.17	Phase squeezed vacuum field in different physical pictures	46
2.18	Variances of the squeezed V_- and anti-squeezed V_+ quadrature for a transition from an ideal system with zero losses and perfect efficiencies to a typical system that was used in the laboratory for an estimated internal loss of 0.006 and a quantum efficiency of 0.94 for the photodiodes.	50
2.19	Comparison of a linear hemilithic cavity and a ring cavity	51
2.20	Squeezed variance V_- plotted for six different OPO systems that all produce the same amount of squeezing especially 6.5 dB at a classical gain $G=10$	53
2.21	Squeezed variance V_- for a homodyne detection scheme with external local oscillator	54
2.22	Squeezed variance V_- for a self homodyne detection scheme	55
2.23	Contour plot of a squeezing ellipse with and without phase fluctuations	56
2.24	Variances V_- and V_+ for an ideal system	56
3.1	Optical layout of a generic squeezing experiment	58
3.2	Schematic of the used Nd:YAG laser	59
3.3	Power spectrum of the laser amplitude noise measured behind the mode-cleaner.	60
3.4	Schematic of the modecleaner, a ring cavity formed by three mirrors with a round-trip length of $L=0.42$ m	61
3.5	Frequency control loop of the modecleaner	63
3.6	The modecleaner's PDH error signal and the corresponding reflected light power.	63
3.7	Measured open-loop transfer function of the modecleaner's frequency control loop	64
3.8	Three-wave mixing processes	66
3.9	Plot of the conversion efficiency of a SHG depending on the temperature of the crystal and the wavelength of the pump	68
3.10	Model for nonlinear processes such as SHG, OPA or OPO inside a cavity	69
3.11	Classical gain of an optical parametric amplifier	71
3.12	Optical layout of three different nonlinear cavities	73
3.13	Photo of a MgO:LiNbO ₃ crystal	74
3.14	Representative schematic of the optical layout of a nonlinear cavity and the beam profiles of the fundamental and harmonic fields	75
3.15	Intra-cavity powers of the fundamental and harmonic field for different combinations of the outcoupling mirror reflectivities	76
3.16	Photo and schematic of the nonlinear cavity	77
3.17	The schematic of the first oven design presented from the front.	78
3.18	A photo of the new oven design and a schematic of its internal setup	80

3.19 CAD explosion drawing of the new quasi-monolithic cavity design	81
3.20 Photos of the new nonlinear cavity in the optical setup	82
3.21 Harmonic output power of the SHG while the temperature of the crystal is changed from below the phase matching temperature to above.	84
3.22 Schematic of the SHG layout including the cavity length control loop . . .	85
3.23 Schematic of the OPA layout including the cavity length control loop . . .	86
3.24 Schematic of the SHG layout including the cavity length and squeezing angle control loop	87
3.25 Comparison of the two homodyne photodetectors transfer functions . . .	88
3.26 Schematic of the homodyne detector layout including the homodyne angle control loop	89
3.27 Amplitude quadrature noise spectra of different quantum states	90
3.28 Zero-span measurement at a sideband frequency of 6 MHz	91
3.29 Dark noise corrected amplitude quadrature noise spectra of different quantum states	92
4.1 Simplified schematic of the gravitational wave detector GEO 600	94
4.2 Comparison of strain sensitivities of a simple Michelson interferometer and the GEO 600	95
4.3 Simplified schematics of a simple Michelson interferometer and the gravitational wave detector GEO 600	97
4.4 Strain sensitivity of a simple Michelson interferometer with an internal power of 7 kW, in comparison to the improvement which can be achieved with squeezed light with fixed and optimized squeezing angle injected through the dark port.	98
4.5 Comparison of the strain sensitivities of GEO 600 with an internal power of 7 kW with and without squeezed light injected into the dark port . . .	99
4.6 Comparison of the strain sensitivities of GEO 600 with an internal power of 7 kW with and without squeezed light injected into the dark port. The different squeezed-light-enhanced strain sensitivities reflect different initial squeezing angles of the injected squeezed light.	100
4.7 Simplified schematic of the gravitational wave detector GEO 600 including a filter cavity	100
4.8 Sideband picture representation of the vacuum and squeezed vacuum . . .	103
4.9 Representation of the squeezed vacuum state in the sideband picture after reflection at a detuned cavity	104
4.10 Representation of the squeezed vacuum state in the sideband picture after the reflection at two cavities, which are slightly detuned from the reference frequency by $\pm\Omega_c$	106
4.11 Schematic of the optical layout of the experiment used to produce frequency-dependent squeezed light.	107
4.12 Layout of the control scheme of the filter cavity	108
4.13 Wigner function of the vacuum state in phase space	110
4.14 Time series and the corresponding histogram of the demodulated differential photocurrent	112

4.15	Series of histograms for the homodyne angle range of 0-180°	113
4.16	Wigner function reconstructed from the data used in 4.15	113
4.17	Homodyne detector signals outputs versus the local oscillator phase . . .	114
4.18	Measured noise power spectra of frequency-dependent squeezed light for a filter cavity detuning frequency of +15.15 MHz	118
4.19	Measured noise power spectra of frequency-dependent squeezed light for a filter cavity detuning frequency of -15.15 MHz	119
4.20	Simulated noise power spectra of frequency-dependent squeezed light for a filter cavity detuning frequency of -15.15 MHz	120
4.21	Comparison of the reconstructed Wigner functions of the vacuum state and a frequency-dependent squeezed state	121
4.22	Contour plots of the Wigner functions of the frequency-dependent squeezed state for different frequencies. The detuning frequency of the filter cavity is -15.15 MHz.	122
4.23	The three dimensional Wigner function of the frequency-dependent squeezed state measured at a frequency of 12 MHz and with a filter cavity detuning of -15.15 MHz	122
4.24	Contour plots of the Wigner functions of the frequency-dependent squeezed state for different frequencies. The detuning frequency of the filter cavity is +15.15 MHz.	123
4.25	Measured rotation angles of the 24 frequency-dependent squeezing ellipses presented in Figures 4.22 and 4.24.	124
5.1	Schematic of the optical layout of the squeezed-light-enhanced dual-recycled Michelson interferometer experiment	128
5.2	Two photographs of the optical table containing the squeezed-light-enhanced dual-recycled Michelson interferometer experiment	129
5.3	Layout of the OPA's control scheme	131
5.4	Layout of the filter cavity's control scheme	132
5.5	Comparison of the simulated and measured transmission and error signal of the filter cavity	133
5.6	Transfer function of one of the homodyne detector photodiodes	134
5.7	Optical layout of the dual-recycled Michelson interferometer	135
5.8	Comparison of the frequency-dependent transmission from the input of the Michelson interferometer into the south port for different Schnupp asymmetries of the interferometer arms	136
5.9	CAD model of the six-axis mirror mounts with the embedded PZT to actuate the longitudinal position of the interferometer mirrors.	137
5.10	Measured visibility of a simple Michelson interferometer	138
5.11	Comparison of the simulated transmission and error signal of the power-recycling cavity with the real ones	141
5.12	Surface plot of the power-recycling cavity error signal versus the tuning of the power-recycling mirror and the east end arm mirror	142
5.13	Surface plot of the power-recycling cavity error signal versus the tuning of the power-recycling mirror and the signal-recycling mirror	143

5.14	Transfer function of a resonant photodiode optimized for a frequency of 134.4 MHz.	144
5.15	Comparison of the simulated and measured error signal of the signal-recycling cavity	145
5.16	Surface plot of the signal-recycling cavity error signal versus the tuning of the signal-recycling mirror and the east end arm mirror	146
5.17	Surface plot of the signal-recycling cavity error signal versus the tuning of the signal recycling and power recycling mirrors	147
5.18	Comparison of the simulated and the measured error signal of the differential arm length of the Michelson interferometer	148
5.19	Layout of the control scheme of the phase-locked loop of the two lasers . .	151
5.20	Signal transfer function of the power-recycled Michelson interferometer . .	152
5.21	Amplitude quadrature noise spectra measured with the homodyne detector to see the effects of the filter and signal-recycling cavities on the formerly frequency-independent squeezing produced by the OPA.	153
5.22	Noise spectra measured with the homodyne detector to observe the effects of the filter and signal-recycling cavities on the formerly frequency independent squeezing produced by the OPA.	154
5.23	Measured signal transfer function of the dual-recycled Michelson interferometer together with the clear demonstration of the increased SNR of the squeezed-light-enhanced dual-recycled Michelson interferometer	155
5.24	Measured squeezing strength versus detection efficiency for three different cases	157
6.1	Schematic of the experiment to generate squeezing at sideband frequencies in the acoustic frequency range.	164
6.2	Complex optical field amplitudes at three different locations in the experiment, which are marked in Figure 6.1.	165
6.3	Cut through the squeezed-light source. The hemilithic cavity is formed by the highly reflection-coated back surface of the crystal and an outcoupling mirror.	166
6.4	Theoretical OPO cavity transmission versus cavity detuning	167
6.5	Measured quantum noise spectra at sideband frequencies $\Omega_s/2\pi$: shot noise and squeezed noise with 88 μ W local oscillator power	171
6.6	Measured quantum noise spectra: shot noise and squeezed noise with 8.9 mW local oscillator power	172
6.7	Time series of shot noise, squeezed noise with locked local oscillator phase and squeezed noise with scanned local oscillator phase at $\Omega_s/2\pi = 5$ MHz sideband frequency	173
6.8	Simplified schematic of the gravitational wave detector GEO 600	174
7.1	Schematic of the optical layout of GEO 600 and its quantum noise limited design strain sensitivity	178

7.2	Strain sensitivities for different signal recycling factors ($R_{\text{SRM}} = 98.05\%$, $R_{\text{SRM}} = 99.05\%$ and $R_{\text{SRM}} = 99.95\%$ and two different signal recycling resonance frequencies (350 Hz and 1 kHz)	180
7.3	Schematic of the potential optical layouts of GEO-HF	182
7.4	Comparison of GEO-HF's quantum noise limited strain sensitivities in the two different operation modes for a detuned signal recycling configuration with $R_{\text{SRM}} = 98.05\%$	184
7.5	Comparison of GEO-HF's quantum noise limited strain sensitivities in the two different operation modes for a detuned signal recycling configuration with $R_{\text{SRM}} = 88\%$ and for the TSR configuration	185
7.6	GEO-HF's quantum noise limited strain sensitivities for a tuned signal recycling configuration with $R_{\text{SRM}} = 80\%$	186
7.7	Comparison of GEO-HF's quantum noise limited strain sensitivities in the two different operation modes for a detuned signal recycling configuration with $R_{\text{SRM}} = 88\%$ and for the TSR configuration and for the tuned signal recycling configuration with $R_{\text{SRM}} = 80\%$	188
7.8	Schematic of the optical layout and the corresponding vacuum system of the current GEO 600 gravitational wave detector	189
7.9	Schematic of the optical layout and the vacuum system for implementation of a short or a long filter cavity into the current infrastructure	190
7.10	Schematic of the optical layout and the vacuum system for integration of a TSR configuration into the current infrastructure	192
B.1	Schematic of measuring a transfer function of a PZT actuated cavity . . .	204
B.2	Measured transfer function of the OPA cavity	204
B.3	Bode plot of the open loop transfer function and servo transfer function of the OPA	207
B.4	Schematic of a control loop with integrated summing amplifier to measure the open loop gain transfer function $L(\omega)$	210
B.5	Measured open loop transfer function of the SHG cavity control loop. The unity gain frequency is about 10 kHz.	211
C.1	Circuit diagram of temperature controller used for stabilizing the temperature of the SHG, OPA and OPO ovens. Part 1/2	214
C.2	Circuit diagram of temperature controller used for stabilizing the temperature of the SHG, OPA and OPO ovens. Part 2/2	215
C.3	Circuit diagram of the HV amplifier. Part 1/4	216
C.4	Circuit diagram of the HV amplifier. Part 2/4	217
C.5	Circuit diagram of the HV amplifier. Part 3/4	218
C.6	Circuit diagram of the HV amplifier. Part 4/4	219
C.7	Circuit diagram of generic servo layout. Part 1/2	220
C.8	Circuit diagram of generic servo layout. Part 2/2	221
C.9	Circuit diagram of the homodyne photodiode	222
C.10	Circuit diagram of a resonant photodiode	223

D.1	Frequency dependence of the transmitted power of a field entering the OPA cavity through the backside of the crystal	226
D.2	Schematic of the experimental setup for the suppression of the technical noise below 3.5 MHz	226
E.1	Light field amplitudes at a Fabry-Perot cavity	230

List of tables

2.1	Physical parameters that are needed for the calculation of the variances V_- and V_+ , divided in three different classes.	48
2.2	Three simulated OPO systems and their individual parameters resulting in a finesse $\mathcal{F} \approx 138$	49
2.3	Degradation of the squeezing by the transition from an ideal to a realistic system with non-unity efficiencies.	51
3.1	Specifications of the Nd:YAG laser	59
4.1	List of the individual efficiencies applied to the squeezed field from generation to detection for the frequency-dependent squeezed light generation and characterization experiment.	116
5.1	List of the individual efficiencies applied to the squeezed field from its generation until its detection for the dual-recycled Michelson interferometer experiment	157

Glossary

AOM	acousto-optical modulator
AR	anti reflective
DAQS	data acquisition
DC	originally: "direct current". In this work also used for frequencies very close to 0 Hz.
DOPA	degenerate optical parametric amplification
DOPO	degenerate optical parametric oscillation
EOM	electro-optical modulator
FFT	fast Fourier transform or discrete Fourier transform (DFT)
FWHM	full width at half maximum
FSR	free spectral range
GW	gravitational wave
HR	high reflective
HUP	Heisenberg uncertainty principle
HUR	Heisenberg uncertainty relation
HV	high voltage
IR	infrared
LCGT	large-scale cryogenic gravitational wave telescope
LIGO	laser interferometer gravitational wave observatory
LSD	linear spectral density
MCE	eastern central mirror
MCN	northern central mirror
ME	east end arm mirror
MFE	eastern folding mirror
MFN	northern folding mirror
MN	north end arm mirror
MSPLIT	split-frequency mirror
MTSR	twin-signal-recycling mirror
NPRO	nonplanar ring-oscillator
Nd:YAG	neodymium-doped yttrium aluminum garnet
NTC	negative temperature coefficient
OLTF	open-loop transfer function
OPA	optical parametric amplification / amplifier
OPO	optical parametric oscillation / oscillator
PBS	polarizing beam splitter
PDH	Pound-Drever-Hall
PLL	phase-locked loop

PD	photodiode
PRM	power-recycling mirror
PS	power spectrum
PSD	power spectral density
PZT	piezoelectric transducer
Q	mechanical quality factor
QCF	quadrature control field
RBW	resolution bandwidth
RoC	radius of curvature
SHG	second harmonic generation / generator
SNR	signal-to-noise ratio
SQL	standard-quantum limit
SRC	signal-recycling cavity
SRM	signal-recycling mirror
TSR	twin-signal-recycling
UGF	unity gain frequency
VBW	video bandwidth

a_j	complex amplitude of the electromagnetic field
\hat{a}	annihilation operator of intra-cavity field
\hat{a}^\dagger	creation operator
$\delta\hat{a}$	fluctuations of the coherent field \hat{a}
α, α_0	coherent amplitude
α	detection efficiency
\hat{A}	free propagating field
B	bandwidth
c	speed of light in vacuum
$\chi^{(1)}$	first order susceptibility
$\hat{D}(\alpha)$	displacement operator
ϵ	strength of the nonlinear interaction
ε	power reflectivity of a beam splitter
ε_0	electrical permeability
e	electron charge
η_{qe}	quantum efficiency of a photodiode
η_{det}	detection efficiency
η_{FI}	transmission efficiency of a Faraday isolator
η_{FR}	transmission efficiency of a Faraday rotator
η_{angle}	transmission efficiency due to the non-optimal brewster angle of the photodiode
$E^{QCF}(t)$	electric field of the QCF field
$\mathbf{E}(\mathbf{r}, t)$	electromagnetic field
f	frequency
f_0	eigenfrequency
Δf	bandwidth

\mathcal{F}	finesse
γ	cavity decay rate
g	total nonlinear gain
G	Newtons gravitational constant
\hbar	Planck's constant
h	strain induced by a gravitational wave
\dot{h}	measured strain by a gravitational wave detector
i	$\sqrt{-1}$
$i(t), i(\omega)$	photocurrent
i_+	photocurrent sum
i_-	photocurrent difference
I^{QCF}	photocurrent evoked by detecting the field QCF
κ_{m1}^a	coupling rate of mirror m1 for field a
k	wave number
\mathbf{k}	wave vector
λ_0	carrier wavelength
I	quadrupole moment
L	geometrical cavity length or distance between test masses or intra-cavity loss
δL	gravitational wave induced length change
l	round-trip length
Δl	arm length difference also called Schnupp asymmetry
μ_0	magnetic permeability
m	mirror test mass or modulation index
mm_{FC}	mode matching efficiency into the filter cavity
mm_{SRC}	mode matching efficiency into the signal-recycling cavity
ν	laser frequency
ν_0	carrier frequency
n	refractive index
ω	angular frequency
ω_j	angular frequency of the mode j
ω_0	angular carrier frequency
Ω	angular sideband frequency or detuning parameter
ϕ	phase angle
ϕ_{PRM}	tuning of the power-recycling mirror
$\delta\phi_{\text{GW}}$	gravitational wave induced phase shift
Φ	relative phase between the second harmonic pump field and the local oscillator field
p	position
P	laser power or circulating laser power
\mathcal{P}	electric polarization
q	momentum
$\hat{q}_{1,\theta}(\Omega, t)$	time-dependent normalized amplitude quadrature field
$\hat{q}_{2,\theta}(\Omega, t)$	time-dependent normalized phase quadrature field
ρ	OPA/OPA escape efficiency or cavity transfer function in reflection

$\rho(\Omega)$	transfer function of a cavity in reflection
r	squeezing factor or distance to a gravitational wave source
r_1	amplitude reflectivity of mirror one
r_c	radius of curvature
\mathbf{r}	position vector
R	power reflectivity
$S_{\text{err}}^{\text{QCF-LO}}$	error signal for the relative phase between the QCF field and the local oscillator field
$\hat{S}(r, \theta)$	squeezing operator
$S_h(f)$	power spectral density of the gravitational wave strain
τ	round-trip time or cavity transfer function in transmission
θ	quadrature angle or squeezing angle
$\delta\theta$	phase fluctuations
t	time or amplitude transmissivity
T	power transmissivity or temperature in Kelvin
\mathbf{u}	mode function containing polarization and spatial phase information
$\delta\hat{v}$	fluctuations of the vacuum field \hat{v}
$V(x)$	variance of variable x
$V(\hat{O})$	Variance of operator \hat{O}
V_-	variance of the squeezed quadrature
V_+	variance of the anti-squeezed quadrature
\mathcal{V}	visibility
$W(q, p)$	Wigner function
ξ	homodyne visibility
ξ^2	homodyne efficiency
\hat{X}_1	amplitude quadrature operator
\hat{X}_2	phase quadrature operator
$\hat{X}_{1,a}$	amplitude quadrature of the coherent field \hat{a}
$\hat{X}_{2,a}$	phase quadrature fluctuations of the coherent field \hat{a}
$\delta\hat{X}_{1,a}$	amplitude quadrature fluctuations of the coherent field \hat{a}
$\delta\hat{X}_{2,a}$	phase quadrature fluctuations of the coherent field \hat{a}
$\delta\hat{X}_{\theta,a}$	fluctuations of the coherent field \hat{a} in an arbitrary quadrature with quadrature angle θ
ζ	propagation efficiency

Chapter 1

Introduction

1.1 Historical overview

Only months after Einstein published his theory of gravitation, the General Theory of Relativity in 1915, he predicted the existence of gravitational waves (GWs) [Ein16]. These waves are a direct consequence of the causality of gravity: any change in sources of gravitation has to be distributed in *spacetime* no faster than the speed of light c . A good introduction to general relativity is provided by [MTW73, Sch02]. The first calculations of GW radiation were done by Einstein himself. These contained an error in the calculation which he corrected himself in 1918 [Ein18]. Einstein's final result stands today as the leading-order *quadrupole formula* for GW radiation [FH05]. This formula plays the same role in gravity theory as the dipole formula for electromagnetic radiation does in the theory of electro-magnetism. Here it can be seen that GW and electromagnetic waves are in close analogy to each other. Both are transverse and propagate with the speed of light c . However, GWs originate from accelerated masses while electromagnetic waves are produced by accelerated charges. The lowest order mode of oscillation for both waves is different, GWs are quadrupole waves, whereas electromagnetic waves show a dipole characteristic. The quadrupole formula tells us that the production of a GW is difficult and for a nominal effect to spacetime, very large masses, moving at relativistic speeds are needed. These requirements can only be satisfied by astrophysical events under extreme conditions, such as supernovae stellar explosions, coalescing binary systems (black hole–black hole, neutron star–neutron star, black hole–neutron star, etc.), pulsars, or the stochastic background of the early Universe. A detailed overview of sources of GW radiation can be found in [Tho83, CT02]. While the generation of GWs is difficult, their detection is even harder. Of the four fundamental interactions known today, the gravitational interaction produces the weakest observable effects on earth.

A GW is a distortion of the curvature of spacetime itself. Its amplitude, also often referred to as strain, is given by the dimensionless quantity [AD05]

$$h = \frac{2 \delta L_{\text{GW}}}{L}, \quad (1.1)$$

where δL_{GW} is the change in the distance L between two spacetime events caused by a GW. The strength of the GW radiation depends on the quadrupole moment I and on its

distance r to the source:

$$h = \frac{2G}{c^4} \frac{1}{r} \frac{\partial^2}{\partial t^2} I. \quad (1.2)$$

It is the factor G/c^4 , with G being Newton's gravitational constant and c the speed of light, that makes the GW interaction so weak. As an example for the amplitude of a GW, let us consider a supernova at a distance of 10 kpc. Such a nearby stellar explosion would result in a strain of only about $h \approx 10^{-20}$ when measured on earth. The performance of a GW detector is usually expressed by the linear spectral density \dot{h} , which is given by the square root of the power spectral density.

$$\dot{h} = \sqrt{S_h(f)} \quad [1/\text{Hz}], \quad (1.3)$$

where $S_h(f)$ is the frequency-dependent variance of h within a bandwidth of 1 Hz. For an almost constant h and a detector bandwidth of Δf one obtains

$$\dot{h} \sqrt{\Delta f} = h. \quad (1.4)$$

The extremely small gravitational wave amplitude may have been the reason that even Einstein did not suspect that GWs could ever be detected. Until today no direct detection of a GW has occurred. However, several indirect measurements from binary neutron star systems have been reported with a variation of the mass quadrupole moment large enough that GWs are being emitted. The resulting change in the orbital frequency is on time scales short enough to be observable. The most prominent example is the *Hulse–Taylor* pulsar, PSR1913+16, reported by Hulse and Taylor in 1975 [HT75]. Observations over a period of 30 years clearly showed the decaying orbit of the two neutron stars. The measured effect matches the values predicted by general relativity to extraordinary precision. Hulse and Taylor were awarded the Nobel Prize in 1993 [Hul94, Tay94] for the discovery of PSR1913+16. The analysis of this and other binary systems prove the existence of GWs, beyond a reasonable doubt. What remains is the first direct detection of a GW, before GWs can be used as a tool to investigate astrophysical objects.

1.2 The first gravitational wave detector

It took until the late 1950's when Joseph Weber started to set up an experiment to detect GWs. He was the first to conduct pioneering experiments with so-called *resonant bar detectors*. These detectors use a solid elastic body with a high mechanical quality factor, resulting in a sharp resonance of the body's eigenmode. The idea is that the GW excites this resonance and the elastic vibrations of the mass are measured with a transducer, that translates displacement into an electric signal. In 1969 Weber claimed that he observed a coincidence in his detectors at the University of Maryland and the Argonne National Laboratory [Web69] and concluded to have measured the first GW. This discovery encouraged several groups to set up resonant bar detectors to study GWs. However, it turned out that no-one could reproduce Weber's results. After a thorough analysis it became clear that Weber's detectors were not sensitive enough to measure GWs. Consequently, Weber's claim of a first direct detection was never accepted within the scientific

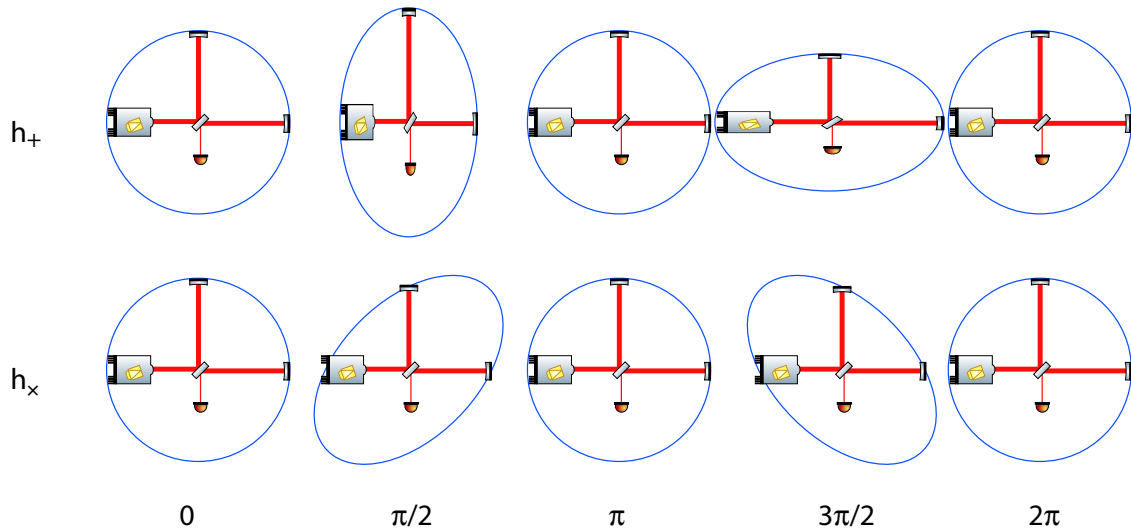


Figure 1.1: The effect of a gravitational wave (GW) on a Michelson interferometer as time evolves. The direction of propagation of the GW is perpendicular to the image plane. The effect is displayed for both polarization modes of the GW. In the case of the $+$ -polarization, the quadrupole characteristic of the GW causes one arm to stretch while the other arm is shortened. It is worth noting that the Michelson interferometer is insensitive to the \times -polarization of the GW.

community. Nevertheless, Weber pioneered the research field of GW detection and since then many scientists have followed in his footsteps.

Groups all over the world started to work with resonant bar detectors and tried to improve their sensitivity ever since. Today several resonant detector projects [AD05] are running: ALLEGRO at Baton Rouge in the USA [HDG⁺02], AURIGA at Legnaro in Italy [VftAC06], EXPLORER at the CERN in Switzerland [ABB⁺06], NAUTILUS at Frascati in Italy [ABB⁺06], Mario Schenberg in São Paulo in Brazil [AAB⁺06] and MiniGRAIL at Leiden in the Netherlands [dWBB⁺06]. They use masses of up to two tons. To minimize thermal noise of the detectors they are typically cooled down to at least liquid helium temperatures and even temperatures of the order of 100 mK are used. These detectors reach peak strain sensitivities from $\dot{h} = 3 \times 10^{-21}/\sqrt{\text{Hz}}$ up to $\dot{h} = 2 \times 10^{-22}/\sqrt{\text{Hz}}$ at their resonances, which are typically of the order of kilohertz. Due to their high Q factors the resonances are very sharp and thus, the detection bandwidth of such a detector is mainly below 100 Hz. Consequently, resonant detectors are not the ideal instrument to perform GW astronomy.

1.3 Gravitational wave detection with laser interferometers

The limited bandwidth of the resonant bar detectors encouraged scientists to use laser interferometers as gravitational wave detectors. The first proposal [GP63] was published in 1963 by Gerstenshtein and Pustovoit in Russia, which included a first estimate of the achievable sensitivity. Collins [Col04] claims Weber and his students considered this

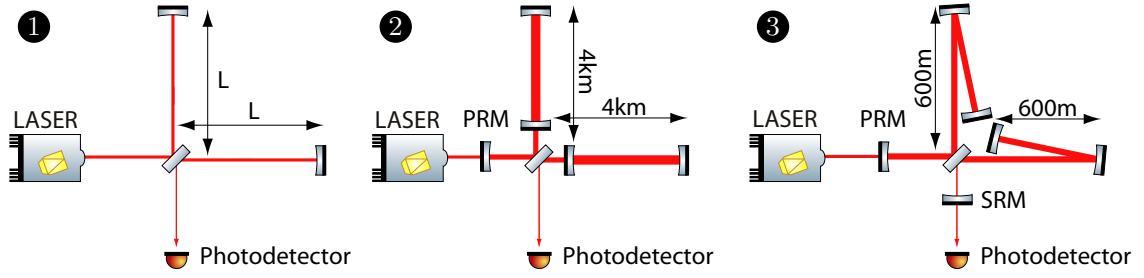


Figure 1.2: Schematic of three different optical layouts of laser interferometric based gravitational wave detectors. All layouts are based on a simple Michelson interferometer, which is displayed in ❶. The second configuration includes power recycling and Fabry-Perot cavities in the arms. This layout is used by the current GW detectors LIGO and VIRGO. The third optical layout is that of GEO 600. It has folded arms to reach a effective arm length of 1200 m and uses power recycling and signal recycling to enhance its sensitivity.

idea independently in 1964. Both groups realized that a laser interferometer is a perfect instrument for detecting GWs. Its major advantage, compared to the resonant detectors, is the broadband detection ability in a frequency band from 10 Hz to some kilohertz.

A GW changes the distance L between two free falling test masses by δL_{GW} . Due to its quadrupole nature, two perpendicularly oriented distances would be changed by the same maximum amount but with different sign if the incoming polarization of the GW is orientated optimally with respect to the two distances. Figure 1.1 shows the two polarization modes of a GW travelling perpendicular to the image plane acting on a simple Michelson based laser interferometer. In an interferometer a laser beam is split into two separate beams by a beam splitter. The two beams propagate individually along the interferometer arms. At the end mirrors, also referred to as test masses, the two light fields are reflected back towards the beam splitter. During this propagation through the interferometer arms, the length change δL_{GW} induces a phase shift between the two light fields of

$$\delta\phi_{\text{GW}} = \frac{4\pi}{\lambda} \delta L_{\text{GW}}. \quad (1.5)$$

Here, λ is the wavelength of the laser. This phase change can be detected with the Michelson interferometer. In the normal operation mode the interferometer arms are adjusted such that all the light is reflected back to the laser source. As a consequence, no light leaves the interferometer at the output port. This so-called *dark port* is controlled by a feedback loop actuating the position of the end mirrors. A GW and its induced phase change of the light fields in the interferometer arms results in a deviation from the dark port condition which can be sensed via a photodetector. Equation 1.1 shows that the sensitivity of such an interferometer depends on the length of its arms. Hence, the longer the detector arms, the better.

The first laser interferometer based GW detector was set up in 1971 under the lead of Forward [MMF71], one of Weber's former coworkers. After Weiss published his analysis of the limiting noise sources of such a laser interferometer [Wei72], a number of groups started to set up prototypes of long baseline GW detectors based on a Michelson interferometer. In the late 1970's at least four groups were running prototype interferometers:

a 30 m one in Garching [SSS⁺88], a 10 m one in Glasgow [NHK⁺86], one at the MIT [LBD⁺86] and a 40 m one at Caltech [Spe86]. These prototypes were mainly used as test facilities to develop techniques that would lead to a successful operation of a large scale Michelson interferometer with arm lengths of 3 to 4 km.

In 1992 the funding of the LIGO Project [AAD⁺92] was approved. This project involves two sites, Livingston, Louisiana and Hanford, Washington. At each site a 4 km interferometer was set up and at the Hanford site an additional 2 km interferometer shares the same vacuum system with the longer one. This project is now close to finish one year of accumulated data taking at design sensitivity. In 1993 the VIRGO project was funded [BFV⁺90]. This French-Italian collaboration has constructed a 3 km interferometer near Pisa, which is close taking science data on a regular basis. The Glasgow and Garching group started collaborating in 1989 and founded the GEO project. It was first planned to build a GW detector in the Harz mountains with an arm length of 3 km [LMR⁺87]. However, this plan was discarded due to financial problems. In 1994 a smaller version, GEO 600, [HtL06] was proposed and its construction started in 1995. GEO 600 is located in Ruthe near Hannover in northern Germany. It uses an arm length of 600 m in conjunction with advanced techniques to achieve a sensitivity comparable to that of the larger LIGO detectors. The TAMA project is located near Tokyo in Japan and started in 1995 [MtTc02]. It utilizes an arm length of 300 m. The schematic of three different interferometer layouts that can be used for GW detection are presented in Figure 1.2.

The second generation of earth-based interferometric GW detectors is currently being planned. It is planned to use laser powers of up to 200 W and to make use of signal recycling or, in the case of Fabry-Perot cavities inside the interferometer arms, the closely related technique of resonant sideband extraction. The mirror mass will be increased to minimize radiation pressure effects in the low-frequency band. The LCGT project [KtLC06] also considers using cryogenic coolers to lower the thermal noise [GC04].

The American second generation detector is called *Advanced LIGO* [Gia05, ADVa]. It will use the existing facilities in Hanford and Livingston. Inspired by the GEO 600 monolithic suspensions, Advanced LIGO will upgrade to quadruple cascaded pendulum suspensions to enlarge the detection band toward lower frequencies. The use of a high-power laser, signal extraction and DC readout [Fri05] will enhance the shot noise limited sensitivity. Overall it is planned to increase the sensitivity compared to initial LIGO by a factor of 10. It is currently planned that Advanced LIGO will take data in 2010/2011. An intermediate step towards Advanced LIGO is Enhanced LIGO [Adh05]. This upgrade of the two initial 4 km GW detectors comprises DC readout and the use of higher laser powers as well as some other modifications. The upgrade to Enhanced LIGO will commence in September 2007.

The VIRGO Collaboration is currently planning its second generation detector *Advanced VIRGO* [ADVb]. It is planned that construction will start in 2011. A minor upgrade of VIRGO to VIRGO+ [Pun05] is scheduled for 2008. This will include for example an upgrade of the laser power and thermal compensation. The optical layout remains unchanged.

The German-British GEO collaboration is aiming for an upgrade of GEO 600 to a high frequency detector called *GEO-HF*. It will use the current GEO 600 infrastructure, such as the vacuum system and optical layout. The circulating light power will be increased by

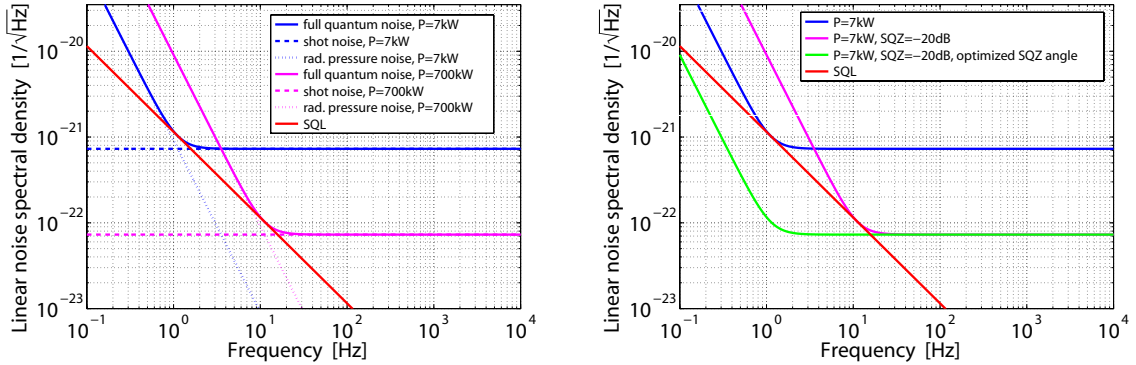


Figure 1.3: Quantum noise limited strain sensitivities of a simple Michelson interferometer plotted for two different circulating light powers (left) and for a squeezed-light-enhanced simple Michelson interferometer (right). If the power is increased by a factor of 100, the shot noise drops and the radiation pressure rises by a factor of 10. The identical result is obtained if a squeezed vacuum with a squeezing strength of 20 dB is injected into the dark port of the interferometer. Only with a proper preparation of the squeezed light can an improvement of the sensitivity over the full bandwidth be achieved. The standard-quantum limit (SQL) for this gravitational wave detector is given in both graphs as a reference (red line).

a factor of 10. To reduce the limiting coating thermal noise, a change of the main optics and the corresponding coatings could be inevitable. Utilizing squeezed light to further reduce the shot noise is also being considered. This would require a filter cavity to compensate the rotation of the squeezing ellipse induced by the reflection at the detuned signal-recycling cavity.

LCGT [KtLC06] is a proposed cryogenic next generation GW detector in Japan with super-attenuator suspensions and a laser with 300 W output power. Its 100 m prototype CLIO [MUY⁺04] is currently set up to demonstrate most of the techniques needed for LCGT.

Currently, the European gravitational wave community is writing a proposal for a design study of a European third generation detector called *ET*, the Einstein gravitational wave telescope, which will be at least a factor of 10 more sensitive than Advanced LIGO and Advanced VIRGO. The aimed peak sensitivity is $\dot{h} = 2 \times 10^{-25} \text{m}/\sqrt{\text{Hz}}$.

The space based GW detector *LISA* [LIS, LIS05] is a combined ESA/NASA project and uses three space crafts in a triangular configuration separated by a distance of five million kilometers. It will measure GWs in the frequency band of 10^{-4} – 10^{-1} Hz. The current schedule predicts the launch of LISA for the year 2017/2018. The LISA technology demonstration mission *LISA Pathfinder* [AAB⁺05] is planned to be launched in late 2009.

The future of laser interferometric gravitational wave detection is very promising. The earth-based detector sensitivities are constantly being improved and space-based detectors will open up new opportunities for GW astronomy.

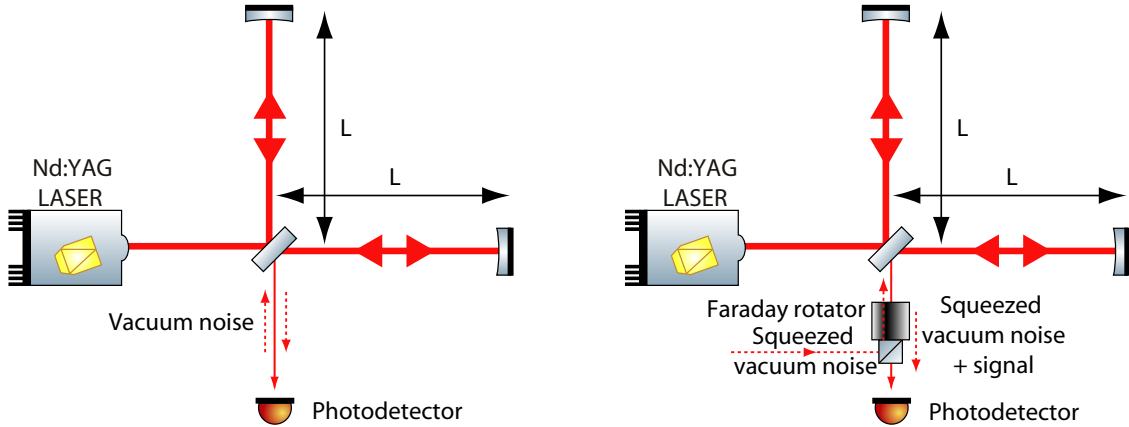


Figure 1.4: Schematic of the layout of a simple Michelson interferometer based GW detector. The left figure shows how the vacuum noise enters through the dark port while the right figure displays how this vacuum can be replaced with squeezed vacuum using a Faraday rotator.

1.4 Noise sources in interferometric gravitational wave detectors

The main noise sources of a laser interferometer based GW detector are [AD05]:

Seismic noise is any kind of ground motion that may displace the test masses. This displacement cannot be distinguished from a signal caused by a GW. Therefore, it is essential to decouple the test masses of the interferometer from the ground. This is achieved with the aid of diverse active and passive seismic isolation systems. The test masses in current GW detectors are suspended with multiple-cascaded pendulum stages. Each pendulum stage suppresses the movement of the test mass proportional to $(1/f)^2$ above its eigenfrequency f_0 , thus acting as a low-pass filter for seismic noise. More details on the suspension system of the GW detector GEO 600 can be found in [Goß04].

Thermal noise can be separated into different sources [RHC05, BGV99]; the three largest for optical substrates are coating thermal noise [CCF⁺04], substrate thermal noise [LT00], and thermorefractive noise [BV01]. The first two result in a displacement of the mirror surface, whereas the thermorefractive noise causes fluctuations in the index of refraction and is therefore important for transmissive optics, such as the beam splitter. Thermal noise also arises from the test-mass suspensions, including the violin modes of the suspension filaments themselves. All of these thermal noises can mask potential GW signals. To avoid this noise deteriorating the GW detection band, materials with a high Q factor are used. These have sharp resonance peaks at their eigenfrequencies concentrating the thermally driven motion within a narrow Fourier-frequency band. It is required to design the suspensions and test masses in a way that all resonances are well outside the detection band. However, thermal noise is expected to set a limit to the sensitivity of next generation GW detectors in the most sensitive frequency band. To further reduce thermal noise the test masses can be cooled to cryogenic temperatures. Currently, the Japanese project LCGT [KtLC06] plans to use cryogenic techniques.

Shot noise and *radiation pressure noise* are both quantum noises that originate from

vacuum noise entering the interferometer through the dark port (see Figure 1.4). These vacuum fluctuations travel through the interferometer, interact with the test masses and are back-reflected towards the photodetector at the dark port. The shot noise contribution to the linear spectral density of the gravitational wave strain amplitude is given by [Sau94]

$$\dot{h}_{\text{s.n.}}(f) = \frac{1}{L} \sqrt{\frac{\hbar c \lambda}{2\pi P}} \quad (1.6)$$

for an interferometer with the arm length L , using a laser wavelength of λ and a total power P inside the interferometer. $\dot{h}_{\text{s.n.}}$ is independent of frequency f . The only parameters influencing $\dot{h}_{\text{s.n.}}$ are the length of the interferometer and the laser power inside. An increase in one of these parameters results in a reduced shot noise contribution to the strain sensitivity. This behavior of the shot noise is displayed in Figure 1.3.

Radiation pressure noise originates from the amplitude fluctuations of the vacuum noise. These fluctuations enter the interferometer through the dark port and lead to a fluctuation of the position of the test masses [BC02]. The contribution from radiation pressure noise to the linear noise spectral density of the gravitational wave strain amplitude, for a simple Michelson interferometer, is given by

$$\dot{h}_{\text{r.p.}}(f) = \frac{1}{m f^2 L} \sqrt{\frac{\hbar P}{2\pi^3 c \lambda}} \quad (1.7)$$

for a given test mass m . In contrast to the frequency independent shot noise contribution, radiation pressure noise falls off as $1/f^2$ slope. Also, the radiation pressure noise contribution rises proportional to \sqrt{P} . This behavior of the radiation pressure noise is presented in Figure 1.3. This figure shows the quantum noise limited sensitivity of a simple Michelson interferometer for a circulating light power of $P = 7 \text{ kW}$ and $P = 700 \text{ kW}$. The increased power results in a reduced shot noise contribution whereas the radiation pressure is increased. Due to the different power scaling a compromise regarding the light power is required to achieve acceptably small contributions from both shot noise and radiation pressure noise. Increasing the mirror test mass can also compensate the rising radiation pressure. In current GW detectors the radiation pressure noise is smaller than the contribution from seismic noise. Nonetheless, radiation pressure noise is expected to limit the sensitivity of Advanced LIGO at lower frequencies.

1.5 Advanced techniques to enhance the quantum noise limited sensitivity of a gravitational wave detector

In the past, diverse advanced techniques and changes in the optical layout have been developed to enhance the sensitivity of a Michelson interferometer based GW detector. The technique of *power recycling* [DHK⁺83] is used in all current GW detectors to enhance the light power inside the interferometer, thereby lowering the shot noise contribution. Power recycling uses an additional mirror, the power-recycling mirror, that is placed between the laser and the interferometer's beam splitter. Due to the fact that GW detectors are stabilized to the dark fringe condition, all the light leaving the interferometer propagates back to the laser. The power-recycling mirror re-uses this otherwise lost light by

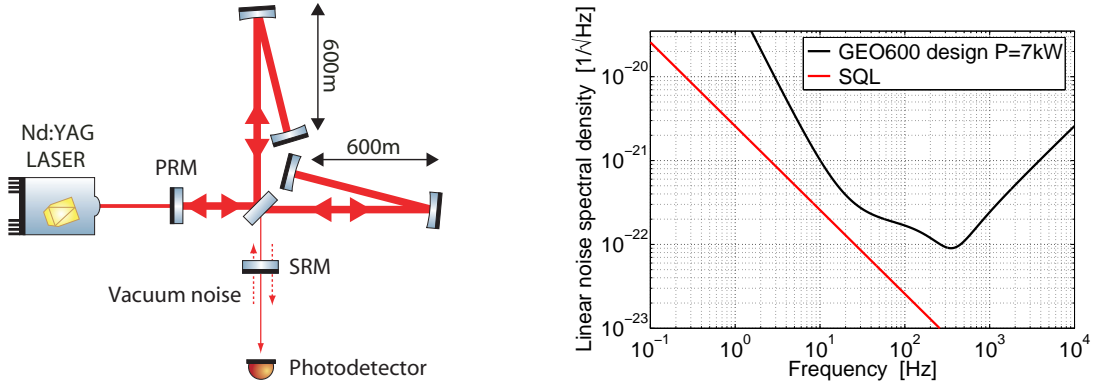


Figure 1.5: Schematic of the optical layout of GEO 600 (left) and its quantum noise limited sensitivity, simulated with the design parameters (right). The SQL for GEO 600 is represented by the red line.

reflecting it back into the interferometer. It forms a cavity, the so-called power-recycling cavity, together with the interferometer, which acts as a compound mirror. This leads to a resonant enhancement of the light power inside the interferometer. It is also possible to use Fabry-Perot cavities inside the interferometer arms to increase the light power. LIGO as well as VIRGO use the combination of power recycling and Fabry-Perot cavities in the arms to lower the shot noise of the detector.

Another advanced technique is *signal recycling* [Mee88]. Signal recycling uses a mirror between the photodetector in the dark port and the beam splitter of the interferometer. This so-called signal-recycling mirror reflects the GW induced signal sidebands, which would otherwise leave the interferometer through the dark port, back into the interferometer. The repeated interaction with the GW at the end mirror test masses enhances the signal sidebands. In contrast to the power-recycling cavity the signal-recycling cavity is normally slightly detuned with respect to the carrier frequency and is resonant for a specific signal-sideband frequency. GEO 600 is the only GW detector that uses *dual recycling*, which is the combination of power and signal recycling, to enhance its sensitivity in the shot noise limited frequency range. Figure 1.5 shows a schematic of the layout of GEO 600 alongside the quantum noise limited design sensitivity for a circulating light power of 7 kW. Due to the use of detuned signal recycling the best sensitivity is achieved around 350 Hz.

This thesis focuses on a third method to enhance the quantum noise limited sensitivity of a GW detector. This method was first suggested by Caves in 1981, who proposed an increased sensitivity of an interferometer using squeezed states of light. The idea is to replace the vacuum fluctuations, which enter the interferometer through the dark port, with a squeezed vacuum to lower the noise contributions in the variable of interest. Figure 1.4 shows that a Faraday rotator is used for the injection of the squeezed field into the dark port of the interferometer. The squeezed field propagates through the interferometer, leaves the interferometer through the dark port, and is eventually detected together with the GW signal by the photodetector.

The Heisenberg uncertainty principle (HUP) allows even for a minimum uncertainty

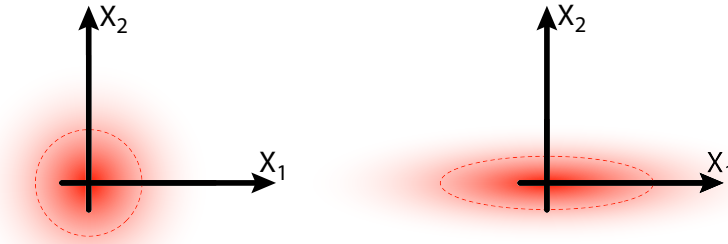


Figure 1.6: Representation of a vacuum (left) and a squeezed vacuum state (right) in quadrature phase space. The noise is equally distributed between the amplitude and phase quadrature in the case of the vacuum state. This changes for a squeezed vacuum state, where the noise in the amplitude quadrature is enlarged and the noise in the phase quadrature is squeezed when compared to the vacuum state. The area of the variance of the distribution is the same for both cases.

state [WM94] to shift the uncertainty between the two noncommuting Hermitian variables from one into the other. In a squeezed light or a squeezed vacuum field the noise distribution is not equally distributed between the two variables as it is in the vacuum state; noise from one variable is relocated into the noncommuting variable in a squeezed vacuum state. A comparison between the vacuum state and a squeezed vacuum state in quadrature phase space is displayed in Figure 1.6. The vacuum state is a minimum uncertainty state with a symmetric 2-D Gaussian distribution. The dashed circle represents the variance of this distribution. In the case of a squeezed vacuum state the noise in one quadrature, here the phase quadrature, is reduced, whereas the noise in the perpendicular quadrature is enhanced such that the area defined by the dashed circle is conserved, due to HUP. In the case of a Michelson interferometer, a phase quadrature squeezed field is needed to enhance the signal-to-noise ratio in the shot noise limited regime. Figure 1.3 presents the resulting sensitivity if a squeezed field, whose noise in the phase quadrature is reduced by 20 dB, is injected into the dark port of the interferometer. The result is the same as if the power of the laser had been increased by a factor of 100. With proper preparation of the squeezed state [KLM⁺01] a reduction of the radiation pressure noise can also be achieved. Hence, an improvement of the sensitivity by a factor of 10 over the whole frequency range can be achieved. Chapter 4 shows that more complex optical layouts and advanced interferometer techniques, such as detuned signal recycling, require a more complex preparation of the injected squeezed field.

The first demonstration of squeezed states was achieved by Slusher *et al.* in 1985 [SHY⁺85]. The squeezing in this experiment was produced by four-wave mixing. Today the most prominent source is optical parametric amplification (OPA), which was used as a source for squeezed light throughout this thesis. Since the first generation of squeezed light this research area has evolved and is now at a state at which squeezing becomes a tool for various applications, including GW detection.

1.6 Structure of the thesis

The aim of this thesis is to demonstrate the compatibility of squeezed light with advanced interferometer techniques for GW detection. The structure follows a logical order to provide the understanding of the basic principles of squeezing before the individual steps, necessary for the enhancement of a future GW detector, are presented in detail.

Chapter 2 provides an overview of the quantum nature of light. Various detection schemes are illustrated as well as a new approach to understand squeezing in the sideband picture. This chapter closes with some calculations of squeezing concerning various loss mechanisms and efficiencies of the components required to generate and detect squeezing.

A typical experiment for the generation and detection of squeezed light is presented in Chapter 3. It comprises all the required elements such as laser, second harmonic generator (SHG), OPA and homodyne detector. The theory behind the second harmonic generation and optical parametric amplification is explained and some measured squeezing spectra are presented.

Chapter 4 will focus on the generation and characterization of frequency-dependent squeezed light. This is needed for the application of squeezed light in GW detection. GEO 600 uses—and future detectors will use—detuned signal-recycling cavities. Hence, the effects on the squeezed field reflected at such a detuned cavity, thereby becoming frequency-dependent, have to be understood beforehand. This chapter includes the theoretical description of frequency-dependent squeezed states of light. These will be characterized by their spectra as well as by their reconstructed Wigner functions, which have been obtained by tomography.

In Chapter 5 the first experimental demonstration of a squeezed-light enhanced dual-recycled Michelson interferometer will be explained in detail. This experiment uses a filter cavity to prepare the squeezed light, which is to be reflected from the detuned Michelson interferometer, in such a way that frequency dependence is compensated. Hence, the resulting squeezing enhanced signal-to-noise ratio is improved across the whole frequency range of interest. Special attention will be given to the locking scheme of the dual-recycled Michelson interferometer.

To cover all topics needed to enhance a current or future GW detector via squeezed light, an experiment to generate squeezed light at frequencies inside the detection band of earth-based GW detectors is described in Chapter 6.

The topic of Chapter 7 is the future application of squeezed light in the next generation detector GEO-HF. Following the proposed increase in laser power, further improvements in the sensitivity by using squeezed-light injection is simulated and compared to the design sensitivity of GEO 600. This includes the calculation of parameters for different filter cavity designs and considerations about the implementation of such a filter cavity into the current vacuum system.

Chapter 2

Quantum nature of light

Introduction

This chapter focuses on the quantum properties and aspects of light. The mathematical tools from quantum mechanics will be used to describe light fields or states in quadrature space. In addition to coherent states, which describe a classical laser beam, the Heisenberg uncertainty principle allows another class of quantum states; the so-called squeezed states of light. Part of the topic of this thesis is the detailed analysis of such squeezed states. In the following different physical pictures are introduced to facilitate an intuitive understanding of squeezed light. In this chapter the reader is introduced to theoretical concepts and their application in the laboratory. The section *detection schemes* comprises an explanation of how spectral analysis is done and shot noise can be analyzed. This knowledge is essential in the section *calculation of the squeezing*, where different loss effects are taken into account and their effects to the squeezing are analyzed.

2.1 The quantization of the electric field

In general, the properties and behavior of light propagating in free space is described by Maxwell's equations. From these one can derive [WM94] the electromagnetic field as a function of position \mathbf{r} and time t

$$\mathbf{E}(\mathbf{r}, t) = i \sum_j \left(\frac{\hbar\omega}{2\epsilon_0} \right)^{\frac{1}{2}} [a_j \mathbf{u}_j(\mathbf{r}) e^{-i\omega_j t} - a_j^* \mathbf{u}_j^*(\mathbf{r}) e^{+i\omega_j t}] . \quad (2.1)$$

Here \mathbf{u}_j are the mode functions which contain polarization and spatial phase information, \hbar is Planck's constant, ω is the angular frequency, ϵ_0 is the electric permittivity of the vacuum, and j is the index of the mode. The normalization factor has been chosen such that the complex amplitudes a_j and a_j^* are dimensionless. In the classical electromagnetic theory these Fourier amplitudes are complex numbers. The quantization is done via a canonical quantization which changes the complex amplitudes to the mutually adjoint operators \hat{a}_j and \hat{a}_j^\dagger . Due to the bosonic character of photons, the operators \hat{a}_j and \hat{a}_j^\dagger

follow the bosonic commutation relations

$$\begin{aligned} [\hat{a}_j, \hat{a}_{j'}] &= 0 \\ [\hat{a}_j^\dagger, \hat{a}_{j'}^\dagger] &= 0 \\ [\hat{a}_j, \hat{a}_{j'}^\dagger] &= \delta_{jj'} . \end{aligned} \quad (2.2)$$

The quantization transforms the electric field to become an ensemble of individual and independent harmonic oscillators with frequency ω_j obeying the above commutation relations. Each of these oscillators describes the dynamical behavior of one individual mode independently of the other modes. The quantum state of each mode can be described by a state vector $|\psi\rangle_j$ of the Hilbert space corresponding to the mode j . The state of the entire field is then defined in the tensor product space of the Hilbert spaces for all the modes.

The classical Hamiltonian for the electromagnetic field in Equation 2.1 is given by

$$\mathcal{H} = \frac{1}{2} \int \left(\varepsilon_0 \mathbf{E} + \frac{\mathbf{B}^2}{\mu_0} \right) dV , \quad (2.3)$$

where \mathbf{B} is the magnetic field vector, and ε_0 and μ_0 are the electrical permittivity and the magnetic permeability of the vacuum, respectively.

Using the canonical quantization of \mathcal{H} and the boundary conditions of the mode functions \mathbf{u}_j together with Equation 2.1 and the equivalent expression for \mathbf{B} the quantized Hamilton operator is given by

$$\hat{\mathcal{H}} = \sum_j \hbar\omega_j \left(\hat{a}_j^\dagger \hat{a}_j + \frac{1}{2} \right) . \quad (2.4)$$

This Hamiltonian represents the number of photons in each mode j multiplied by the according photon energy $\hbar\omega_j$. The additional energy $\frac{1}{2}\hbar\omega_j$ represents the zero-point energy of the harmonic oscillator. In the following different representations of the electromagnetic field will be considered.

2.2 Fock states

The eigenvalues of the Hamiltonian given in Equation 2.4 are $\hbar\omega_j(n_j + \frac{1}{2})$, where n_j is a positive integer number $n_j \in \mathbb{N}$. The corresponding eigenstates $|n_j\rangle$ are known as number or Fock states. They are eigenstates of the number operator $\hat{n}_j = \hat{a}_j^\dagger \hat{a}_j$ so that [WM94]

$$\hat{n}_j |n_j\rangle = n_j |n_j\rangle . \quad (2.5)$$

The vacuum state, which is the ground state of the harmonic oscillator, is defined by

$$\hat{n}_j |0\rangle = 0 . \quad (2.6)$$

Combined with Equation 2.4 this results in the ground state energy

$$\langle 0 | \hat{\mathcal{H}} | 0 \rangle = \frac{1}{2} \sum_j \hbar\omega_j . \quad (2.7)$$

Each oscillator at frequency j has a non-zero energy, which gives rise to the vacuum fluctuations as will be shown in Section 2.5. This non vanishing zero-point energy results in the fact, that the energy of the vacuum state is infinite, which is a conceptual difficulty of quantum field theory. However, since experiments measure only changes in the total energy of the electromagnetic field the infinite zero-point energy does not lead to any divergence.

The raising and lowering operators \hat{a}_j^\dagger and \hat{a}_j of the harmonic oscillator describe the creation and annihilation of photons. Application of these operators to number states yields:

$$\begin{aligned}\hat{a}_j|n_j\rangle &= \sqrt{n_j}|n_j-1\rangle \\ \langle n_j|\hat{a}_j^\dagger &= \langle n_j+1|\sqrt{n_j+1}.\end{aligned}\tag{2.8}$$

Hence, they are referred to as annihilation and creation operators.

All higher excited states can be obtained by a successive application of the creation operator to the vacuum state successively

$$\langle n_j| = \langle 0|\frac{(\hat{a}_j^\dagger)^{n_j}}{\sqrt{n_j!}}, \quad n_j = 0, 1, 2, \dots.\tag{2.9}$$

The number states are orthogonal

$$\langle n_j|m_j\rangle = \delta_{nm}\tag{2.10}$$

and complete

$$\sum_{n_j=0}^{\infty} |n_j\rangle\langle n_j| = 1.\tag{2.11}$$

The eigenstates $|n_j\rangle$ form a complete set of basis vectors for a Hilbert space.

The number states are particularly useful in e.g. high energy physics where the number of photons is small. In most optical fields the number of photons is high and thus, the fields are either a superposition or a mixture of number states.

2.3 Coherent states

Laser light, as commonly used in quantum optics experiments, are represented by coherent states $|\alpha\rangle$, where α is a complex number. In contrast to the number states, where the photon number is known accurately but the phase remains unknown, knowledge about both the amplitude and phase of a coherent state can be obtained. However, the Heisenberg uncertainty principle (HUP) puts an upper bound on the accuracy of this knowledge.

The generation of a coherent state is described by the displacement operator $\hat{D}(\alpha)$ [Whi97] acting on the vacuum state

$$|\alpha_j\rangle = \hat{D}(\alpha_j)|0_j\rangle,\tag{2.12}$$

with

$$\hat{D}(\alpha_j) = e^{\alpha_j \hat{a}_j^\dagger - \alpha_j^* \hat{a}_j}, \quad (2.13)$$

where α_j is an arbitrary complex number. Coherent states are eigenstates of the annihilation and creation operators \hat{a}_j and \hat{a}_j^\dagger

$$\begin{aligned} \hat{a}_j |\alpha_j\rangle &= \alpha_j |\alpha_j\rangle \\ \langle \alpha_j | \hat{a}_j^\dagger &= \langle \alpha_j | \alpha_j^*. \end{aligned} \quad (2.14)$$

Thereby, illustrating that the naming convention of these operators is very poor with respect to coherent states as they neither annihilate nor create coherent states.

An operator \hat{O} is Hermitian if $\hat{O} = \hat{O}^\dagger$. This requires its eigenvalues to be real. Since the annihilation and creation operators are non-Hermitian their eigenvalues α_j and α_j^* are complex.

Coherent states can be expressed in terms of number states as

$$|\alpha_j\rangle = e^{-\frac{|\alpha_j|^2}{2}} \sum_{n_j=0}^{\infty} \frac{\alpha_j^{n_j}}{\sqrt{n_j!}} |n_j\rangle. \quad (2.15)$$

Note that the frequency index j is kept to see that in a freely propagating field, which does not carry any classical noise or technical noise, every mode j is still a coherent state that carries quantum noise. This feature is discussed in more detail when the sideband picture is introduced (Figure 2.10).

The mean value of the photon number \bar{n}_j of the coherent state $|\alpha_j\rangle$ is given by [Whi97]

$$\begin{aligned} \bar{n}_j &\equiv \langle n_j \rangle = \langle \alpha_j | n_j | \alpha_j \rangle \\ &= \langle \alpha_j | \hat{a}_j^\dagger \hat{a}_j | \alpha_j \rangle \\ &= \langle \alpha_j | \alpha_j^* \alpha_j | \alpha_j \rangle \\ &= |\alpha_j|^2 \langle \alpha_j | \alpha_j \rangle \\ &= |\alpha_j|^2. \end{aligned} \quad (2.16)$$

The probability distribution of the photons in the coherent state is Poissonian:

$$P(n_j) = |\langle n_j | \alpha_j \rangle|^2 = e^{-\langle n_j \rangle} \frac{\langle n_j \rangle^{n_j}}{n_j!}. \quad (2.17)$$

By definition, the values for the mean and the variance are identical for a Poissonian

distribution. The variance of a quantum observable \hat{O} of a state $|\psi\rangle$ is given by

$$\begin{aligned}
 V(\hat{O})_\psi &= \langle \Delta\hat{O} \rangle_\psi^2 \\
 &= \langle \psi | \left(\hat{O} - \langle \hat{O} \rangle_\psi \right)^2 | \psi \rangle \\
 &= \langle \psi | \left(\hat{O}^2 - 2\langle \hat{O} \rangle_\psi \hat{O} + \langle \hat{O} \rangle_\psi^2 \right) | \psi \rangle \\
 &= \langle \psi | \hat{O}^2 | \psi \rangle - \langle \psi | 2\langle \hat{O} \rangle_\psi \hat{O} | \psi \rangle + \langle \psi | \langle \hat{O} \rangle_\psi^2 | \psi \rangle \\
 &= \langle \hat{O}^2 \rangle_\psi - 2\langle \hat{O} \rangle_\psi \langle \hat{O} \rangle_\psi + \langle \hat{O} \rangle_\psi^2 \\
 &= \langle \hat{O}^2 \rangle_\psi - \langle \hat{O} \rangle_\psi^2,
 \end{aligned} \tag{2.18}$$

where $\langle \hat{O} \rangle_\psi = \langle \psi | \hat{O} | \psi \rangle$ and $\langle \hat{O}^2 \rangle_\psi = \langle \psi | \hat{O}^2 | \psi \rangle$. The positive square root of the variance is known as the uncertainty (or standard deviation)

$$(\Delta\hat{O})_\psi = \sqrt{\langle \hat{O}^2 \rangle_\psi - \langle \hat{O} \rangle_\psi^2}. \tag{2.19}$$

Now the variance of the photon number of a coherent state $|\alpha\rangle$ can be derived:

$$\begin{aligned}
 V(\hat{n}_j)_{\alpha_j} &= \langle \alpha_j | \hat{n}_j^2 | \alpha_j \rangle - \langle \alpha_j | \hat{n}_j | \alpha_j \rangle^2 \\
 &= \langle \alpha_j | \left(\hat{a}_j^\dagger \hat{a}_j \right)^2 | \alpha_j \rangle - \langle \alpha_j | \hat{a}_j^\dagger \hat{a}_j | \alpha_j \rangle^2 \\
 &= \langle \alpha_j | \hat{a}_j^\dagger \hat{a}_j \hat{a}_j^\dagger \hat{a}_j | \alpha_j \rangle - |\alpha_j|^4 \\
 &= \langle \alpha_j | \hat{a}_j^\dagger \hat{a}_j | \alpha_j \rangle + \langle \alpha_j | \hat{a}_j^\dagger \hat{a}_j^\dagger \hat{a}_j \hat{a}_j | \alpha_j \rangle - |\alpha_j|^4 \\
 &= |\alpha_j|^2 + |\alpha_j|^4 - |\alpha_j|^4 \\
 &= \bar{n}_j,
 \end{aligned} \tag{2.20}$$

which proves that for a Poissonian distribution the variance equals the mean. For the vacuum state $|0\rangle$, we also find

$$\bar{n}_j = \langle 0 | \hat{n}_j | 0 \rangle = 0 \tag{2.21}$$

$$V(\hat{n}_j)_0 = \langle 0 | \hat{n}_j^2 | 0 \rangle - \langle 0 | \hat{n}_j | 0 \rangle^2 = 0. \tag{2.22}$$

Thus, one can be sure that the vacuum state does not contain a photon.

2.4 Quadrature operators

The description of an electromagnetic field, as given in Equation 2.1, can be rewritten for a field with a certain frequency [BR03] as

$$\mathbf{E}(\mathbf{r}, t) = E_0 \left[a(\mathbf{r})e^{-i\omega t} - a(\mathbf{r})^*e^{+i\omega t} \right] \mathbf{p}(\mathbf{r}). \tag{2.23}$$

The complex amplitude $a(\mathbf{r}) = a_0(\mathbf{r})e^{i\phi(\mathbf{r})}$ contains the phase information of the wavefront as well as the absolute phase with respect to a reference wave. Because the wavefront is only interesting for phenomena like interference and diffraction, it is useful to have a description which only contains the absolute phase. An equivalent form of Equation 2.23 can be expressed as

$$\mathbf{E}(\mathbf{r}, t) = E_0 [X_1 \cos(\omega t) - X_2 \sin(\omega t)] \mathbf{p}(\mathbf{r}, t). \quad (2.24)$$

Here $\mathbf{p}(\mathbf{r}, t)$ is the polarization vector and X_1 and X_2 are the quadrature amplitudes, which are proportional to the complex amplitude

$$\begin{aligned} X_1(\mathbf{r}) &= a^*(\mathbf{r}) + a(\mathbf{r}) \\ X_2(\mathbf{r}) &= i[a^*(\mathbf{r}) - a(\mathbf{r})]. \end{aligned} \quad (2.25)$$

The absolute phase is then given by

$$\phi = \tan^{-1} \left(\frac{X_2}{X_1} \right). \quad (2.26)$$

If the above considerations are applied to the quantized form of the electromagnetic field, the quadrature operators

$$\begin{aligned} \hat{X}_1 &= \hat{a}^\dagger + \hat{a} \\ \hat{X}_2 &= i(\hat{a}^\dagger - \hat{a}) \end{aligned} \quad (2.27)$$

are found. Namely, these are the amplitude quadrature operator \hat{X}_1 and the phase quadrature operator \hat{X}_2 . Any quadrature between the amplitude and phase quadrature can be defined by

$$\begin{aligned} \hat{X}_\theta &= \hat{X}_1 \cos(\theta) + \hat{X}_2 \sin(\theta) \\ &= \hat{a}^\dagger e^{i\theta} + \hat{a} e^{-i\theta} \end{aligned} \quad (2.28)$$

with the quadrature angle θ .

2.5 The Heisenberg uncertainty principle

For two noncommuting Hermitian operators \hat{P} and \hat{Q} one cannot simultaneously measure their physical quantities P and Q with arbitrary precision. This is known as the Heisenberg uncertainty principle [Hei27]:

$$\Delta\hat{P}\Delta\hat{Q} \geq \frac{1}{2} |\langle [\hat{P}, \hat{Q}] \rangle|. \quad (2.29)$$

From Equation 2.29 it is clear that the smaller the uncertainty in the observable \hat{P} the greater the uncertainty in the observable \hat{Q} .

The commutator for the quadrature operators is given by

$$[\hat{X}_1, \hat{X}_2] = 2i. \quad (2.30)$$

In conjunction with $|\langle [\hat{X}_1, \hat{X}_2] \rangle| = 2$ the uncertainty relation for the quadrature operators follows

$$\Delta\hat{X}_1\Delta\hat{X}_2 \geq 1. \quad (2.31)$$

When considering a vacuum state and its variance of the amplitude and phase quadrature we could naively expect to find zero for the quadrature variances as it is the case for the uncertainty and number of photons. However, the Heisenberg uncertainty principle forbids this. The variance of the amplitude quadrature of the vacuum state is given by [Whi97]

$$\begin{aligned} V(\hat{X}_1)_0 &= \langle \Delta\hat{X}_1 \rangle_0^2 \\ &= \langle 0 | \Delta\hat{X}_1^2 | 0 \rangle \\ &= \langle 0 | \hat{X}_1^2 | 0 \rangle - \langle 0 | \hat{X}_1 | 0 \rangle^2 \\ &= \langle 0 | (\hat{a} + \hat{a}^\dagger)^2 | 0 \rangle - \langle 0 | (\hat{a} + \hat{a}^\dagger) | 0 \rangle^2 \\ &= \langle 0 | \hat{a}^2 + \hat{a}\hat{a}^\dagger + \hat{a}^\dagger\hat{a} + \hat{a}^{\dagger 2} | 0 \rangle - 0 \\ &= 0 + \langle 0 | (1 + \hat{a}^\dagger\hat{a}) | 0 \rangle + 0 + 0 \\ &= 1 \\ \langle \Delta\hat{X}_1 \rangle_0 &= 1. \end{aligned} \quad (2.32)$$

And similarly for its phase quadrature:

$$\begin{aligned} V(\hat{X}_2)_0 &= 1 \\ \langle \Delta\hat{X}_2 \rangle_0 &= 1. \end{aligned} \quad (2.33)$$

The index 0 stands for the state of interest, in this case the vacuum state $|0\rangle$. As a result we find that the vacuum state is noisy. This noise arises due to the zero-point energy of $\frac{1}{2}\hbar\omega$ of the quantum harmonic oscillator at each frequency (mode) of the electromagnetic field. Throughout this thesis the noise level of the vacuum state is referred to as vacuum noise or shot noise.

It is of particular interest to compare the uncertainty of a coherent state to the uncertainty of a vacuum state. The variance of the amplitude quadrature of a coherent state

is

$$\begin{aligned}
 V(\hat{X}_1)_\alpha &= \langle \Delta \hat{X}_1 \rangle_\alpha^2 \\
 &= \langle \alpha | \Delta \hat{X}_1^2 | \alpha \rangle \\
 &= \langle \alpha | \hat{X}_1^2 | \alpha \rangle - \langle \alpha | \hat{X}_1 | \alpha \rangle^2 \\
 &= \langle \alpha | (\hat{a} + \hat{a}^\dagger)^2 | \alpha \rangle - \langle \alpha | (\hat{a} + \hat{a}^\dagger) | \alpha \rangle^2 \\
 &= \langle \alpha | \hat{a}^2 + \hat{a}\hat{a}^\dagger + \hat{a}^\dagger\hat{a} + \hat{a}^{\dagger 2} | \alpha \rangle - \left(\langle \alpha | \hat{a} | \alpha \rangle + \langle \alpha | \hat{a}^\dagger | \alpha \rangle \right)^2 \\
 &= \langle \alpha | \hat{a}^2 | \alpha \rangle + \langle \alpha | (1 + \hat{a}^\dagger\hat{a}) | \alpha \rangle + \langle \alpha | \hat{a}^\dagger\hat{a} | \alpha \rangle + \langle \alpha | \hat{a}^{\dagger 2} | \alpha \rangle - (\alpha + \alpha^*)^2 \\
 &= \alpha^2 + 1 + |\alpha|^2 + |\alpha|^2 + \alpha^{*2} - (\alpha^2 + 2|\alpha|^2 + \alpha^{*2}) \\
 &= 1,
 \end{aligned} \tag{2.34}$$

and similarly for the phase quadrature:

$$V(\hat{X}_2)_\alpha = 1. \tag{2.35}$$

This is exactly the same results as for the vacuum state. Both—the coherent states and the vacuum state—fulfill the special case of the Heisenberg uncertainty principle

$$\langle \Delta \hat{X}_1 \rangle_\alpha \langle \Delta \hat{X}_2 \rangle_\alpha = 1. \tag{2.36}$$

All states satisfying this equation are known as minimum uncertainty states.

2.6 Squeezed states

Squeezed states are a special class of minimum uncertainty states. Even though squeezed states obey Equation 2.36 the uncertainty is not equally distributed among the two quadratures. In fact the uncertainty of one quadrature is reduced at the expense of the other.

Any of the quadratures defined by Equation 2.28 can be smaller than vacuum noise. In this case the quadrature is *squeezed* while its complementary quadrature is *anti-squeezed*.

There exist two types of minimum uncertainty squeezed states which obey Equation 2.36: The squeezed vacuum state and bright squeezed states. Mathematically speaking, a squeezed vacuum state is generated by applying the squeezing operator $\hat{S}(r, \theta)$ [WM94]

$$\hat{S}(r, \theta) = \exp\left(\frac{1}{2}re^{-2i\theta}\hat{a}^2 - \frac{1}{2}re^{2i\theta}\hat{a}^{\dagger 2}\right) \tag{2.37}$$

to the vacuum state $|0\rangle$, resulting in

$$|0, r, \theta\rangle = \hat{S}(r, \theta)|0\rangle. \tag{2.38}$$

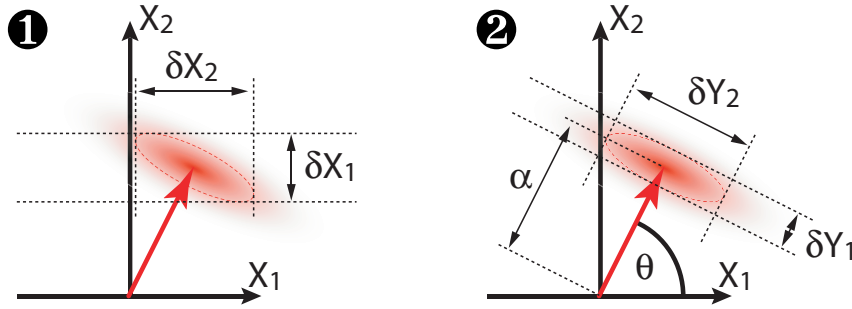


Figure 2.1: A bright squeezed state in the quantum phase picture (see Section 2.7). **1** shows the bright squeezed state with its variances measured in the \hat{X}_1, \hat{X}_2 coordinate system. **2** shows the same state, but the measurement of the variances is done in a new coordinate system \hat{Y}_1, \hat{Y}_2 which is co-aligned with the coherent amplitude to measure the maximum amount of squeezing and anti-squeezing.

A bright squeezed state is, however, defined by

$$|\alpha, r, \theta\rangle = \hat{D}(\alpha)\hat{S}(r, \theta)|0\rangle, \quad (2.39)$$

where $\hat{D}(\alpha) = e^{\alpha\hat{a}^\dagger - \alpha^*\hat{a}}$ is the displacement operator, r is the squeezing factor and θ is the quadrature angle of the squeezing: $\theta = 0$ corresponds to amplitude squeezing and $\theta = \pi/2$ to phase squeezing. It is worth mentioning that a bright squeezed state is generated by first squeezing the vacuum and then displacing it. In Figure 2.1 we see an arbitrary bright squeezed state in the quadrature space. We can define new quadrature operators \hat{Y}_1 and \hat{Y}_2 [Whi97], which are rotated with respect to the amplitude and phase quadrature. These define a rotated complex amplitude β

$$\begin{aligned} \beta &= \alpha e^{i\theta} \\ &= \frac{1}{2} \left(\langle \hat{X}_1 \rangle + i \langle \hat{X}_2 \rangle \right) e^{i\theta} \\ &= \frac{1}{2} \left(\langle \hat{Y}_1 \rangle + i \langle \hat{Y}_2 \rangle \right). \end{aligned} \quad (2.40)$$

The squeezing operator attenuates one of the newly defined quadrature operators, whereas the other one gets amplified by $\hat{S}(r, \theta)$. The degree of amplification and attenuation is given by the squeezing factor r . The uncertainties of the rotated quadratures of the squeezed state are given by

$$\begin{aligned} \langle \Delta \hat{Y}_1 \rangle_{\alpha, r} &= e^{+r} \\ \langle \Delta \hat{Y}_2 \rangle_{\alpha, r} &= e^{-r}, \end{aligned} \quad (2.41)$$

which fulfill the minimum uncertainty relation provided in Equation 2.36.

If we calculate the photon number of a squeezed state, we find

$$\langle \hat{n} \rangle_{\alpha, r} = |\alpha|^2 + \sinh^2(r), \quad (2.42)$$

which is slightly increased compared to the photon number of a coherent state. Interestingly the squeezed vacuum state ($\alpha = 0$) contains photons and therefore it contains more energy than the vacuum state. This implies that it requires energy to alter the uncertainty circle of the quantum noise limited states, regardless of whether they are vacuum or coherent states.

2.7 The quantum phasor picture

It is always useful to have a certain picture to explain a complex physical situation. The quantum phasor picture is such a picture for a quantum state of light. It is a mixture of the classical phasor picture, known in classical physics for the electro-magnetic field, and the quantum noise properties of light. Figure 2.2 displays how one can interpret the quantum phasor picture [Lam98]. The large red arrow represents the classical steady state field vector in the former complex plane

$$\boldsymbol{\alpha} = \alpha e^{i\theta}. \quad (2.43)$$

The small arrows attached to the end of the classical field vector represent the quantum noise in the quadrature plane. Hence, these small arrows represent the uncertainty of the quadrature operators. Each small arrow changes its length and its angle θ_{qn} from one time step to the next time step because every time a different quantum state from an ensemble is contributing. Thus, the quantum state given by the sum of the long (coherent) arrow and the short (quantum) arrow does change in time. From Equations 2.32–2.35 we know that the variance of the quadrature operators for the vacuum state as well as for the coherent states is equal to unity. This allows to represent the quantum noise by a two dimensional Gaussian distribution with a variance of one, sitting on top of the classical phasor that represents the coherent amplitude. The circle that is overlapping the Gaussian noise represents the variance of the Gaussian distribution. Together they form the quantum phasor picture. One should keep in mind that the quantum noise distribution, decomposed of the small quantum arrows, evolves in time.

The quantum phasor picture has a frequency dependence such that it can be drawn for every frequency $\omega > 0$ (or mode j), representing the classical field amplitude and the quantum noise of a field with that specific frequency ω . Figure 2.3 shows the representation of four different quantum states of light in the quantum phasor picture. The vacuum state is just a two dimensional Gaussian distribution in quadrature phase space, its coherent amplitude is zero. The amplitude squeezed state is easily recognized by its elliptical shape of the quantum noise. If the amplitude quadrature is squeezed the phase quadrature must be anti-squeezed so that the squeezed state is in accordance with the HUP (see Equation 2.41).

2.8 Linearization

In quantum optics the linearization of the operators facilitates a more intuitive interpretation. The linearization leads to simpler mathematical expressions in the case of bright beams, i.e. the amplitude is much larger than the fluctuations [Whi97]. Hence,

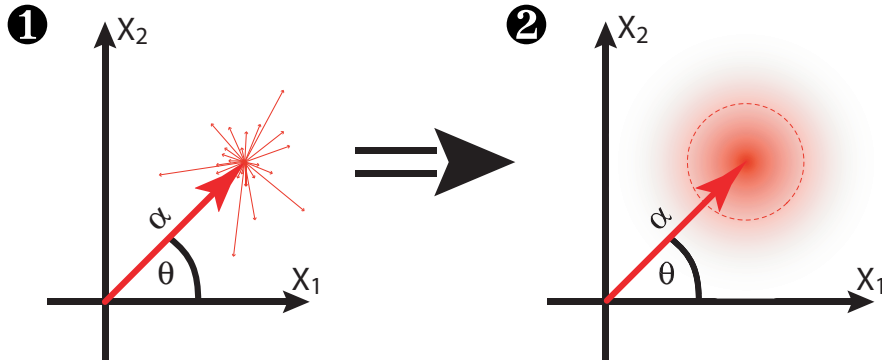


Figure 2.2: Illustrative figure to explain the quantum phasor picture. The large red arrow in **1** represents the classical steady state solution of the field vector in the quadrature phase space. Its length is α and the angle to the amplitude quadrature axis is given by θ . The small arrows on top of the classical phasor represent the quantum noise in the quadrature plane. Each of these arrows represents quantum noise contributions from a different member of an ensemble of quantum states. The quantum noise arrow does change its length and phase θ_{qn} indeterministically with time. The distribution of the quantum noise arrows is Gaussian. They are replaced by a two-dimensional Gaussian distribution in **2**. The dashed circle marks the variance of this distribution.

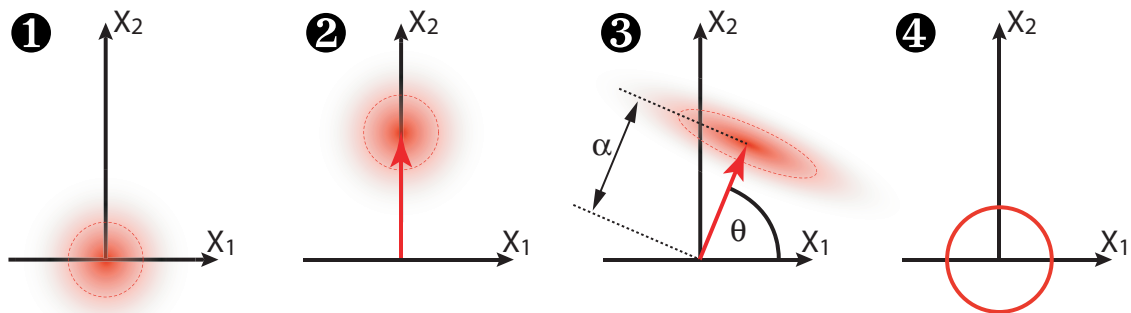


Figure 2.3: The representation of four different quantum states of light in the quantum phasor picture. Namely these are **1** the vacuum state, **2** a coherent state, **3** an amplitude squeezed state and **4** a Fock state.

we can decompose operators into two components, one is a complex-number representing the steady state solution whereas the other is an operator which contains only the time dependent fluctuations. For the annihilation and creation operators follows

$$\begin{aligned}\hat{a} &= \alpha + \delta\hat{a} \\ \hat{a}^\dagger &= \alpha^* + \delta\hat{a}^\dagger.\end{aligned}\tag{2.44}$$

Here, α and α^* are complex numbers corresponding to the steady state solution of the field or the field amplitude. $\delta\hat{a}$ and $\delta\hat{a}^\dagger$ are the time-dependent fluctuations of the field. It is worth noting that by definition $\langle \delta\hat{a} \rangle = 0$, $\langle \hat{a} \rangle = \alpha$, and respectively $\langle \delta\hat{a}^\dagger \rangle = 0$, $\langle \hat{a}^\dagger \rangle = \alpha^*$. In conjunction with Equation 2.27 one finds

$$\begin{aligned}\delta\hat{X}_1 &= \delta\hat{a}^\dagger + \delta\hat{a} \\ \delta\hat{X}_2 &= i(\delta\hat{a}^\dagger - \delta\hat{a}).\end{aligned}\tag{2.45}$$

This is the mathematical equivalent of the quantum noise distribution in the quantum phasor picture described in the previous section.

To see the applicability of the linearized quadrature operators one should have a look on the number operator

$$\begin{aligned}\hat{n} &= \hat{a}^\dagger\hat{a} \\ &= (\alpha^* + \delta\hat{a}^\dagger)(\alpha + \delta\hat{a}) \\ &= |\alpha|^2 + \alpha^*\delta\hat{a} + \alpha\delta\hat{a}^\dagger + \delta\hat{a}^\dagger\delta\hat{a}.\end{aligned}\tag{2.46}$$

To obtain the linearized version of this equation, we have to neglect the higher order term $\delta\hat{a}^\dagger\delta\hat{a}$. Using Equation 2.45 and choosing α to be real, we can write

$$\begin{aligned}\hat{n} &= n + \delta\hat{n} \\ \hat{n} &\approx \alpha^2 + \alpha\delta\hat{X}_1,\end{aligned}\tag{2.47}$$

thereby applying the linearization. The resulting equation for the photon number operator corresponds to the fact that the number of photons is proportional to the square of the amplitude and the quantum noise scales linearly with the amplitude of the field (or linearly to the square root of the power).

2.9 Detection schemes

The following section describes how light is detected and how its physical properties can be accessed by using different detection schemes.

2.9.1 Direct detection

The simplest way of detecting light is a direct measurement using a semiconductor photodiode (see Figure 2.4). The photodiode converts the intensity of the light into a photocurrent which is the same as to say that it converts the photons into electrons with a

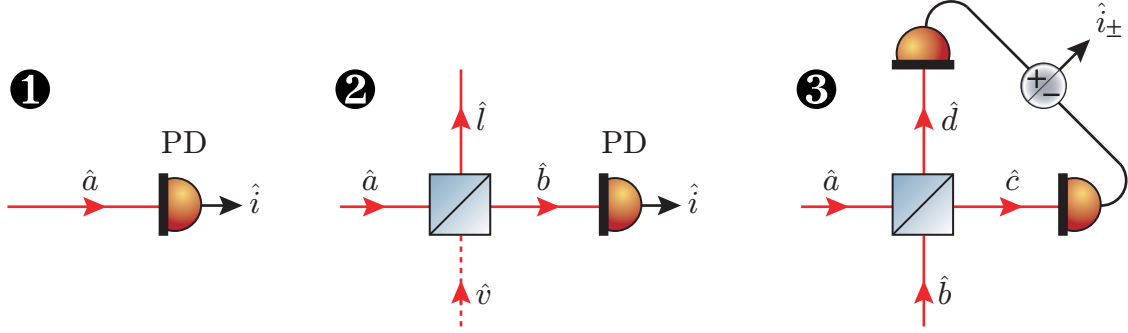


Figure 2.4: Three different detection schemes: **1** shows an ideal (lossless) direct measurement of the light field \hat{a} . **2** shows a realistic direct measurement of the light field \hat{a} including losses \hat{l} which results in a new field \hat{b} which is a superposition of \hat{a} and vacuum fluctuations \hat{v} . **3** shows an ideal homodyne measurement of the incoming fields \hat{a} and \hat{b} which are superimposed on the beam splitter. The resulting fields \hat{c} and \hat{d} are detected with two photodiodes and the sum and the difference of the photocurrents is evaluated.

certain quantum efficiency η_{qe} . This resulting photocurrent is proportional to the photon number operator \hat{n} and can be derived directly from Equation 2.47

$$\begin{aligned}\hat{i}(t) &\propto \alpha^2 + \alpha(\delta\hat{a}^\dagger + \delta\hat{a}) \\ &= \alpha^2 + \alpha \delta\hat{X}_{1,a}(t),\end{aligned}\tag{2.48}$$

where $\delta\hat{X}_{1,a}$ are the fluctuations in the amplitude quadrature of the field \hat{a} . The resulting photocurrent contains a DC term α^2 —which is proportional to the intensity—and an AC term which is scaled with the DC field amplitude. A measurement device which gives only access to the DC term is often referred to as a power meter. It measures the average photocurrent [BR03]

$$\bar{i}(t) = \frac{n_e(t) e}{\Delta t} = \frac{\eta_{\text{qe}} \bar{P}_{\text{opt}}(t) e}{\hbar\omega},\tag{2.49}$$

which is proportional to the average optical power $\bar{P}_{\text{opt}}(t)$ of the light beam. Here η_{qe} is the quantum efficiency of the photodiode, e is the electron charge, and $n_e(t)/\Delta t$ is the rate of photons that reach the detector. The AC term of the detected photocurrent is the more interesting part in quantum optics. If we perform a Fourier transform of Equation 2.48, we find

$$\hat{i}(\omega) \propto \hat{n}(\omega) = \alpha^2 + \alpha \delta\hat{X}_{1,a}(\omega).\tag{2.50}$$

The AC fluctuations $\delta\hat{X}_{1,a}(\omega)$ can be determined with a spectrum analyzer. From Equation 2.50 we learn that the measurement of the AC fluctuation is enhanced if one uses higher powers.

2.9.2 Shot noise

The quantity we are most interested in are the fluctuations of the photocurrent. To do a quantitative analysis of these, we need the variance $V(i(t))$ which is given by [BR03]:

$$V(i(t)) = \Delta \left(\frac{n_e(t)e}{\Delta t} \right)^2 = \frac{\Delta(n_e(t))^2 e^2}{\Delta t^2}. \quad (2.51)$$

Due to the fact that the counting statistics of the photons is a Poissonian distribution the variance $\Delta(n_e(t))^2 = n_e = \bar{i}\Delta t/e$. For large numbers of electrons this results in a Gaussian distribution in each counting interval. The variance is then given by

$$V(i(t)) = \frac{\bar{i} e}{\Delta t}. \quad (2.52)$$

We will investigate the spectrum of this variance throughout this thesis. The measurement time Δt is related to the measurement bandwidth B with the Shannon theorem $1/\Delta t = 2B$ [Sha49] which leads to

$$V(i(t)) = 2\bar{i} e B. \quad (2.53)$$

This is the well known shot noise formula in electronics which also applies for photodetection. To transform this into a formula including the light power we have to use Equation 2.49 together with Equation 2.53 resulting in

$$V(i(t)) = 2\eta_{qe}\bar{P}_{opt} \frac{e^2}{\hbar\omega} B. \quad (2.54)$$

2.9.3 Calculation of the shot noise level

In the previous section we have derived the variance of a photocurrent that is produced by detecting a light field with a photodiode. In this section we discuss the detection scheme in more detail and note considerations one should make when using a specific detection device.

In Figure 2.5 we find a schematic of certain detection schemes that are normally used in this thesis for measuring the noise of a light beam with a spectrum analyzer or a FFT analyzer. We see that the optical field with the power P_{opt} is detected with a photodiode which has a quantum efficiency of η_{qe} . The resulting photocurrent i_{pd} is transformed by a transimpedance amplifier into a voltage U_{pd} with a gain g [V/A]. Depending on the measurement device used (spectrum analyzer or FFT analyzer) the power spectral density of the power P_{pd} going through the 50 Ohm resistor or the linear spectral density of U_{pd} is measured respectively.

First we have to derive the relation between the power spectral density of the photocurrent i_{pd} and the variance of the photocurrent $V(i_{pd}(t))$, before we can calculate the shot noise level measured with these devices for a given light field with an optical power P_{opt} . The power spectral density is defined by the covariance [Har06]

$$\langle i_{pd}(t) \cdot i_{pd}(t + \tau) \rangle = \int_0^\infty df \text{PSD}_{i_{pd}}(f) \cdot e^{i\tau f}, \quad (2.55)$$

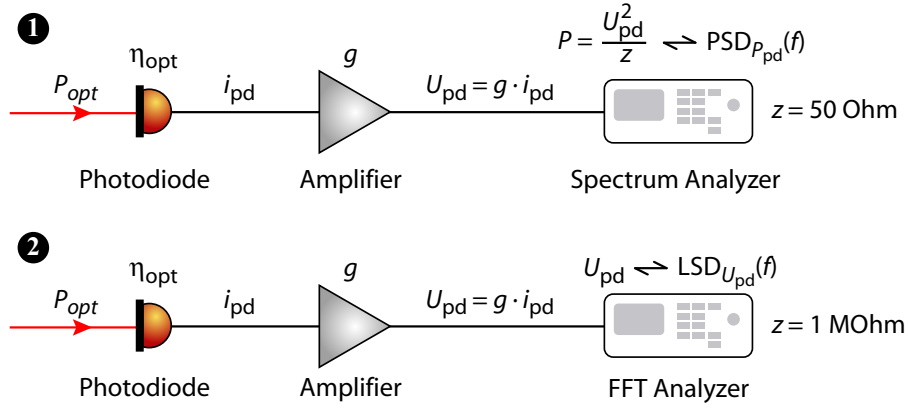


Figure 2.5: Schematic of the detection schemes for measuring the fluctuations of a light field that are used throughout this thesis. In **1** a light field with the optical power P_{opt} is detected with a photodiode that has a quantum efficiency of η_{qe} . The resulting photocurrent i_{pd} is transformed by an transimpedance amplifier with a gain g to the corresponding voltage U_{pd} . The spectrum analyzer measures the power $P = U^2/z$ where z is the input impedance. The spectrum analyzer output is a power spectral density (PSD) or a power spectrum (PS) of the measured power. **2** shows the same detection scheme but utilizes a FFT analyzer. The difference to a spectrum analyzer is that the FFT analyzer parses the voltage instead of the power. Its output is a linear spectral density or linear spectrum of the measured voltage.

which changes for $\tau = 0$ to

$$V(i_{\text{pd}}(t)) = \int_0^\infty df \text{PSD}_{i_{\text{pd}}}(f). \quad (2.56)$$

Due to the fact that the quantum noise of a coherent state is white, the power spectral density $\text{PSD}_{i_{\text{pd}}}(f)$ is constant in frequency space. Thus simplifying Equation 2.56 to

$$V(i_{\text{pd}}(t)) = \text{PSD}_{i_{\text{pd}}} \cdot B, \quad (2.57)$$

with the measurement bandwidth B . Combining Equations 2.53 and 2.56 we see the power spectral density $\text{PSD}_{i_{\text{pd}}}(f)$ of the photocurrent i_{pd} is given by

$$\text{PSD}_{i_{\text{pd}}}(f) = 2\bar{i}_{\text{pd}} e. \quad (2.58)$$

In general the linear spectral density is given by

$$\text{LSD}_{i_{\text{pd}}}(f) = \sqrt{\text{PSD}_{i_{\text{pd}}}(f)}. \quad (2.59)$$

Hence, the shot noise level which is measured by the FFT analyzer (Stanford Research SR785) in Figure 2.5 is given by

$$\text{LSD}_{U_{\text{pd}}}(f) = \text{LSD}_{i_{\text{pd}}}(f) \cdot g = \sqrt{2\bar{i}_{\text{pd}} e} \cdot g \quad (2.60)$$

$$= \sqrt{\left(2\eta_{\text{qe}}\bar{P}_{\text{opt}} \frac{e^2}{\hbar\omega}\right) \cdot g} \left[\frac{\text{V}}{\sqrt{\text{Hz}}} \right], \quad (2.61)$$

using Equation 2.49 and the transimpedance gain factor g . Mostly the FFT analyzer measures in dBV, in which the measured value is referenced to 1 V. The shot noise level in this case is then calculated to be

$$\text{LSD}_{U_{\text{pd}}}(f) = 20 \times \log_{10} \left(\sqrt{\left(2 \eta_{\text{qe}} \bar{P}_{\text{opt}} \frac{e^2}{\hbar \omega} \right)} \cdot g \cdot \frac{1}{1 [\text{V}]} \right) \left[\frac{\text{dBV}}{\sqrt{\text{Hz}}} \right]. \quad (2.62)$$

If one uses the FFT analyzer to measure a linear spectrum instead of the linear spectral density, the bandwidth of the detection has to be taken into account. The linear spectrum is then given by

$$\text{LS}_{U_{\text{pd}}}(f) = \sqrt{\left(2 \eta_{\text{qe}} \bar{P}_{\text{opt}} \frac{e^2}{\hbar \omega} \cdot B \right)} \cdot g \quad [\text{V}] \quad (2.63)$$

and the corresponding result for a measurement performed in dBV with a reference value of 1 V is calculated to be

$$\text{LS}_{U_{\text{pd}}}(f) = 20 \times \log_{10} \left(\sqrt{\left(2 \eta_{\text{qe}} \bar{P}_{\text{opt}} \frac{e^2}{\hbar \omega} \cdot B \right)} \cdot g \cdot \frac{1}{1 [\text{V}]} \right) \quad [\text{dBV}]. \quad (2.64)$$

For the case that the measurement of the shot noise level is performed with a spectrum analyzer (Rhode & Schwarz FSP3 or FSU3, Agilent 4395A) we need to know the variance

$$V(P_{\text{pd}}(t)) = V\left(\frac{U_{\text{pd}}^2}{z}\right) = V\left(\frac{g^2 i_{\text{pd}}^2}{z}\right) \quad (2.65)$$

$$= \frac{g^4}{z^2} V(i_{\text{pd}}(t)^2). \quad (2.66)$$

Together with $V(i_{\text{pd}}(t)^2) = 2V(i_{\text{pd}}(t))^2$ one can derive the linear spectral density (or linear spectrum), measured by such a spectrum analyzer in analogy to the previously derived linear spectral density for the FFT analyzer.

Overall one has to be very careful when calculating the shot noise level for a given light power. Many factors are not included in the above calculation e.g. internal attenuators, units of a voltage (V_{rms} , V_{pk} or V_{pkpk}), differences between calculated electrical gains and measured electrical gains, different internal detector types and strategies of the used analyzer, a voltage drop by a factor of two due to the 50 Ohm input impedance of the spectrum analyzer etc.

2.9.4 Optical losses and detection efficiencies

A realistic detection including losses can be modelled with the help of a beam splitter (see Figure 2.4). This device has a certain power reflectivity ε , two input and two output ports. If the two input fields are \hat{a} and \hat{b} then we determine the outgoing fields \hat{c} and \hat{d} with the help of the transfer matrix of the beam splitter. This transfer matrix can be written as [BR03]

$$\begin{pmatrix} \hat{c} \\ \hat{d} \end{pmatrix} = \begin{pmatrix} \sqrt{1-\varepsilon} & \sqrt{\varepsilon} \\ -\sqrt{\varepsilon} & \sqrt{1-\varepsilon} \end{pmatrix} \begin{pmatrix} \hat{a} \\ \hat{b} \end{pmatrix}. \quad (2.67)$$

This is a valid definition of a beam splitter as its determinant is equal to unity [KL66].

If we do a direct measurement including a detection efficiency $\eta_{\text{det}} = 1 - \varepsilon$ then we can imagine that vacuum fluctuations are coupling in through the beam splitter (see Figure 2.4, $\textcircled{2}$). In this case the field $\hat{a} = \alpha + \delta\hat{a}$ is superimposed with the vacuum field $\hat{v} = \delta\hat{v}$ and we find the resulting field \hat{b}

$$\hat{b} = \sqrt{\eta_{\text{det}}}\hat{a} + \sqrt{1 - \eta_{\text{det}}}\delta\hat{v}. \quad (2.68)$$

If we now detect this field, we find

$$\begin{aligned} \hat{b}^\dagger\hat{b} &= \left(\sqrt{\eta_{\text{det}}}\hat{a}^\dagger + \sqrt{1 - \eta_{\text{det}}}\delta\hat{v}^\dagger\right) \left(\sqrt{\eta_{\text{det}}}\hat{a} + \sqrt{1 - \eta_{\text{det}}}\delta\hat{v}\right) \\ &= \eta_{\text{det}}\hat{a}^\dagger\hat{a} + \sqrt{\eta_{\text{det}}(1 - \eta_{\text{det}})} \left(\hat{a}^\dagger\delta\hat{v} + \delta\hat{v}^\dagger\hat{a}\right) + (1 - \eta_{\text{det}})\delta\hat{v}^\dagger\delta\hat{v}. \end{aligned} \quad (2.69)$$

Using Equation 2.50, $\alpha \in \mathbb{R}$ and neglecting higher order terms we find

$$\hat{b}^\dagger\hat{b} = |\beta|^2 + \beta\delta\hat{X}_{1,b} \quad (2.70)$$

$$= \eta_{\text{det}} \left(\alpha^2 + \alpha\delta\hat{X}_{1,a}\right) + \underbrace{\sqrt{\eta_{\text{det}}(1 - \eta_{\text{det}})} \left(\hat{a}^\dagger\delta\hat{v} + \delta\hat{v}^\dagger\hat{a}\right)}_{=0} \quad (2.71)$$

$$\begin{aligned} &= (\alpha + \delta\hat{a}^\dagger)\delta\hat{v} + \delta\hat{v}^\dagger(\alpha + \delta\hat{a}) \\ &= \alpha\delta\hat{v} + \delta\hat{a}^\dagger\delta\hat{v} + \alpha\delta\hat{v}^\dagger + \delta\hat{v}^\dagger\delta\hat{a} \\ &= \alpha\delta\hat{X}_{1,v} \end{aligned}$$

$$= \eta_{\text{det}}\alpha^2 + \sqrt{\eta_{\text{det}}}\alpha \left(\sqrt{\eta_{\text{det}}}\delta\hat{X}_{1,a} + \sqrt{1 - \eta_{\text{det}}}\delta\hat{X}_{1,v}\right), \quad (2.72)$$

with $\beta = \sqrt{\eta_{\text{det}}}\alpha$ and $\delta\hat{X}_{1,b} = \sqrt{\eta_{\text{det}}}\delta\hat{X}_{1,a} + \sqrt{1 - \eta_{\text{det}}}\delta\hat{X}_{1,v}$. The variance of $\delta\hat{X}_{1,b}$ is then given by

$$\begin{aligned} V(\delta\hat{X}_{1,b}) &= (\Delta\delta\hat{X}_{1,b})^2 = \langle (\sqrt{\eta_{\text{det}}}\delta\hat{X}_{1,a} + \sqrt{1 - \eta_{\text{det}}}\delta\hat{X}_{1,v})^2 \rangle \\ &= \langle \eta_{\text{det}}\delta\hat{X}_{1,a}^2 \rangle + \langle (1 - \eta_{\text{det}})\delta\hat{X}_{1,v}^2 \rangle \\ &\quad + \underbrace{\langle \sqrt{\eta_{\text{det}}(1 - \eta_{\text{det}})}\delta\hat{X}_{1,a}\delta\hat{X}_{1,v} \rangle}_{=0} + \underbrace{\langle \sqrt{\eta_{\text{det}}(1 - \eta_{\text{det}})}\delta\hat{X}_{1,v}\delta\hat{X}_{1,a} \rangle}_{=0} \\ &= \eta_{\text{det}}V(\delta\hat{X}_{1,a}) + (1 - \eta_{\text{det}})V(\delta\hat{X}_{1,v}). \end{aligned} \quad (2.73)$$

The mixed terms $\delta\hat{X}_{1,a}\delta\hat{X}_{1,v}$ will average to zero as long as the two inputs are independent of each other. Note that the detection efficiency η_{det} in the above calculation can include diverse types of losses, e.g. propagation loss due to the non perfect optics and also the quantum efficiency of the photodiodes.

If the field \hat{a} has a variance of $V(\delta\hat{X}_{1,a}) = x$ [dB] then the resulting variance $V(\delta\hat{X}_{1,b})$ is

$$V(\delta\hat{X}_{1,b}) = 10 \times \log_{10} \left[\eta_{\text{det}} 10^{\frac{x \text{ [dB]}}{10}} + (1 - \eta_{\text{det}}) \overbrace{V(\delta\hat{X}_{1,v})}^{=1} \right]. \quad (2.74)$$

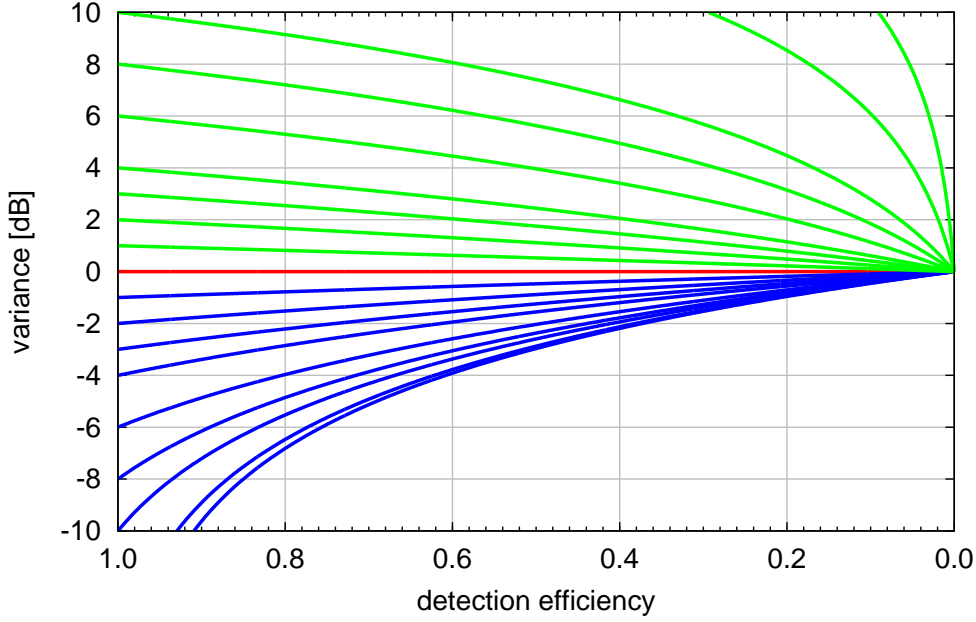


Figure 2.6: Resulting variance for different input variances and losses. The shot noise in red is located at 0 dB. Squeezed variances are shown in blue and anti-squeezed variances are shown in green. It is clearly visible that for increasing losses the variances get closer to the shot noise, but the squeezed variance is more fragile, because the effect of the losses is much greater than for the more robust anti-squeezed variance.

The evaluation of the variance over detection efficiency is explicitly shown in Figure 2.6. It is clearly visible that for increasing losses the variances get closer to the shot noise, but the squeezed variance is more fragile, because the effect of the losses is much greater than for the more robust anti-squeezed variance. It is worth mentioning that the vacuum state is not affected from the loss effect at all, attenuated vacuum stays vacuum.

2.9.5 Balanced homodyne detection

The disadvantage of detecting only amplitude fluctuations with a direct measurement can be overcome with the method of homodyne detection. This allows the detection of amplitude and phase fluctuations. As always when measuring phase fluctuations a reference is needed. In the case of homodyne detection this is a reference light field which is often referred to as local oscillator. There are different kinds of homodyne detection setups, in the following we will concentrate on the balanced homodyne detection scheme. This can be found in Figure 2.4 if the used beam splitter is a 50/50 beam splitter. This is also the reason for naming this a balanced detection scheme, because the ingoing fields \hat{a} and \hat{b} are equally split into the ports \hat{c} and \hat{d} .

$$\begin{aligned}\hat{c} &= \frac{1}{\sqrt{2}} \hat{a} + \frac{1}{\sqrt{2}} \hat{b} \\ \hat{d} &= -\frac{1}{\sqrt{2}} \hat{a} + \frac{1}{\sqrt{2}} \hat{b}.\end{aligned}\tag{2.75}$$

We can decompose the incoming fields in classical excitations and fluctuations and write

$$\begin{aligned}\hat{a} &= \alpha + \delta\hat{a} \\ \hat{b} &= \beta + \delta\hat{b},\end{aligned}\tag{2.76}$$

where α and β are the mean values and $\delta\hat{a}$ and $\delta\hat{b}$ are the fluctuations of the fields \hat{a} and \hat{b} . The intensities on the photodiodes are given by

$$\hat{c}^\dagger\hat{c} = \frac{1}{2}(\hat{a}^\dagger + \hat{b}^\dagger)(\hat{a} + \hat{b})\tag{2.77a}$$

and

$$\hat{d}^\dagger\hat{d} = \frac{1}{2}(-\hat{a}^\dagger + \hat{b}^\dagger)(-\hat{a} + \hat{b}).\tag{2.77b}$$

We can now separate the relative phase between the two incoming fields from the complex amplitude $\hat{a} = \hat{a}_o e^{i\theta} = \alpha_o e^{i\theta} + \delta\hat{a} e^{i\theta}$ of the local oscillator; note that α_o is now real. Together with the definition in Equation 2.28 and choosing β to be real the intensity can be expressed by

$$\begin{aligned}\hat{c}^\dagger\hat{c} &= \frac{1}{2}(\alpha e^{-i\theta} + \delta\hat{a}^\dagger e^{-i\theta} + \beta + \delta\hat{b}^\dagger)(\alpha e^{i\theta} + \delta\hat{a} e^{i\theta} + \beta + \delta\hat{b}) \\ &= \frac{1}{2}\left[\alpha_o^2 + \beta^2 + 2\alpha_o\beta \cos\theta + \alpha_o(\delta\hat{X}_{1,a} + \delta\hat{X}_{\theta,b})\right. \\ &\quad \left.+ \beta(\delta\hat{X}_{-\theta,a} + \delta\hat{X}_{1,b}) + \delta\hat{a}^\dagger\delta\hat{a} + \delta\hat{a}^\dagger\delta\hat{b}e^{-i\theta} + \delta\hat{b}^\dagger\delta\hat{a}e^{i\theta} + \delta\hat{b}^\dagger\delta\hat{b}\right]\end{aligned}\tag{2.78a}$$

and

$$\begin{aligned}\hat{d}^\dagger\hat{d} &= \frac{1}{2}(-\alpha e^{-i\theta} - \delta\hat{a}^\dagger e^{-i\theta} + \beta + \delta\hat{b}^\dagger)(-\alpha e^{i\theta} - \delta\hat{a} e^{i\theta} + \beta + \delta\hat{b}) \\ &= \frac{1}{2}\left[\alpha_o^2 + \beta^2 - 2\alpha_o\beta \cos\theta + \alpha_o(\delta\hat{X}_{1,a} - \delta\hat{X}_{\theta,b})\right. \\ &\quad \left.- \beta(\delta\hat{X}_{-\theta,a} - \delta\hat{X}_{1,b}) + \delta\hat{a}^\dagger\delta\hat{a} - \delta\hat{a}^\dagger\delta\hat{b}e^{-i\theta} - \delta\hat{b}^\dagger\delta\hat{a}e^{i\theta} + \delta\hat{b}^\dagger\delta\hat{b}\right].\end{aligned}\tag{2.78b}$$

By neglecting all higher order terms this can be approximated to

$$\hat{c}^\dagger\hat{c} \approx \frac{1}{2}\left[\alpha_o^2 + \beta^2 + 2\alpha_o\beta \cos\theta + \alpha_o(\delta\hat{X}_{1,a} + \delta\hat{X}_{\theta,b}) + \beta(\delta\hat{X}_{-\theta,a} + \delta\hat{X}_{1,b})\right]\tag{2.79a}$$

$$\hat{d}^\dagger\hat{d} \approx \frac{1}{2}\left[\alpha_o^2 + \beta^2 - 2\alpha_o\beta \cos\theta + \alpha_o(\delta\hat{X}_{1,a} - \delta\hat{X}_{\theta,b}) - \beta(\delta\hat{X}_{-\theta,a} - \delta\hat{X}_{1,b})\right].\tag{2.79b}$$

The sum and difference photocurrents are given by

$$\hat{i}_+ \propto \hat{c}^\dagger\hat{c} + \hat{d}^\dagger\hat{d} = \alpha_o^2 + \beta^2 + \alpha_o\delta\hat{X}_{1,a} + \beta\delta\hat{X}_{1,b}\tag{2.80a}$$

$$\hat{i}_- \propto \hat{c}^\dagger\hat{c} - \hat{d}^\dagger\hat{d} = 2\alpha_o\beta \cos\theta + \alpha_o\delta\hat{X}_{\theta,b} + \beta\delta\hat{X}_{-\theta,a}.\tag{2.80b}$$

This result is different compared with the one which can be found in literature today [BR03]. The difference is, that in the sum and in the difference the fluctuations from

one input field are scaled with the coherent amplitude of the other input field. As a consequence, even if $\alpha_o \gg \beta$, the terms $\alpha_o \delta\hat{X}_{\theta,b}$ and $\beta \delta\hat{X}_{-\theta,a}$ can be of the same size if $\delta\hat{X}_{\theta,b}$ corresponds to shot noise fluctuations and $\delta\hat{X}_{-\theta,a}$ corresponds to large technical noise. Nevertheless this is a remarkable result, because in the case that $\alpha_o \gg \beta$ and $\alpha_o \delta\hat{X}_{\theta,b} \gg \beta \delta\hat{X}_{-\theta,a}$ the equation can be rewritten to the form that is found in the literature

$$\hat{i}_+ \propto \hat{c}^\dagger \hat{c} + \hat{d}^\dagger \hat{d} = \alpha_o^2 + \alpha_o \delta\hat{X}_{1,a} \quad (2.81a)$$

$$\hat{i}_- \propto \hat{c}^\dagger \hat{c} - \hat{d}^\dagger \hat{d} = 2\alpha_o \beta \cos \theta + \alpha_o \delta\hat{X}_{\theta,b}. \quad (2.81b)$$

Now the current \hat{i}_- contains only the fluctuations of the signal field \hat{b} that are scaled with the local oscillator amplitude. The fluctuations from the local oscillator itself vanish completely, meaning that even large technical noise on the local oscillator does not deteriorate the measurement, as long as $\alpha_o \delta\hat{X}_{\theta,b} \gg \beta \delta\hat{X}_{-\theta,a}$ is valid. We can now distinguish between two different homodyne detection cases.

Difference between self-homodyne detection and homodyne detection with an external local oscillator

The first case to be analyzed is called self-homodyne detection, which is shown in Figure 2.7. Here the signal field $\hat{s} = \sigma_o + \delta\hat{s}$ and the local oscillator field $\hat{l} = \lambda_o + \delta\hat{l}$ form the incoming field $\hat{a} = \alpha_o + \delta\hat{a}$. The second incoming field $\hat{b} = \beta + \delta\hat{b}$ is the vacuum field $\hat{v} = 0 + \delta\hat{v}$. Due to the fact that we cannot measure a phase difference with respect to the vacuum field, the self-homodyne measurement allows only the measurement in the amplitude quadrature. Using Equations 2.80a and 2.80b together with the definitions of the incoming fields, we can derive the sum and difference photocurrents for the self-homodyne case

$$\hat{i}_+ \propto \alpha_o^2 + \alpha_o \delta\hat{X}_{1,a} \quad (2.82a)$$

$$\hat{i}_- \propto \alpha_o \delta\hat{X}_{1,v}. \quad (2.82b)$$

We see that the self-homodyne detection scheme allows us to measure amplitude fluctuations of the field \hat{a} , which are scaled with the amplitude α_o , by detecting the sum of the photocurrents \hat{i}_+ . The shot noise level, which is also scaled with the amplitude α_o , is given by the difference of the photocurrents \hat{i}_- . As a result the self-homodyne detection scheme allows measurements of amplitude fluctuations relative to the shot noise level with high precision.

The variances of \hat{i}_+ and \hat{i}_- are

$$V(\hat{i}_+) = \alpha_o^2 \langle \delta\hat{X}_{1,a}^2 \rangle \quad (2.83a)$$

$$V(\hat{i}_-) = \alpha_o^2 \langle \delta\hat{X}_{1,v}^2 \rangle. \quad (2.83b)$$

This is exactly what is measured by a spectrum analyzer, as we have seen in Section 2.9.3. The variance of the shot noise is measured in the difference and the variance of the noise of field \hat{a} is measured in the sum. It is worth noting, that $\delta\hat{X}_{1,a}$ can contain different types of

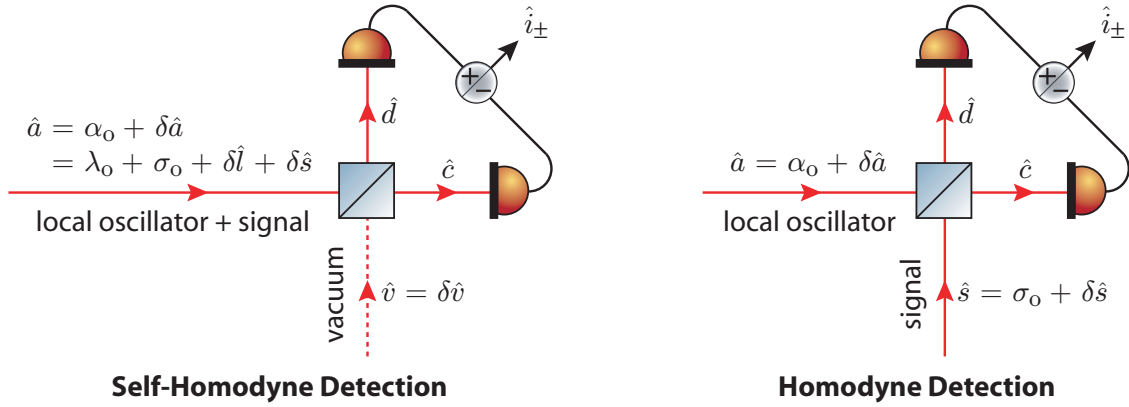


Figure 2.7: Schematic of the two balanced homodyne detection schemes, self-homodyne detection (left) and homodyne detection with an external local oscillator (right).

noise, which can typically be separated into two groups: shot noise $\delta\hat{X}_{1,asn}$ and technical noise $\delta\hat{X}_{1,atn}$. Because most technical noise strengths $\delta\hat{X}_{1,atn}$ (e.g. amplitude noise, beam jitter noise, phase noise, ...) depend linearly on the power of the field, whereas the shot noise strength $\delta\hat{X}_{1,asn}$ does not change with increasing power, the photocurrent shows a different behavior for these two noise sources. By measuring the linear spectral density of the photocurrent with a spectrum analyzer (see Section 2.9.3), this noise gets amplified depending on the used light power. Thereby the shot noise scales linearly but technical noise scales quadratically with the light power in the measured data. In more practical words, shot noise increases by 3 dB, whereas technical noise increases by 6 dB if the light power is doubled.

The other possible case is the homodyne detection scheme with external local oscillator mostly just called homodyne detection. Here the signal field is spatially separated from the local oscillator field (see Figure 2.7). The signal field can be described by $\hat{s} = \sigma_o + \delta\hat{s}$ and we find for the sum and difference current

$$\hat{i}_+ \propto \alpha_o^2 + \sigma_o^2 + \alpha_o \delta\hat{X}_{1,a} + \sigma_o \delta\hat{X}_{1,s} \quad (2.84a)$$

$$\hat{i}_- \propto 2\alpha_o\sigma_o \cos\theta + \alpha_o \delta\hat{X}_{\theta,s} + \sigma_o \delta\hat{X}_{-\theta,a}. \quad (2.84b)$$

Presuming that $\alpha_o \gg \sigma_o$ and $\alpha_o \delta\hat{X}_{\theta,b} \gg \sigma_o \delta\hat{X}_{-\theta,a}$ is valid, this can be simplified to

$$\hat{i}_+ \propto \alpha_o^2 + \alpha_o \delta\hat{X}_{1,a} \quad (2.85a)$$

$$\hat{i}_- \propto 2\alpha_o\sigma_o \cos\theta + \alpha_o \delta\hat{X}_{\theta,s}. \quad (2.85b)$$

We see that the difference of the photocurrents allows us to measure the fluctuations of the signal beam in every quadrature. The measured quadrature can be actuated by changing the relative phase θ between the local oscillator and signal field. The DC term of \hat{i}_- depends on θ , which enables a derivation of the actual phase θ . The fluctuations of the signal field are scaled with the amplitude of the local oscillator field. To measure a reference shot noise one has to replace the signal field with a vacuum field, by blocking the signal input port of the homodyne beam splitter.

If we calculate the variances of \hat{i}_+ and \hat{i}_- from Equation 2.84, we obtain

$$V(\hat{i}_+) = \alpha_o^2 \langle \delta\hat{X}_{1,a}^2 \rangle + \sigma_o^2 \langle \delta\hat{X}_{1,s}^2 \rangle \quad (2.86a)$$

$$V(\hat{i}_-) = \alpha_o^2 \langle \delta\hat{X}_{\theta,s}^2 \rangle + \sigma_o^2 \langle \delta\hat{X}_{-\theta,a}^2 \rangle. \quad (2.86b)$$

This represents the result one gets from a spectrum analyzer measurement. As long as we analyze the noise characteristics of the signal beam in a regime, where the local oscillator is shot noise limited and the coherent amplitude of the signal beam is small compared to the local oscillator field strength, we can neglect the second terms. But if we want to do these measurements in a frequency range where the laser and thereby the local oscillator holds large technical noise (e.g. frequencies around the relaxation oscillation and lower frequencies), we have to carefully choose the ratio of two coherent amplitudes. The crucial factor is given by

$$\left(\frac{\sigma_o}{\alpha_o}\right)^2 \frac{\langle \delta\hat{X}_{-\theta,a}^2 \rangle}{\langle \delta\hat{X}_{\theta,s}^2 \rangle} \ll 1. \quad (2.87)$$

If we assume that the signal beam only holds shot noise, then $\langle \delta\hat{X}_{\theta,s}^2 \rangle = 1$. Further let us say that we have technical noise on the local oscillator beam which is a factor of one hundred (20 dB) larger than the shot noise. If now the signal beam power is 1% of the local oscillator power, the second term is also equal to unity. Thus the measured noise level is increased by a factor of two, by amplifying the technical noise of the local oscillator beam with the signals coherent amplitude. This can cause structures in the normally white shot noise and the setup should be examined in detail for this effect if one measures a non-white shot noise.

2.9.6 Homodyne mode mismatch

A homodyne detection is done by overlapping two optical fields on a beam splitter. However, in a real experiment the interference is not always perfect. The reasons for imperfect interference are generally spatial mode mismatch or polarization mismatch. If one of the beam shapes is slightly elliptical this can be described by a superposition of a TEM₀₀ and higher order modes. Due to the fact that TEM_{mn} modes form an orthogonal basis only the same spatial modes interfere with each other, meaning that a mode distortion leads to a reduced detection efficiency. A measure for the interference of two fields is the visibility \mathcal{V} , which is given by scanning the relative phase of the two beams relative to each other and measuring the fringe maximum and minimum intensities with a photodiode. The visibility is then calculated as [Lam98]

$$\mathcal{V} = \frac{I_{\max} - I_{\min}}{I_{\max} + I_{\min}}. \quad (2.88)$$

The effect of a mode mismatch to a homodyne measurement can be modelled by linearization of the operators. The result looks exactly like the beam splitter loss calculation in Section 2.9.4, where the efficiency η is given by the square of the visibility

$$\eta = \mathcal{V}^2. \quad (2.89)$$

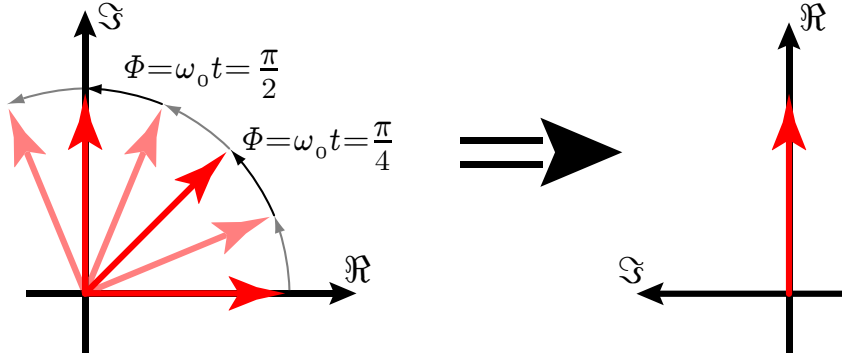


Figure 2.8: Phasor representing the field given in Equation 2.90. On the left-hand side the phasor rotates with frequency ω_0 in the fixed coordinate system anti-clockwise, whereas in the rotating frame (right) the phasor rotates together with the coordinate system, allowing a static display of the electrical field vector. The coordinate axes in the rotating frame are rearranged in such a way that the real axis points upwards to keep a right handed system in the sideband picture.

This makes the mode matching on the homodyne beam splitter of the local oscillator and the signal field very essential, especially for measuring squeezed states. These states are very fragile, meaning every loss has to be minimized otherwise every loss event transforms the squeezed field more into a vacuum field (see also Figure 2.6).

2.10 Squeezing in the sideband picture

Before we can understand squeezing in the sideband picture, we need a general understanding of the sideband picture.

2.10.1 The classical sideband picture

The sideband picture is a good way to describe modulations of light fields. If we take for example the electrical field at a certain position we find

$$E(t) = E_0 e^{i\omega_0 t}, \quad (2.90)$$

where we omit the complex conjugate term for simplicity. This field can be displayed in a complex plane as a vector with the length E_0 and a phase $\omega_0 t$. The vector rotates anti-clockwise in time if the coordinate system is rigid. One can choose a coordinate system that rotates with the same frequency ω_0 , so that one gets a stationary picture. The choice of the rotating coordinate system is often referred to as *rotating frame*. If we have more than one field with different frequencies then it is obvious that we can have only one frequency for the rotating frame. In the case of light fields, the carrier frequency ω_0 is mostly chosen for the rotating frame. This kind of visualization of a field is called a *phasor diagram* (see Figure 2.8). A more detailed introduction to the classical phasor picture can be found in [Mal06]

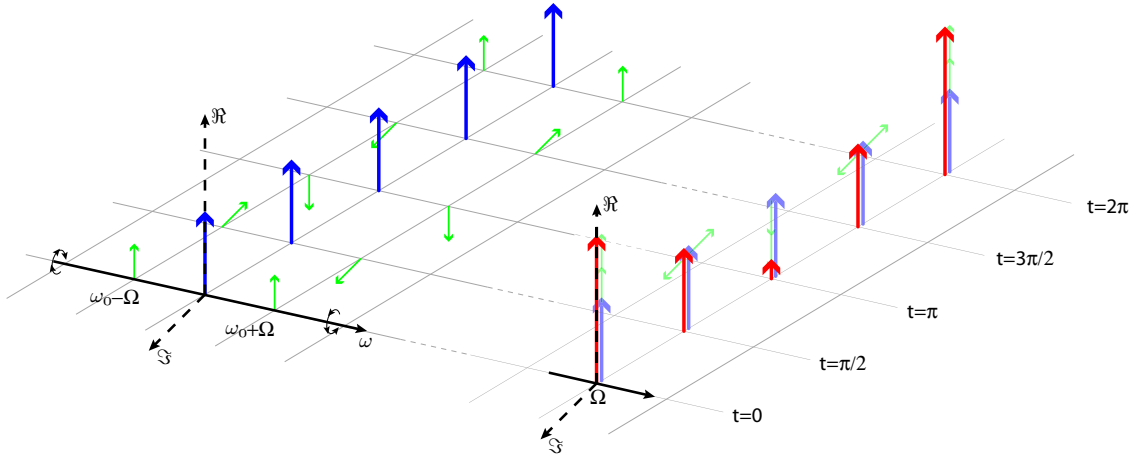


Figure 2.9: Amplitude modulated field from Equation 2.91 in the sideband picture for different times within one modulation period. On the left-hand side we see the sideband picture representation which corresponds to the right-hand side of Equation 2.91b. The two green sidebands rotate at frequency Ω in opposite directions around the frequency axis, whereas the carrier field in blue does not change in time. On the right-hand side we see the sum of the three (green and blue) individual fields for the sideband frequency Ω as a red phasor. This corresponds more to the right-hand side of Equation 2.91a spectrally filtered with a certain bandwidth such that only the sideband frequency Ω remains. As one can see, the sum phasor alters its length periodically in time due to the different orientations of the sidebands but the phase stays constant.

Now let us focus on an amplitude modulated field

$$E_{\text{am}}(t) = E_0 e^{i\omega_0 t} \left(1 + m \cos(\Omega t) \right) \quad (2.91a)$$

$$= E_0 e^{i\omega_0 t} \left(1 + \frac{m}{2} e^{+i\Omega t} + \frac{m}{2} e^{-i\Omega t} \right). \quad (2.91b)$$

Here we see that an amplitude modulated field at frequency ω_0 with modulation index m can be separated into one carrier field with amplitude E_0 at frequency ω_0 and two sidebands at frequencies $\omega_0 \pm \Omega$ with amplitude $E_0 \frac{m}{2}$. In the rotating frame the carrier is stationary but the sidebands at $\omega_0 - \Omega$ and $\omega_0 + \Omega$ rotate clockwise and anti-clockwise with frequency Ω , respectively. This separation of one field into a carrier field and sideband fields characterizes the *sideband picture*. Figure 2.9 is a graphical representation of Equation 2.91. There we see a time evolution of the amplitude modulated field. On the left-hand side we see the sideband picture representation which corresponds to the right-hand side of Equation 2.91b. The two green sidebands rotate at frequency Ω in opposite directions around the frequency axis. Whereas the carrier field in blue does not change in time. On the right-hand side we see the sum of the three (green and blue) individual fields for the sideband frequency Ω as a red phasor. This corresponds more to the right-hand side of Equation 2.91a spectrally filtered with a certain bandwidth such that only the sideband frequency Ω remains. As one can see, the sum phasor alters its length periodically in time due to the different orientations of the sidebands but the phase stays constant.

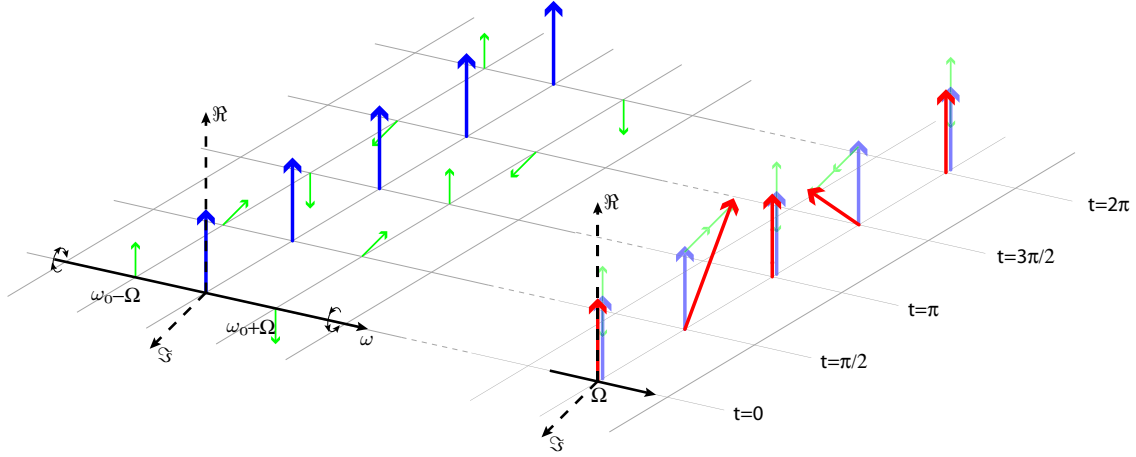


Figure 2.10: Phase modulated field from Equation 2.92 in the sideband picture for different times within one modulation period. On the left-hand side we see the sideband picture representation which corresponds to the right-hand side of Equation 2.92c. The two green sidebands rotate at frequency Ω in opposite directions around the frequency axis, whereas the carrier field in blue does not change in time. On the right-hand side we see the sum of the three (green and blue) individual fields for the sideband frequency Ω as a red phasor. This corresponds more to the right-hand side of Equation 2.92a spectrally filtered with a certain bandwidth such that only the sideband frequency Ω remains. As one can see, the sum phasor alters its phase periodically in time due to the different orientations of the sidebands but the amplitude stays constant for small modulation indices.

A phase modulation of the field in Equation 2.90 can be described by

$$E_{\text{pm}}(t) = E_0 e^{i(\omega_0 t + m \cos \Omega t)} \quad (2.92a)$$

$$\approx E_0 e^{i\omega_0 t} (1 + i m \cos(\Omega t)) \quad (2.92b)$$

$$= E_0 e^{i\omega_0 t} \left(1 + i \frac{m}{2} e^{+i\Omega t} + i \frac{m}{2} e^{-i\Omega t} \right), \quad (2.92c)$$

where we used the approximation that our modulation index m is small compared to unity, otherwise we would get a comb of sidebands at frequencies $j\Omega$, $j \in \mathbb{N}$. The result of Equation 2.92c means that we can separate the phase modulated field into three components again, a stationary carrier field at frequency ω_0 with amplitude E_0 and two sidebands at frequencies $\omega_0 \pm \Omega$ with amplitude $iE_0 \frac{m}{2}$ which are directed along the complex axis because of their complex amplitude. In Figure 2.10 we can see a time evolution of this phase modulated field in the sideband picture and the sum of the fields in a phasor diagram. This figure is the phase modulation equivalent to Figure 2.9 which has been explained in the former paragraph.

2.10.2 Quantum noise in the sideband picture

In the previous section the classical sideband picture was presented. The question arises how quantum fluctuations can be understood in this picture. In Section 2.7 we have introduced the quantum phasor picture, where the fluctuations of a quantum state of light

are visualized by a two dimensional Gaussian distribution and its variance is marked by a dashed circle. The derivation of this distribution is done in Figure 2.2. There we see that if the origin of this fluctuation is quantum noise and not technical noise, it can be visualized by a small quantum arrow that changes its phase and length randomly within the two dimensional distribution. Recalling that the quantum arrows in Figure 2.2 represents the fluctuations $\delta\hat{a}$ at a specific frequency ω and we generalize this in frequency space, we end up with Figure 2.11, which shows among other things a time evolution of the quantum noise in the sideband picture. Note, that the former real and imaginary axis \Re and \Im are now replaced by the axis of the quadrature space \hat{X}_1 and \hat{X}_2 . In this figure we see at time t_1 six little quantum phasors oriented in the quadrature plane and distributed along the frequency axis. These quantum phasors individually evolve indeterministically in time, meaning that their length changes with a Gaussian distribution with unity variance and their phase changes randomly in time. In other words, at each frequency ω exists a quantum mechanical oscillator in the ground state. As shown in Equations 2.32 and 2.33 each of these oscillators fluctuate in quadrature space with unity variance.

2.10.2.1 The quantum sideband picture

Figure 2.11 shows the transition of this quantum noise into the quantum sideband picture. The quantum sideband picture is deduced from the classical sideband picture by looking at the time average of each sideband. Due to the complete random behavior of each sideband, the result is a two dimensional Gaussian distribution (shown in red) with a variance of one, visualized by the red dashed circle. This quantum noise distribution is then replacing the former quantum noise phasors at frequencies $\pm\Omega$. If we do this procedure for all frequencies $\pm\Omega$, we have generated a quantum sideband picture for quantum noise or vacuum noise.

2.10.2.2 Vacuum noise in the quantum sideband picture

The representation of vacuum noise in the quantum sideband picture is shown in Figure 2.12. On the left-hand side we have a quantum noise distribution at every sideband frequency $\pm\Omega$ and no coherent amplitude at frequency ω_0 . The time evolution within one modulation period is shown which does not change due to the fact that the quantum noise distribution already marks an average of the quantum noise phasors in time. In the middle of the figure we see the time evolution of the sum of the two vacuum noise distributions at frequency Ω which also does not change in time. This represents a measurement of a vacuum state with arbitrary high time resolution, spectrally filtered with a certain bandwidth so that only the sideband frequency Ω remains. Hence, the labels of the axes change from the quadratures to the measured photocurrents $i_{\theta=0^\circ}$ and $i_{\theta=90^\circ}$ of the corresponding quadratures. To the right we find the quantum phasor picture for the vacuum state at frequency Ω , which can be derived by averaging the measurement shown in the middle.

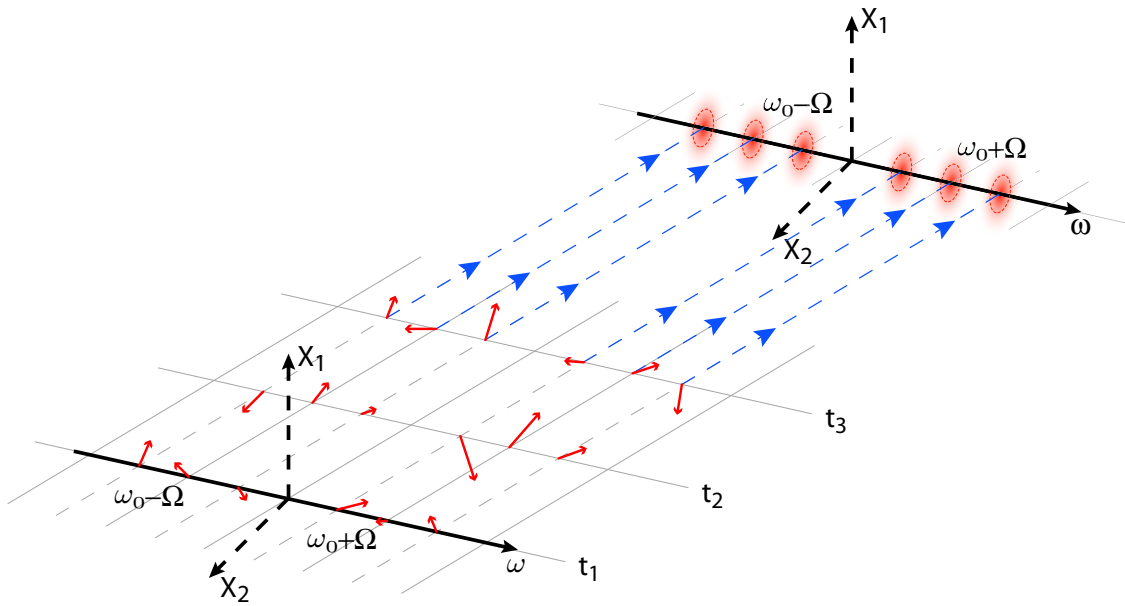


Figure 2.11: Representation of vacuum noise in the sideband picture and its transition into the quantum sideband picture. Quantum noise is visualized in the sideband picture by small phasors in quadrature space at each frequency. Here these quantum noise phasors are shown for six frequencies explicitly. A property of such a quantum noise phasor is that its length changes in time with a Gaussian distribution and that its phase does change indeterministically in time. This behavior is shown for three specific times. The transition into the quantum sideband picture is done by beating the two quantum noise phasors at frequencies $\omega_0 \pm \Omega$, $\Omega \in \mathbb{R}_+$ and averaging in time. The resulting two-dimensional Gaussian distribution has a unity variance (red dashed circle). This quantum noise distribution is then drawn at frequencies $\omega_0 \pm \Omega$ instead of the quantum noise phasors. Performing this procedure for all frequencies Ω will end up in the quantum sideband picture shown in the upper right corner of the figure.

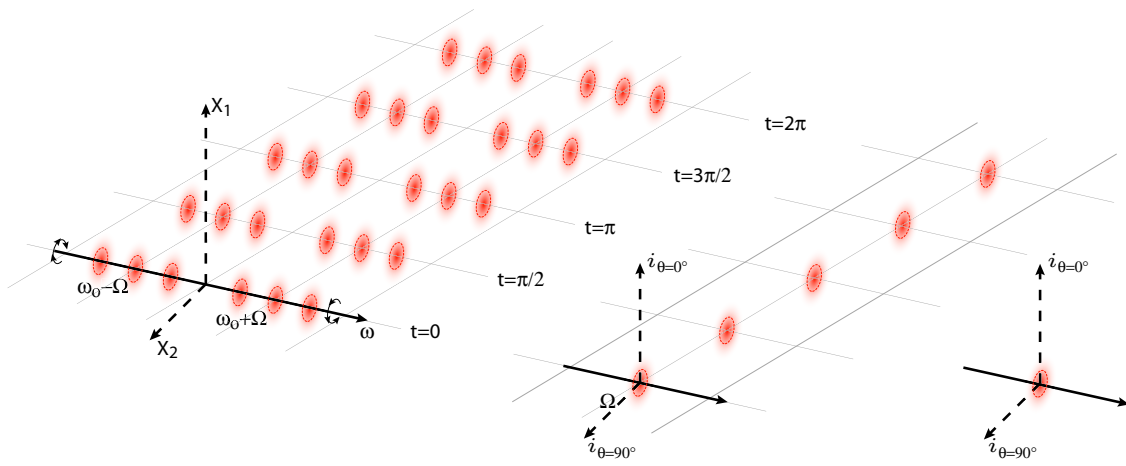


Figure 2.12: Representation of vacuum state in different physical pictures. On the left-hand side we see a time evolution of the vacuum noise in the quantum sideband picture. At all sideband frequencies $\pm\Omega$ a red quantum noise distribution can be drawn to represent the vacuum noise at this frequency $\omega_0 \pm \Omega$. This is explicitly shown for three different sideband frequencies. During time this picture does not change because the quantum noise distribution already represent an average of a time evolution. In the middle of the picture we see the time evolution of the sum of the two vacuum noise distributions at frequency Ω which also does not change in time. This represents a measurement of a vacuum state with arbitrary high time resolution, spectrally filtered with a certain bandwidth such that only the sideband frequency Ω remains. Hence, the labels of the axes change from the quadratures to the measured photocurrents $\hat{i}_{\theta=0^\circ}$ and $\hat{i}_{\theta=90^\circ}$ of the corresponding quadratures. To the right we find the quantum phasor picture for the vacuum state at frequency Ω , which is derived by averaging the measurement shown in the middle.

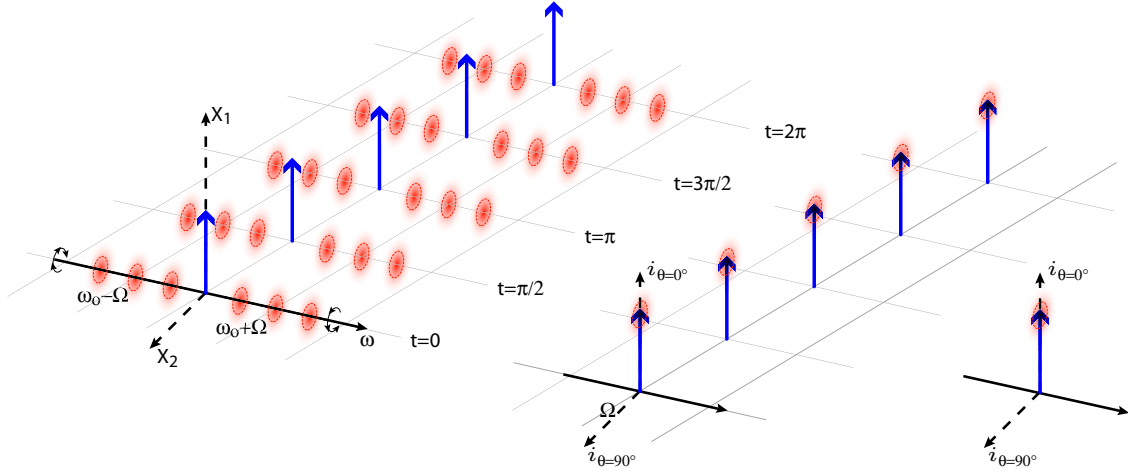


Figure 2.13: Representation of coherent state in different physical pictures. On the left-hand side we see a time evolution of the coherent state in the quantum sideband picture. At frequency ω_0 we see a blue phasor which represents the coherent amplitude of the carrier field and at all sideband frequencies $\pm\Omega$ a red quantum noise distribution can be drawn to represent the vacuum noise at this frequency $\omega_0 \pm \Omega$. This is explicitly shown for three different sideband frequencies. During time this picture does not change because in the rotating frame the coherent phasor is fixed on its location and the quantum noise distribution already represent an average of a time evolution. In the middle of the figure one sees the time evolution of the measured quadratures of the photocurrent at frequency Ω of the coherent state. On the right-hand side we see the quantum phasor picture for this coherent state at a frequency Ω , which is derived by averaging the measurement shown in the middle.

2.10.2.3 A coherent state in the quantum sideband picture

A time evolution of a coherent state is shown in Figure 2.13. We see a coherent amplitude at frequency ω_0 and the vacuum noise distributions at all sideband frequencies. The time evolution of the measured photocurrent at frequency Ω of the coherent state quadratures can be seen in the center of Figure 2.13. To the right we see the corresponding quantum phasor picture, which can be derived by averaging the measurement shown in the middle.

2.10.2.4 Amplitude modulation in the quantum sideband picture

If we combine the amplitude modulation shown in Figure 2.9 with vacuum noise, we obtain Figure 2.14. The phasors of the two figures are exactly the same but in the latter one the vacuum noise distribution is added. For convenience the vacuum noise distributions are displayed only at the modulation frequencies $\pm\Omega$ and dropped at all other frequencies. The time evolution of the measured quadratures of the photocurrent at frequency Ω of the amplitude modulated state can be seen in the middle of Figure 2.13. During one modulation period the length of the resulting red phasor is altered periodically. Additionally the quantum phasor picture is added in Figure 2.14 to the right-hand side, which is derived by averaging the measurement shown in the middle. Compared to the vacuum noise distribution the obtained amplitude noise distribution is elliptical. The variance

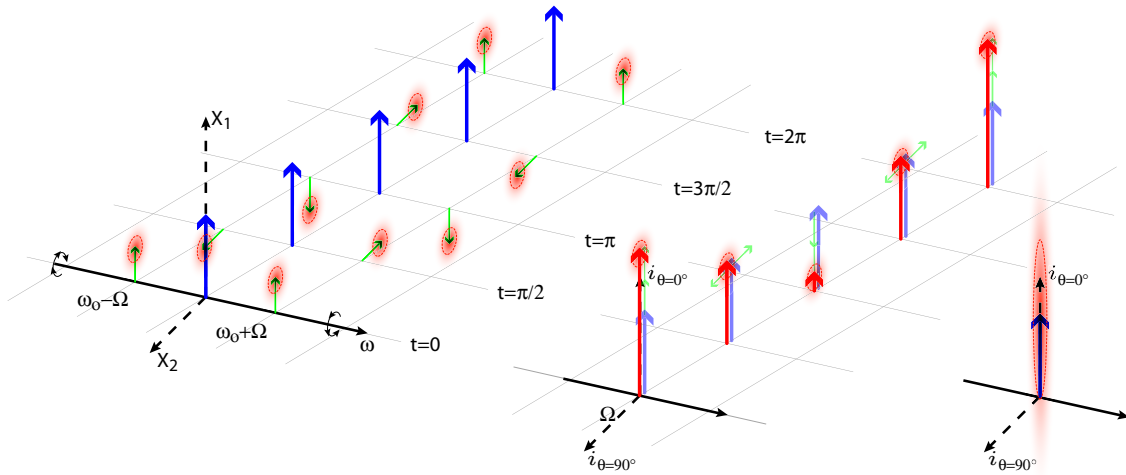


Figure 2.14: Amplitude modulated field for different times within one modulation period. On the left-hand side the quantum sideband picture representation is displayed. The two green sidebands rotate with frequency Ω in opposite directions around the frequency axis, whereas the carrier field in blue does not change in time. On top of the sideband phasors the vacuum noise distributions are located, whereas all other vacuum noise distributions are not shown for clarity. In the middle the result of measurement—with arbitrary high time resolution—of the photocurrent at frequency Ω for the different quadratures is illustrated. This can be represented by the sum of the three (green and blue) individual fields as a red phasor including the vacuum noise distribution. The sum phasor alters its length periodically in time due to the different orientations of the sidebands but the phase stays constant. On the right-hand side the representation of this amplitude modulation is shown in the quantum phasor picture. The blue phasor represents the constant coherent amplitude of the amplitude modulated field and in red the amplitude noise distribution is displayed. Compared to the vacuum noise distribution this is enlarged along the amplitude quadrature due to the beat and averaging process of the two amplitude modulation sidebands and their corresponding vacuum noise distribution. Along the phase quadrature the amplitude noise distribution is equivalent to the vacuum noise distribution.

of the amplitude noise distribution is much bigger in amplitude quadrature, due to the coherent sidebands, but the identical to the variance of the quantum noise distribution in phase quadrature. Hence, this amplitude modulated field has large amplitude noise and small phase noise at frequency Ω .

2.10.2.5 Phase modulation in the quantum sideband picture

If we do the same kind of combination for the phase modulated field shown in Figure 2.10 and vacuum noise we end up with Figure 2.15. Here we obtain the result that the quantum phasor picture to the right-hand side of the figure also shows an elliptical noise distribution. The variance in the phase quadrature is much bigger compared to the vacuum noise, but the variance along the amplitude quadrature stays the same. Hence, this phase modulated field has large phase noise and small amplitude noise at frequency Ω .

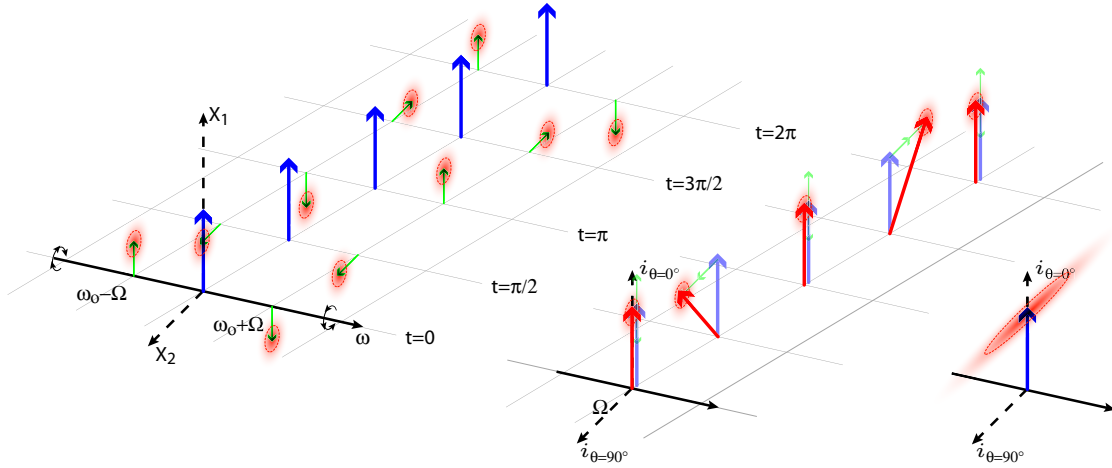


Figure 2.15: Phase modulated field for different times within one modulation period. On the left-hand side the quantum sideband picture representation is displayed. The two green sidebands rotate with frequency Ω in opposite directions around the frequency axis. Whereas the carrier field (in blue) does not change in time. On top of the sideband phasors the vacuum noise distribution are located, whereas all other vacuum noise distribution are not shown for clarity. In the middle the result of measurement—with arbitrary high time resolution—of the photocurrent at frequency Ω for the different quadratures is illustrated. This can be represented by the sum of the three (green and blue) individual fields as a red phasor including the vacuum noise distribution. The sum phasor alters its phase periodically in time due to the different orientations of the sidebands but the amplitude stays constant for small modulation indices. On the right-hand side the representation of this phase modulation in the quantum phasor picture is shown. The blue phasor represents the constant coherent amplitude of the phase modulated field and in red the phase noise distribution is displayed. Compared to the vacuum noise distribution this is enlarged along the phase quadrature due to the beat and averaging process of the two phase modulation sidebands and their corresponding quantum noise distribution. Along the amplitude quadrature the amplitude noise distribution is equivalent to the vacuum noise distribution.

2.10.2.6 Squeezed states in the quantum sideband picture

Now all tools and knowledge have been presented to understand squeezing in the quantum sideband picture. Equation 2.42 shows that, in contrast to a vacuum state, a squeezed vacuum state does contain photons. These photons are linked to fields that are represented by sideband phasors which are in general equally distributed along the frequency axis but can also be limited to a certain bandwidth due to the experimental setup e.g. linewidth of the OPA cavity. The length of these phasors is connected to the amount of squeezing and it turns out that the sidebands at $\pm\Omega$ are correlated depending on the kind of squeezing that is produced. If we want to produce for example amplitude squeezing (see Figure 2.16), the sidebands have to be co-aligned in the phase quadrature and counter-aligned in the amplitude quadrature. Contrary to a phase or amplitude modulation (see Figures 2.15 and 2.14) these squeezing sidebands do not rotate continuously and evolve in time. Instead the orientation of the correlated sideband pair is totally random in time, whereas the orientation of the two sidebands to each other is always correlated. Hence, the two sideband phasors at frequency $\pm\Omega$ represent the correlated part of the squeezed state at frequency Ω . In Figure 2.16 they are visualized as green phasors. The uncorrelated part of a squeezed state is represented by quantum noise distribution with a smaller standard deviation than the vacuum noise distribution. These squeezed vacuum noise distribution are the purple distributions attached to the correlated sidebands. Both, the uncorrelated and correlated parts of an amplitude squeezed state are presented in Figure 2.16. On the left-hand side the time evolution is shown. No carrier field is available and only at the sideband frequencies $\pm\Omega$ the correlated and uncorrelated fractions of the squeezed states are shown, while these are dropped at all other frequencies for simplification. In comparison to amplitude and phase modulation the random orientation of the sidebands in time is clearly visible. In the middle of Figure 2.16 the result of a measurement of the photocurrent is shown. This measurement is done with an arbitrary small time resolution and frequency filter with a bandwidth so that only the sideband frequency Ω is detected. The resulting red phasor can be constructed by the sum of the correlated fractions of the amplitude squeezing (green phasors) with the uncorrelated distribution on top. On the right-hand side the result of the averaged measurement is shown, which corresponds to the quantum phasor picture of an amplitude squeezed state. The average coherent amplitude is zero and the fluctuations are represented by the large purple distribution that is a result of the correlated and uncorrelated fractions of the squeezed state. The elliptical shape of the amplitude squeezed state is clearly visible. The variance of the photocurrent's amplitude quadrature $\hat{i}_{\theta=0^\circ}$ matches the variance of the squeezed vacuum noise distribution. The distribution along the phase quadrature is enlarged compared to the vacuum noise distribution. This quadrature represents the anti-squeezed quadrature of the squeezed state.

In Figure 2.17 the corresponding figure for a phase squeezed state is displayed. The same properties as for the amplitude squeezed states apply here, with the exception that the correlated fractions of the squeezed state are now co-aligned in the amplitude quadrature and counter-aligned in the phase quadrature. This results in the quantum phasor picture representation of the phase squeezed state shown on the right-hand side of the figure. The variance of the photocurrent's phase quadrature $\hat{i}_{\theta=90^\circ}$ matches the variance

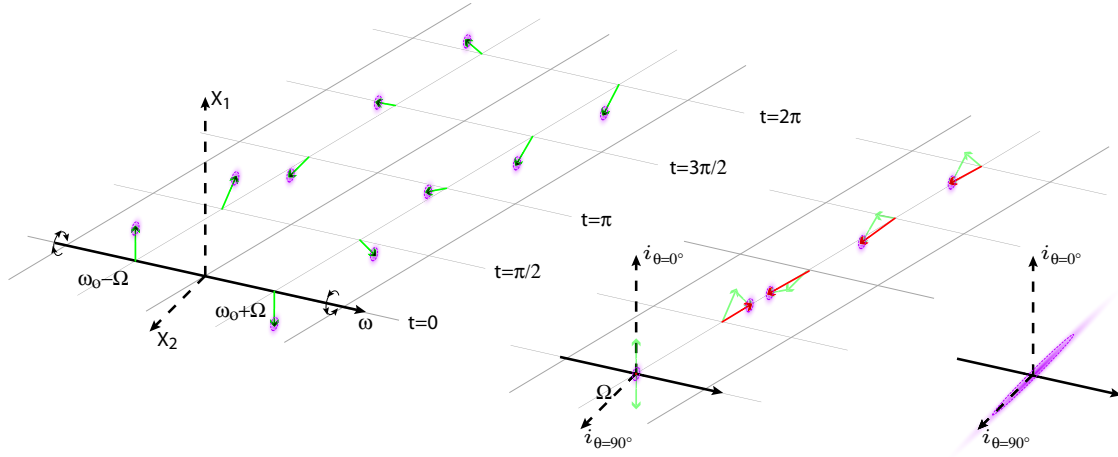


Figure 2.16: Amplitude squeezed vacuum field for different times within one modulation period. On the left-hand side the quantum sideband picture representation is displayed. The correlated fraction of the amplitude squeezed state is represented by the green phasors, explicitly shown here at the frequencies $\pm\Omega$, whereas the uncorrelated fraction is visualized by the purple squeezed vacuum noise distribution. The correlated fraction does not evolve in time like phase and amplitude modulation. The orientation of the correlated sidebands is always co-aligned in the phase quadrature and counter-aligned in the amplitude quadrature, but the general orientation of sideband pair is completely random in time. In the middle of the figure a measurement of the photocurrent provoked by the amplitude squeezed state is shown. This measurement is done with an arbitrary time resolution and a spectral filter such that only the sideband frequency Ω is analyzed. The result is displayed by a red phasor that can be obtained by the sum of the correlated green sideband phasors and their corresponding uncorrelated fractions in purple. On the right-hand side the average of the detected photocurrent is presented. Here the correlated and uncorrelated fractions form the desired squeezing ellipse, which shows a squeezed variance along the amplitude quadrature and an anti-squeezed variance along the phase quadrature of the photocurrent compared to the vacuum state presented in Figure 2.12.

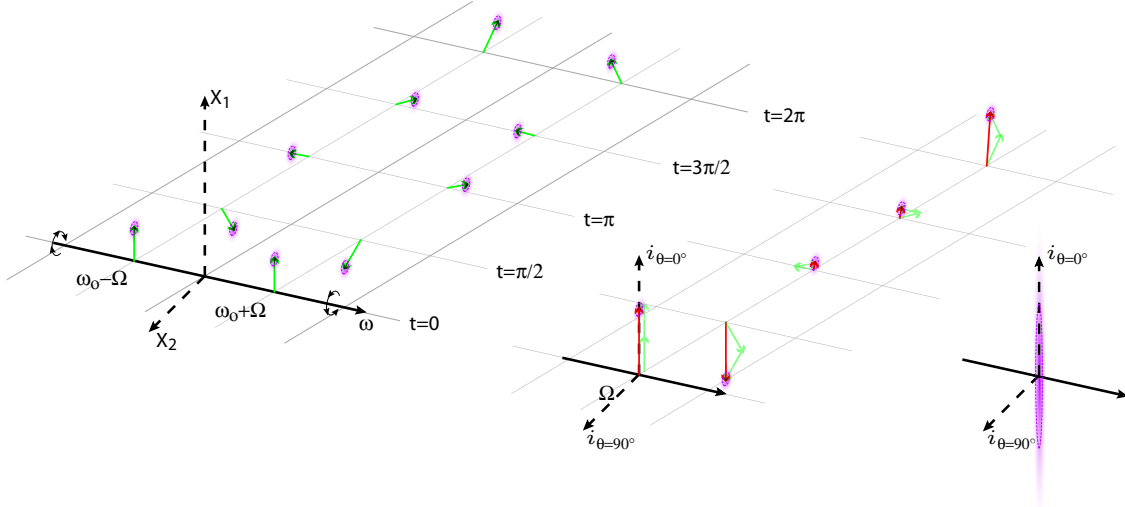


Figure 2.17: Phase squeezed vacuum field for different times within one modulation period. On the left-hand side the quantum sideband picture representation is displayed. The correlated fraction of the phase squeezed state is represented by the green phasors, explicitly shown here at the frequencies $\pm\Omega$, whereas the uncorrelated fraction is visualized by the purple squeezed vacuum noise distribution. The orientation of the correlated sidebands is always co-aligned in the amplitude quadrature and counter-aligned in the phase quadrature, but the general orientation of sideband pair is completely random in time. In the middle of the figure a measurement of the photocurrent provoked by the phase squeezed state is shown. This measurement is done with an arbitrary time resolution and a spectral filter such that only the sideband frequency Ω is analyzed. The result is displayed by a red phasor that can be obtained by the sum of the correlated green sideband phasors and their corresponding uncorrelated fractions in purple. On the right-hand side the average of the detected photocurrent is presented. Here the correlated and uncorrelated fractions form the desired squeezing ellipse, which shows a squeezed variance along the phase and an anti-squeezed variance along the amplitude quadrature of the photocurrent compared to the vacuum state presented in Figure 2.12.

of the squeezed vacuum noise distribution. For the amplitude quadrature of the photocurrent the distribution is enlarged compared to the vacuum state, which corresponds to the anti-squeezed variance of the squeezed state.

2.11 Calculation of squeezing from an OPO cavity

Introduction

Polzik *et al.* were the first who announced a theory which allowed the calculation of squeezing that can be produced inside an optical parametric oscillator (OPO) cavity [PCK92]. Later this theory was used to derive the maximum amount of the detected squeezing for a real system which included losses [LRB⁺99] and phase noise [ZGC⁺03] between the production of a squeezed state and its detection. This theory was tested in [ATF06] and will be used in the following.

The variances of a squeezed state are given by

$$V_{\pm} = 1 \pm \alpha \rho \frac{4x}{(1 \mp x)^2 + \Omega^2}, \quad (2.93)$$

where V_- and V_+ are the variances in the squeezed and anti-squeezed quadrature respectively. The detection efficiency α is a product of the propagation efficiency ζ , the quantum efficiency of the photodiodes η and the homodyne efficiency ξ^2 , with ξ being the homodyne visibility. ρ is the escape efficiency of the OPO which can be written as

$$\rho = \frac{T}{T + L}. \quad (2.94)$$

Here the transmissivity T of the outcoupling mirror and the intra-cavity losses L are taken into account. The pump parameter x contains the classical gain G of the OPO, given by

$$G = \frac{1}{(1 - x)^2}. \quad (2.95)$$

This can be rearranged to

$$x = 1 - \sqrt{\frac{1}{G}}. \quad (2.96)$$

Here, only the result with the minus in front of the square root is taken into account, because the other solution shows a nonphysical behavior for gain $G = 1$ (squeezing without any pump field). The detuning parameter Ω is given by the ratio of the measured sideband frequency ω and the OPO cavity decay rate $\gamma = c(T + L)/l$ (l = round-trip length of the cavity), i.e.

$$\Omega = \frac{\omega}{\gamma}. \quad (2.97)$$

2.11.1 Simulations

For the calculation of the variances V_- and V_+ one needs to know all of the physical parameters that are specified in Table 2.1. These parameters can be divided into two groups. One group consists of parameters that are easily accessible or measurable, whereas the other group is not. The latter group consists of the intra-cavity losses L and the quantum efficiency η of the photodiodes. A precise measurement of the quantum efficiency of the photodiodes is very difficult, because the needed power meters have usually an absolute error of 5% which directly couples into the resulting quantum efficiency of the photodiodes. Later we will see that this error makes it difficult to predict the amount of squeezing an OPO or OPA system can produce. The second parameter that is not easily accessible is the total intra-cavity loss. If we look at the hemilithic design that is mostly used in this thesis (see Figure 3.14), one realizes that the AR coating and the internal loss of the crystal make up the total intra-cavity loss. The specification for the AR coating of the crystal is $R < 0.05\%$. To measure this coating in reflection one has to deviate from normal incidence and then measure the reflected power with a power meter, which has again an error of 5%. But even if one knows the reflectivity of the AR coating one still

	easily measured parameters
ω	measured frequency
ζ	propagation efficiency
ξ	homodyne visibility \rightarrow homodyne efficiency = ξ^2
T	transmissivity of the cavity outcoupling mirror
l	roundtrip length of the cavity
	not so easily measured parameters
η	quantum efficiency of the photodiodes
L	intra-cavity losses
	calculated parameters from measurement
$\alpha = \zeta\eta\xi^2$	product of the efficiencies
$\gamma = c(T + L)/l$	cavity decay rate
$G = \frac{1}{(1-x)^2}$	classical gain
$\Omega = \frac{\omega}{\gamma}$	detuning parameter
$\rho = T/(T + L)$	cavity escape efficiency
$x = 1 - \sqrt{\frac{1}{G}}$	pump parameter follows from the classical gain G

Table 2.1: Physical parameters that are needed for the calculation of the variances V_- and V_+ , divided in three different classes.

has to determine the internal loss of the crystal. This can vary from crystal to crystal even if they are from the same manufacturer, as a result of the process of growing these crystals. Small impurities deteriorate the homogeneity of the crystal resulting in local absorption fluctuations. An effective way to obtain the intra-cavity losses of our OPO cavities is to make a finesse measurement with a high reflecting outcoupling mirror. The finesse has to be very high if the intra-cavity loss is low, to get into a regime where the finesse is dominated by the losses. Such a measurement is planned in the future to obtain a better knowledge of the intra-cavity losses. At present the intra-cavity loss can only be estimated from a normal finesse measurement (see Section 2.11.2).

In Figure 2.18 the transition from an ideal OPO system with zero losses and perfect efficiencies to a typical system used in the laboratory is shown. This illustrates how these different parameters couple into V_- and V_+ .

2.11.2 Estimation of the intra-cavity losses

To get a measure of T and L, we can take a finesse measurement and model our system with the best known parameters and their individual errors. In Table 2.2 the parameters of three different systems are given. Each of these systems has a finesse $\mathcal{F} \approx 138$ but a different value for the overall loss.

From the squeezing values we can achieve with the current setup—up to 7.5 dB—and the measurement of all easy accessible parameters given in Table 2.1 together with the individual measurement of the photodiode quantum efficiency η , we can make an estimation of the internal losses L of the OPO cavity. We know that η is not larger than

system with maximum loss	parameters
hemilithic cavity: outcoupling mirror: R=0.961, T=0.039 AR-coating: R=0.05% crystal's internal losses: 0.025%	$\mathcal{F} = 137.1$ L = 0.58% max. SQZ: -8.87 dB
ring cavity	$\mathcal{F} = 145$ L=0.33992%; max. SQZ: -10.95 dB
system with minimum loss	resulting values
hemilithic cavity: outcoupling mirror: R=0.956, T=0.044 AR-coating: R=0.01% crystal's internal losses: 0.02%	$\mathcal{F} = 137.7$ L = 0.061% max. SQZ: -18.58 dB
ring cav.	$\mathcal{F} = 138$ L=0.0421%; max. SQZ: -20.15 dB
realistic system	resulting values
hemilithic cavity: outcoupling mirror: R=0.958, T=0.042 AR-coating: R=0.03% crystal's internal losses: 0.1%	$\mathcal{F} = 137.9$ L = 0.253% max. SQZ: -12.44 dB
ring cav.	$\mathcal{F} = 141$ L=0.157%; max. SQZ: -14.41 dB

Table 2.2: Three simulated OPO systems and their individual parameters having a finesse of $\mathcal{F} \approx 138$. The model includes a hemilithic cavity consisting of an outcoupling mirror and a nonlinear crystal with an AR coating at the front and an HR coated back surface. The values for the ring cavity are for a doubly AR coated crystal with the same outcoupling mirror as the hemilithic cavity. To compensate the smaller interaction length due to only one pass through the crystal per round trip, the pump power has to be doubled. The fixed parameters for all of the above cavities are the length $l = 0.075$, the HR-coating reflectivity $R=0.99996$ and sideband frequency of $\omega = 2\pi \cdot 5 \times 10^6$ Hz. All squeezing values are for an ideal system with no propagation and detection losses.

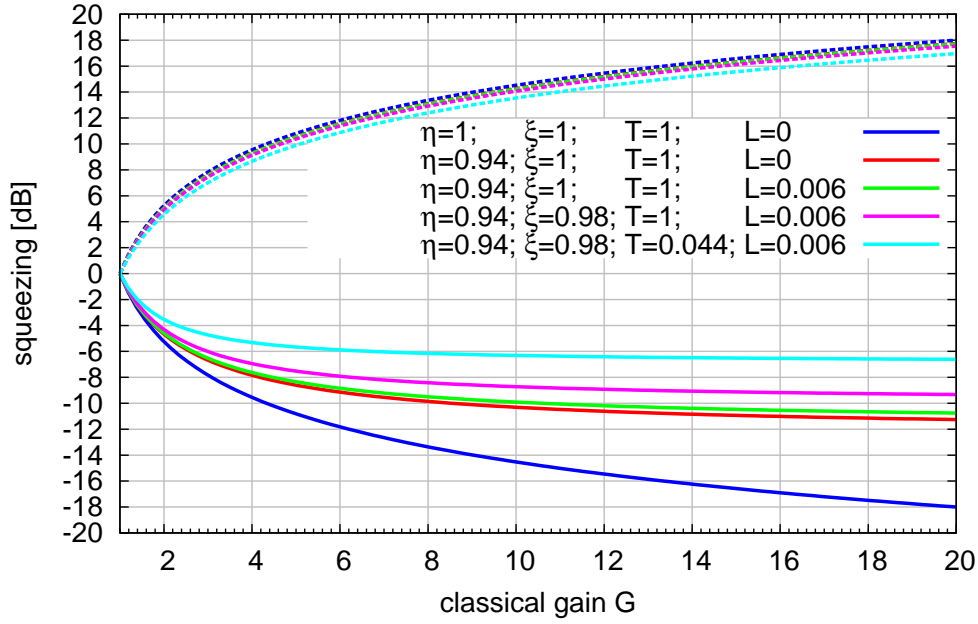


Figure 2.18: Variances of the squeezed V_- (solid) and anti-squeezed V_+ (dashed) quadrature for a transition from an ideal system with zero losses and perfect efficiencies to a typical system that was used in the laboratory for an estimated internal loss of 0.006 and a quantum efficiency of 0.94 for the photodiode.

0.97, which gives an upper limit for L of 0.006, otherwise our squeezing results cannot be obtained. On the other hand we know that η is not smaller than 0.87, which sets an lower limit for L of 0.001. Resulting from this estimation, the intra-cavity loss of the OPO cavity is

$$0.001 < L < 0.006. \quad (2.98)$$

Differences between linear cavity and ring cavity

As seen in Table 2.2 the squeezing values for the ring cavity are larger than the hemilitic ones. This is due to losses inside the crystal dominating the intra-cavity loss. In a ring cavity with the same finesse as a linear cavity, the light passes the crystal only once per round-trip (see Figure 2.19). To compensate the lower interaction length (or equivalent interaction time) of the pump field with the nonlinear crystal, the pump power has to be doubled for the ring cavity to achieve the same nonlinear effect as in a linear cavity.

If we take the values for the maximally achievable squeezing from Table 2.2 and see how these degrade in a real experiment with propagation efficiency ($\zeta = 0.97$) and detection losses ($\eta = 0.94$ and $\xi = 0.98$), we get the squeezing values shown in Table 2.3. The advantages of the ring cavity diminish and it nearly performs like the linear cavity. At least the additional complexity of a ring cavity are not worth the small performance increase.

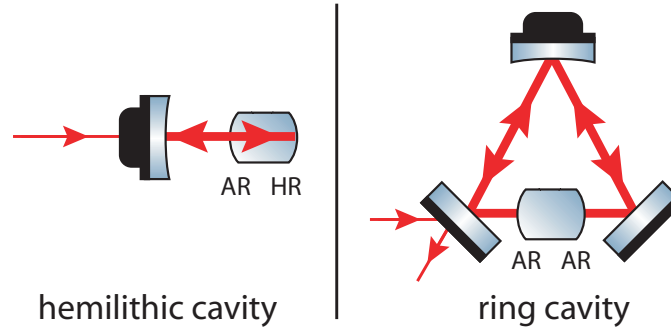


Figure 2.19: Comparison of a linear hemilithic cavity and a ring cavity. In the linear design the light passes the crystal twice per round trip whereas in the ring cavity the crystal is only passed once. This doubles the losses due to the crystal absorption in the linear cavity compared to the ring cavity. HR: high reflective coating; AR: anti reflective coating.

parameters: propagation efficiency $\zeta = 0.97$, quantum efficiency of the photodiodes: $\eta = 0.94$ and homodyne visibility: $\xi = 0.98$	ideal system	realistic system
hemilithic cavity with maximum losses:	-8.87 dB	-6.24 dB
hemilithic cavity with minimum losses:	-18.58 dB	-8.65 dB
hemilithic cavity with realistic losses:	-12.44 dB	-7.59 dB
ring cavity with maximum losses:	-10.95 dB	-7.11 dB
ring cavity with minimum losses:	-20.15 dB	-8.77 dB
ring cavity with realistic losses:	-14.41 dB	-8.07 dB

Table 2.3: Degradation of the squeezing by the transition from an ideal—calculated in Table 2.2—to a realistic system with non-unity efficiencies.

2.11.3 An example of a typical OPO

To learn more about the consequences of Equation 2.93, it is useful to consider an example. Imagine an OPO that produces 6.5 dB of squeezing with a classical gain of $G = 10$. The parameters we know about the system are: $\zeta = 0.97$, $\xi = 0.985$, $T = 0.044$, $l = 0.075$, $\omega = 2\pi \cdot 5 \times 10^3$ Hz. As seen in Figure 2.20 there are many possible configurations that produce the same amount of squeezing in particular 6.5 dB for a classical gain of 10. These systems differ in the photodiode quantum efficiency η and the internal losses L . The shown curves in Figure 2.20 are a result from the loss estimation in Equation 2.98. To compensate the influence of the different intra-cavity losses, the quantum efficiency of the photodiodes has to be re-adjusted in the simulation to obtain the same amount of squeezing. All other parameters remain the same.

The escape efficiency ρ of the OPO (see Equation 2.94) is generally limited by the transmissivity of the outcoupling mirror. The loss inside the crystal is fixed and the AR coatings used have reflectivities $R < 0.05\%$. The evolution of the squeezing strength with a changing outcoupling transmissivity is presented in Figure 2.21, which shows a comparison of two different OPO systems. The first system uses $\eta = 0.97$ and $L=0.006$, whereas the other system uses $\eta = 0.93$ and $L=0.004$. For both systems the dependency of the squeezed variance V_- with the classical gain for five different transmissivities of the outcoupling mirror is shown. It is clearly visible that V_- decreases for higher transmissivities. A comparison of ❶ and ❷ of Figure 2.21 shows that the curves for $T=0.044$ are the same, but the curves for higher T 's have more squeezing in the first case where $\eta = 0.97$. Note that it is important to know the internal losses of the OPO cavity or the quantum efficiency of the photodiodes, because only then a prediction of the variances V_- and V_+ can be accurate.

To further decrease the losses and thereby detect more squeezing, one can think of a self-homodyne detection scheme (see Section 2.9.5). No additional external local oscillator is required and has to be mode matched with the squeezed beam. Hence, the homodyne visibility is increased to $\xi = 1$, which results in a minimization of loss. The consequences for the systems from Figure 2.21 for a homodyne visibility $\xi = 1$ are presented in Figure 2.22, which clearly shows an improvement in the squeezing strength. Consequently, to detect the maximum possible squeezing the self-homodyne detection scheme should be used.

2.11.4 Phase fluctuation

In the homodyne detection scheme with external local oscillator the relative phase θ between the local oscillator and the squeezed beam determines the measured quadrature (details see Section 2.9.5). As a consequence, fluctuations of θ couple into the measurement process and it looks like the squeezing ellipse is jittering with respect to a fixed quadrature. This effect mixes the squeezed and anti-squeezed quadratures, which results in a degradation of the squeezed variance V_- (see Figure 2.23).

In a very simple model [ZGC⁺03] this degradation can be described by

$$V_{\pm} \approx V_{\pm} \cos^2(\delta\theta) + V_{\mp} \sin^2(\delta\theta). \quad (2.99)$$

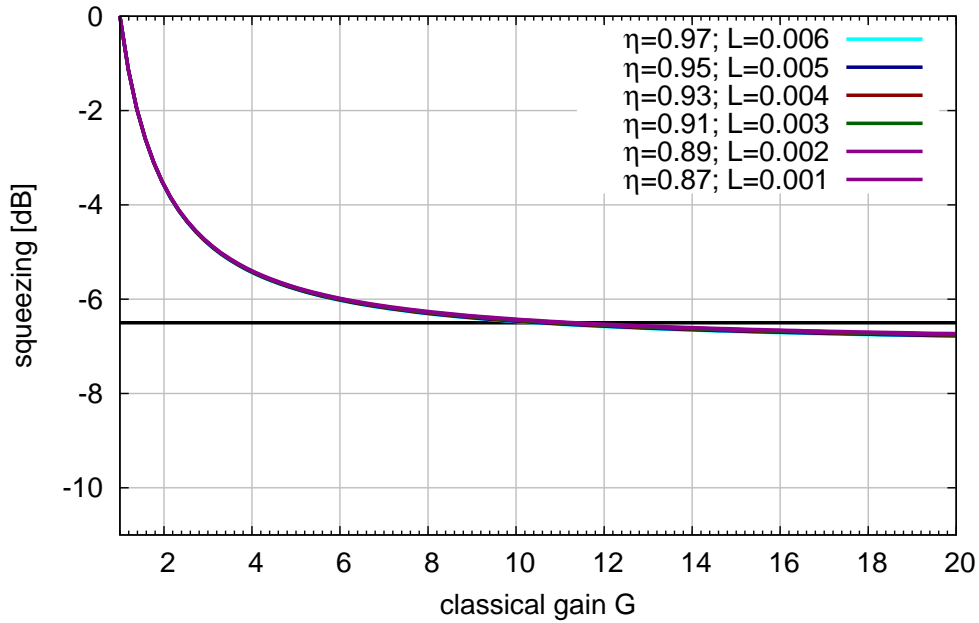


Figure 2.20: Squeezed variance V_- plotted for six different OPO systems that all produce the same amount of squeezing especially 6.5 dB at a classical gain $G=10$. All of these different systems differ in the internal loss L and in the quantum efficiency η . The other parameters that have been used for the simulation are $\zeta = 0.97$, $\xi = 0.985$, $T = 0.044$, $l = 0.075$, $\omega = 2\pi \cdot 5 \times 10^3$.

In Figure 2.24 the effect of these phase fluctuations for different $\delta\theta$'s on the variances V_- and V_+ can be seen. In the simulation a system without any losses is modelled. This system produces more than -15 dB of squeezing for $G = 12$ and $\delta\theta = 0^\circ$. In the case that the phase fluctuations are $\delta\theta = 10^\circ$ this squeezing value is deteriorated to $+0.4$ dB, and squeezing cannot be detected.

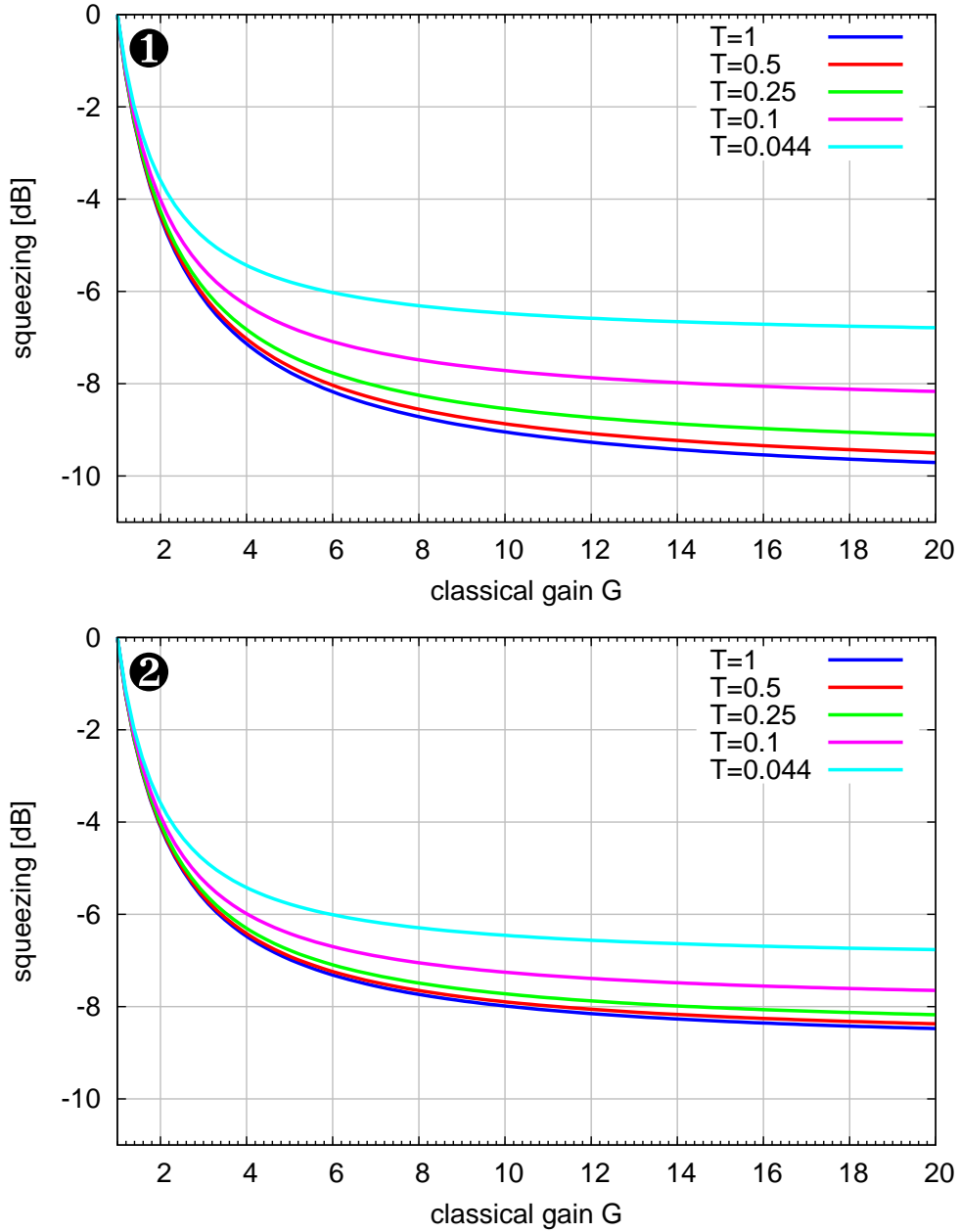


Figure 2.21: Squeezed variance V_- for a homodyne detection scheme with external local oscillator: The different curves represent different transmissivities T of the outcoupling mirror. ❶ shows the squeezed variance V_- for a system with the following parameters: $\zeta = 0.97$, $\eta = 0.97$, $\xi = 0.985$, $L = 0.006$, $l = 0.075$, $\omega = 2\pi \cdot 5 \times 10^3$ Hz. ❷ shows the squeezed variance V_- for a system with the following parameters $\zeta = 0.97$, $\eta = 0.93$, $\xi = 0.985$, $L = 0.004$, $l = 0.075$, $\omega = 2\pi \cdot 5 \times 10^3$ Hz. In both graphs the cyan curve for $T = 0.044$ is the same (see Figure 2.20), but the curves for higher transmissivities show more squeezing in ❶, due to a higher quantum efficiency used for of the photodiodes.

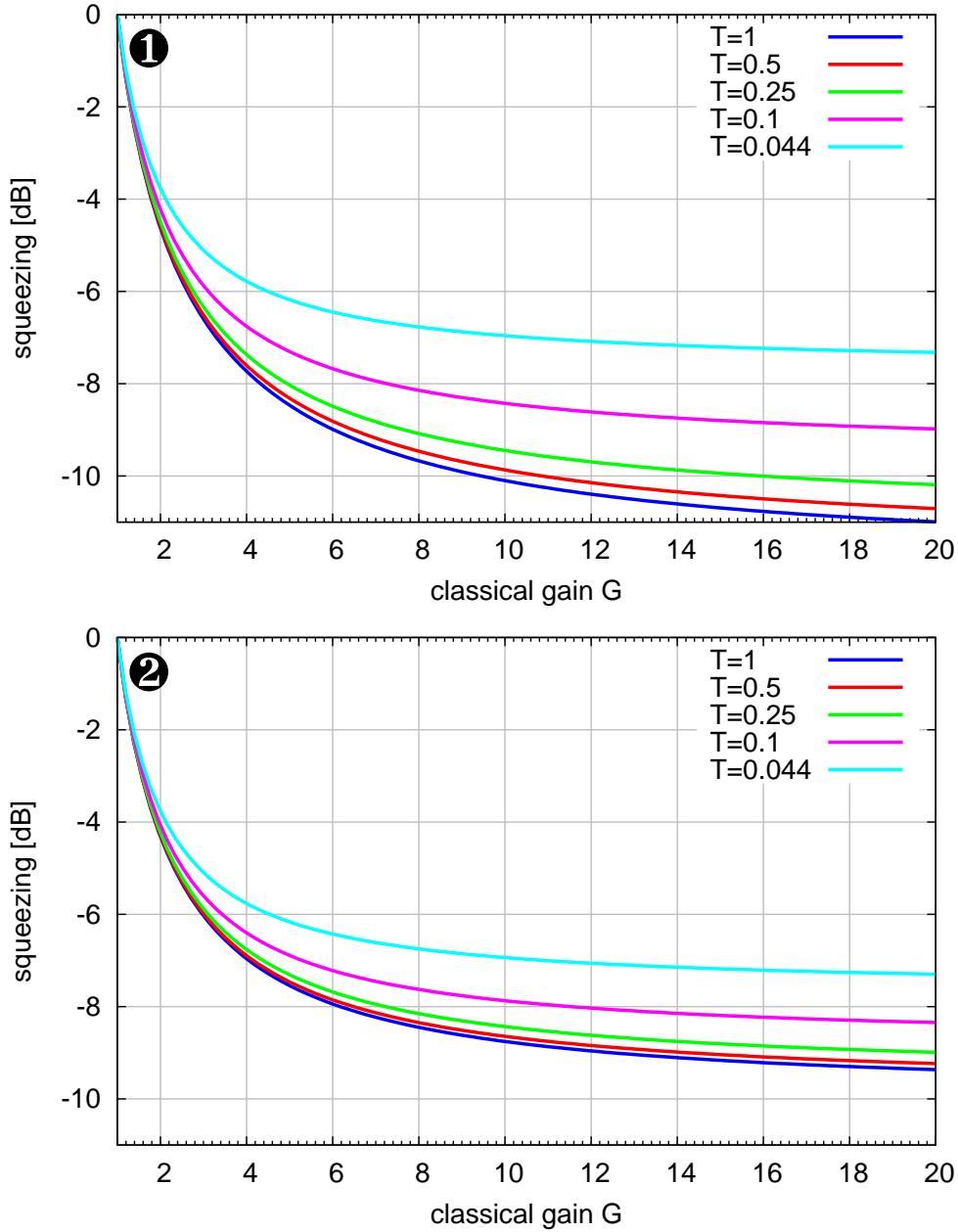


Figure 2.22: Squeezed variance V_- for a self homodyne detection scheme: The different curves represent different transmissivities T of the outcoupling mirror. **1** shows the squeezed variance V_- for a system with the following parameters: $\zeta = 0.97$, $\eta = 0.97$, $\xi = 1$, $L = 0.006$, $l = 0.075$, $\omega = 2\pi \cdot 5 \times 10^3$ Hz. **2** shows the squeezed variance V_- for a system with the following parameters $\zeta = 0.97$, $\eta = 0.93$, $\xi = 1$, $L = 0.004$, $l = 0.075$, $\omega = 2\pi \cdot 5 \times 10^3$ Hz. In both graphs the cyan curve for $T = 0.044$ is the same (see Figure 2.20), but the curves for higher transmissivities show more squeezing in **1**, due to the higher quantum efficiency used for the photodiodes. In comparison to Figure 2.21 the amount of squeezing is increased.

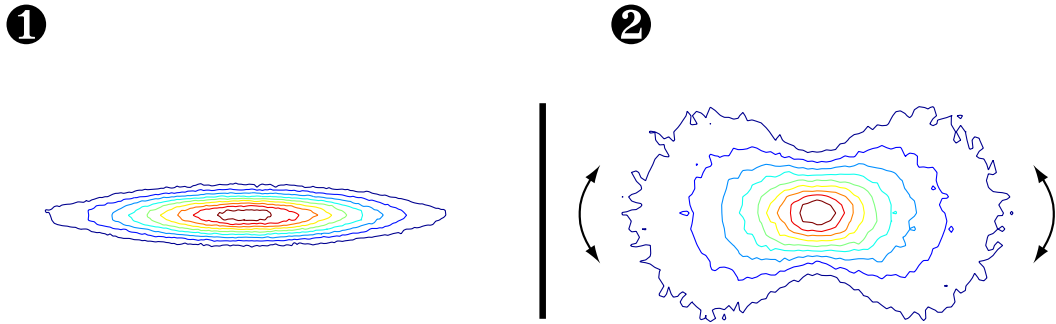


Figure 2.23: ❶: Contour plot of a squeezing ellipse. ❷: Contour plot of the same squeezing ellipse including phase fluctuations of $\delta\theta = 45^\circ$. Due to these fluctuations V_- is increased.

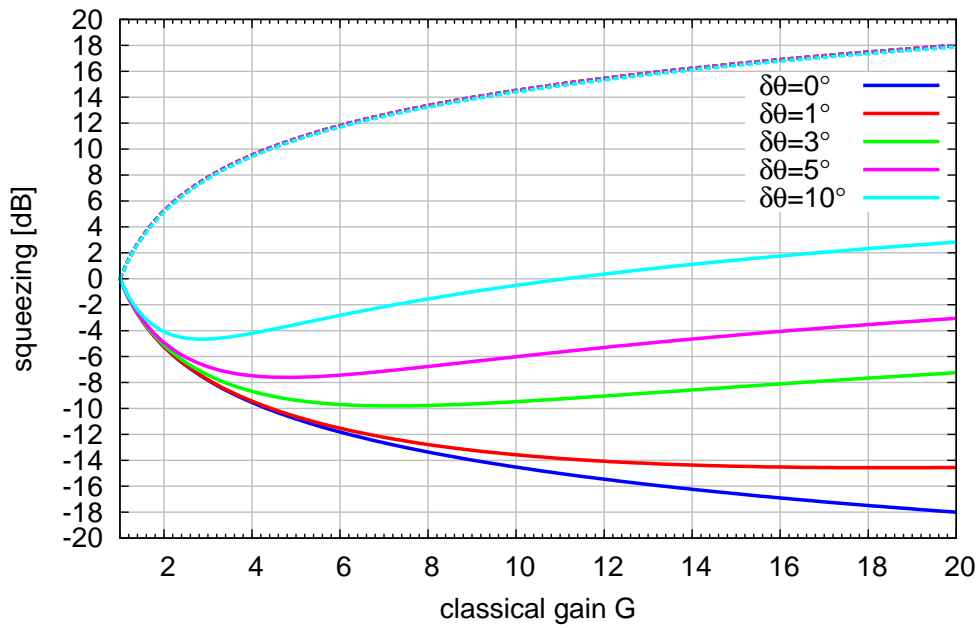


Figure 2.24: Variances V_- and V_+ for an ideal system with $l = 0.075$ and $\omega = 2\pi \cdot 5 \times 10^6$. A degradation of squeezed variance due to increasing phase fluctuations $\delta\theta$ is clearly visible. The effect to the anti-squeezed variance is too small to be seen in this graph.

Chapter 3

A typical squeezing experiment

Introduction

This chapter describes all optical components and techniques required for the generation of squeezed light. It provides the basic information for all the other experimental chapters in this thesis. This avoids multiple descriptions of the same basic element. At first the optical layout of a squeezing experiment is presented. Afterwards the three main sections of the setup—laser preparation, nonlinear experimental stage and experimental area and detection zone—are described in separate sections in more detail. The laser preparation stage is used to produce a stable laser beam in terms of mode purity, and beam position (see Section 3.2). This stage is followed by the nonlinear experimental stage, which contains the second harmonic generation (SHG) and the optical parametric amplifier (OPA). The SHG is needed to produce a strong harmonic pump field at a wavelength of 532 nm and the OPA generates the squeezed light. Both of these nonlinear phenomena, their corresponding theories and the experimental realization are represented in Section 3.3. The experimental area and detection zone (Section 3.4) in this first experiment consists only of the homodyne detector due to the fact that the experiment focuses only on the production of squeezed light. The homodyne detector is required to perform the measurements which characterize the produced squeezed quantum states. This experiment has been set up in close collaboration with my colleagues A. Franzen and H. Vahlbruch, who both wrote their Diploma theses [Fra04, Vah04] on different aspects of this setup and experiments performed with this setup.

This chapter closes with the presentation of some squeezing spectra produced and measured with the described setup. In the following chapters of this thesis the experiments will all contain the basic elements presented in this chapter. In addition, the experimental area will contain various experiments, in which the squeezed light is transformed or used as a tool to achieve a specific goal.

3.1 Optical components and layout

A typical squeezing experiment can be divided into three individual sections (see Figure 3.1). The first section is the laser preparation. Here we find components such as the main laser source and the modecleaner. The second part is the nonlinear optics stage, including the SHG and the OPA/OPO. The SHG produces the needed harmonic pump

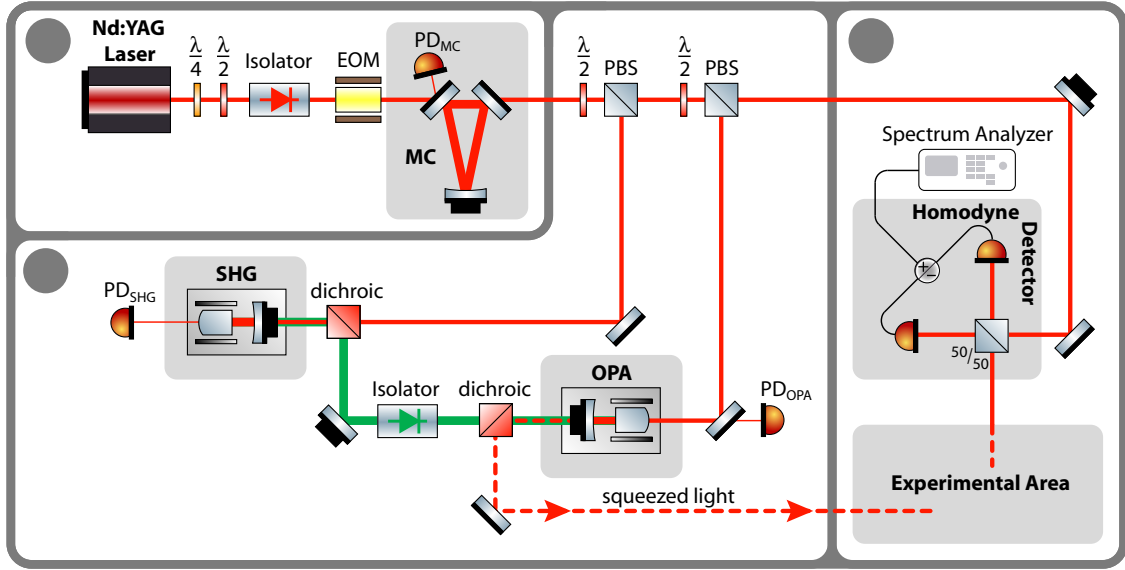


Figure 3.1: Optical layout of a generic squeezing experiment. One can divide the experiment in three sections: ❶ laser preparation, ❷ nonlinear experimental stage and ❸ experimental area including the detection zone.

light for the OPA/OPO, which then generates the desired squeezed vacuum field. The third part is the experimental stage, where the squeezing can be used as a tool in diverse experiments. This stage includes the detection zone and therefore the homodyne detector.

3.2 Laser preparation

This section contains the detailed descriptions of the main laser source, a mode cleaner and a frequency stabilization circuit. These components are needed to provide a laser beam with a pure mode profile and stable beam position for the experiment on generating and characterizing squeezed light.

3.2.1 Laser

The used laser for all experiments presented in this thesis is a monolithic nonplanar ring-oscillator (NPRO) Nd:YAG laser. It is a *Mephisto* fabricated by *Innolight*. The two pump diodes produce a power of 5.5 W at a wavelength of 808 nm. This is converted inside of the NPRO into a power of 2 W at a wavelength of 1064 nm. Characteristic for this kind of laser is the high quality beam with an $M^2 < 1.1$. This and other laser specifications are given in Table 3.1

A schematic of this laser can be found in Figure 3.2. The fields of the two pump diodes are combined with a polarizing beam splitter (PBS) and focused into the laser crystal. Here the pump field is converted into light with $\lambda_0 = 1064$ nm wavelength. The Nd:YAG crystal itself forms a cavity for the generated light. A static magnetic field is

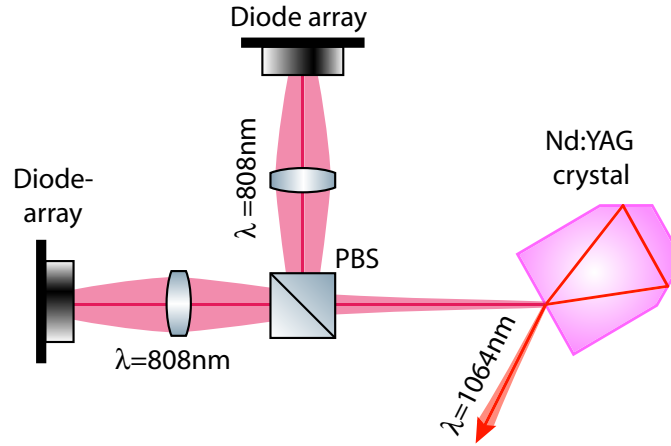


Figure 3.2: Schematic of the used Nd:YAG laser. Two pump diodes are mode matched into the laser crystal to pump the lasing process. The laser crystal forms a nonplanar ring-oscillator where an applied magnetic field selects the round trip direction of the produced light field. The generated laser radiation of 1064 nm is then propagating downwards.

output power [W]	2
beam quality, M^2	< 1.1
thermal tuning coefficient [GHz/K]	-3
thermal tuning range [GHz]	30
PZT tuning coefficient [MHz/V]	> 1
PZT tuning range [MHz]	± 100
spectral linewidth [kHz/100 ms]	1
coherence length [km]	> 1
frequency drift [MHz/min]	1
relative intensity noise, RIN [dB/Hz]	< -100
noise eater option, RIN [dB/Hz]	< -150
waist size, radius [μm]	170
waist location (inside laser head) [mm]	90

Table 3.1: Specifications of the Nd:YAG laser

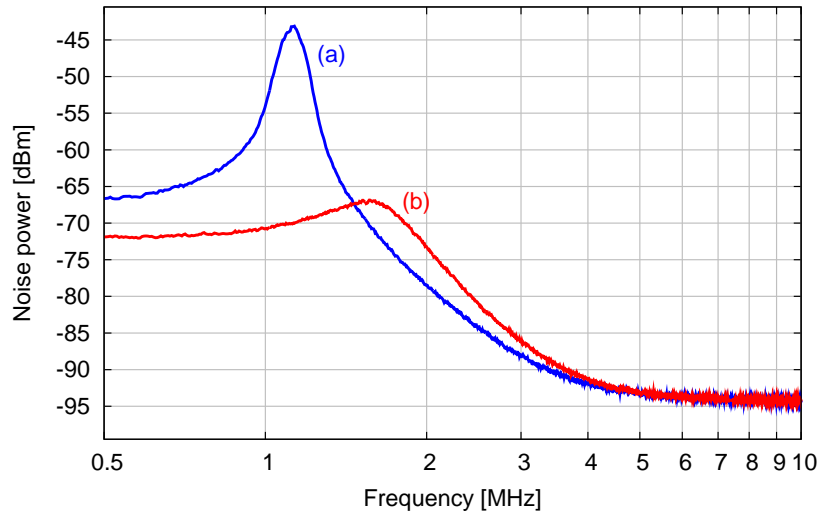


Figure 3.3: Power spectrum of the laser amplitude noise measured behind the modecleaner: (a) shows the generic laser amplitude noise with a relaxation oscillation at 1.1 MHz, (b) shows the Noise Eater improved amplitude noise of the laser. Here a small part of the laser power is detected with a photodiode and fed back to the pump diode current. As a result the laser relaxation oscillation is reduced.

applied to the area where the laser crystal is located. It induces the Faraday effect on the laser light travelling inside the cavity. This ensures that the outgoing mode is highly s-polarized. The waist size radius of the laser was measured to be $170\ \mu\text{m}$. It is located 110 mm behind the front of the laser casing.

Two different actuators are used to change the length of the laser resonator and thereby change the laser frequency. The laser crystal is mounted on a Peltier element. This allows the change of the crystal temperature which corresponds to a change in length. With this temperature actuator a tuning range of the laser frequency of 3 GHz/K can be achieved. Due to the thermal capacity of the laser crystal, the control bandwidth of the temperature is limited to about 1 Hz. For fast actuation a piezoelectric transducer (PZT) is used, which is clamped onto the laser crystal. By applying a voltage to the PZT, it changes its length. The stress that is induced on the laser crystal also changes its length. Thus a tuning range of 1.5 MHz/V with a control bandwidth of about 100kHz is possible.

Solid state lasers typically have relaxation oscillations, which reveal large amplitude noise in a certain frequency range [HRH⁺97]. A compensation of these is made for the used laser by a servo—called *Noise Eater*—which senses these oscillations with a photodiode and controls the current of the pump diodes. The performance improvement of this Noise Eater is visible in Figure 3.3

In general the laser is composed of three more components, which are essential for a well operating laser. Figure 3.1 shows that directly behind the laser there is a quarter-wave plate, a half-wave plate, and a Faraday isolator. At first the quarter-wave plate is used to eliminate the remaining elliptical polarization from the laser field. Afterwards the combination of the half-wave plate and the Faraday isolator ensures a maximum

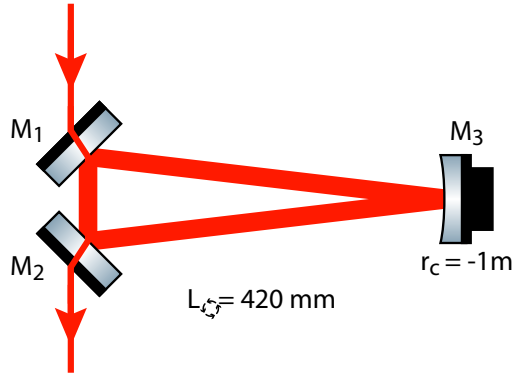


Figure 3.4: Schematic of the modecleaner, a ring cavity formed by three mirrors with a round-trip length of $L=0.42$ m. The input and output mirrors (M1 and M2) are flat and have a power transmissivity of $T_s = 700$ ppm for s-polarization and $T_p = 1.2\%$ for p-polarization. The high reflective end mirror has a transmissivity of $T_s = 100$ ppm and a radius of curvature of $r_c = -1$ m. The cavity's waist position is between the two flat mirrors and has a radius of $w_0 = 370$ μm .

attenuation of laser light that is reflected directly from the experiment to the laser to guarantee an undisturbed laser generation process.

3.2.2 Modecleaner

A modecleaner [Ueh97] can be used to improve the properties of the laser beam. A schematic of the modecleaner that was used in most experiments described in this thesis is displayed in Figure 3.4. This ring cavity is formed by three mirrors with a round-trip length of $L=0.42$ m. The input and output mirrors (M1 and M2) are flat and have a power transmissivity of $T_s = 700$ ppm for s-polarization and $T_p = 1.2\%$ for p-polarization. The high reflective end mirror has a transmissivity of $T_s = 100$ ppm and a radius of curvature of $r_c = -1$ m. The cavity's waist position is between the two flat mirrors and has a radius of $w_0 = 370$ μm . The finesse of the modecleaner depends on the input polarization of the laser light. The measured finesse in s-polarization is $\mathcal{F}_s \approx 4000$ and in p-polarization $\mathcal{F}_p \approx 256$. The free-spectral-range (FSR) of the modecleaner can be calculated to be $\text{FSR} = c/L \approx 714$ MHz. Hence, the resulting linewidth's $\Delta\nu$ full width at half maximum (FWHM) of the modecleaner is 170 kHz in s- and 2.75 MHz in p-polarization.

To ensure a high rigidity of the modecleaner all three mirrors are glued onto an Invar spacer. Invar is chosen because its low thermal expansion coefficient minimizing the alignment variances due to temperature fluctuations. To control the length of the modecleaner a piezoelectric transducer¹ (PZT) is positioned between the curved mirror and the spacer.

The modecleaner has two properties which are helpful in squeezing experiments. At first, the modecleaner acts like a low-pass filter for amplitude noise of the ingoing laser field, meaning amplitude noise gets attenuated after the transmission through the modecleaner. The modecleaner's transfer function is shown in Figure 3.7. The amplitude noise

¹Manufacturer: Physik Instrumente, type: P-016.00H, displacement: 5 $\mu\text{m}@1000$ V, length: 7 mm, diameter OL: 16 mm, diameter: 8 mm, resonance frequency: 144 kHz

at a frequency of $\Delta\nu/2$ is attenuated by a factor of two in power. For higher frequencies this attenuation is largely increased. Hence, the technical noise of the laser gets smaller and is shot noise limited at a lower frequency compared to not using a modecleaner. The second improvement by the modecleaner is the transversal mode healing effect, due to the large number of round-trips inside the cavity. The incoming beam parameters have to be exactly the same as the cavity's own mode parameters to fulfill the resonance condition and thereby pass through the modecleaner. Hence, the transmitted mode shape is much better than the incoming one.

3.2.3 Frequency stabilization

To match the frequency of the laser with the resonance frequency of the modecleaner, one of the two has to be the frequency reference whereas the other one has to be adjusted to follow the reference. Fundamental research has determined [Que03] that the used NPRO laser has a much lower frequency drift than the used Invar based modecleaner, as long as the modecleaner is not placed into a vacuum chamber. Hence, the laser is used as the frequency reference and the modecleaner is locked to the laser. The PZT of the modecleaner is used to change the length and thereby change the resonance frequency of the desired TEM₀₀ cavity mode. The needed error signal for this length control of the modecleaner is generated by a standard Pound-Drever-Hall (PDH) scheme, details of this scheme can be found in [Bla00].

The experimental layout of the frequency stabilization can be found in Figure 3.5. An oscillator with frequency $\Omega/2\pi = 15$ MHz is used to drive a phase modulator², which induces a phase modulation (see Equation 2.92) on the laser field. The beam passes two lenses to match its transversal mode shape to the eigenmode of the modecleaner. A half-wave plate in front of the modecleaner can be used to select one of the two orthogonal polarization modes. In general the low finesse p-polarization is used because the implemented modecleaner showed large absorptions, resulting in a low transmitted power, thereby not allowing a reasonable use of the high finesse mode. The incoming beam is reflected at the modecleaner and detected with a photodiode. The imprinted phase modulation is transformed into an amplitude modulation with frequency Ω if the laser light is not resonant with the modecleaner. This amplitude modulation can be sensed by the photodiode. The resulting photocurrent is electronically demodulated with a mixer and low-pass filtered. As a result one obtains an error signal for the desired modecleaner length control. This error signal is processed by a servo, which generates a feedback signal. A high-voltage (HV) amplifier boosts the feedback signal and feeds it back to the PZT that actuates the length of the modecleaner. The circuits of the used Servo and HV amplifier can be found in Appendices C.2 and C.3.

The generated PDH error signal can be found in Figure 3.6. By scanning over more than one FSR one can see the good mode matching quality. The error signal has a nice and steep slope at the locking point, where the TEM₀₀ mode is resonant inside the cavity.

The quality of the modecleaner lock can be estimated by the open-loop transfer function of the control loop. This special transfer function is measured while the frequency

²Manufacturer: Gsänger, type: PM25

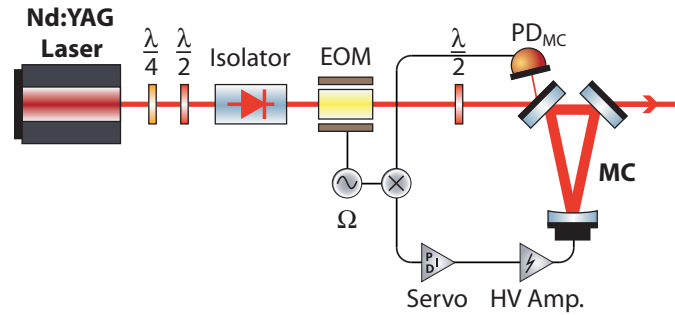


Figure 3.5: Frequency control loop of the modecleaner. An EOM generates phase modulation sidebands on the laser field, which are transformed by the modecleaner into an amplitude modulation, that is detected with a photodiode. The resulting photocurrent is mixed with the modulation frequency Ω , thereby generating an error signal that is amplified and fed back to the modecleaner's PZT.

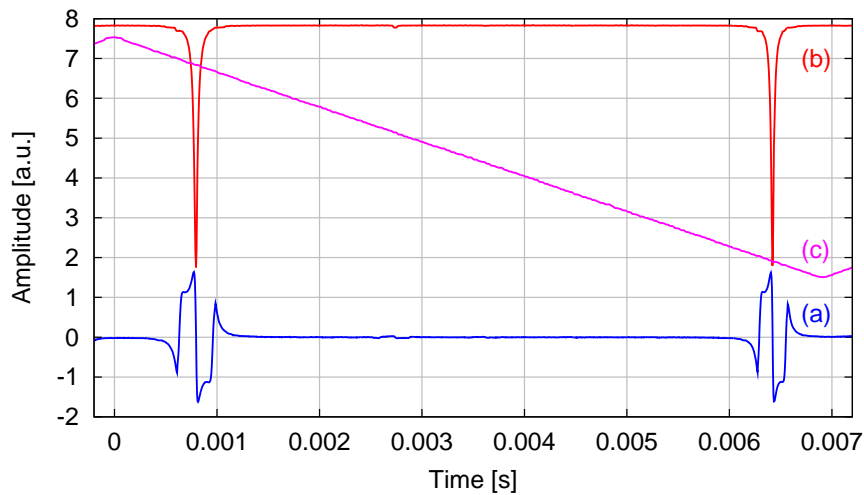


Figure 3.6: The modecleaner's PDH error signal (a) and the corresponding reflected light power (b). Trace (c) shows the high-voltage (HV) ramp applied to the PZT. The scan ranges over more than one FSR and the mode matching quality is quite remarkable. Only one tiny mode other than the TEM_{00} mode is visible.

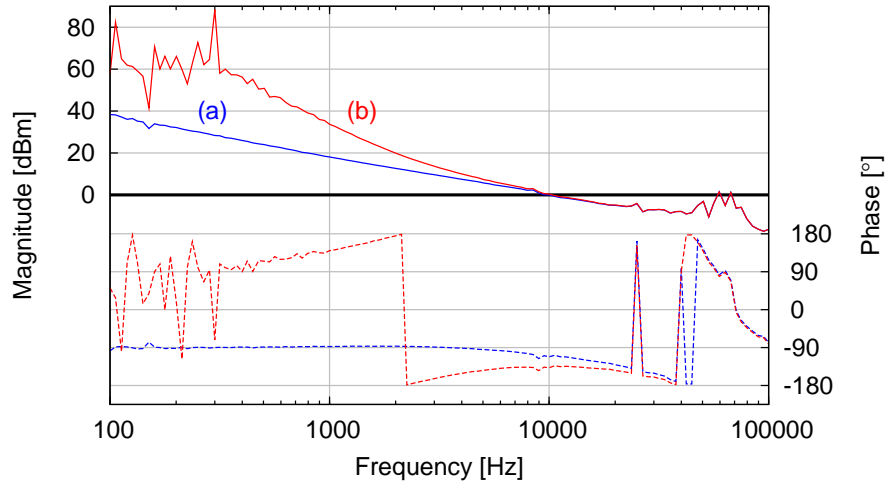


Figure 3.7: Measured open-loop transfer function (OLTF) of the modecleaner’s frequency control loop. (a) shows the OLTF for a servo with one integrator, whereas (b) was measured by using two integrators. The unity gain frequency (UGF) of both OLTFs is about 10kHz. However (b) is only conditionally stable around the UGF unlike (a), which is stable for all UGFs below 10kHz.

control loop is working and the feedback gain of the loop that is used to suppress a disturbance at a specific frequency is measured. A detailed description of the open-loop transfer function and how it is measured can be found in Appendix B.2. The servo that was used for the modecleaner control loop used two integrators that could be activated individually. The measured open-loop transfer function of the modecleaner is shown in Figure 3.7. The unity gain frequency is approximately 10 kHz. Using both integrators results in a gain of 20 dB per decade. The control with one integrator is stable for all unity gain frequencies below 10 kHz, whereas the control with two integrators is only conditionally stable around a unity gain frequency of 10 kHz. Due to the higher gain at low frequencies the loop was mostly operated with two integrators.

3.3 Nonlinear experimental stage

The next components of a typical squeezing experiment are the nonlinear cavities, namely the second harmonic generator (SHG) and the optical parametric amplifier/oscillator OPA/OPO. At first, the theory of the underlying nonlinear optical effects is introduced in Sections 3.3.1 and 3.3.2. Afterwards, the optical and mechanical setup is described in detail in Section 3.3.3.

3.3.1 Theory of second harmonic generation—SHG

Second harmonic generation is a well understood and developed physical effect to convert energy from frequency ω_0 to the new frequency $2\omega_0$. It was first demonstrated in 1961 with a Q-switched ruby laser with a conversion efficiency of $2 \cdot 10^{-8}$ [FHPW61]. Today the technique has advanced and conversion efficiencies for continuous wave (cw) systems

of up to 89% have been demonstrated [SSM⁺96]. Many of the commercially available high power lasers working in the visible range are in fact frequency doubled solid state infrared lasers e.g. the *Verdi* manufactured by Coherent.

3.3.1.1 Requirements for a SHG

Nonlinear susceptibility

Second harmonic generation (SHG) is typically done inside a crystalline material. From nonlinear optics one knows that the electric polarization \mathcal{P} of a crystal is described by the response of the outer valence electron to an electric driving force E . \mathcal{P} can be expressed by

$$\mathcal{P} = \epsilon_0 \left(\chi^{(1)} E + \chi^{(2)} E^2 + \chi^{(3)} E^3 + \dots \right). \quad (3.1)$$

The first order term is connected to the refractive index of the crystal by

$$n = \sqrt{1 + \chi^{(1)}}, \quad (3.2)$$

so that for typical materials $\chi^{(1)} \approx 1$. In most materials the second and higher order susceptibility terms can be neglected [Boy92]. Even materials with a strong second order susceptibility have $\chi^{(2)} \approx 10^{-10} - 10^{-13}$ m/V, which seems to be quite small but sufficient for second harmonic generation and optical parametric amplification. Other nonlinear processes based on the $\chi^{(2)}$ -term can be found in Figure 3.8. The Kerr effect [Boy92] is based on the $\chi^{(3)}$ -term and requires large amplitudes because most materials have an almost vanishing $\chi^{(3)}$ value.

To take a closer look at the SHG process, imagine an electric field

$$E = E_0 \cos(\omega_0 t). \quad (3.3)$$

If one considers Equation 3.1 only up to the quadratic term, the driving field will yield a polarization

$$\begin{aligned} \mathcal{P} &= \epsilon_0 \left(\chi^{(1)} E_0 \cos(\omega_0 t) + \chi^{(2)} E_0^2 \cos^2(\omega_0 t) \right) \\ &= \epsilon_0 \left(\chi^{(1)} E_0 \cos(\omega_0 t) + \frac{\chi^{(2)} E_0^2}{2} + \frac{\chi^{(2)} E_0^2}{2} \cos(2\omega_0 t) \right). \end{aligned} \quad (3.4)$$

The $2\omega_0$ term describes a higher order oscillation of the crystals valence electron. This motion gives rise to a propagating electric field with the frequency $2\omega_0$. The factor $\chi^{(2)}$ shows that for a reasonably frequency doubled output field, the input electric field must be very large. For continuous wave SHG with high conversion efficiencies the favorable design is intra-cavity SHG. This can be achieved internally, meaning the nonlinear crystal is included into the laser resonator, or externally, where the nonlinear crystal is located in a separate cavity. Throughout this thesis only external cavity SHG, which was also been used to demonstrate a conversion efficiency of 89% [SSM⁺96] will be considered. The detailed description of the SHG cavity can be found in Sections 3.3.3 and 3.3.4.

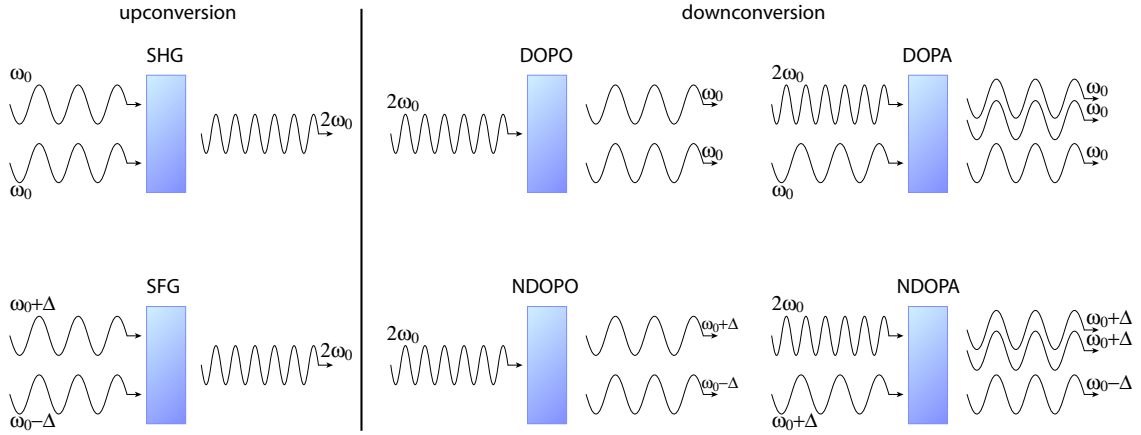


Figure 3.8: Three-wave mixing processes. There are two groups of nonlinear effects which can be divided into upconversion and downconversion processes. The upconversion processes are second harmonic generation (SHG) and sum frequency generation, which is the non-degenerate case of SHG. The upconversion processes are degenerate optical parametric oscillation (DOPO) and amplification (DOPA) and the corresponding non degenerate processes NDOPO and NDOPA. The difference between OPO and OPA is, that the OPA is seeded with fundamental field, whereas this seed is replaced with a vacuum field for the OPO.

Phase matching

The second requirement for an efficient SHG is the conservation of momentum throughout the conversion process [Boy92]. In nonlinear optics the conservation of momentum is often referred to as phase matching.

In Figure 3.8 the different processes that are based on three wave mixing are shown. SHG belongs to the group of upconversion and represents the degenerate case, meaning only one input field with a specific frequency ω_0 is used for the generation of the harmonic field with frequency $2\omega_0$. The other processes that are used throughout this thesis are degenerate optical parametric amplification (DOPA) and oscillation (DOPO) in the following named for simplification OPA and OPO respectively. All cases in Figure 3.8 require momentum conservation which can be expressed by

$$\mathbf{k}_2 = \mathbf{k}_1 + \mathbf{k}_{1'} . \quad (3.5)$$

The index corresponds to the frequency ω_j of the corresponding field. This thesis concentrates on the degenerate cases SHG, OPA and OPO, where $\mathbf{k}_1 = \mathbf{k}_{1'}$. The wave vector can be expressed using the refractive index of the material. In the case of collinearly propagating fields it is found

$$\frac{n_1 \omega_1}{c} = 2 \frac{n_2 \omega_2}{c} . \quad (3.6)$$

For the degenerate cases ($2\omega_1 = \omega_2$) this reduces to

$$n_1 = n_2 . \quad (3.7)$$

Consequently the fields have to propagate with the same speed through the crystal. This is the origin of the term *phase matching*. If the phase matching is not perfect, the fields

will become out of phase during the propagation through the crystal and the efficiency will be decreased. The phase mismatch is expressed by

$$\Delta \mathbf{k} = \mathbf{k}_2 - 2\mathbf{k}_1. \quad (3.8)$$

Experimentally, phase matching can be achieved in various ways for birefringent crystals.

- Type I phase matching is satisfied if the two incoming fundamental fields have the same polarization and the harmonic field is orthogonally polarized. This can be achieved by adjusting the angle of incidence, changing the crystal temperature or both. The phase matching is said to be *noncritical* if the refractive indices are matched for light fields propagating in the plane which is orientated 90° to the optical axis of the crystal.
- Type II phase matching is satisfied for the case that the two fundamental fields are orthogonally polarized to each other and the harmonic has the same polarization as one of the fundamental fields. Again this can be achieved by adjusting the angle of incidence, changing the crystal temperature or both.
- Quasi phase matching is done via a periodic manipulation of the cumulated relative optical phase. The crystal's domain is inverted periodically on short length scales resulting in a phase mismatch of

$$\Delta k_{\text{QPM}} = k_1 + k_{1'} - k_2 - \frac{2\pi}{\Lambda}, \quad (3.9)$$

where Λ is the crystal inversion period. Hence, the equal refractive index for the fundamental and harmonic is not necessary anymore, due to the periodic poling term. It is an advantage of the periodic poled materials that phase matching can be achieved at room temperature over a very wide temperature range compared to the other two phase matching methods. Also materials with higher nonlinearities can be used, which are otherwise unreachable with temperature or angle tuning.

In this thesis only phase matching type I is used for the nonlinear crystals in the SHG, OPA or OPO. The actual phase matching is tuned with the temperature. The temperature and wavelength dependence of the phase mismatch is described by the Sellmeier equation [ENKB91]

$$\Delta k = -8666 \left(1 - \frac{\lambda_0}{\lambda}\right)^2 \text{ cm}^{-1} + 7.49 (T - T_0) \text{ cm}^{-1} \text{ K}^{-1}, \quad (3.10)$$

where λ is the pump wavelength, T is the crystal temperature in $^\circ\text{C}$, $\lambda_0 = 1064 \text{ nm}$ and T_0 is the phase matching temperature. To see the effect of the phase matching on the conversion efficiency of the SHG one needs to look at the power of the harmonic beam [Boy92]

$$P_{2\omega_0} = P_{2\omega_0}^{\text{max}} \cdot \text{sinc}^2\left(\frac{\Delta k z}{2}\right), \quad (3.11)$$

where z is the interaction length and $P_{2\omega_0}^{\text{max}}$ is the maximum second harmonic output power. Using these two equations one can plot the conversion efficiency over temperature and wavelength (see Figure 3.9).

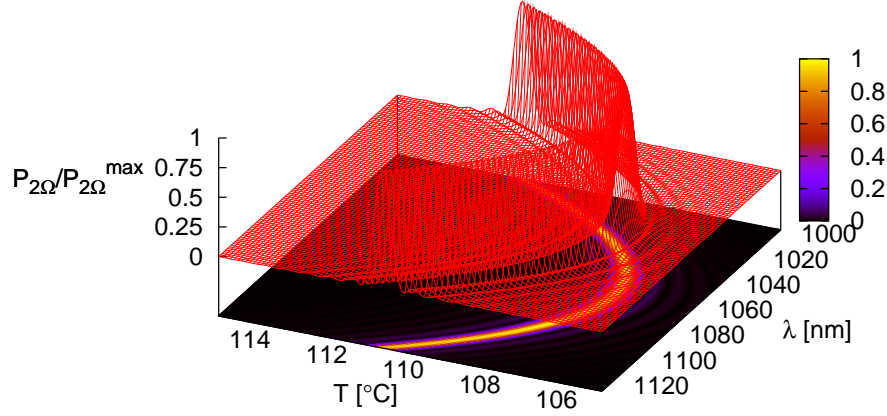


Figure 3.9: Plot of the conversion efficiency of a SHG depending on the temperature of the crystal and the wavelength of the pump. The parameters used in this plot are $T_0 = 107^\circ\text{C}$, $\lambda_0 = 1064\text{ nm}$ and $z = 7.5\text{ mm}$.

3.3.2 Theory of optical parametric amplification/oscillation—OPA/OPO

This section will mainly focus on the general equations of motion for nonlinear processes such as SHG, OPA or OPO [BR03, Buc01]. These will be solved for the OPA case which will lead to a classical and a quantum analysis of the resulting field.

The model for such nonlinear processes inside a cavity is presented including all optical fields and coupling constants in Figure 3.10. The various optical fields are:

- \hat{a} and \hat{b} , the fundamental and harmonic cavity mode;
- \hat{A}_{in} and \hat{B}_{in} , the fundamental and harmonic input field to the cavity;
- \hat{A}_{out} and \hat{B}_{out} , the fundamental and harmonic output field from the cavity;
- $\delta\hat{A}_{\text{loss}}$ and $\delta\hat{B}_{\text{loss}}$, the vacuum modes coupled in by intra-cavity losses; and
- $\delta\hat{A}_v$ and $\delta\hat{B}_v$, the vacuum modes at the output mirror.

Note the propagating fields \hat{A}_j and \hat{B}_j are distinguished from the intra-cavity fields \hat{a} and \hat{b} by using capital letters. The dimensions are also different, whereas the propagating fields have the dimension of a photon flux or energy flux, the intra-cavity fields have the dimension of photons or energy. The connection between the propagating and intra-cavity fields is achieved with the coupling rates κ_j at each mirror. These are

- κ_{m1}^a and κ_{m1}^b , the coupling rates of the mirror m1;
- κ_{m2}^a and κ_{m2}^b , the coupling rates of the mirror m2; and

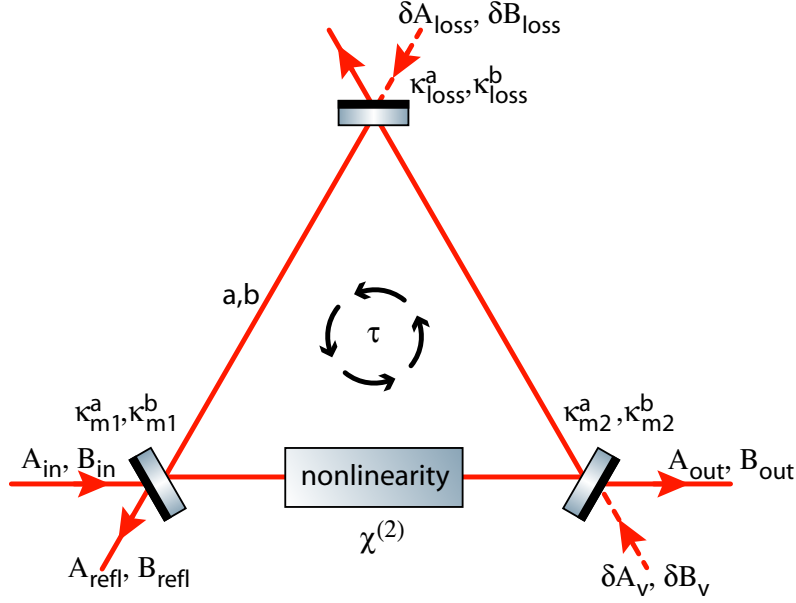


Figure 3.10: Model for nonlinear processes such as SHG, OPA or OPO inside a cavity. The relation between the propagating fields ($\hat{A}_{\text{in}}, \hat{B}_{\text{in}}, \hat{A}_{\text{refl}}, \hat{B}_{\text{refl}}, \hat{A}_{\text{out}}$ and \hat{B}_{out}) and the intra-cavity fields (\hat{a} and \hat{b}) are given by the coupling rates $\kappa_j^{a,b}$. The round trip time of the cavity is given by τ .

- κ_{loss}^a and κ_{loss}^b , the coupling rates for the intra-cavity loss.

For high reflectivities ($\rho_j \approx 1$) the coupling rates κ_j can be expressed by

$$\kappa_j = \frac{T_j}{2\tau}, \quad (3.12)$$

with the power reflectivity T_j of the mirror j and the round trip time τ . To obtain the propagating fields from the intra-cavity field one can use the following boundary conditions for the case of high mirror reflectivities ($\rho_j \approx 1$)

$$\begin{aligned} \hat{A}_{\text{refl}} &= \sqrt{2\kappa_{m1}^a} \hat{a} - \hat{A}_{\text{in}}, \\ \hat{A}_{\text{out}} &= \sqrt{2\kappa_{m2}^a} \hat{a} - \hat{A}_v. \end{aligned} \quad (3.13)$$

The reversible Hamilton operator of such a system is given by [WM94]

$$\mathcal{H}_{\text{rev}} = \hbar\omega_0 \hat{a}^\dagger \hat{a} + \hbar\omega_1 \hat{b}^\dagger \hat{b} + \frac{i\hbar\epsilon}{2} (\hat{a}^\dagger \hat{a} \hat{b} - \hat{a} \hat{a}^\dagger \hat{b}^\dagger). \quad (3.14)$$

The first term is related to the fundamental mode, whereas the second term is related to the harmonic mode. The last term describes the nonlinear interaction between the two fields. Here ϵ corresponds to the strength of the nonlinear interaction, which depends on the second order susceptibility $\chi^{(2)}$ and experimental parameters such as phase matching, crystal imperfections and beam focussing.

Using the quantum Langevin equation [Hak70] and the formalism derived by Gardiner and Collett [GC85] the equations of motion of the fundamental and harmonic intra-cavity fields in the rotating frame of the fundamental field can be derived for the case that the cavity is on resonance

$$\begin{aligned}\dot{\hat{a}} &= -\kappa_a \hat{a} + \epsilon \hat{a}^\dagger \hat{b} + \sqrt{2\kappa_{m1}^a} \hat{A}_{in} + \sqrt{2\kappa_{m2}^a} \delta \hat{A}_v + \sqrt{2\kappa_{loss}^a} \delta \hat{A}_{loss}, \\ \dot{\hat{b}} &= -\kappa_b \hat{b} - \frac{\epsilon}{2} \hat{a}^2 + \sqrt{2\kappa_{m1}^b} \hat{B}_{in} + \sqrt{2\kappa_{m2}^b} \delta \hat{B}_v + \sqrt{2\kappa_{loss}^b} \delta \hat{B}_{loss}.\end{aligned}\quad (3.15)$$

Here κ_a and κ_b are the total coupling rates given by $\kappa_{m1}^{a,b} + \kappa_{m2}^{a,b} + \kappa_{loss}^{a,b} = \kappa_{a,b}$. These equations are valid for the degenerate nonlinear processes such as SHG, OPA and OPO (Figure 3.8). The special cases only differ in the coupling rates and choice of input fields. It has been assumed that only vacuum fluctuations are used as input at mirror m2, thus only the quantum fluctuations $\delta \hat{A}_v$ and $\delta \hat{B}_v$ are used in the equations of motion. The input fields \hat{A}_{in} and \hat{B}_{in} are normally a combination of a classical coherent amplitude α_0 and β_0 and quantum fluctuations $\delta \hat{A}_{in}$ and $\delta \hat{B}_{in}$.

For the case of an OPA the harmonic pump field is much larger than the fundamental seed field. Therefore one can assume that the pump field strength will change only slightly and one can consider the pump field as a classical field and combine it with the nonlinear coupling constant ϵ to the combined quantity $g = \epsilon \hat{b}$ that describes the total nonlinear gain. The equations of motion for the fundamental field in the OPA process then simplify to

$$\begin{aligned}\dot{\hat{a}} &= -\kappa_a \hat{a} + g \hat{a}^\dagger + \sqrt{2\kappa_{m1}^a} \hat{A}_{in} + \sqrt{2\kappa_{m2}^a} \delta \hat{A}_v + \sqrt{2\kappa_{loss}^a} \delta \hat{A}_{loss}, \\ \dot{\hat{a}^\dagger} &= -\kappa_a \hat{a}^\dagger + g^* \hat{a} + \sqrt{2\kappa_{m1}^a} \hat{A}_{in}^\dagger + \sqrt{2\kappa_{m2}^a} \delta \hat{A}_v^\dagger + \sqrt{2\kappa_{loss}^a} \delta \hat{A}_{loss}^\dagger.\end{aligned}\quad (3.16)$$

3.3.2.1 Classical properties of parametric amplification

First of all the classical properties of an OPA are derived. Afterwards an analysis of its quantum properties is given in the next section. The classical steady state intra-cavity field is defined by $\dot{\hat{a}} = 0$ and $\hat{a} \rightarrow \alpha$. One can choose the input field \bar{A}_{in} to be real without loss of generality. For the intra-cavity steady state field one finds [Buc01]

$$\alpha = \frac{(1 + \frac{g}{\kappa_a}) \sqrt{2\kappa_{m1}^a}}{\kappa_a (1 - \frac{|g|^2}{\kappa_a^2})} \bar{A}_{in}.\quad (3.17)$$

For the case that no seed field is used ($\bar{A}_{in} = 0$) one finds in general ($g < \kappa_a$) only the solution $\alpha = 0$. But directly at the threshold, which is defined by $g = \kappa_a$ a second solution is possible with $\alpha \neq 0$. The cases at and above the threshold have not been studied in this thesis.

The propagating output field is then found by combining Equation 3.13 with Equation 3.17 resulting in

$$\bar{A}_{out} = \frac{(1 + \frac{g}{\kappa_a}) \sqrt{2\kappa_a \kappa_{m1}^a}}{\kappa_a (1 - \frac{|g|^2}{\kappa_a^2})} \bar{A}_{in}.\quad (3.18)$$

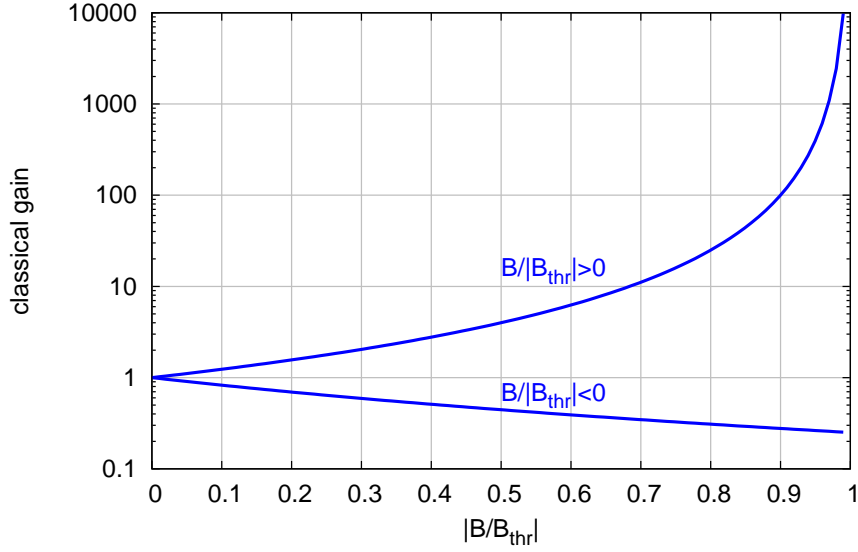


Figure 3.11: Classical gain of an optical parametric amplifier

A comparison of this output field with the output field for zero gain results in

$$\frac{\bar{A}_{\text{out}}}{\bar{A}_{\text{out}}|_{g=0}} = \frac{1 + \frac{g}{\kappa_a}}{1 - \frac{|g|^2}{\kappa_a^2}}. \quad (3.19)$$

This can be expressed in terms of the optical output power P_{out} of the cavity, which represents the classical gain G

$$G = \frac{\bar{P}_{\text{out}}}{\bar{P}_{\text{out}}|_{g=0}} = \frac{\left(1 + \frac{g}{\kappa_a}\right)^2}{\left(1 - \frac{|g|^2}{\kappa_a^2}\right)^2}. \quad (3.20)$$

The term g/κ_a reflects the ratio of the actual harmonic pump field strength to the threshold pump field strength and is equal to the ratio $\bar{B}/|\bar{B}_{\text{thr}}|$. As result we find

$$G = \frac{\bar{P}_{\text{out}}}{\bar{P}_{\text{out}}|_{g=0}} = \frac{\left(1 + \frac{\bar{B}}{\bar{B}_{\text{thr}}}\right)^2}{\left(1 - \left|\frac{\bar{B}}{\bar{B}_{\text{thr}}}\right|^2\right)^2}. \quad (3.21)$$

The equation describes the classical gain of the parametric OPA process. Below the threshold two distinct cases for amplification and deamplification are found. These two cases differ in the phase of the harmonic pump field. Amplification is found for \bar{B} to be real and positive, whereas deamplification is found for \bar{B} being real and negative. This behavior is shown in Figure 3.11.

3.3.2.2 Quantum properties of parametric amplification

The quantum properties of the optical parametric amplifier reflect the classical properties, but here the quantum fluctuations are being amplified and deamplified, leading to phase

quadrature and amplitude quadrature squeezing, respectively. The spectrum of the OPA output field has to be derived to see this behavior. Therefore, the quadrature operators \hat{X}_1 and \hat{X}_2 are needed, which can be deduced from the equations of motion in Equation 3.16. Using the definition of the quadrature operators from Equation 2.25 and assuming that g is real, one obtains the quadrature amplitudes for the intra-cavity field [Buc01]

$$\begin{aligned}\dot{\hat{X}}_{1,a} &= -\kappa_a \hat{X}_{1,a} + g \hat{X}_{1,a} + \sqrt{2\kappa_{m1}^a} \hat{X}_{1,\text{in}} + \sqrt{2\kappa_{m2}^a} \delta \hat{X}_{1,v} + \sqrt{2\kappa_{\text{loss}}^a} \delta \hat{X}_{1,\text{loss}}, \\ \dot{\hat{X}}_{2,a} &= -\kappa_a \hat{X}_{2,a} - g \hat{X}_{2,a} + \sqrt{2\kappa_{m1}^a} \hat{X}_{2,\text{in}} + \sqrt{2\kappa_{m2}^a} \delta \hat{X}_{2,v} + \sqrt{2\kappa_{\text{loss}}^a} \delta \hat{X}_{2,\text{loss}}.\end{aligned}\quad (3.22)$$

The frequency dependence of the quadrature amplitudes is found by the Fourier transform

$$\begin{aligned}i\Omega \tilde{X}_{1,a} &= -\kappa_a \tilde{X}_{1,a} + g \tilde{X}_{1,a} + \sqrt{2\kappa_{m1}^a} \tilde{X}_{1,\text{in}} + \sqrt{2\kappa_{m2}^a} \delta \tilde{X}_{1,v} + \sqrt{2\kappa_{\text{loss}}^a} \delta \tilde{X}_{1,\text{loss}}, \\ i\Omega \tilde{X}_{2,a} &= -\kappa_a \tilde{X}_{2,a} - g \tilde{X}_{2,a} + \sqrt{2\kappa_{m1}^a} \tilde{X}_{2,\text{in}} + \sqrt{2\kappa_{m2}^a} \delta \tilde{X}_{2,v} + \sqrt{2\kappa_{\text{loss}}^a} \delta \tilde{X}_{2,\text{loss}}.\end{aligned}\quad (3.23)$$

Here Ω corresponds to the sideband frequency besides the carrier frequency, which is the actual frequency of interest.

Together with the boundary condition for the in- and output given by Equation 3.13 one obtains the frequency-dependent output quadrature amplitudes

$$\begin{aligned}\tilde{X}_{1,a}(\Omega) &= \frac{2\sqrt{\kappa_{m1}^a \kappa_{m2}^a} \tilde{X}_{1,\text{in}} + (2\kappa_{m2}^a - i\Omega - \kappa_a + g) \delta \tilde{X}_{1,v} + 2\sqrt{\kappa_{m2}^a \kappa_{\text{loss}}^a} \delta \tilde{X}_{1,\text{loss}}}{i\Omega + \kappa_a - g}, \\ \tilde{X}_{2,a}(\Omega) &= \frac{2\sqrt{\kappa_{m1}^a \kappa_{m2}^a} \tilde{X}_{2,\text{in}} + (2\kappa_{m2}^a - i\Omega - \kappa_a - g) \delta \tilde{X}_{2,v} + 2\sqrt{\kappa_{m2}^a \kappa_{\text{loss}}^a} \delta \tilde{X}_{2,\text{loss}}}{i\Omega + \kappa_a + g}.\end{aligned}\quad (3.24)$$

The spectrum of the quadrature fields is then found to be

$$\begin{aligned}V_{1,\text{out}}(\Omega) &= 1 + \eta_{\text{esc}} \frac{4\frac{g}{\kappa_a} + 4\frac{\kappa_{m1}^a}{\kappa_a} (V_{1,\text{in}} - 1)}{\frac{\Omega^2}{\kappa_a^2} + \left(1 - \frac{g}{\kappa_a}\right)^2}, \\ V_{2,\text{out}}(\Omega) &= 1 + \eta_{\text{esc}} \frac{-4\frac{g}{\kappa_a} + 4\frac{\kappa_{m1}^a}{\kappa_a} (V_{2,\text{in}} - 1)}{\frac{\Omega^2}{\kappa_a^2} + \left(1 + \frac{g}{\kappa_a}\right)^2},\end{aligned}\quad (3.25)$$

with the escape efficiency $\eta_{\text{esc}} = \kappa_{m2}^a / \kappa_a$, which determines the efficiency with which the squeezing may exit the OPA cavity. For high reflectivities of the mirrors m1 and m2 one can substitute the coupling rates by

$$\kappa_{m1}^a = \frac{T_{m1}}{2\tau}, \quad (3.26)$$

$$\kappa_{m2}^a = \frac{T_{m2}}{2\tau}, \quad (3.27)$$

$$\kappa_{\text{loss}}^a = \frac{T_{\text{loss}}}{2\tau}, \quad (3.28)$$

with T_j being the power transmissivity of the corresponding element and τ the cavity round trip time. This leads to Equation 2.94 for the escape efficiency used in Section 2.11.

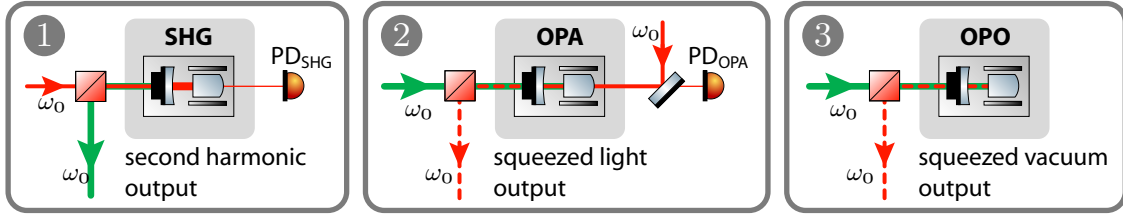


Figure 3.12: Optical layout of three different nonlinear cavities

It is essential to have small losses to maximize the escape efficiency. For a more detailed analysis of Equation 3.25 see Section 2.11.

In the limit of weak input couplings, meaning $\kappa_{m1} \ll \kappa_a$ the second term of the numerator can be neglected. Substituting g/κ_a again with the ratio $\bar{B}/|\bar{B}_{\text{thr}}|$ of the pump actual field strength to the threshold value, one can rewrite Equation 3.25 to

$$\begin{aligned}
 V_{1,\text{out}}(\Omega) &= 1 + \eta_{\text{esc}} \frac{4 \frac{\bar{B}}{|\bar{B}_{\text{thr}}|}}{\frac{\Omega^2}{\kappa_a^2} + \left(1 - \frac{\bar{B}}{|\bar{B}_{\text{thr}}|}\right)^2}, \\
 V_{2,\text{out}}(\Omega) &= 1 - \eta_{\text{esc}} \frac{4 \frac{\bar{B}}{|\bar{B}_{\text{thr}}|}}{\frac{\Omega^2}{\kappa_a^2} + \left(1 + \frac{\bar{B}}{|\bar{B}_{\text{thr}}|}\right)^2}.
 \end{aligned} \tag{3.29}$$

It is easily to be seen that the best squeezing is achieved at the threshold. The best amplitude squeezing is achieved for $\bar{B}/|\bar{B}_{\text{thr}}| = +1$ and the best phase squeezing for $\bar{B}/|\bar{B}_{\text{thr}}| = -1$.

The classical analysis led to the result that a classical field entering through the input coupler can best be deamplified to a quarter of its initial value. On the contrary, the quantum analysis for the weak input coupling regime shows no limit for the deamplification. Leaving the weak coupling regime by using the equations 3.25, any noise entering the input mirror ($V_{1,2,\text{in}} - 1$) is indeed deamplified to a quarter of its initial value as it is predicted by the classical result.

3.3.3 Nonlinear cavities

In this section the optical and mechanical setup of the implemented nonlinear cavities will be introduced. Afterwards the SHG and OPA/OPO cavity and their parameters are presented in detail.

3.3.3.1 Optical layout

Throughout this thesis three different types of nonlinear cavities are used (Figure 3.12). All nonlinear cavities use a hemilitic cavity design where the resonator is formed by an outcoupling mirror and the back surface of the nonlinear crystal (Figure 3.14). The crystals are basically $\text{MgO}:\text{LiNbO}_3$ (Figure 3.13), where the MgO doping varies between 5–7%. Generally their front surface is flat and coated with an anti-reflective (AR) coating

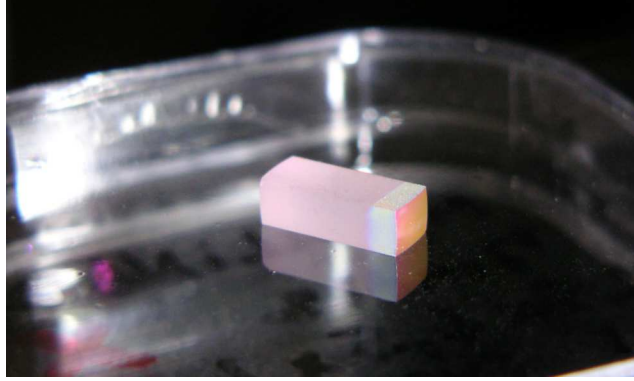


Figure 3.13: Photo of a MgO:LiNbO₃ crystal

for the fundamental ($R_{1064\text{nm}} < 0.05\%$) and harmonic wavelength ($R_{532\text{nm}} < 0.2\%$). The back surface is curved and has a radius of curvature $\text{RoC}=8\text{mm}$ and exhibits a high reflective (HR) coating for both wavelength. The dimensions of the crystal slightly differ between the experiments presented throughout this thesis, mostly crystals with a dimension of $2 \times 6.5 \times 2.5\text{mm}$ (length \times width \times depth) with respect to the orientation shown in Figure 3.14. For the used wavelength of 1064 nm and 532 nm these crystals show absorption. The losses for the individual wavelength were measured to be $l_{1064\text{nm}} \approx 0.1\%/cm$ and $l_{532\text{nm}} \approx 0.3 - 1\%/cm$, depending on the specific crystals used.

In the first squeezing experiments described in this chapter and in Chapter 4, modulation plates—orientated perpendicular to the optical axis of the crystal—were used for generating an internal phase modulation onto the optical fields via the electro-optical effect [Sie86] utilizing an electrical resonance (see Section 3.3.4) for the generation of an error signal for the length of the nonlinear cavities. In the experiments presented in Chapters 5 and 6 this internal phase modulation has been substituted by an external phase modulation using an EOM. Hence, the modulation frequencies do not depend on a resonance and can be chosen independently.

A general difference between the SHG and OPA/OPO is the reflectivity of the out-coupling mirror. In the case of a SHG a high reflectivity for the fundamental field is needed. Hence, the interaction time or length between this field and the nonlinear crystal can be increased utilizing a good conversion efficiency, despite the fact that the susceptibility $\chi^{(2)}$ of MgO:LiNbO₃ is very small compared to other nonlinear materials [God06]. The prospects for the outcoupling mirror reflectivity of an OPA/OPO are different. The amount of squeezing depends primarily on the average pump power (see Equation 3.29). Hence, the reflectivity for the pump wavelength can be used to control the internal pump power if the overall available power is limited. Moreover, the reflectivity for the fundamental wavelength is linked with the escape efficiency and the cavity linewidth. Both of these influence the amount of squeezing likewise. The cavity linewidth is responsible for the frequency dependent amount of squeezing because only quantum noise that enters the cavity can be affected by the nonlinear effect. The escape efficiency, determined by the reflectivity for the fundamental wavelength and the transmissivity of the AR coating on the front surface of the crystal, on the other hand controls the loss of the produced

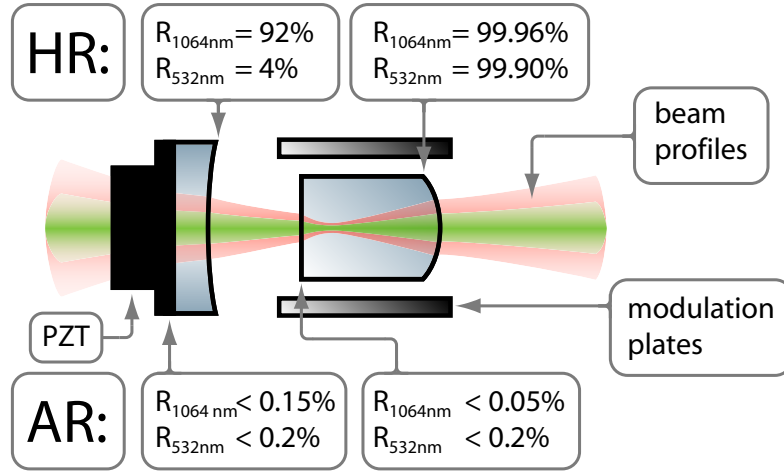


Figure 3.14: Representative schematic of the optical layout of a nonlinear cavity and the beam profiles of the fundamental and harmonic fields. Power reflectivity values of the coated surfaces are given for the SHG.

squeezed field inside the cavity. A high escape efficiency results in low losses on the produced squeezing and vice versa (details see Equation 2.93). This effect is visualized in Figures 2.21 and 2.22.

Overall there exist three reasonable cases for the composition of the two internal light fields, which would result in a working OPA/OPO. The individual field strengths are controlled by the two mirror reflectivities. The different cases are presented in Figure 3.15. It shows the transmission of an OPA/OPO cavity for diverse outcoupling mirror reflectivity combinations of $R_{1064\text{nm}}$ and $R_{532\text{nm}}$. The first and third combinations are used throughout this thesis, whereas the second case for our wavelength and crystals generally caused locking problems due to the large thermal effects that are produced by the high internal harmonic power due to the higher absorption for 532 nm. The fourth case uses the same reflectivities as the third one, but shows a more realistic situation. Here the transmission peaks are not overlapping at their maxima. The reason is a wavelength specific phase shift at the crystals HR coated back surface. This causes different resonance conditions for the two used wavelength. For achieving a result as presented in the third case of Figure 3.15, this additional phase shift has to be taken into account.

The other difference between the SHG and the OPA/OPO is the optical layout of the incoming fields. A comparison of the SHG, OPA and OPO is shown in Figure 3.12. The SHG is a cavity for the fundamental wavelength, which enters the cavity through the outcoupling mirror. The length control is generally performed with a PDH locking scheme. Phase modulation sidebands are imprinted onto the fundamental field by an external EOM or by the modulation plates inside the nonlinear cavity. The needed photodiode, detecting the induced amplitude modulation is placed in transmission, behind the back surface of the crystal. The generated harmonic field propagates through the outcoupling mirror and is separated from the incoming fundamental field with a dichroic beam splitter cube. A cube is used to minimize the mode distortion for the incoming and outgoing fields. Compared with a dichroic beam splitter plate under an angle of 45° , the

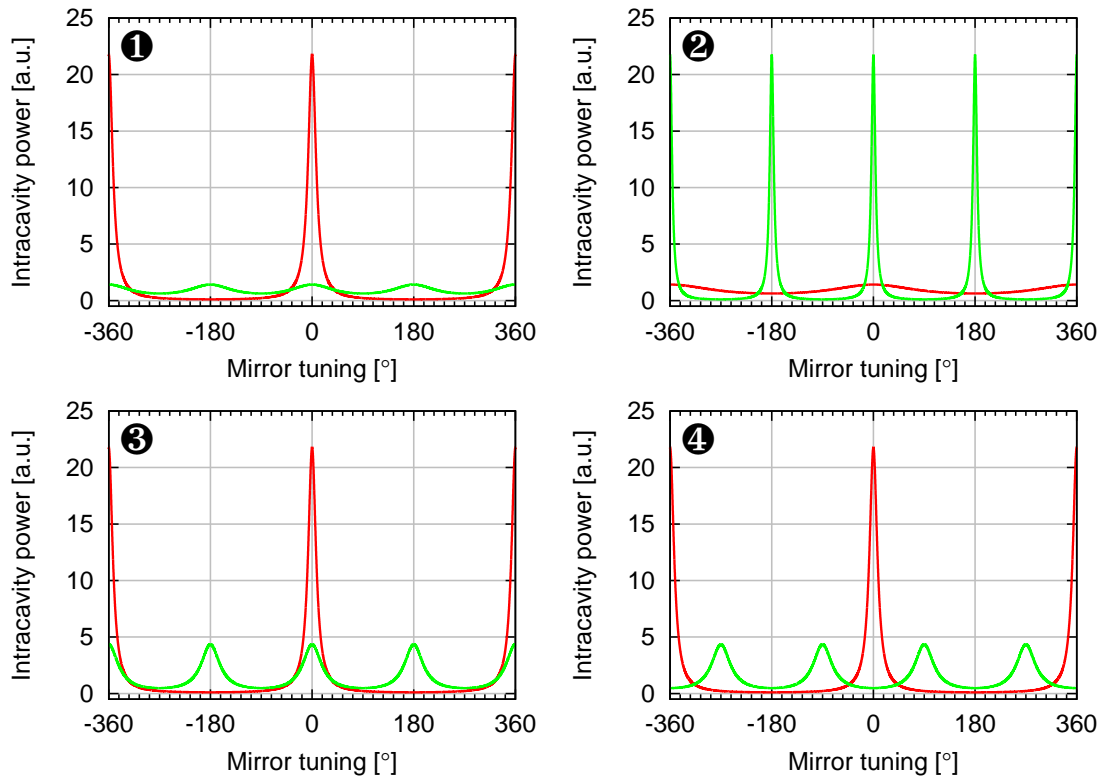


Figure 3.15: Intra-cavity powers of the fundamental and harmonic field for different combinations of the outcoupling mirror reflectivities. **1** infrared (IR) cavity outcoupling mirror reflectivities $R_{1064\text{ nm}} \approx 1$ and $R_{532\text{ nm}} = 0.04$. **2** green cavity outcoupling mirror reflectivities $R_{1064\text{ nm}} \approx 0.04$ and $R_{532\text{ nm}} = 1$. **3** doubly resonant cavity—high finesse for the fundamental and low finesse for harmonic field—outcoupling mirror reflectivities $R_{1064\text{ nm}} \approx 1$ and $R_{532\text{ nm}} = 0.25$, **4** same as **3** but an additional phase shift for the harmonic field at the back surface of the crystal has been taken into account.

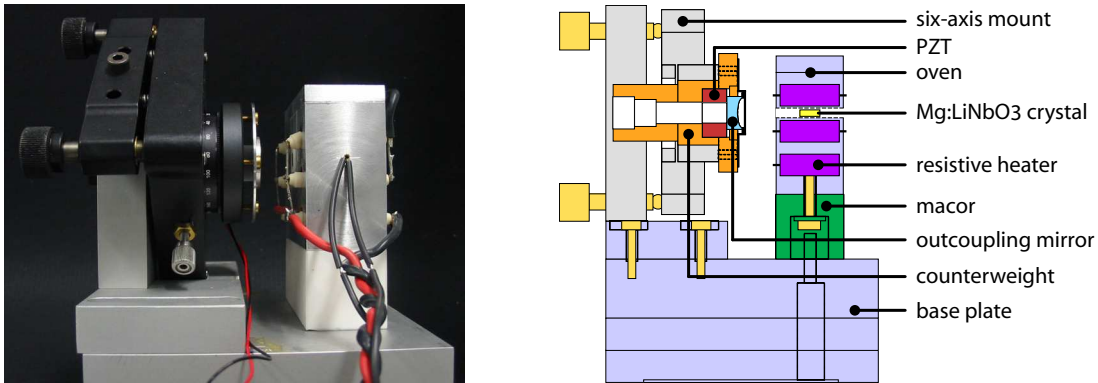


Figure 3.16: Nonlinear cavity: A photo of the nonlinear cavity design is shown on the left-hand side. To the right the schematic of this setup is illustrated. The cavity is formed by the crystal’s back surface, housed in the oven, and the outcoupling mirror, mounted with a counterweight into a six-axis mirror mount. Both—oven and mirror mount—share a base plate, which makes an adjusted cavity portable without introducing any misalignment.

mode matching efficiency was increased by at least 5%.

The OPA cavity is pumped with a strong harmonic field that enters and leaves the cavity through the outcoupling mirror. The length of the cavity is controlled by a fundamental seed field that is coupled in through the backside of the crystal. For the control a photodiode is placed in reflection of the back surface. The generated bright³ squeezed field propagates through the outcoupling mirror and is separated from the harmonic pump field with a dichroic beam splitter cube.

The OPO cavity uses the same layout as the OPA cavity. The only difference is, that the former classical seed field in the case of an OPA is replaced by a vacuum field for the OPO. This enables the generation of squeezed vacuum fields⁴. The problem in the case of an OPO is the length control of the cavity to satisfy the frequency selection of the generated squeezed vacuum. In Chapter 6 one possible locking scheme for OPO cavities is described in detail.

3.3.3.2 Mechanical setup

The mechanical setup of the nonlinear cavities has changed during my Ph.D., but the main concepts have not. I will present the generic mechanical setup of the nonlinear cavities with the most simple cavity design. Later in this section this design is modified in two steps to enhance the performance of the oven and the mechanical stability of the resonator.

Cavity design MK I

In the previous section the hemilithic design of the nonlinear cavity was introduced. In Figure 3.16 a photo in comparison to a schematic of this setup is presented. On the left-

³bright squeezed field, because it carries a small part from the seed field carrier

⁴Compared to a bright squeezed field, a squeezed vacuum field does not contain a carrier.

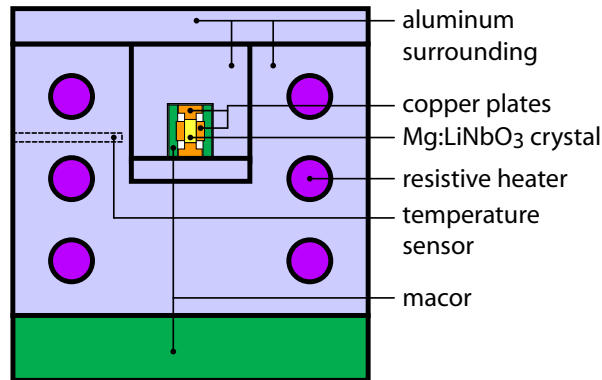


Figure 3.17: The schematic of the first oven design presented from the front. The inner part, containing the crystal and modulation plate in the center is surrounded by the resistive heated aluminum outer part.

hand side one can see the mount for the outcoupling mirror. The half inch sized mirror is embedded into a brass counterweight together with a PZT. On the front face the stack made of the counterweight, the PZT and the mirror is clamped together with a aluminum cap. A Viton ring between the cap and the mirror protects the mirror from local stresses. The counterweight is screwed onto a K6X six-axis mirror mount from Thorlabs. On the right-hand side the aluminum oven is located, that houses the crystal. Both elements—mirror mount and oven—are unified on one aluminum base plate. This makes the design portable without misaligning the cavity. The embedment of the outcoupling mirror into the six-axis mirror mount simplifies the alignment of the cavity and the adjustment of the cavity's air gap. A disadvantage of this design is that the cavity's rigidity is low, which limits the locking performance. Mechanical drifts of the mirror mount also result in misalignments of the cavity.

The phase matching temperature of 5% doped MgO:LiNbO₃ for 1064 nm and 532 nm is around 106°C (see Equation 3.10). The 7% doped crystals have a phase matching temperature of approximately 67°C. As a consequence the nonlinear crystal needs to be heated. Hence, the crystal is embedded into an aluminum oven, which is used as a heat bath. The basic setup of the oven is shown in Figure 3.17. In the center the MgO:LiNbO₃ crystal is located, with an end face of 2.5×5 mm. The crystal is thermally contacted to the outer surrounding aluminum oven with T-shaped copper plates. To the sides of the crystal two rectangular shaped copper plates are located. These could be used for the internal modulation of the refractive index—inducing phase modulation sidebands on the internal light field—by applying a voltage with a modulation frequency Ω . The electrical insulation to the oven is achieved with macor plates between the copper plates and the aluminum oven. For a simplified assembly this inner part of the oven consists of the crystal, the four copper plates and the two macor plates and is embedded into a small aluminum block, which itself is mounted into the outer U-shaped aluminum oven. The outer part of the oven contains six resistive heaters—each has 12 Ohm such that the parallel circuit results in a total resistance of 2 Ohm—and the temperature sensor which is mounted near the intersection of the inner and outer oven part. The temperature

sensor is a simple NTC⁵, which shows a high accuracy in the desired temperature range.

This design has two big disadvantages. First, the NTC is near the resistive heaters but far away from the crystal. Hence, the temperature control loop controls the crystal's temperature to within a very low accuracy and large delay time. The second disadvantage is the lack of active cooling. The resistive heaters transform a current into heat. If the current drops to zero, no more heat is produced. Due to the thermal isolation of the oven the only cooling mechanism is radiation. This is a very slow process compared to the heating via resistors. As a result the thermal control of the oven is very asymmetric, which makes the control performing non-optimal.

Oven design MK II

A new oven design has been developed to solve the problems of the first oven. The main problem of the first oven design was a bad temperature control due to the position of the temperature sensor and the resistive heaters. These allowed only active heating whereas cooling was achieved only due to the emission of thermal radiation. The new design of the oven uses a different inner part consisting of Peltier elements for active heating and cooling. A schematic of the inner setup and a photo of the oven can be found in Figure 3.18. The outer surrounding of the oven has not been changed. The resistive heaters can be installed optionally to use the outer part as a heat bath for the Peltier elements. Hence, large temperature gradients between the Peltier elements and the aluminum oven can be minimized. The newly used Peltier elements⁶ are compatible with high temperatures and allow an operation up to 150°C. Two Peltier elements were used in the inner part of the oven and are placed below and on top of the crystal. To the sides of the crystal macor plates have been placed as a thermal shield avoiding thermal fluxes into or from the outer part of the oven. The crystal is thermally contacted to two L-shaped copper plates via 0.1 mm thick indium foil to the Peltier elements. This guarantees the best thermal flux between the Peltier and the crystal. Each of the L-shaped copper plates contains a small drilling into which a NTC temperature sensor can be placed. A small distance of approximately 2.5 mm to the center of the crystal ensures a good signal quality for the temperature stabilization servo. The front and back surfaces of the inner oven part are covered with macor. This minimizes the thermal fluxes between the inner part and the laboratory. Optical access for the laser beams was ensured by two small holes with a diameter of 2.5 mm.

A further improvement to the design of the oven is the material mixture that is used for separating the inner from the outer oven part. The inner part of the oven is placed into a copper U-shaped case that is separately mounted into the aluminum surrounding. The old design used an aluminum to aluminum connection, which tended to form a unified aluminum block once heated to the phase matching temperature. The new material mixture solves this problem and an easy disassembly of the oven is guaranteed.

Compared to the old design, the new oven allows a much more accurate control of the setpoint, thereby decreasing the smallest possible temperature step size by a factor of three. Furthermore, the smaller distance between the NTC and the crystal largely

⁵Manufacturer: Conrad Elektronik, Type: NTC-SEMI833, Part number: 188506

⁶Manufacturer: Eureka Messtechnik, Type: TEC1M-9.1-9.9-4.3/76-D

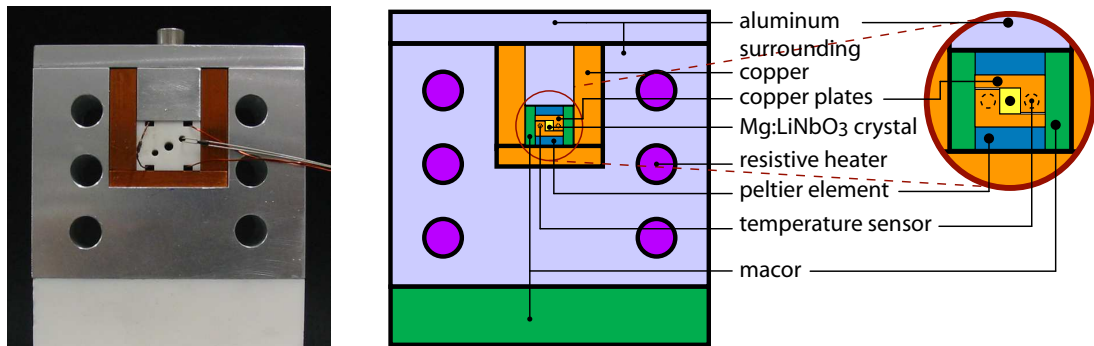


Figure 3.18: A photo of the new oven design (left) and a schematic showing the internal setup (right). The crystal is thermally shielded from the outer surrounding with macor and Peltier elements which are used to control its temperature. The corresponding temperature sensor is placed besides the crystal and is part of the Peltier-copper-crystal sandwich. The outer part of the oven can be optionally heated with resistive heaters to minimize the temperature gradient between the inner and outer oven parts.

reduced the delay time. As a result the response of the control loop to a temperature change is much faster and the settle time, the time until the actual temperature reaches the setpoint temperature, could be increased by at least a factor of six. As an example, if the temperature was changed only by a small amount of some micro-kelvin, the old oven needed at least a minute to reach the new setpoint, whereas the new oven needed roughly 10 seconds to reach the setpoint.

In summary all the new advantages and features compared to the old oven design allowed a much more stable control of the temperature. Hence, the phase matching temperature of the crystal could be controlled more accurately and the generated optical beam had a much higher quality.

Cavity design MK II

The new oven design described in the previous section gave rise to a new cavity design, which minimized mechanical instabilities due to the separation of the outcoupling mirror mount and the oven that houses the crystal. The cavity—formed by the crystals back surface and the outcoupling mirror—contained a large air gap, due to the hemilithic setup with two separated mounts. This gap allows almost free movement of the air and also turbulences due to the temperature gradient between the mirror mount and the oven. A cover placed onto the oven suppressed such effects only by a small amount. Another disadvantage of the old cavity design was, that the outcoupling mirror and the crystal were placed in separate mounts. This non-rigid mechanical setup resulted in individual movements between these two mounts, changing the cavity length. Hence, a new way of mounting the outcoupling mirror to the oven had to be developed in collaboration with my colleague B. Hage.

The new cavity design solved both problems mentioned in the former paragraph. A schematic of this new design is presented in Figure 3.19. The six-axis mirror mount is replaced by an aluminum plate that houses the outcoupling mirror and the PZT needed

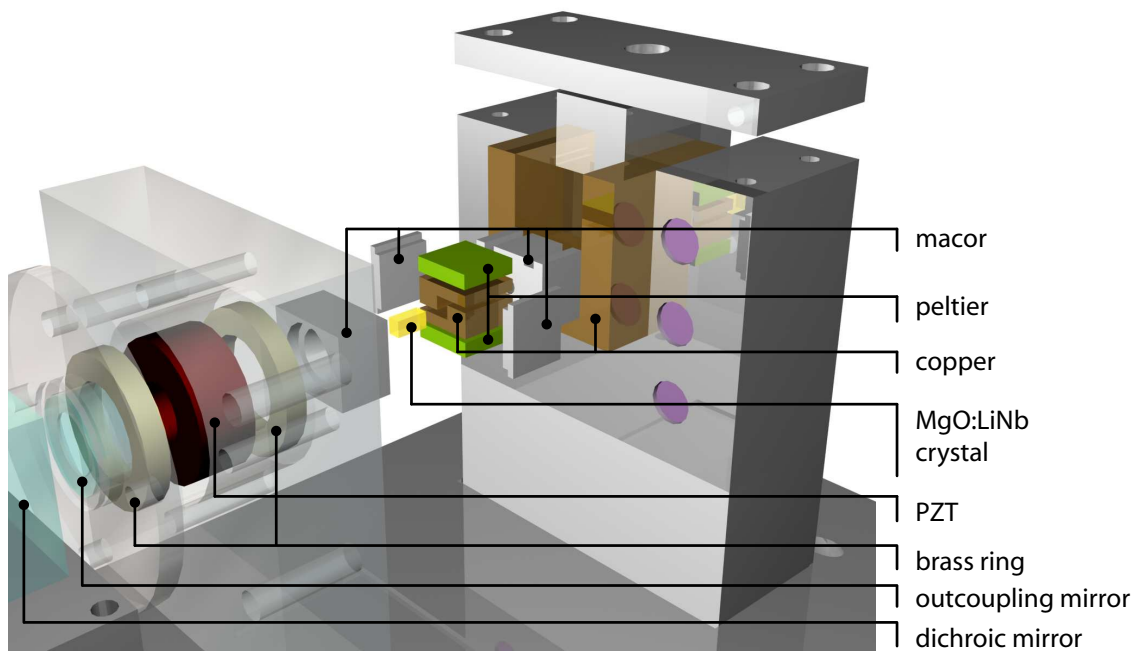


Figure 3.19: CAD explosion drawing of the new quasi-monolithic cavity design. The new out coupling mirror mount drawn semitransparent is shown on the left-hand side. It houses the outcoupling mirror and the PZT. These two are pressed together by an aluminum cap with an embedded Viton ring. This rigid outcoupling mirror mount is screwed directly onto the oven. In the center of the drawing, the yellow MgO:LiNbO₃ crystal is embedded into the two L-shaped copper plates and the Peltier elements. This inner part is thermally shielded with macor and placed into the U-shaped copper case attached to the aluminum surrounding. Optionally this outer part of the oven can be heated with resistive heaters to a temperature near the phase matching temperature.

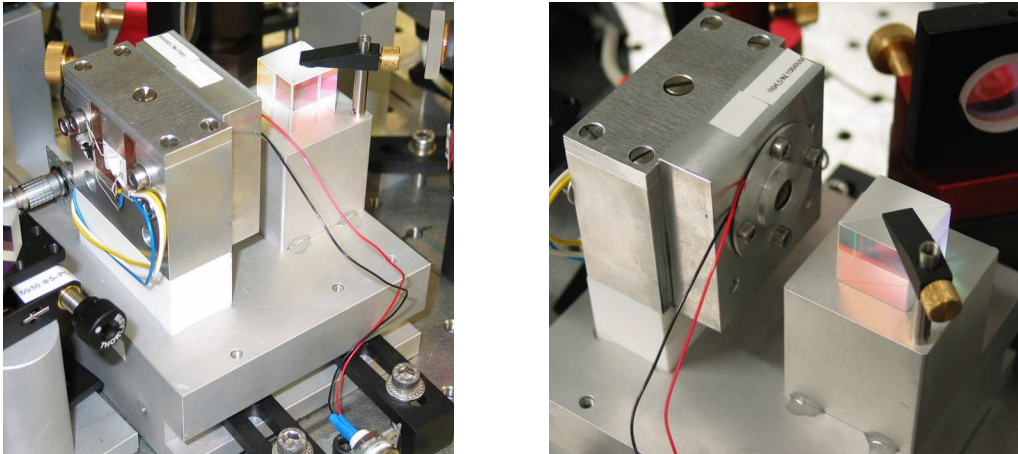


Figure 3.20: Photos of the new nonlinear cavity integrated into the experimental setup. One can recognize the cavity setup has decreased its size largely. The same base plate that housed formerly only the oven and the outcoupling mirror, now offers enough space for the hole cavity and the dichroic beam splitter cube. This simplifies the mode matching into the cavity.

for the active length control of the cavity. The sandwich of the PZT, outcoupling mirror and a Viton ring is pressed together with the help of a small aluminum cap. This resulted in a improved pre-load of the PZT which was still able to expand almost freely. This new outcoupling mirror mount is then screwed directly onto the oven, thereby forming a quasi-monolithic cavity. The rigid setup increased the long term stability by an enormous amount. An once aligned cavity did not have to be realigned after several month. Obviously the initial alignment of the new cavity design is more challenging than before with the six-axis mirror mount. But if the assembly was done precisely it took only a couple of minutes for pre-aligning the outcoupling mirror. The accurate alignment was achieved with a mirror set matching the parameters of the incoming beam to the cavity parameters. The implementation of the new design into the experimental setup can be seen in Figure 3.20.

3.3.3.3 Temperature stabilization

The temperature stabilization of the $\text{MgO}:\text{LiNbO}_3$ crystal inside the oven of the SHG, OPA and OPO was achieved with an active control loop. A negative temperature coefficient (NTC) thermistor⁷, placed near the crystal inside the oven, senses its actual temperature. The temperature-dependent resistance can be used to stabilize the temperature of the oven. A temperature controller⁸ senses the actual resistance of the NTC and compares it with a desired resistance value. The slope of the temperature-dependent resistance is evaluated and an error signal is generated by the internal PID servo of the temperature controller. This error signal is fed back to the resistors or Peltier elements of the oven and changes the actual temperature until it matches the desired one. The

⁷Manufacturer: Conrad Elektronik, Type: NTC-SEMI833, Part number: 188506

⁸Manufacturer: Wavelength Electronics, Type: LFI3751 DIGITAL

maximum output current of the controller is 5 A. The temperature controller also allows a transformation of the measured resistance into a temperature, which is then displayed at the front instead of the resistance. The temperature-resistance behavior can be approximated by the Steinhart-Hart Equation

$$\frac{1}{T [^{\circ}\text{K}]} = A + B \ln R [\text{Ohm}] + C \ln R [\text{Ohm}]^2. \quad (3.30)$$

The three coefficients A, B , and C are typically given in the data sheet of the NTC. The temperature display mode of the temperature controller is best if the main interest is the absolute temperature of the oven. It is not appropriate for the temperature stabilization of the nonlinear crystals, whereas an accurate temperature has to be stabilized in the milli-Kelvin region. Hence, the resistance mode was mostly used. The commercial temperature controller utilizes a digital PID servo to generate the feedback signal. Officially this controller is equipped with an analog input. It turns out, this input is not internally connected to the digital PID. As a consequence, the analog input cannot be used at all. Therefore a custom-made temperature controller with an analog input has been developed (see Appendix C.1), which allows the measurement of transfer functions of the oven. The custom-made temperature controller also shows a much better performance than the commercial one, which makes the custom-made controller the favorable one.

3.3.4 SHG cavity

The SHG used in this first experiment is based on the MK I cavity layout introduced in Section 3.3.3.2. The approximate pump power of the SHG is 1.1 W. The outcoupling mirror of the SHG has a flat surface which is AR coated ($R_{1064\text{ nm}} < 0.15\%$ and $R_{532\text{ nm}} < 0.2\%$) for both wavelength and a curved surface with RoC=25 mm and power reflectivities of $R_{1064\text{ nm}} = 92\%$ and $R_{532\text{ nm}} \approx 4\%$. The used crystal is a flat/curved MgO:LiNbO₃ with 5% MgO doping. The physical dimensions of the crystal are $2.5 \times 7.5 \times 5$ mm (length \times width \times depth) with respect to the orientation shown in Figure 3.14. The flat surface of the crystal holds an AR coating with $R_{1064\text{ nm}} < 0.05\%$ and $R_{532\text{ nm}} < 0.2\%$, whereas the curved back surface with a RoC=10 mm is HR coated ($R_{1064\text{ nm}} = 99.96\%$ and $R_{532\text{ nm}} = 99.9\%$). The cavity for the fundamental wavelength is formed and has a waist size of approximately $27\ \mu\text{m}$ inside the nonlinear crystal. The air gap between the outcoupling mirror and the crystal's flat surface is approximately 23 mm resulting in an FSR=3.77 MHz for the SHG. The reflectivities of the mirrors limit the linewidth to $\Delta\nu_{\text{SHG}} = 50$ MHz which corresponds to a Finesse of $\mathcal{F} = 75$. The temperature control of the crystal was based on the *Wavelength Electronics* temperature controller and has been described in detail in Section 3.3.3.3. Scanning the temperature from below to above the phase matching temperature reveals the sinc-function presented in Equation 3.10 (see Figure 3.21). Taking the mode matching efficiency into account, the conversion efficiency is approximately 65% producing a harmonic field with an output power of 650 mW at phase matching temperature.

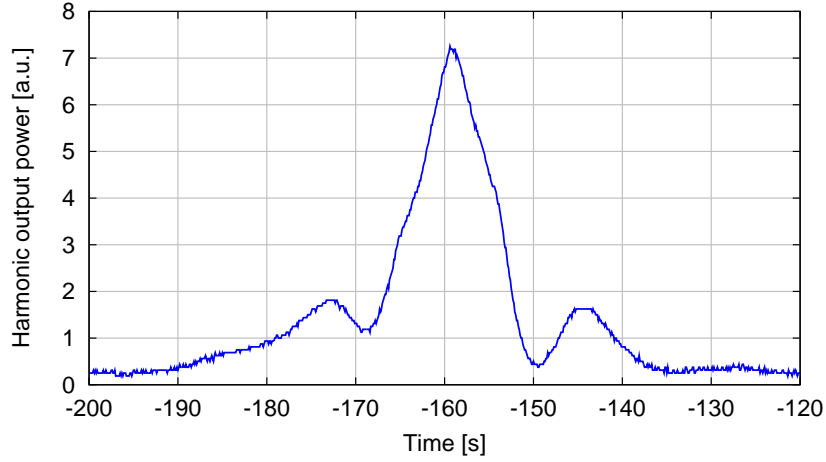


Figure 3.21: Harmonic output power of the SHG while the temperature of the crystal is changed from below the phase matching temperature to above. The sinc-function structure with one large maximum and two small local maxima beside the absolute maximum is clearly visible.

3.3.4.1 Cavity length locking scheme

The SHG length control scheme is comparable to the control of the modecleaner cavity described in Section 3.2.3. Instead of an external phase modulation with an EOM the SHG uses an internal modulation scheme to generate phase modulation sidebands on the intra-cavity fields. There are two possible ways for an internal modulation. A sinusoidal electrical modulation can be applied either to the modulation plates of the SHG cavity changing the length of the cavity by changing the refractive index of the crystal or to the PZT of the outcoupling mirror, thereby changing the length of the cavity directly. For the SHG the PZT modulation is used. Figure 3.22 shows the schematic of the SHG cavity length control. It is worth noting, that on both light fields inside the cavity phase modulation sidebands are generated. The fundamental field is affected directly from the length change and thereby phase modulated. The $\chi^{(2)}$ -process inside the MgO:LiNbO₃ crystal then converts this phase modulated fundamental field into a phase modulated harmonic field. The frequency used for the modulation is $\Omega_{\text{SHG}}/2\pi = 19.73$ MHz, which is a resonance frequency of an electrical RC-circuit setup by the HV-amplifier's output impedance and the electrical capacity of the crystal including the modulation plates. This resonance satisfies a good conversion from electrical to mechanical power. The error signal for the length control is derived by detecting the fundamental field in transmission of the SHG cavity. A dichroic cube is placed between the cavity's back surface and the photodiode to minimize the harmonic field reaching the photodiode. The photocurrent of the photodiode is processed by a servo generating the error signal. This is then amplified and fed back to the PZT of the outcoupling mirror. To avoid any cross talk between the servo and the oscillator used for the internal modulation—both are applied to the PZT—the error signal coming from the HV-amplifier is low-pass filtered, whereas the electrical modulation is high-pass filtered before both signals are added and their sum applied to the PZT.

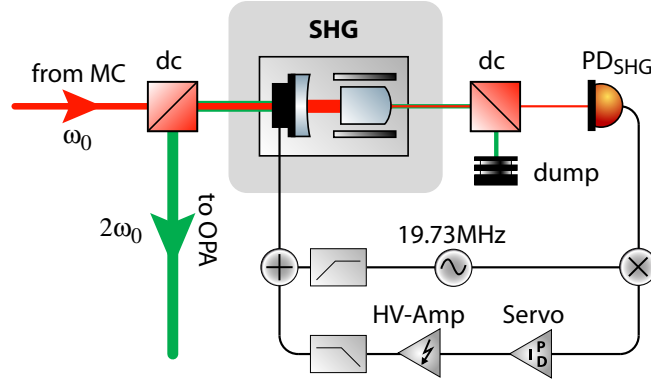


Figure 3.22: Schematic of the SHG layout including the cavity length control loop. An oscillation of $\Omega_{\text{SHG}}/2\pi = 19.73 \text{ MHz}$ is applied to the PZT of the SHG's outcoupling mirror evoking a phase modulation to all intra-cavity fields. The transmitted fields are separated with a dichroic beam splitter cube and the infrared field is detected with a photodiode. The photocurrent is demodulated with Ω_{SHG} by a mixer and processed with a servo generating an error signal for the cavity length. This error signal is amplified and fed back to the outcoupling mirrors PZT.

3.3.5 OPA cavity

The OPA used for generating the squeezed field is based on the MK I cavity layout described in Section 3.3.3.2. The optical and electrical layout is shown in Figure 3.23. The OPA crystal is identical to the one used in the SHG. The outcoupling mirror of the OPA has a flat surface which is AR coated ($R_{1064 \text{ nm}} < 0.15\%$ and $R_{532 \text{ nm}} < 0.2\%$) for both wavelength and a curved surface with $\text{RoC}=25 \text{ mm}$ and power reflectivities of $R_{1064 \text{ nm}} = 94.7\%$ and $R_{532 \text{ nm}} \approx 4\%$. This results in a Finesse of $\mathcal{F} = 115$, which corresponds to a linewidth of 33 MHz. The FSR of 3.77 GHz and the waist size of $27 \mu\text{m}$ are identical to the SHG's ones. The temperature control is accomplished with the wavelength controller and is described in detail in Section 3.3.3.3. Due to the high thermal capacity of the oven and the limited temperature step size, the pump power is adjusted slightly to approach the phase matching temperature. The pump field enters and leaves the OPA cavity through the outcoupling mirror, whereas the fundamental seed field enters the OPA through the HR coated back surface of the crystal. A 50/50 beam splitter in front of the crystal is used to separate the ingoing from the outgoing field, which is detected with a photodiode. The adjustment of the produced squeezing angle θ of the squeezed field is done with a PZT-mounted mirror in the pump field path, which will be described in Section 3.3.5.2.

3.3.5.1 Cavity length locking scheme

The control scheme of the OPA is presented in Figure 3.23. It uses an internal modulation scheme to generate the needed phase modulation sidebands. In contrast to the SHG, the internal modulation of the OPA is evoked by applying an electrical oscillation with frequency $\Omega_{\text{OPA}}/2\pi = 19.77 \text{ MHz}$ to the modulation plates near the crystal. The generated electrical field changes the refractive index of the crystal resulting in a phase modulation of all intra-cavity fields. The photodiode placed in reflection at the back surface of the

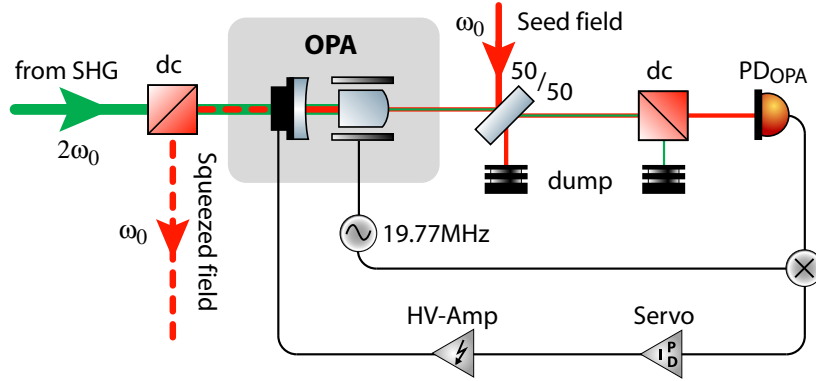


Figure 3.23: Schematic of the OPA layout including the cavity length control loop. An oscillation of $\Omega_{\text{OPA}}/2\pi = 19.77\text{ MHz}$ is applied to the modulation plates inside the OPA cavity evoking a phase modulation to all intra-cavity fields. The outgoing fields on the right side are separated with a dichroic beam splitter cube and the infrared field is detected with a photodiode. The photocurrent is demodulated with Ω_{OPA} by a mixer and processed with a servo generating an error signal for the cavity length. This error signal is amplified and fed back to the outcoupling mirror's PZT.

crystal is detecting the fundamental infrared outgoing field. A dichroic cube prevents that parts from the second harmonic field, transmitted through the OPA cavity, are also detected by this photodiode. The generated photocurrent is demodulated with a mixer at frequency Ω_{OPA} and processed by a servo generating an error signal for the length of the OPA cavity. This error signal is amplified and fed back to the outcoupling mirror's PZT.

3.3.5.2 Control of the squeezing angle

The control of the squeezing angle is determined by the relative phase between the fundamental and harmonic fields inside the crystal (for details see Section 3.3.2). A minimal outgoing field corresponds to producing amplitude squeezing whereas a maximized outgoing field corresponds to the generation of phase squeezing. In all experiments described in this thesis the production of amplitude squeezing is favored, which corresponds to a minimized outgoing field strength. The needed error signal for the control can be derived from the phase modulation carried by the harmonic pump field. This phase modulation corresponds to a constant modulation of the relative phase relation with frequency Ω_{SHG} resulting in a modulation of the outgoing field strength. This modulation can be detected with the OPA's photodiode named PD_{OPA} . The demodulation of the provoked photocurrent with Ω_{SHG} generates an error signal for the squeezing angle. A servo processed the error signal and generates the needed feedback signal for a stable control. This feedback signal is amplified by a HV-amplifier and fed back to a PZT-mounted mirror in the path of the pump field on the way to the OPA. The complete optical and electrical layout of the squeezing angle control is presented in Figure 3.24.

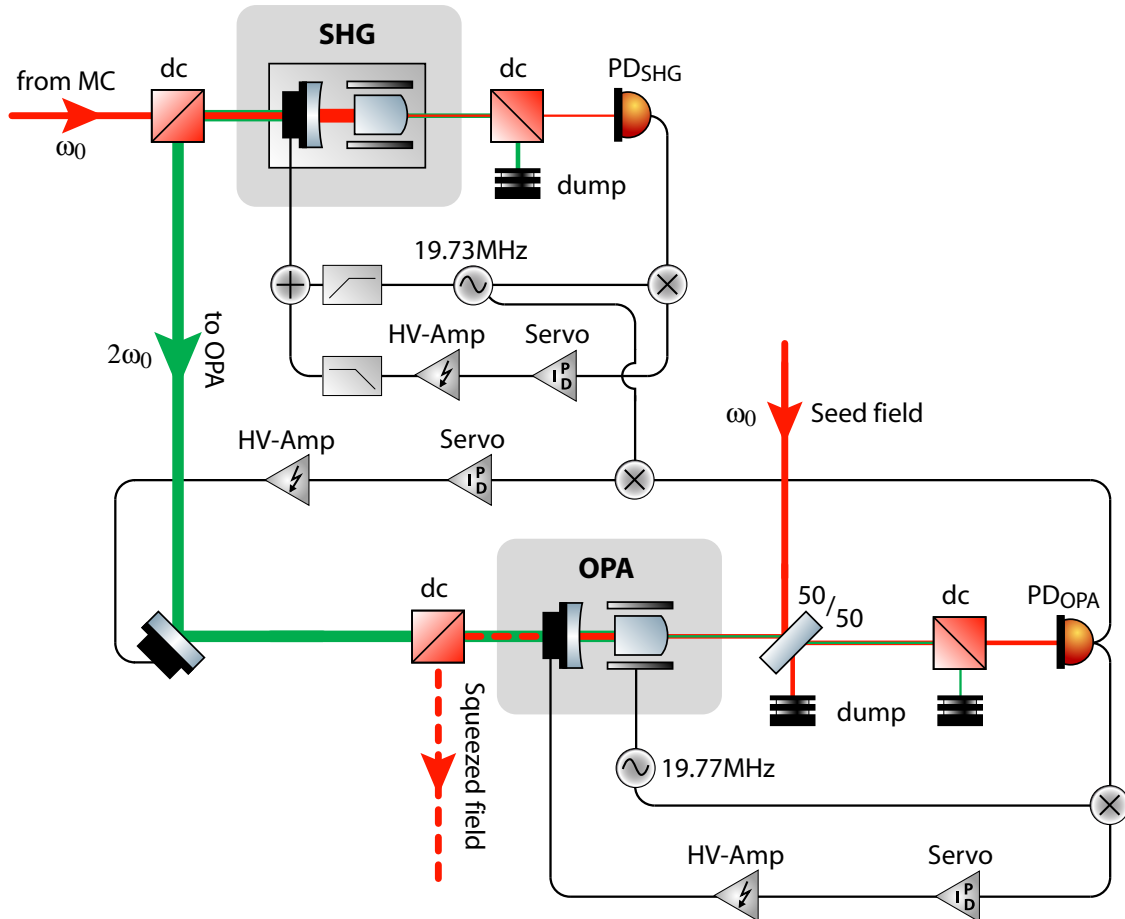


Figure 3.24: Schematic of the SHG layout including the cavity length and squeezing angle control loop. The relative phase between the harmonic and the fundamental field inside the cavity determines the squeezing angle of the produced squeezed field (see Equation 2.85b). Hence, this relative phase has to be stabilized with a control loop to produce only the desired type of squeezing e.g. amplitude squeezing. The phase modulation on the harmonic field with frequency Ω_{SHG} is used to derive an error signal, which is amplified and fed back to a PZT-mounted mirror in the path of the harmonic pump field.

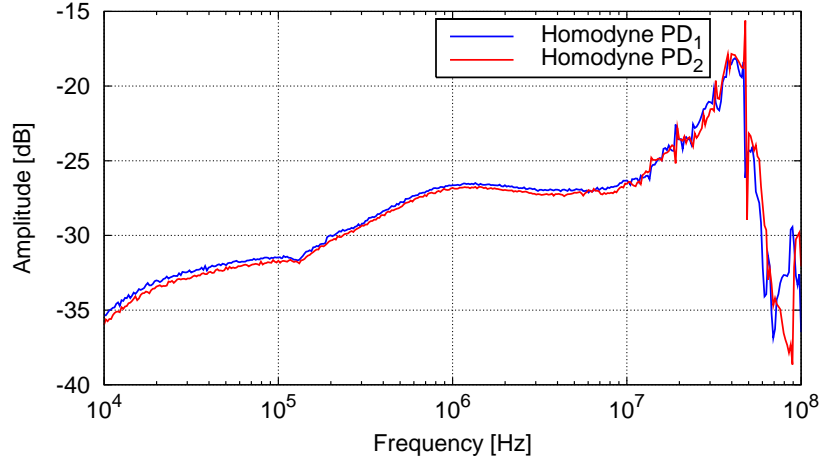


Figure 3.25: Comparison of the two homodyne photodetectors transfer functions

3.4 Experimental area and detection

The aim of this first squeezing experiment presented in this thesis is the generation of squeezing. For this reason the experimental area, a subsection of the experimental layout presented in Figure 3.1, only contains a homodyne detector, which is used for the characterization of the generated squeezed fields. The theory of homodyne detection has already been presented in Section 2.9.5. Its optical and electrical setup is described in detail in the following section.

3.4.1 Homodyne detection

The optical layout of the homodyne detector used in this experiment for the characterization of the generated squeezed fields is presented in Figure 3.26. The homodyne detector consists of a 50/50 beam splitter and two custom made photodetectors. These contain Epitaxx ETX-500 InGaAs-photodiodes with a quantum efficiency of approximately $93\pm 3\%$. The electronic amplification limits each photodetector to a maximal detectable light power of 10mW. The bandwidth of the photodetectors is measured to be at least 25 MHz (see Figure 3.25). Homodyne detection always assumes to have a perfect 50/50 beam splitter and identical photodetectors. The transfer functions of the two photodetectors are not perfectly identical (see Figure 3.25). As a result one of the photocurrents has to be attenuated by a certain amount to obtain the best results. A variable attenuator was used to compensate the optical and electrical mismatches. The adjustment of the attenuator is most effectively achieved by minimizing the technical laser relaxation oscillation.

The optical mode overlap of the two incoming beams has to be matched to minimize the optical losses which would decrease the squeezing performance. Hence, the amount of optical components in the path of the squeezed field is minimized as well. Therefore, the mode matching of the two beams is achieved by adjusting only the local oscillator beam. The resulting homodyne visibility is measured to be $\xi=97.5\%$.

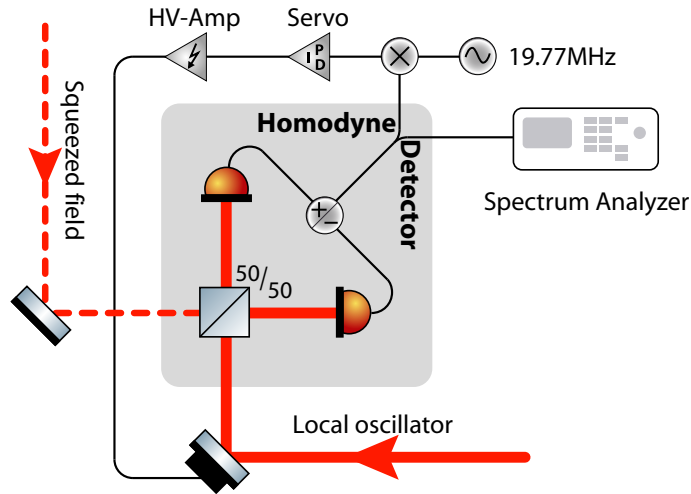


Figure 3.26: Schematic of the homodyne detector layout including the homodyne angle control loop. The squeezed field carries a phase modulation of frequency Ω_{OPA} due to the applied internal modulation in the OPA cavity (see Figure 3.23). The difference of the homodyne photodiodes is demodulated with Ω_{OPA} by a mixer and processed with a servo generating an error signal for the homodyne angle θ . This error signal is amplified and fed back to the PZT-mounted mirror in the local oscillator path. The difference photocurrent is also parsed by a spectrum analyzer e.g. measuring the power spectrum of the squeezed beam.

The homodyne angle—meaning the quadrature angle in phase space that the light field is going to be analyzed in—depends on the relative phase of the local oscillator and the signal field with respect to each other (see Equation 2.81). For the analysis of the squeezing performance of an amplitude squeezed beam, the homodyne angle θ has to be equal to zero, i.e. a maximal asymmetric allocation of the light fields in the beam splitter’s output ports (see Equations 2.28 and 2.81). The photocurrents are subtracted from each other with a common mode rejection of approximately 90 dB and the difference is then measured with a spectrum analyzer.

The control of the homodyne angle is achieved by using the phase modulation of the squeezed field due to the internal modulation of the OPA. In Figure 3.26 the control scheme of the homodyne detector is presented in detail. The phase modulation with frequency Ω_{OPA} is converted by the homodyne detector into an amplitude modulation which strength depends strongly on the relative phase between the two incoming fields. For analyzing amplitude squeezed states the difference of the photocurrents has to be mixed with an electronic local oscillator of frequency Ω_{OPA} . The resulting error signal is processed by a servo. The generated feedback signal is amplified and fed back to a PZT-mounted mirror in the path of the local oscillator light field.

3.5 Experimental results

The spectral distribution of the squeezed field generated by the OPA is presented in Figure 3.27. The squeezed vacuum noise [trace (a)] holds large technical noise—mainly

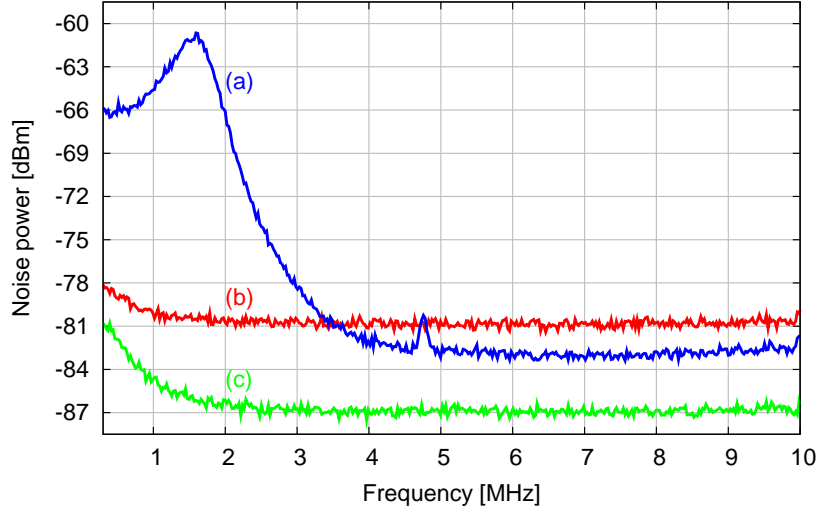


Figure 3.27: Amplitude quadrature noise spectra of different quantum states. The blue trace (a) shows the squeezed vacuum noise of an amplitude squeezed state. At 3.5 MHz it crosses the noise level of the vacuum noise and shows a noise reduction roughly 2.5 dB with respect to the vacuum noise shown in red [trace (b)]. The electronic dark noise of the measurement device is presented in green [trace (c)]

remnants of the laser relaxation oscillation—at frequencies below 3.5 MHz. However, above this frequency the noise drops below the vacuum noise level [trace (b)] by an amount of 2.5 dB. The feature at 4.7 MHz is the beat frequency of the modecleaner’s and the OPA’s control frequency. The squeezed field was generated with a pump power of 350 mW resulting in a classical parametric gain of $G=7$. To generate an amplitude squeezed field, the OPA has to be locked to deamplification which resulted in a reduction of the seed field down to a level of 38%. To characterize the squeezing noise performance the vacuum noise has to be measured as a reference. It can be measured by blocking the signal port of the homodyne beam splitter. The resulting vacuum noise spectrum is shown in Figure 3.27 as the red trace (b). Trace (c) represents the electronic dark noise measured if no light is detected by the photodetectors. This electronic dark noise is a combination of the photodetector electronic amplifier noise, the differential amplifier noise and the spectrum analyzer noise. The distance of the vacuum noise to the dark noise can be adjusted by the local oscillator power. In this experiment the local oscillator power was 8 mW. In comparison to the power of the squeezed field of approximately $200 \mu\text{W}$ this satisfies the condition that the local oscillator field has to be much larger than the signal field (see Section 2.9.5).

The characterization of the squeezed field can also be performed with a zero-frequency-span measurement. One focuses on a specific sideband frequency and analyzes a time series of the desired field while scanning the local oscillator phase. In Figure 3.28 such a zero-span measurement is shown for a sideband frequency of 6 MHz. Trace (a) shows the measurement result for the squeezed field and trace (b) is the corresponding vacuum noise. The anti squeezing level is roughly 10 dB above the vacuum noise level. Hence,

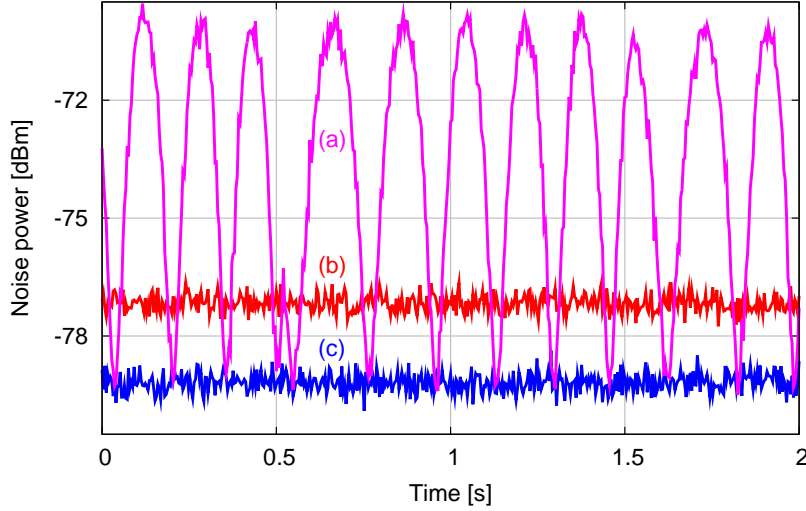


Figure 3.28: Zero-span measurement at a sideband frequency of 6 MHz. Trace (a) shows the time series of the squeezed state generated by the OPA with a gain of $G=7$, while the homodyne detector angle is scanned continuously. The corresponding vacuum noise is shown in red [trace (b)] and the squeezed quadrature is marked by the blue trace (c).

the detected squeezed state is not a pure state. This can be explained by the losses to the squeezed field. Losses act differently on squeezed and anti-squeezed variances (see Section 2.9.4 and Figure 2.6 for comparison).

3.5.1 Dark noise correction

The measured vacuum and squeezed vacuum spectra and time series presented in the former section included the electronic dark noise of the measurement device. If the dark noise level is close to the measured noise level, the result will be influenced by the dark noise and tend to be higher than if it would be with a much smaller dark noise. As an example one can see in Figure 3.27 that the white vacuum noise tends to rise at low frequencies due to the small distance to the dark noise. This behavior can be eliminated by a so-called dark noise correction of the measured data. Therefore, the measured dark noise variance V_d in dBm has to be subtracted from the measured signal variance V_s in dBm on a linear scale to get the corrected signal variances V_c in dBm. The mathematical procedure is expressed by

$$V_c = 10 \cdot \log_{10} \left(10^{\frac{V_s}{10}} - 10^{\frac{V_d}{10}} \right). \quad (3.31)$$

If one applies the dark noise correction to the data from Figure 3.27, one obtains the dark noise corrected data shown in Figure 3.29. The vacuum noise shows a white behavior and the squeezed vacuum noise improvement has increased from 2.5 dB to 3.1 dB due to the dark noise correction.

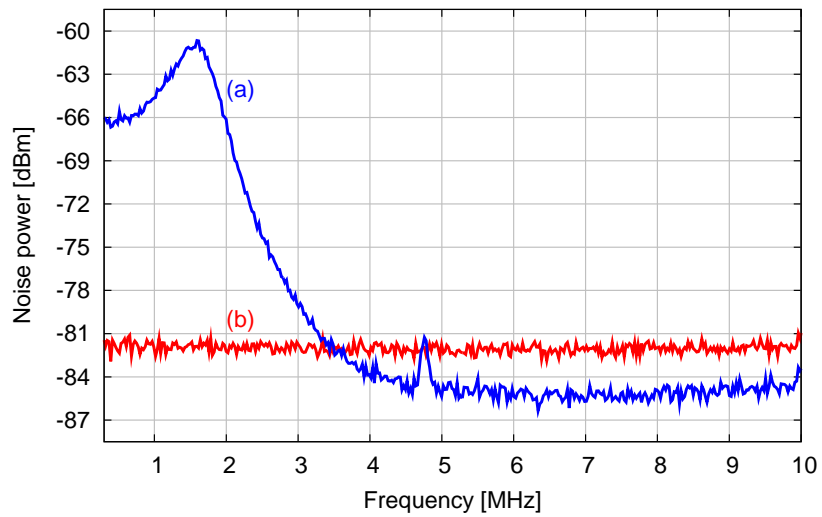


Figure 3.29: Dark noise corrected amplitude quadrature noise spectra of different quantum states. The blue trace (a) shows the squeezed vacuum noise of an amplitude squeezed state. At 3.5 MHz it crosses the noise level of the vacuum noise and shows a noise reduction of roughly 3.1 dB with respect to the vacuum noise shown in red [trace (b)].

Chapter 4

Frequency-dependent squeezed light

Introduction

This chapter describes an experiment for generating frequency-dependent squeezed light and characterizes the frequency-dependent squeezed states by measuring their noise power spectra and by tomography and reconstruction of the quantum states' Wigner function. This experiment is motivated by the fact that actual and future GW detectors use signal-recycling cavities [Mee88] to further enhance the GW signal by sending it multiple times through the interferometer, thereby increasing the interaction with the mirror test mass. It has been shown that squeezed light can enhance the sensitivity of such a GW detector by replacing the vacuum field entering the dark port of the interferometer with a squeezed field [Cav81, GBL87, JR90, PCW93]. In interferometers with signal recycling techniques the squeezing-improved sensitivity only shows an enhancement in a small frequency range. This can be circumvented with the help of a filter cavity preparing the squeezed state in such a way that the sensitivity improvement can be enlarged over the whole GW detection frequency band. This has been analyzed theoretically in [HCC⁺03, SHSD04]. The experimental results of this chapter have been published in [CVH⁺05].

The chapter is divided into four sections. First we investigate the interaction between a squeezed state and a detuned cavity. We analyze theoretically how the initial frequency-independent squeezed state becomes frequency-dependent after being reflected at the detuned cavity. In the second section the optical layout of the experiment is presented and the differences to the generic squeezing experiment presented in Chapter 3 are described in detail. The third section will present the theoretical background of tomography. The technique to reconstruct the Wigner functions from measured data of quantum states is described as well as the details of the data acquisition system (DAQ) and the specific homodyne control electronics used in the experiment. In the last section, the experimental results including the spectra of frequency-dependent light, and the tomographically reconstructed Wigner function of the measured states are described and interpreted.

4.1 Squeezed light reflected at a detuned cavity

In this section we closely examine the effects on squeezed light if it is reflected at a detuned (with respect to the carrier) locked cavity. This must be examined in more

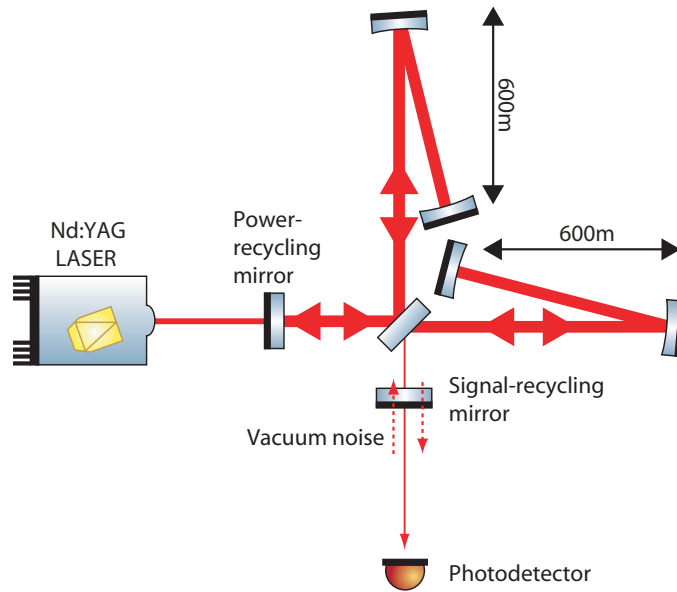


Figure 4.1: Simplified schematic of the gravitational wave detector GEO 600. The dashed arrows represent the relevant vacuum fields entering and leaving the interferometer if optical loss inside the interferometer is neglected.

detail because the current German-British gravitational wave (GW) detector GEO 600 and future generation detectors such as Advanced LIGO will use detuned signal recycling [Mee88]. It is likely that squeezed light will be used in the future to enhance the sensitivity of these detectors. Therefore effects happening to the squeezed light from interaction with the detuned cavity have to be understood beforehand.

4.1.1 Quantum noise inside gravitational wave interferometers

To understand the effects on the squeezed light we have to investigate the general behavior of quantum noise inside GW Interferometers first. In the following we mostly focus on GEO 600 [GEO]: a schematic of its optical layout is presented in Figure 4.1. A more detailed description of the GW detector GEO 600 and its subsystems can be found in [Gro03, Fre03, Goß04]. GEO 600 is currently the only GW detector using the technique of *dual recycling*, which is the combination of *power recycling* [DHK⁺83] and *signal recycling* [Mee88]. Power recycling is used to enhance the stored energy in the interferometer arms and thereby the sensitivity of the interferometer (see [Miz95]). Signal recycling enhances the GW signal by reinjecting the signal sidebands back into the interferometer which would normally leave the interferometer through the dark port. The repeated interaction with the GW test masses enhances the signal and consequently the sensitivity around the resonance frequency of the signal-recycling cavity (SRC), further. The latter is formed by the signal recycling mirror (SRM) and the end mirrors of the Michelson interferometer. In the case of GEO 600, the resonance frequency of the SRC is usually chosen to have an 350 Hz offset to the carrier frequency. In other words, one says that the SRC detuning is chosen to be 350 Hz. The detuning frequency is only determined

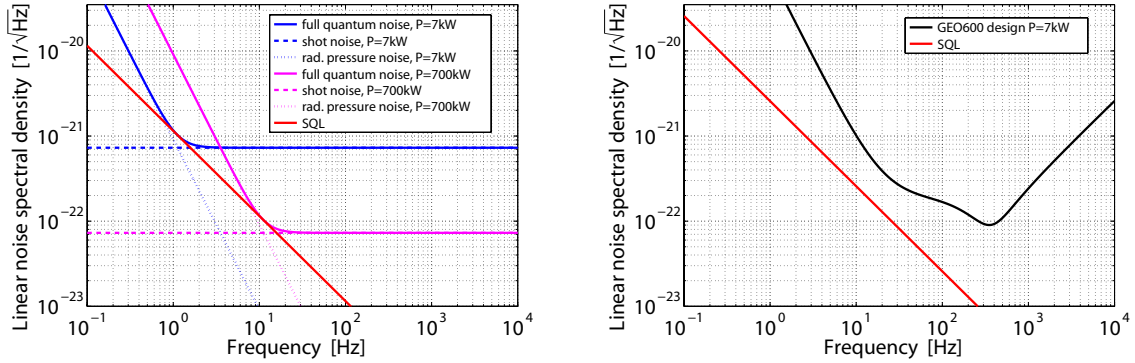


Figure 4.2: Comparison of strain sensitivities of a simple Michelson interferometer (left) and the GEO 600 configuration (right) shown in Figures 4.3 and 4.1 respectively. Simple Michelson interferometer: The SQL of this configuration is shown by the red curve. The blue curve shows the full quantum noise contribution for a laser power of 7 kW inside the interferometer. The blue dashed curve represents the shot noise contributions and the dotted curve represents the noise contributions due to radiation pressure noise. To see the individual power scalings of the different noise sources, the curves for the total noise, shot noise and radiation pressure noise are given in magenta for a total power of 700 kW. Increasing the power by a factor of 100 results in a reduced shot noise contribution by a factor of 10 and an increase in the radiation pressure noise contributions also by a factor of 10. The exact form of the different noise contributions are given in Equations 4.1 and 4.2. GEO 600 configuration: The SQL of the detector is given by the red curve. In comparison to that of the simple Michelson interferometer, the SQL of GEO 600 is a factor of $\sqrt{5}$ higher due to the different layout. The quantum noise limited sensitivity of GEO 600 for 7 kW inside the interferometer is given by the black curve. Compared to the 7 kW curve of the simple Michelson interferometer, the peak sensitivity is enlarged due to the signal recycling, but the low and high frequency performance is worse. The decreased sensitivity in the low-frequency range does not really matter, because generally in a real GW detector seismic noise prevents the detector from being limited by radiation pressure noise. The decreased sensitivity above 3 kHz is a tradeoff from the large improvement around the signal recycling resonance frequency.

by the micro scale length of the SRC and can therefore be adjusted quite easily. The comparison of the quantum noise limited linear noise spectral density of the strain sensitivity between a simple Michelson interferometer without any recycling techniques and the GEO 600 design sensitivity is shown in Figure 4.2. The two quantum noises limiting the sensitivity are the radiation pressure noise and shot noise. In the case of a simple Michelson interferometer the contribution of the shot noise to the linear noise spectral density of the gravitational wave strain amplitude is given by

$$h_{s.n}(f) = \frac{1}{L} \sqrt{\frac{\hbar c \lambda}{2\pi P}}, \quad (4.1)$$

for an interferometer with an arm length L , using a laser wavelength of λ and a total power P inside the interferometer. \hbar is the Planck constant and c is the speed of light in vacuum. Note that h_{vac} is independent of the frequency f , which corresponds to the gravitational wave frequency. Thus, plotted as a spectrum, the strain amplitude shows a white frequency dependence. The only non-constant parameters that change h_{vac} are the length of the interferometer arms and the power inside the interferometer.

An increase in one of these results in a lower contribution from the shot noise. The frequency independence and the scaling with the laser power are presented in Figure 4.2.

The contribution from radiation pressure noise to the linear noise spectral density of the gravitational wave strain amplitude in the simple Michelson case is given by

$$h_{\text{r.p.}}(f) = \frac{1}{mf^2L} \sqrt{\frac{\hbar P}{2\pi^3 c \lambda}}, \quad (4.2)$$

with the mirror test mass m . In contrast to h_{vac} , $h_{\text{r.p.}}(f)$ shows a f^{-2} frequency dependence. Also $h_{\text{r.p.}}(f)$ gets larger for increased laser power. These two properties are clearly visible in Figure 4.2. As a reference, the standard-quantum limit (SQL) of each GW detector is plotted in both graphs as a red line. Note that the point where the radiation pressure noise and the shot noise cross each other always lies on the SQL curve because this point and its power dependency defines the SQL. It is important to understand, that the quantum noise which limits the sensitivity of a GW detector such as GEO 600 does not originate from the laser source. The source of the quantum noise is the vacuum noise entering the dark port of the interferometer, as shown in Figure 4.1. Inside it interacts with the test masses, is back-reflected and then detected with the photodetector in the dark port of the interferometer. To understand how the vacuum noise fluctuations cause the radiation pressure effects see [BC02]. The analysis of the power dependency of the shot noise and radiation pressure noise contributions for the simple Michelson case is presented in Figure 4.2. The sensitivity in this figure is plotted for two different powers inside the interferometer, $P = 1\text{W}$ and $P = 100\text{W}$. One can see that by increasing the power by a factor of 100, the shot noise—which limits the high-frequency range—drops by a factor of 10. In contrast, the radiation pressure limiting the lower frequency range is increased by a factor of 10. Hence, one has to make a tradeoff between the power in the interferometer and the mirror test mass to achieve a good sensitivity in the desired frequency band.

If one compares the result of the simple Michelson interferometer with the GEO 600 design sensitivity curve one can see that the GEO 600 design sensitivity is much better in the frequency band of interest from 10Hz–10kHz than the simple Michelson case. Furthermore, the shape of the sensitivity curve is changed; there is a resonance structure around 350 Hz originating from using signal recycling which also deteriorates the high frequency performance because the signal-recycling cavity corresponds to a pole of first order. An additional resonance structure caused by the optical spring [HCC⁺03] is suppressed in this simulation by tuning the signal-recycling cavity to the sideband, where the optical spring is damped instead of resonantly enhanced.

4.1.2 GW detector enhancement with squeezed light

It was first proposed by Caves [Cav81] that squeezed light can be used to increase the sensitivity of a GW interferometer by injecting it into the dark port of the detector, thereby replacing the ordinary vacuum with a squeezed vacuum. Later Jaekel [JR90] showed that even the SQL can be beaten by using squeezed light. The replacement of the ordinary vacuum with a squeezed vacuum can be achieved by placing a Faraday rotator into the dark port of the interferometer, which guides the squeezed vacuum into

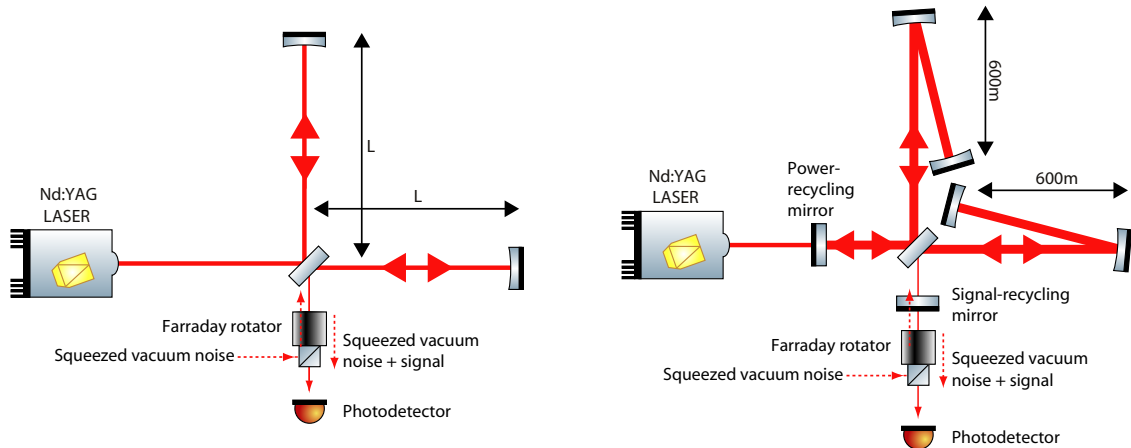


Figure 4.3: Simplified schematics of a simple Michelson interferometer (left) and the gravitational wave detector GEO 600 (right). Compared to the simple Michelson interferometer, GEO 600 uses folded arms to double its arm length. Furthermore, it uses power recycling to enhance the light power inside the interferometer arms which increases the sensitivity. A so-called signal-recycling mirror placed at the dark port forms the signal-recycling cavity together with the Michelson interferometer for the GW signal sidebands. This cavity is resonant to a specific sideband frequency. Thus, the GW generated signal sidebands are sent back to the test masses to sense the GW signal again. This leads to an enhancement of the sensitivity at frequencies around the of the signal-recycling cavity’s resonance frequency. The dashed arrows represent the relevant vacuum fields entering and leaving the interferometer if optical loss inside the interferometer is neglected.

the interferometer, such that it is detected by the photodetector (see Figure 4.3). The effect of the squeezed vacuum to the sensitivity of the GW detector is comparable to an increase in the laser power. The improvement scales with the square root of the amount of injected squeezing. As an example one can inject squeezed vacuum into the dark port of the interferometer where the variance of the squeezed state is $-6\text{ dB}=0.25$ below the normal vacuum noise level. The improvement in the sensitivity will be $-3\text{ dB}=0.5$ in the shot noise limited frequency range. The effect of the injected squeezed vacuum to the sensitivity of the simple Michelson interferometer can be seen in Figure 4.4. The shot noise limited sensitivity is enhanced whereas the radiation pressure dominated sensitivity is reduced by the injection of squeezed vacuum into the interferometer’s dark port. A broadband improvement can only be achieved with a filter cavity that optimizes the squeezing angle. Thus, if the limiting noise source is quantum noise and the laser power cannot be increased further due to thermal effects inside the optical substrates or other technical limits, the only possibility of enhancing the sensitivity of the GW detector without changing the detector configuration is the use of squeezed light.

If the configuration of the GW detector is changed from the simple Michelson case to e.g. the GEO 600 configuration—which uses power recycling and signal recycling—the situation changes. The behavior of squeezing in a signal-recycled GW Michelson interferometer has been studied in great detail in [HCC⁺03]. If one injects squeezed vacuum with the help of a Faraday rotator into the dark port of the interferometer as shown in Figure 4.3, the squeezed vacuum state gets a frequency-dependent phase shift.

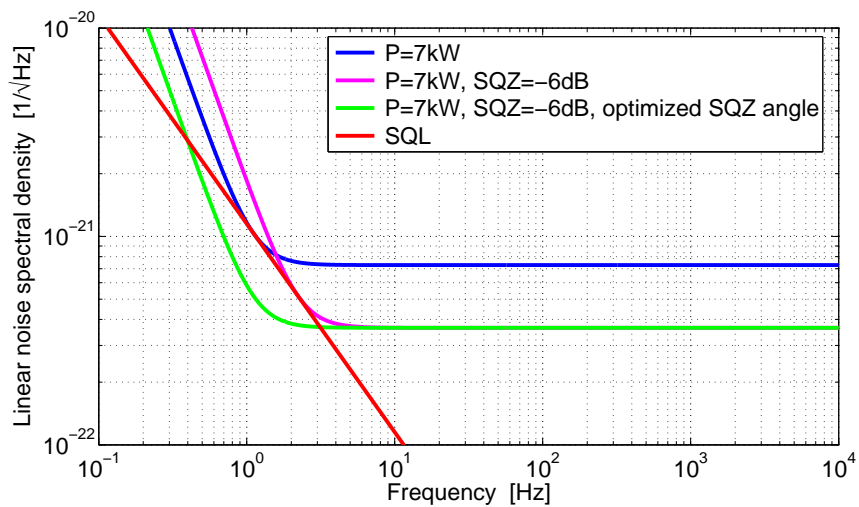


Figure 4.4: Strain sensitivity of a simple Michelson interferometer with an internal power of 7 kW (blue curve), in comparison to the improvement which can be achieved with squeezed light with fixed (magenta curve) and optimized squeezing angle (green curve) injected through the dark port as shown in the schematic in Figure 4.3. The result is the same as if the laser power has been increased by a factor of four. The radiation pressure rises and the shot noise drops by a factor of two, respectively. Squeezing by -6 dB only results in a broadband enhancement of the strain sensitivity by a factor of two if a filter cavity is used (green curve), which optimizes the squeezing angle. Compensation of radiation pressure noise by squeezed light is described in detail in [KLM⁺01]. The SQL, shown as a red line, is beaten by the optimized squeezed-light-enhanced strain sensitivity in the range between 40 mHz–4 Hz.

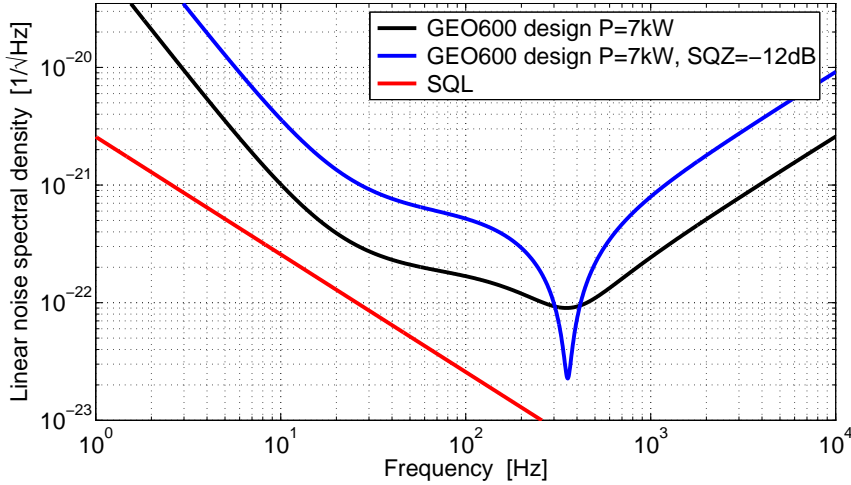


Figure 4.5: Strain sensitivity of GEO 600 with an internal power of 7 kW (black curve). The blue curve is the resulting strain sensitivity if one injects -12 dB of squeezing into the dark port of the dual-recycled Michelson interferometer. Figure 4.3 shows how the injection of the squeezing into the GW detector can be achieved. Squeezing by -12 dB results in an enhancement of the strain sensitivity by a factor of four only in a small frequency range around the resonance frequency. At all other frequencies the sensitivity is decreased by a factor of four. The SQL of the GEO 600 GW detector is shown as a red line.

This frequency-dependent phase shift leads to a frequency-dependent rotation of the squeezing ellipse, thereby changing the quadrature in which the best squeezing can be measured. The change to the sensitivity of the GEO 600 detector is shown in Figure 4.5. Note, that the improvement is not broadband over the full detector bandwidth as it is the case for the simple Michelson interferometer. Here the improvement of the sensitivity is only in a small region near the optical resonance frequency. At all other frequencies the sensitivity is decreased by the squeezing amount. If one starts varying the squeezing angle (see Section 3.3.5.2 for details on how to change the squeezing angle) one obtains different sensitivity curves. Each curve shows a maximal increase in the sensitivity at a different frequency.

As a consequence one has to optimize the squeezing angle for every sideband frequency. The sensitivity curve of GEO 600 with an optimized squeezing angle for every frequency is shown in Figure 4.6. Optimization of the squeezing angle can be achieved by the use of filter cavities as proposed in [KLM⁺01]. Figure 4.7 shows the optical layout of GEO 600 including one filter cavity to prepare the squeezed vacuum state such that the effects of the signal-recycling cavity are cancelled and a broadband increase in the sensitivity can be obtained.

The quantum noise in the sideband picture will be analyzed in Section 4.1.4 to understand the influences on the squeezed vacuum due to the reflection at the detuned signal-recycling cavity. However, a detailed mathematical description of the generation of frequency-dependent light is given in the following section.

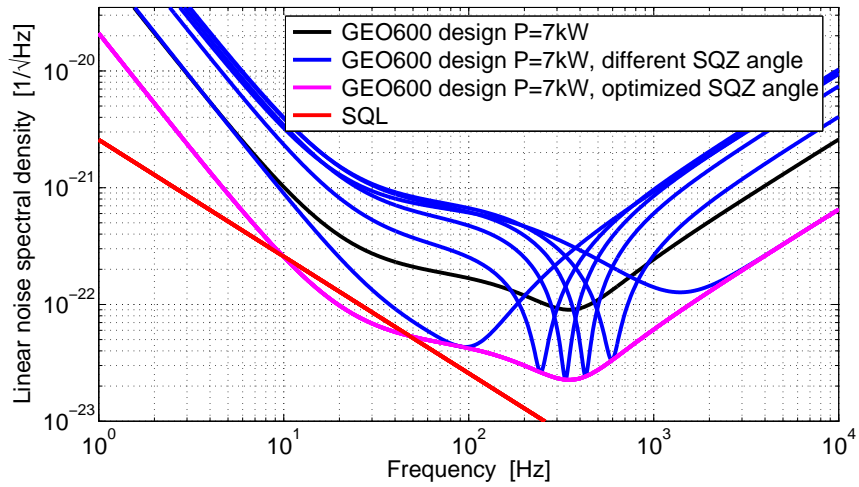


Figure 4.6: Strain sensitivity of GEO 600 with an internal power of 7 kW (black curve). The blue curves are the resulting strain sensitivities if one injects -12 dB of squeezing into the dark port of the dual-recycled Michelson interferometer with different initial squeezing angles. Note, that for each squeezing angle the strain sensitivity is enhanced by a factor of four at a different frequency i.e. the squeezing angle has to be optimized for every frequency. After such an optimization one obtains the magenta curve, which shows a broadband increase in the strain sensitivity. The SQL of the GEO 600 GW detector is shown as a red line and is surpassed in a small frequency range by the squeezing enhanced strain sensitivity with optimized squeezing angle.

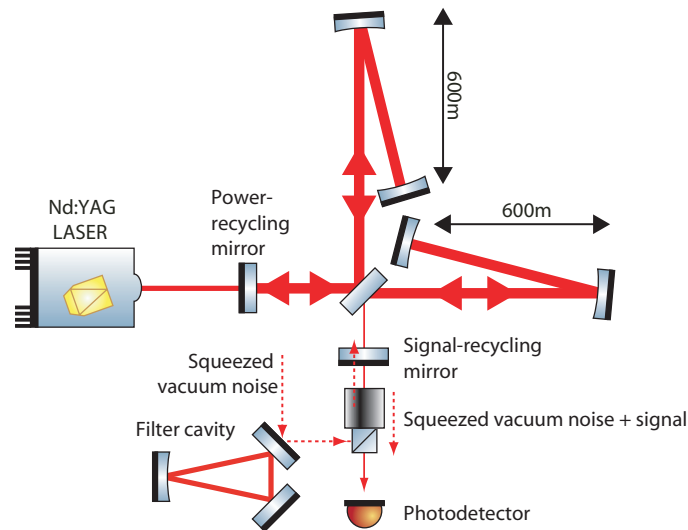


Figure 4.7: Simplified schematic of the gravitational wave detector GEO 600 as already presented and described in Figure 4.3. Here an additional filter cavity is added to compensate the effects of the signal-recycling cavity, detuned to a frequency Ω_c , onto the injected squeezed vacuum. The properties of the filter cavity are matched to those of the signal-recycling cavity to ensure that the dispersions of the cavities are the same. The effects of the signal-recycling cavity are only compensated if the filter cavity is locked to the opposite sideband frequency $-\Omega_c$.

4.1.3 Theoretical description of frequency-dependent light

A single mode of the electromagnetic field can be described by its field amplitude or annihilation operator $\hat{a}(\omega)$, which has the commutation relation $[\hat{a}(\omega), \hat{a}^\dagger(\omega)] = 1$. The non-Hermitian operator $\hat{a}(\omega)$ can be decomposed according to

$$\sqrt{\frac{\omega_0 + \Omega}{\omega_0}} \hat{a}(\omega_0 + \Omega) = \frac{\hat{X}_1(\Omega) + i\hat{X}_2(\Omega)}{\sqrt{2}}, \quad (4.3)$$

$$\sqrt{\frac{\omega_0 - \Omega}{\omega_0}} \hat{a}^\dagger(\omega_0 - \Omega) = \frac{\hat{X}_1(\Omega) - i\hat{X}_2(\Omega)}{\sqrt{2}}, \quad (4.4)$$

where $\hat{X}_{1,2}(\Omega)$ are the amplitude (subscript 1) and phase (subscript 2) quadrature operators of the two-photon formalism acting in the space of modulation frequencies Ω [CS85]. Correspondingly, the carrier frequency of the field is denoted by ω_0 . The discrete commutation relation $[\hat{X}_1(\Omega), \hat{X}_2^\dagger(\Omega)] = i$ follows directly from the commutation relation of $\hat{a}(\omega)$ and $\hat{a}^\dagger(\omega)$. This relation places a fundamental limit on how well one quadrature of an optical beam can be determined, given some knowledge of the orthogonal quadrature. This is expressed by the uncertainty relation

$$\Delta^2 \hat{X}_1(\Omega) \Delta^2 \hat{X}_2(\Omega) \geq \frac{1}{4}, \quad (4.5)$$

where the operator variances are denoted by

$$\Delta^2 \hat{X}_{1,2} = \frac{1}{2} \langle \hat{X}_{1,2} \hat{X}_{1,2}^\dagger + \hat{X}_{1,2}^\dagger \hat{X}_{1,2} \rangle - |\langle \hat{X}_{1,2} \rangle|^2. \quad (4.6)$$

For pure states minimum uncertainty is given by the equal sign in Equation 4.5. For conciseness where possible we omit the explicit frequency dependence (Ω) and since $\Omega \ll \omega_0$, we introduce the following approximation to Equation 4.3

$$\hat{X}_1 = \frac{\hat{a} + \hat{a}^\dagger}{\sqrt{2}}, \quad (4.7)$$

$$\hat{X}_2 = \frac{\hat{a} - \hat{a}^\dagger}{i\sqrt{2}}. \quad (4.8)$$

One should keep in mind that amplitudes on the right-hand side act at different sideband frequencies; however, for all practical purposes, the quadrature amplitudes are Hermitian operators and therefore will be used as representatives of measurement results. With their continuous eigenvalue spectra, these operators span the phase space where the Wigner function is defined. An arbitrary quadrature in this phase space can be defined as

$$\hat{X}_\theta = \frac{1}{\sqrt{2}} (\hat{a} e^{-i\theta} + \hat{a}^\dagger e^{i\theta}) \quad (4.9)$$

$$\text{or } \hat{X}_\theta = \hat{a}_1 \cos \theta + \hat{a}_2 \sin \theta. \quad (4.10)$$

We move into the rotating frame at carrier frequency ω_0 where the carrier (local oscillator) is stationary on the real axis. Using a photodiode and demodulating the

photoelectric current at Ω we actually observe the beat of the two sidebands contrarily rotating at $\pm\Omega$ with the carrier. If some apparatus changes the phase of only one sideband by the angle Φ keeping the carrier as well as the other sideband unchanged, we find that the quadrature angle of constructive interference changes by half the amount of the single sideband rotation,

$$\begin{aligned}\hat{X}_{\theta'} &= \frac{1}{\sqrt{2}}(\hat{a}e^{i\theta} + \hat{a}^\dagger e^{-i(\theta+\Phi)}) \\ &= \frac{e^{-i\Phi/2}}{\sqrt{2}}(\hat{a}e^{i\theta'} + \hat{a}^\dagger e^{-i\theta'}) \\ &\text{with } \theta' = \theta + \Phi/2.\end{aligned}\tag{4.11}$$

The transfer function ρ of the reflection from a cavity with round-trip length $2L$ and reflectivities r_1 and r_2 is given by

$$\rho(\Omega) = \frac{r_1 - r_2 e^{2i(\Omega-\Omega_c)L/c}}{1 - r_1 r_2 e^{2i(\Omega-\Omega_c)L/c}},\tag{4.12}$$

where $\omega_0 + \Omega_c$ is a resonance frequency (see Appendix E). Hence, sidebands are phase shifted by the amount $\arg(\rho)$, which depends on the sideband frequency Ω . As we will see in Section 4.2.1, a reflectivity for r_2 is chosen close to unity, resulting in a strongly overcoupled filter cavity.

Now consider squeezing at a certain frequency generated by the beat of two sidebands with the carrier. A squeezed state $|r, \theta, \alpha\rangle$ is obtained by applying the squeezing operator [WM94]

$$S(r, \theta) = \exp\left\{-r[\exp(-2i\theta)\hat{a}^2 - \exp(2i\theta)\hat{a}^{\dagger 2}]\right\}\tag{4.13}$$

to a coherent state $|\alpha\rangle$. The resulting squeezed state comes with the desired noise power reduction of $\exp(-r)$ in quadrature \hat{X}_θ compared to coherent noise. Exactly as in classical sideband modulations the phase relation of the sidebands and the carrier determine the quadrature angle, here the angle of the squeezed quadrature.

Initially, the angle of the squeezed quadrature does not depend on frequency and the variance of the quadrature operator $\Delta^2\hat{X}_\theta$ reads [Har02]

$$\Delta^2\hat{X}_\theta = \cosh(2r) - \sinh(2r)\cos[2(\theta - \theta_s)].\tag{4.14}$$

The light beam noise powers are therefore white in frequency space at all angles when leaving the source. If the squeezed beam is then reflected from a detuned cavity having a small linewidth compared to its detuning, the squeezing angle in phase space, θ_s , will depend on the sideband frequency by virtue of $\arg(\rho)$ in Equation 4.12, yielding

$$\theta_s(\Omega) = \theta_{\text{OPA}} + \frac{1}{2}\arg[\rho(\Omega)].\tag{4.15}$$

Here θ_{OPA} is the initial, frequency-independent, but variable angle of the squeezed quadrature.

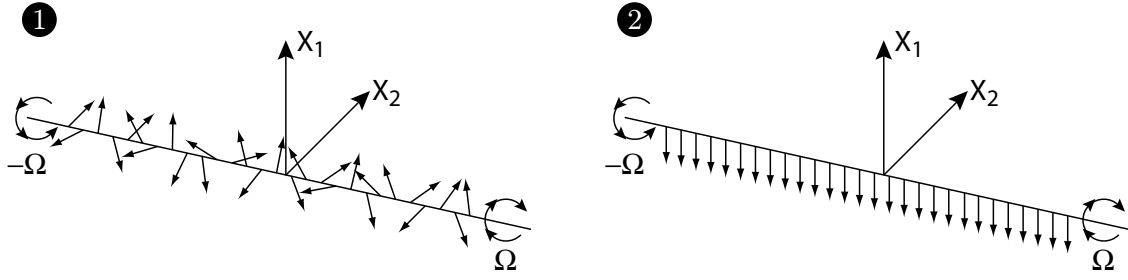


Figure 4.8: Representation of the vacuum ❶ and squeezed vacuum ❷ in the sideband picture. The vacuum is represented by an ensemble of phasors, each located at an individual frequency. The variance of the length distribution of the phasors is determined by the zero-point energy of the quantum mechanical oscillator at that frequency. The phase of the phasor is completely random. Thus, there exists no correlation between the phasors at $\pm\Omega$. The sideband picture representation of a perfect squeezed state is shown in ❷. In contrast to the vacuum shown in ❶, the squeezed vacuum shows perfect correlations between the upper and lower sidebands at frequencies $\pm\Omega$. The state shown here is a perfectly phase squeezed state, meaning that the beat of the sidebands at $\pm\Omega$ adds up in the amplitude quadrature and vanishes completely in the phase quadrature.

The time-dependent normalized quadrature fields $\hat{q}_{1,2,\theta}(\Omega, t)$ whose variances are directly proportional to our measurement quantities are defined by

$$\hat{q}_{1,2,\theta}(\Omega, t) = \hat{X}_{1,2,\theta}(\Omega)e^{-i\Omega t} + \hat{X}_{1,2,\theta}^\dagger(\Omega)e^{i\Omega t}. \quad (4.16)$$

Note that the right-hand side of Equation 4.5 is equal to unity if the quadrature fields $\hat{q}_{1,2}(\Omega, t)$ are considered instead of its amplitudes.

The following section gives a more figurative and intuitive explanation of the generation of frequency-dependent light by reflecting a frequency-independent state at a detuned locked filter cavity.

4.1.4 Frequency-dependent light in the sideband picture

Section 2.10 already discussed quantum noise in the sideband picture. Here a more simple picture is used to introduce the properties of quantum noise and squeezing, which is then used to give a simple explanation to understand the effects on squeezed vacuum by reflection at a detuned cavity.

Figure 4.8 (left) represents vacuum noise in the sideband picture. At each frequency there exists an individual phasor in quadrature phase space with a certain length and a random phase. The origin of these phasors is the non-vanishing ground state energy of the quantum mechanical oscillators at the frequencies Ω ; often called the zero-point fluctuations. Because the phase of each phasor is distributed in a completely random way, there are no correlations between the phasors at $\pm\Omega$. Thus, the beat between these two sidebands measured for example with a photodetector is also completely random. In a measured spectrum this causes the white vacuum noise floor.

Compared to the vacuum noise in the sideband picture, a perfectly phase squeezed state is also presented in Figure 4.8. Here a perfectly squeezed state is chosen for simplification. The differences between the two are quite obvious. The squeezed state shows

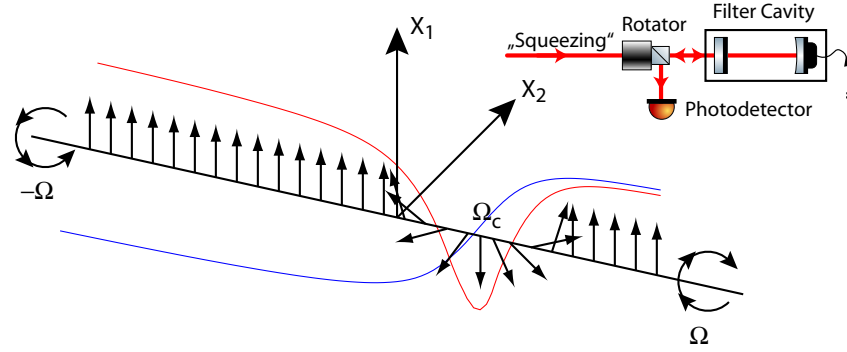


Figure 4.9: Representation of the squeezed vacuum state in the sideband picture, presented in Figure 4.8 **Q**, after reflection at a cavity, which is slightly detuned to the reference frequency by Ω_c . The frequency-dependent reflectivity (red) and dispersion (blue) of the cavity are overlapped with the sideband picture. For large frequencies $\pm\Omega$ the phase shift added to the phasors is $\pm 180^\circ$ due to the reflection at the cavity. Around the resonance frequency the phase shift is smaller than 180° and becomes 0° exactly at the resonance frequency Ω_c . Thus, the quadrature of the squeezing, where it can be detected optimally, changes with frequency. For large frequencies $\pm\Omega$, the squeezing quadrature is still the phase quadrature. Directly at the resonance frequency the squeezing is now found to be in the amplitude quadrature due to the fact that only the negative sideband is phase shifted by 180° . Around the resonance the squeezing quadrature changes continuously with rising frequency from the phase quadrature to amplitude quadrature and back to phase quadrature. This behavior can be interpreted as a frequency-dependent rotation of the squeezing ellipse in quadrature space and will be presented in the experimental results (Section 4.4). A simplified schematic of the experimental optical layout of the reflection of a squeezed vacuum at a detuned locked cavity is presented in the upper right corner.

perfect correlations between the two sidebands at $\pm\Omega$. Thus, the beat of the two sidebands add up in the amplitude quadrature and cancel in the phase quadrature.

Using this perfectly squeezed state and reflecting it at a detuned locked cavity changes the phase of every phasor in the sideband representation in a frequency-dependent way. Figure 4.9 shows the resulting sideband representation of the reflected state. The figure also shows the frequency-dependent reflectivity of the detuned cavity in red with the resonance frequency Ω_c . The dispersion of the cavity is visible as a blue line. Due to the frequency-dependence of the dispersion, the phasors at large frequencies $\pm\Omega$ are phase shifted by $\pm 180^\circ$ and the phasors are now orientated upwards. In these frequency ranges the beat of the phasors still results in perfect phase quadrature squeezing. Around the resonance frequency Ω_c the phase shift is less than 180° and the phasors are therefore phase shifted less. The phase shift is 0° exactly at the resonance. Consequently, the beat of the phasors at the resonance frequency results in perfect amplitude squeezing, meaning that if one measures a spectrum in the phase quadrature, one measures squeezing at high frequencies and anti-squeezing directly at resonance. Around the resonance frequency, where the phase shift satisfies $0^\circ < |\phi| < 180^\circ$, the squeezed quadrature is slowly varied with increasing frequency from the phase quadrature to the amplitude quadrature and back to the phase quadrature. As we will see in Section 4.4 the noise level of the spectra around the resonance frequency changes from the noise level of the squeezing to the

anti-squeezed noise level and back. This frequency-dependent change of the phase shift and the resulting frequency-dependent change in the squeezing quadrature can also be interpreted as a frequency-dependent rotation of the squeezing ellipse. In Section 4.4.2 we will see this rotation of the squeezing ellipse when the tomography of the experimentally created states is evaluated.

A second filter cavity can be used to compensate the effect of the frequency-dependent rotation of the squeezing induced by the first filter cavity. This is shown in Figure 4.10. Here, the combined transfer function in reflection of the two filter cavities is displayed by the red curve, whereas the combined dispersion of the two filter cavities is represented by the blue curve. Note that now the overall phase shift for large negative frequencies and positive frequencies corresponds to $\pm 360^\circ$. The phasors displayed in the figure are phase shifted according to the combined dispersion of the two filter cavities. The phasors are orientated along the amplitude quadrature axis for large positive and negative frequencies as well as in the range around the reference frequency ω_0 in the center. Near the two resonances at frequencies $\pm \Omega_c$ the phase shift is less than 360° and becomes $\pm 180^\circ$ exactly at the resonance. Comparing the individual sideband frequencies $\pm \Omega$, one sees that if the phase shift at a frequency $+\Omega$ is equal to $+\phi$, then the phase shift at the negative sideband frequency $-\Omega$ is equal to $-\phi$. Thus, the relative phase shift is cancelled and the beat between the two sidebands is the same and found in the amplitude quadrature. Hence, a measured spectrum of such a state, reflected at two detuned cavities with opposite detuning frequencies but identical dispersions, is indistinguishable from a phase quadrature squeezed state, which is measured directly and not reflected at a detuned cavity at all. Therefore, one can conclude that the effects on a squeezed state reflected at a detuned cavity, like the SRC in GEO 600, can be compensated with a filter cavity detuned to the opposite sideband frequency.

To prove the theoretical predictions discussed here, the setup of an experiment is described in the next section. In this experiment a squeezed state is generated by an OPA and reflected at detuned locked filter cavity. The resulting state is evaluated by a homodyne detector and the spectra in different quadratures of this state are analyzed. Later, tomography of this state is performed at different frequencies to gain a view of the squeezing ellipse in quadrature phase space and its frequency-dependence.

4.2 Optical layout

In this section the basic optical layout of the experiment is described. The idea of the experiment is to generate frequency-dependent squeezed light. An OPA produces frequency-independent squeezed states which become frequency-dependent after reflection at a filter cavity [KLM⁺01] which is slightly detuned at a frequency Ω_c from the carrier frequency ω_0 . This frequency-dependent light is then analyzed with a homodyne detector, which allows the measurement of noise spectra in every quadrature with an accuracy of approximately 1%. The measurement of the noise distribution of a quantum state in every quadrature at a single frequency allows the reconstruction of the Wigner function of this particular quantum state in quadrature space at the given frequency by using the inverse Radon transformation, see Section 4.3 for details. Thus, a measurement of noise spectra

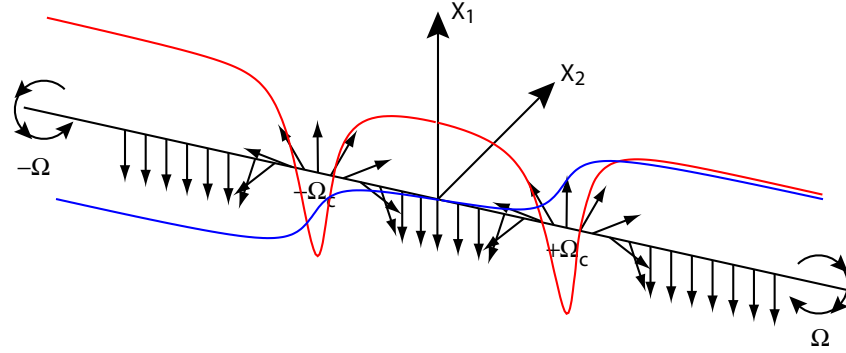


Figure 4.10: Representation of the squeezed vacuum state in the sideband picture, presented in Figure 4.8 ②, after the reflection at two cavities, which are slightly detuned from the reference frequency by $\pm\Omega_c$. The frequency-dependent reflectivity (red) and dispersion (blue) of the combined cavity transfer functions are overlapped with the sideband picture. For large frequencies $\pm\Omega$ the phase shift added to the phasors is $\pm 360^\circ$ due to the double reflection at the detuned cavities. Near the reference frequency ω_0 in the center, the phase shift is 0° . Around the resonance frequencies $\pm\Omega_c$ the phase shift is smaller than 360° and becomes $\pm 180^\circ$ exactly at the resonance frequencies $\pm\Omega_c$. Comparing the individual sideband frequencies $\pm\Omega$, one sees that if the phase shift at a frequency $+\Omega$ is equal to $+\phi$, then the phase shift at the negative sideband frequency $-\Omega$ is equal to $-\phi$. Thus, the relative phase shift is cancelled and the beat between the two sidebands is the same and found in the amplitude quadrature. Hence, the squeezed state after two reflections at the detuned cavities is indistinguishable from a measurement of the initial squeezed state.

in every quadrature allows the reconstruction of Wigner functions at various frequencies, enabling us to see the evolution of e.g. the orientation of the squeezing ellipse in quadrature space.

The basic optical layout is shown in Figure 4.11. The setup is almost identical to the setup of the generic squeezing experiment presented in Chapter 3. The parts of the experiment unchanged compared to the generic squeezing experiment are the laser, the modecleaner, the SHG, and the OPA (described in detail in Sections 3.2.1, 3.2.2, 3.3.4, and 3.3.5, respectively). All related control loops are identical to those described in Chapter 3. Minor changes have been made to the homodyne detector. The photodiodes have been changed (see Section 4.2.2) and a sophisticated electronic control loop now allows the measurement of an arbitrary quadrature by using a combined rf-dc error signal generation. The rf-phase modulation sidebands on the dim squeezed signal beam allow measurement in the amplitude quadrature. The phase quadrature measurement is controlled by the difference photocurrent of the two homodyne photodiodes. A mathematical combination of these two error signals allows the control of the homodyne detector to measure an arbitrary quadrature. Details on the generation of the two individual error signals and the new homodyne control electronics can be found in Section 4.3.4. To perform tomography on the measured quantum state, a computer based data acquisition has to be made, which is described in Section 4.3.2.

The major difference of this experiment compared with the generic squeezing experiment described in Chapter 3 is the use of the filter cavity for the generation of

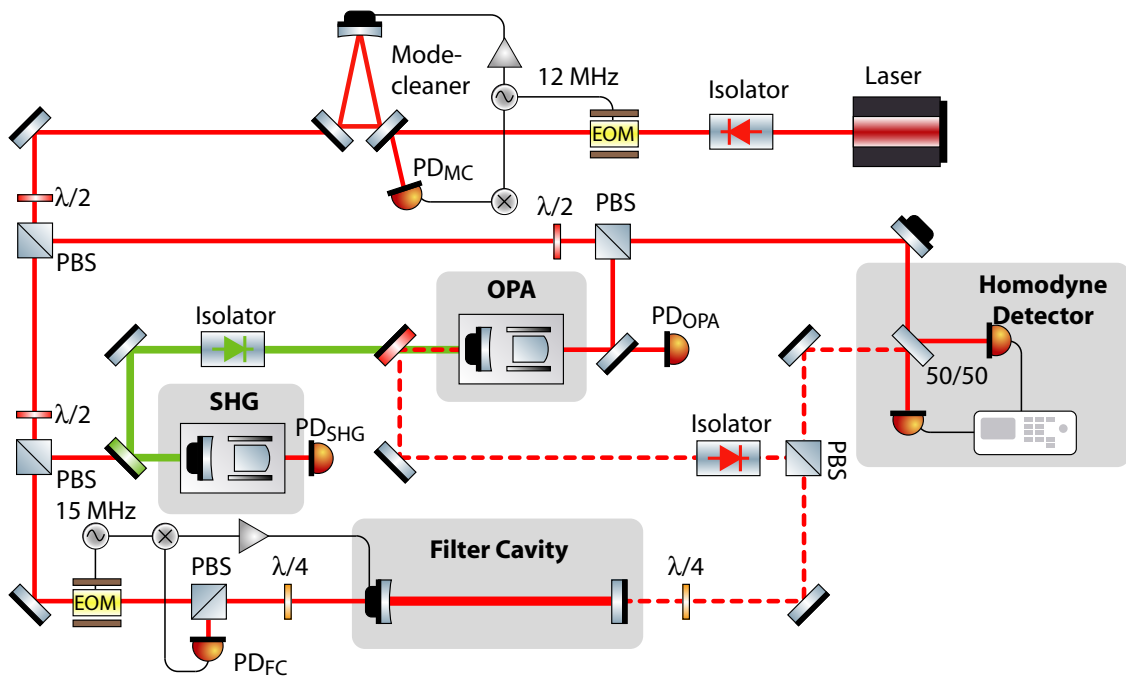


Figure 4.11: Schematic of the optical layout of the experiment used to produce frequency-dependent squeezed light. The basic setup includes all components of the generic squeezing setup. This is extended to include a filter cavity for generation of frequency-dependent squeezed states.

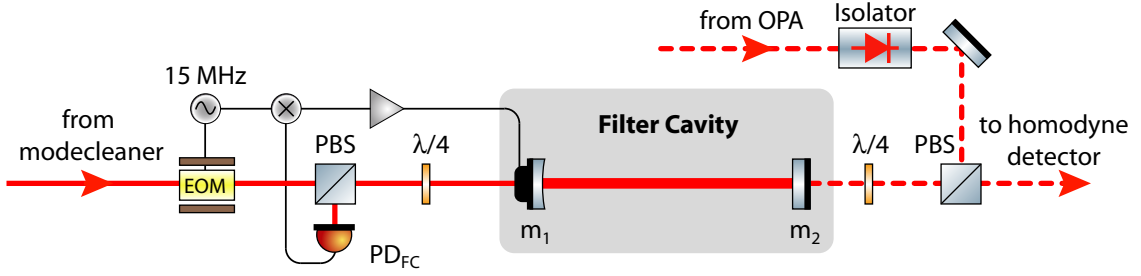


Figure 4.12: Layout of the control scheme of the filter cavity. A fraction of the light transmitted through the modecleaner is phase modulated by an EOM with 15 MHz. A combination of a polarizing beam splitter (PBS) and a quarter-wave plate enables the detection of the back-reflected light in reflection of the filter cavity. Demodulation of the provoked photocurrent with 15 MHz creates an error signal, which is processed by a servo, amplified, and fed back to the PZT-mounted input coupler of the filter cavity.

frequency-dependent squeezed light. Its parameters and the control are described in detail in Section 4.2.1. A Faraday isolator between the OPA and the filter cavity is used to suppress the parts of the light field used for locking the filter cavity, which otherwise would propagate directly into the OPA cavity, seeding it through the outcoupling mirror.

4.2.1 Filter cavity

The filter cavity in this experiment is used to transform frequency-independent squeezed light—as being generated by the OPA—into frequency-dependent squeezed light. A theoretical picture of this effect was given in Section 4.1.4 and the mathematical background has been described in Section 4.1.3. A schematic of the filter cavity’s optical layout and its control scheme is presented in Figure 4.12. The filter cavity is a linear two mirror cavity with a length of 50 cm. The cavity is composed of a curved mirror m_1 with a power reflectivity $R_1 = 99.95\%$ and a radius of curvature $r_c = 1.5$ m and a plane mirror m_2 of reflectivity $R_2 = 97\%$. The resulting linewidth of the cavity is 1.48 MHz and the finesse is approximately $\mathcal{F}_{FC} = 200$. The length control scheme of the filter cavity is achieved by a Pound-Drever-Hall locking technique. Approximately 10 mW from the output of the modecleaner are used as a length control beam. This is phase modulated by an EOM with 15 MHz. A combination of a PBS and a quarter-wave plate enables the detection of the reflected light with the photodiode PD_{FC} . The photocurrent is demodulated with 15 MHz to generate the desired error signal, which looks much the same as the error signal presented in Figure 3.6. The three step slopes of the error signal allows the locking of the cavity to the reference frequency ω_0 or at one of the sidebands with frequency $\omega_0 + \Omega_c$; $\Omega_c/2\pi = 15$ MHz. This error signal is processed by a servo, amplified and fed back to the cavity PZT to control the cavity length. Since the cavity is an undercoupled cavity for the cavity length control field, only a small fraction is transmitted through the cavity. Along this path it passes two quarter-wave plates and propagates towards the OPA. To prevent any back-reflected light from reaching the OPA, a Faraday isolator is placed in between the filter cavity and the OPA. The squeezed field coming from the OPA passes the Faraday isolator with small losses of approximately 2%. Again, a combination of a

quarter-wave plate and a PBS ensures that the back-reflected, now frequency-dependent, squeezed field is sent to the homodyne detector. From this side, the cavity is strongly overcoupled. The losses to the squeezed field are small due to the high reflectivity of the curved mirror $m1$.

4.2.2 Homodyne detector

The homodyne detector is in principle the same as that used in the former experiments (see Section 3.4.1). Changes are made to the photodiode electronics and the photodiodes used in these detectors have changed to Perkin Elmer C30619, which have only a quantum efficiency of $\eta = 0.87 \pm 3\%$. The electronic circuit of the photodetectors can be found in Appendix C.4. A transimpedance resistor of 510 Ohm is chosen to achieve a bandwidth of 30 MHz and a maximum light power of 15 mW is able to be detected.

4.3 Tomography of quantum states

Tomography [Her80, KS89] is a procedure to obtain the more dimensional spatial information of an object. In this section the object of interest is the quasi-probability distribution of a quantum state, the Wigner function. Reconstruction of the more dimensional spatial information is done by sectioning the object i.e. for a quantum state one measures the distribution of the measured noise power for different quadrature angles. From this ensemble of distributions the representation of the corresponding quantum state in phase space can be reconstructed via inverse Radon transformation. The data acquisition system and associated locking scheme of the homodyne detector used in this experiment, which allows a pc controlled stable adjustment of an arbitrary homodyne angle, is developed by B. Hage during his Diplomarbeit [Hag04].

4.3.1 The Wigner function

The Wigner function is a quasi-probability distribution in phase space widely used in quantum physics. It was first introduced by Wigner in 1932 [Wig32]. The term quasi-probability is used because the Wigner function is not positive definite and thus not a “real” probability distribution. The Wigner function is defined by [Leo97]

$$W(q, p) = \frac{1}{2\pi} \int_{-\infty}^{\infty} e^{ipx} \langle q - \frac{x}{2} | \rho | q + \frac{x}{2} \rangle dx, \quad (4.17)$$

and characterizes the statistics e.g. of the position q and the momentum p . The Wigner function is real for Hermitian operators $\hat{\rho}$ and normalized

$$\int_{-\infty}^{\infty} \int_{-\infty}^{\infty} W(q, p) dq dp = 1. \quad (4.18)$$

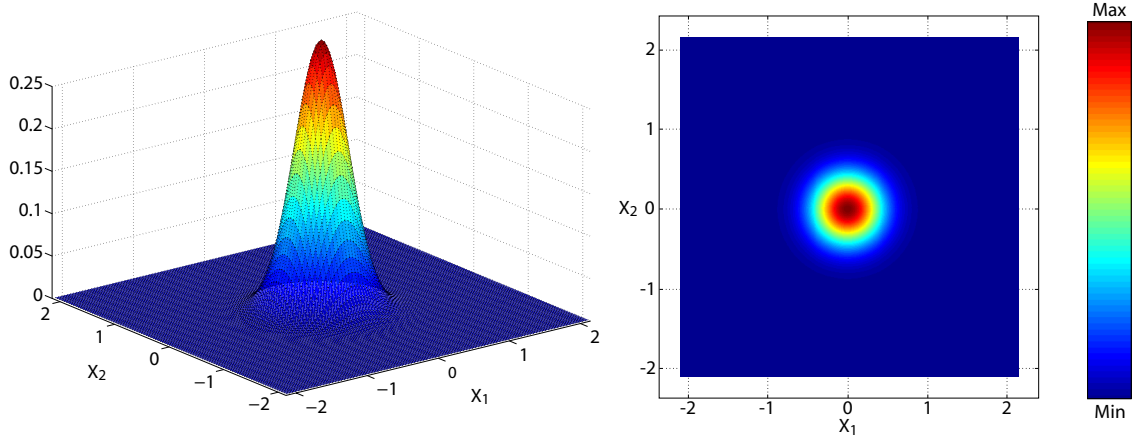


Figure 4.13: 3D-Wigner function of the vacuum state in phase space (left) and a contour plot of the same function (right).

If one integrates the Wigner function in one direction

$$\begin{aligned}
 \int_{-\infty}^{\infty} W(q, p) dp &= \frac{1}{2\pi} \int_{-\infty}^{\infty} \int_{-\infty}^{\infty} e^{ipx} \langle q - \frac{x}{2} | \rho | q + \frac{x}{2} \rangle dp dx \\
 &= \frac{1}{2\pi} \int_{-\infty}^{\infty} \int_{-\infty}^{\infty} e^{ipx} \text{const}|_p dp dx \\
 &= \langle q | \hat{\rho} | q \rangle \\
 &= P(q),
 \end{aligned} \tag{4.19}$$

one obtains a probability density. This integration can be made in an arbitrary direction, not only along p .

A remarkable feature of the Wigner function is that it can be used to calculate expectation values of an arbitrary operator \hat{O} by

$$\langle \hat{O} \rangle = \text{tr}\{\hat{\rho}\hat{O}\} = 2\pi \int_{-\infty}^{\infty} \int_{-\infty}^{\infty} W(q, p) W_{\hat{O}}(q, p) dq dp. \tag{4.20}$$

Here $W_{\hat{O}}(q, p)$ is the same as $W(q, p)$, but the density matrix $\hat{\rho}$ has been exchanged with the arbitrary operator \hat{O} .

An example of a Wigner function is given in Figure 4.13. This shows the Wigner function of the vacuum state in phase space as a 3D surface plot and also as a shaded contour plot. The vacuum state's Wigner function is given by

$$W_{|0\rangle}(\hat{X}_1, \hat{X}_2) = \frac{1}{\pi} e^{-\hat{X}_1^2 - \hat{X}_2^2}, \tag{4.21}$$

where \hat{X}_1 and \hat{X}_2 are the amplitude and phase quadratures, respectively. Since any coherent state can be generated by applying the displacement operator onto the vacuum

state (see Equation 2.12), the Wigner function of a coherent state is just displaced from the phase space origin. The Wigner function of a coherent state is therefore given by

$$W_{c.s.}(\hat{X}_1, \hat{X}_2) = \frac{1}{\pi} e^{-(\hat{X}_1 - \hat{X}_{1,0})^2 - (\hat{X}_2 - \hat{X}_{2,0})^2} \quad (4.22)$$

with $\hat{X}_{1,0}$ and $\hat{X}_{2,0}$ defining the amount of displacement.

In the experimental results (see Section 4.4) the Wigner functions of the measured frequency-dependent squeezed quantum states are presented.

4.3.2 Data acquisition

Because one cannot measure the Wigner function directly in an experiment, the only useful and accessible measure, the differential photocurrent of the two homodyne photodetectors, has to be evaluated to reconstruct the Wigner function. This process of reconstruction can be split into two parts. The first part is the data acquisition (DAQ) and the second part the reconstruction of the Wigner function by inverse Radon transformation, described in the next section. For the DAQ the photocurrents of the two homodyne detectors are high-pass filtered with a cut-off frequency of 16kHz and amplified by a factor of 25. Both resulting photocurrents are subtracted with a differential line receiver MAX4145 from Maxim. This differential signal is demodulated with the detection frequency of interest. To suppress the aliasing effect a four pole Chebychev-low-pass filter with a cutoff frequency of 100 kHz is used to filter the demodulated signal before it is converted with an AD-converter.

The data acquisition system is PC based and uses a commercial NI PCI-6014 card from National Instruments. The DAQ card offers a sampling frequency of 200 kS/s, that can be multiplexed up to 16 channels each allowing a resolution of 16 bit. Because only one channel has to be sampled in the experiment, the full bandwidth is able to be used. Furthermore, the card offers two analog output channels with 16 bit resolution which allow a feedback to the experiment, e.g. the change of the homodyne detection angle.

The time series of the demodulated differential photocurrent is stored with the help of the DAQ system. An example can be found in Figure 4.14. To minimize the amount of storage, the LabView program used to control the DAQ processes the time series in real time and stores every data point into one of the bins of a histogram. This real-time data processing reduces the amount of data to be stored by a factor of 1000. The histogram is essential for the reconstruction of the Wigner function, which is described in detail in the next section.

The LabView program is also responsible for setting the quadrature angle of interest. The details of the adjustment of this quadrature angle and the generation of an error signal for the homodyne detector for an arbitrary quadrature is described in Section 4.3.4. After adjustment of the correct quadrature angle, the program waits for half a second to let all control loops settle at their current operating point. Then it takes a preselected number of data points. After this measurement the new quadrature angle is adjusted and the process repeats itself until the final measurement is made.

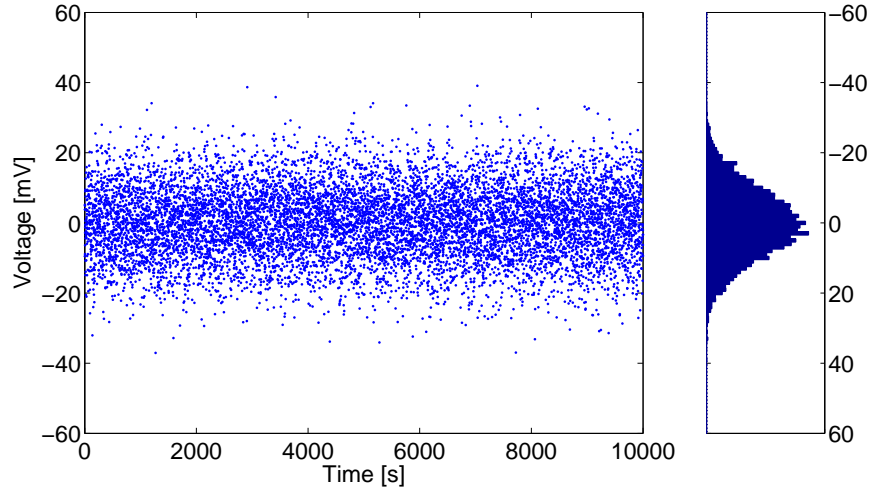


Figure 4.14: Time series and the corresponding histogram of the demodulated differential photocurrent

4.3.3 Inverse Radon transformation

As described in the previous section, the data is stored as a histogram of the demodulated differential photocurrent time series. The number of bins of the histogram and the voltage range it covers can be adjusted in the `LabView` program used for the DAQ. From Equation 2.81 we know that the differential photocurrent output of a balanced homodyne detector is proportional to the fluctuations in one quadrature of the signal field. Thus, the histogram measured by the DAQ system is the probability distribution $P_\theta(q)$, which itself is the projection of the Wigner function of a specific angle θ (see Equation 4.19). This transformation is called the *Radon transformation* [Rad17]

$$P_\theta(q) = \int_{-\infty}^{\infty} W(q \cos \theta - p \sin \theta, q \sin \theta + p \cos \theta) dp. \quad (4.23)$$

Radon transformations are studied in the mathematical theory of tomography [Her80]. The fact that it is invertible leads directly to the *inverse Radon transformation*, which is the mathematical key for quantum state tomography and the reconstruction of a quantum state in phase space. It is also used in other fields of tomography such as X-Ray-, Nuclear-Spin-, Positron-Emission-, and Gamma-Absorption-tomography, which mostly concentrates on medical diagnostics. With the help of the inverse Radon transformation, the ensemble of histograms for individual quadrature angles (Figure 4.15) can be transformed into the Wigner function and thereby allows the reconstruction of quantum states in quadrature phase space. For the calculation of the inverse Radon transformation the built-in `MATLAB` function is used, which is based on a Fourier transformation algorithm. This is much faster than an algorithm, which uses the direct inversion of the Radon transformation, see [Hag04, Bre98]. The result of such a reconstructed quantum state is given in Figure 4.16, where the Wigner function of the histogram series from Figure 4.15 is presented. The reconstruction process includes the normalization of the

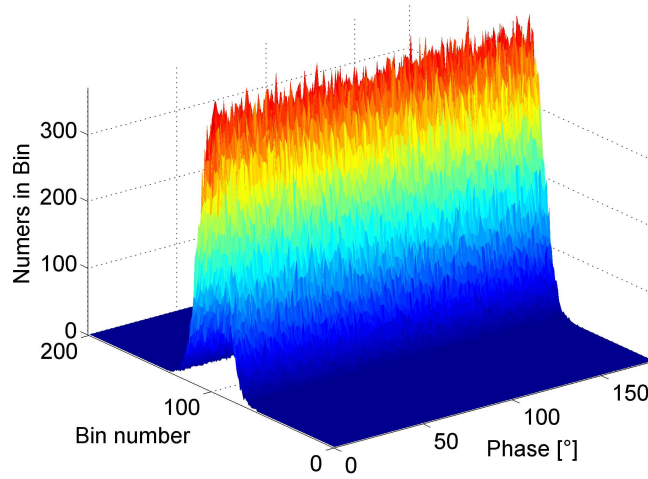


Figure 4.15: Series of histograms for the homodyne angle range of 0-180°. This is the input data for the inverse Radon transformation algorithm which reconstructs the Wigner function. This reconstruction is shown in Figure 4.16.

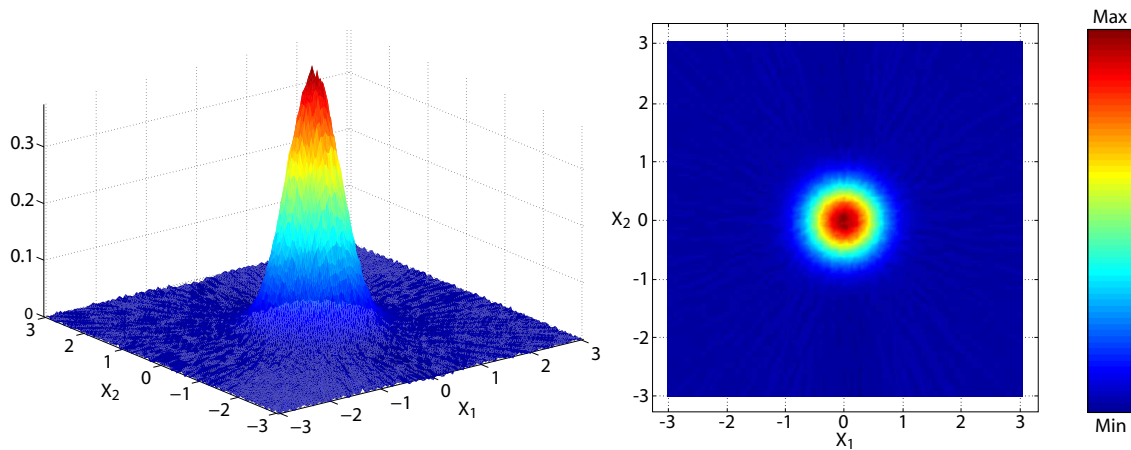


Figure 4.16: Wigner function reconstructed from the data used in Figures 4.14 and 4.15

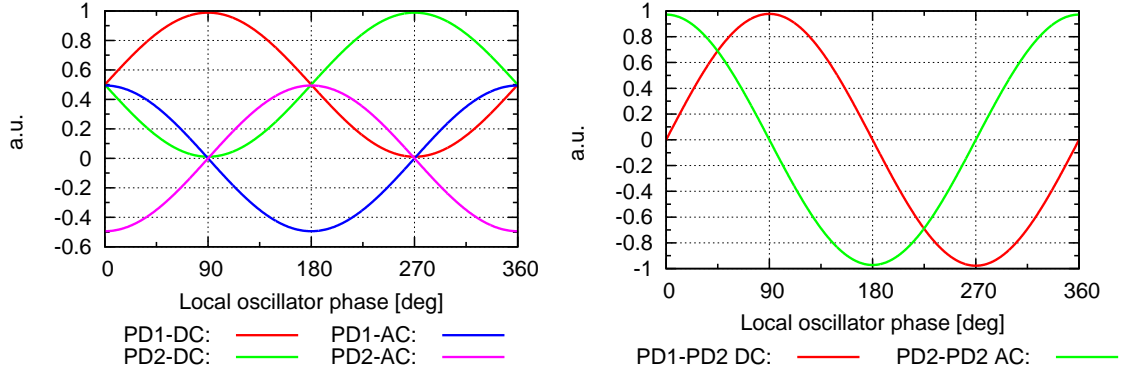


Figure 4.17: Homodyne detector signals outputs versus the local oscillator phase. The left graph shows the power of the two homodyne detector photodiodes of the direct measurement (DC) and after modulation with the phase modulation frequency Ω_{mod} present in the signal beam over the local oscillator phase. One can see that the DC and AC signals are 90° out of phase. The differences of the DC and AC signals are shown in the graph to the right. Here, one can see that the DC differential signal can be used to lock the homodyne detector to 0° and 180° , which corresponds to the phase quadrature. The differential AC signal on the other hand can be used for locking to 90° and 270° , which corresponds to the amplitude quadrature. Using a linear combination of these two differential signals, an error signal for an arbitrary quadrature angle can be generated. See Equation 4.24 for more details.

Wigner function. The axes are scaled in such a way that the full-width-half-maximum (FWHM) of the Wigner function of the vacuum is set to unity.

4.3.4 Locking a homodyne detector to an arbitrary quadrature angle

From the previous section we know that the reconstruction of the Wigner function can be achieved by the inverse Radon transformation. Thus, the data of the demodulated differential photocurrent has to be obtained for a quadrature angle range $0^\circ < \theta < 180^\circ$. This data is stored by the DAQ system and processed by the inverse Radon transformation.

Section 3.4.1 shows that an error signal for the amplitude quadrature can be obtained by demodulating the difference current of the two homodyne photodetectors at a frequency corresponding to a phase modulation frequency carried by the signal field. This error signal, from now on called the rf-error signal $S_{\text{err}}^{\text{rf}}$, is sinusoidal and produces a zero-crossing if one homodyne photodetector senses all the light, whereas the other detector is dark. This corresponds to a local oscillator phase of $\phi = 90^\circ$ and $\phi = 270^\circ$ in Figure 4.17. To obtain an error signal for the case where both homodyne photodetectors sense the same light power ($\phi = 0^\circ$ and $\phi = 180^\circ$), one has to take the difference of the two photocurrents directly without any demodulation. This error signal is called the dc-error signal $S_{\text{err}}^{\text{dc}}$ and allows measurements in the phase quadrature. Both error signals and the corresponding signals of each photodetector are presented in Figure 4.17. These two error signals can be used to generate an error signal S_{err}^θ for an arbitrary quadrature by

$$S_{\text{err}}^\theta(\phi) = b S_{\text{err}}^{\text{dc}}(\phi) + (1 - b) S_{\text{err}}^{\text{rf}}(\phi), \quad (4.24)$$

where ϕ is the relative phase between the local oscillator and the signal field and θ is the quadrature angle. Depending on the parameter b the zero-crossing of the error signal $S_{\text{err}}^\theta(\phi)$ can be changed from the relative phase of 0° to 180° . Thus, $S_{\text{err}}^\theta(\phi)$ allows the stable control of the relative phase relation between the local oscillator and signal beam entering the homodyne detector, which corresponds to a stabilization of the measured homodyne quadrature angle θ . As described in Section 3.4.1, this error signal is sent through an high voltage amplifier which drives a PZT-mounted mirror in the path of the local oscillator beam.

A remaining problem is that the inverse Radon transformation of MATLAB expects histograms of the demodulated differential photocurrent with an equidistant phase angle ϕ . However, a linear change of the parameter b results in a nonlinear distance between the measured phase angles. Therefore, the parameter b has to be calculated precisely for every desired phase angle ϕ_{set} . A short calculation using Equation 4.24 and setting $S_{\text{err}}^\theta = 0$ reveals

$$b = \frac{S_{\text{err}}^{\text{rf}}(\phi_{\text{set}})}{S_{\text{err}}^{\text{rf}}(\phi_{\text{set}}) - S_{\text{err}}^{\text{dc}}(\phi_{\text{set}})} = \frac{1}{1 - \tan \phi_{\text{set}}}, \quad (4.25)$$

with $S_{\text{err}}^{\text{dc}}(\phi) \propto \sin \phi$ and $S_{\text{err}}^{\text{rf}}(\phi) \propto \cos \phi$ and expecting that the error signals $S_{\text{err}}^{\text{dc}}$ and $S_{\text{err}}^{\text{rf}}$ are offset free and have the same amplitude. This is easily achieved in the experiment by matching these two parameters with an offset compensation and an individual gain control for each error signal. Details of the electronics used for locking the homodyne detector can be found in [Hag04].

The calculation of the parameter b is performed by the Labview program and the two analog output channels of the DAQ card are used to send a corresponding voltage to b and $1 - b$ to the analog servo to control the homodyne detection angle.

4.4 Experimental results

The results of the experiment to generate frequency-dependent light can be separated into different parts. In the first part we analyze the properties of the generated frequency-dependent states and compare them with the vacuum and frequency-independent squeezed states. This comparison is made for the detuning frequencies ± 15.15 MHz of the filter cavity. Next, tomography of the generated states is performed at different sideband frequencies to see the frequency-dependent rotation of the squeezing ellipse in quadrature phase space. Finally, a comparison of this rotation for the two different locking states of the filter cavity concludes the experimental results.

The experiment uses an OPA, which is described in Section 3.3. The coherent seed power used for the OPA measured in front of the crystal's back surface is 15 mW. The second harmonic pump power is 300 mW inducing a classical gain of 5 for the OPA. The OPA deamplifies the classical seed field in the cavity, resulting in a dim amplitude-quadrature-squeezed beam leaving the OPA with a power of approximately $70 \mu\text{W}$. A local oscillator power of 18 mW for the homodyne detector is chosen such that each photodiode detected about half of its maximum capable light power. The individual losses to the squeezed field are listed in Table 4.1; the overall loss for the squeezed field was 42%.

OPA escape efficiency:	ρ	88%
Propagation efficiency:	ζ	95%
Faraday rotator transmission efficiency:	η_{FR}	97%
Mode matching efficiency to the filter cavity:	mm_{FC}	94%
Homodyne efficiency	ξ^2	91%
Quantum efficiency of the photodiodes:	η_{PD}	87%
Efficiency due to the angle of the photodiodes:	η_{angle}	96%
Overall efficiency:		58%

Table 4.1: List of the individual efficiencies applied to the squeezed field from generation to detection for the frequency-dependent squeezed light generation and characterization experiment.

4.4.1 Frequency-dependent squeezing spectra

All spectra presented in this section are obtained from the differential homodyne detector output photocurrent analyzed by a Rohde&Schwarz FSP3 spectrum analyzer. The resolution bandwidth is chosen to be 100 kHz and the video bandwidth is 100 Hz. To compare the results of the frequency-dependent squeezing more easily, frequency independent spectra of the OPA generated squeezed states are measured first. A beam dump is placed into the filter cavity so that the squeezed light is no longer reflected at a cavity but at a single mirror with a reflectivity of 97%. This squeezed state is measured by the homodyne detector in the amplitude and phase quadrature to compare the frequency independent squeezing and anti-squeezing spectrum against the measured vacuum spectrum. These spectra are shown in Figure 4.18. The squeezing spectra (black) and the spectrum of the vacuum state (gray) are used as references. The effect of the additional 3% loss can be neglected due to the high overall loss of 42%. Note that the dark noise of the homodyne detector has been taken into account for all spectra shown in Figure 4.18. The other noise power spectra shown in Figure 4.18 represent the frequency-dependent squeezing spectra, each measured at a different quadrature angle with a separation of 10° . Here, an angle of 0° defines the amplitude quadrature, which fixes the phase quadrature to 90° . For these measurements the filter cavity is detuned and locked to a sideband frequency of $\Omega_c/2\pi = +15.15$ MHz with respect to the reference frequency ω_0 . The small offset in frequency compared to the modulation frequency of 15 MHz used for generation of the filter cavity's error signal, is chosen to minimize the overlap of the remnants of the modulation frequency. It allows a clear view at the sideband frequencies with the maximum phase shift ($\Omega_c/2\pi = \pm 15.15$ MHz) of the frequency-dependent field in the sideband picture. For a comparison see Figure 4.9.

As shown in Figure 4.18, the frequency-dependent spectra are bounded by the measured frequency-independent spectra (black). The maximum amount of squeezing lies between 1.5–2 dB below the vacuum noise. If one focuses e.g. at the frequency-dependent spectrum measured in the amplitude quadrature shown (blue), the predicted behavior given by Equation 4.14 and Figure 4.9 can be reproduced. Starting at the lowest frequency of 12 MHz one can see that the spectrum shows amplitude squeezing which deteriorates at higher frequencies. Around 14 MHz the blue spectrum shows the same noise power as

the vacuum state. At the filter cavity's detuning frequency of +15.15 MHz, the spectrum has the same noise power as the frequency-dependent anti-squeezing. The noise power of the blue curve then drops and touches the vacuum noise level at 16.4 MHz before it again reaches the amplitude squeezed noise level at 18 MHz. Section 4.4.2 will show this behavior of the frequency-dependent spectra measured in amplitude quadrature can also be interpreted as the rotation of the squeezing ellipse, starting from amplitude quadrature squeezing at 12 MHz over phase quadrature squeezing at 15.15 MHz and again amplitude quadrature squeezing at 18 MHz. The features at 15 MHz result from the already mentioned remnants of the filter cavity locking field that is partially transmitted through the filter cavity. This field should be p-polarized after passing through the filter cavity and the two quarter-wave plates, however due to imperfections in the wave plates and a limited adjustment accuracy a fraction is also s-polarized and gets superimposed with the frequency-dependent squeezed field. Therefore the modulation imprinted on the filter cavity locking field is measured by the homodyne detector. To minimize this effect, the power of the filter cavity locking field is reduced as far as possible without losing stable control of the filter cavity. The features at 17.4 MHz are due to stray fields.

The long term stability of the experiment is shown in the lower part of Figure 4.18. Here, a measured noise power time series over 50 minutes of the fully locked experiment is presented. The homodyne detector angle is locked to 10° and the spectrum analyzer is used in the zero span mode at a frequency of 14.7 MHz. Note that the noise power stays very accurately at an average noise level of -58.4 dB.

The frequency-dependent spectra presented in Figure 4.18 are also measured for a negative cavity detuning of $\Omega_c/2\pi = -15.15$ MHz. The results are shown in Figure 4.19. The main difference to the spectra shown before is that the measured minima of the frequency-dependent spectra move with increasing homodyne detection angle from low to high frequencies. To be more precise, starting at a homodyne angle of 0° the minimum of the noise power for that spectrum lies below 12 MHz. For 10° homodyne angle this minimum lies at 12.3 MHz, for 20° at 13.1 MHz and so on for noise spectra with larger homodyne angle. A close look at the frequency-dependent spectra for a cavity detuning of $\Omega_c/2\pi = +15.15$ MHz, presented in Figure 4.18, reveals that the minima move with increasing homodyne detection angle from high to low frequencies. Figure 4.19 also shows remnants of the 15 MHz modulation frequency of the filter cavity locking field, which are a little bit smaller compared to spectra of a positive detuning frequency. This is achieved by further lowering the power of the filter cavity locking field. A stable lock is still achieved due to a small asymmetry in the filter cavities' error signal. For comparison with the theory (Section 4.1.3), Figure 4.20 displays simulated results (obtained from Equation 4.14) for the experimental data shown in Figure 4.19. To simplify the comparison, the same colors are used for the curves with the same homodyne detection angle. In the simulation one can clearly see the movement of the minimum in the noise power with increasing homodyne detection angle to higher frequencies. The simulated results do not include losses or the cavity transfer function.

The next section uses the DAQ system presented in Section 4.3 to obtain the histograms of the measured time series at different quadrature angles to reconstruct the Wigner function of the corresponding quantum state.

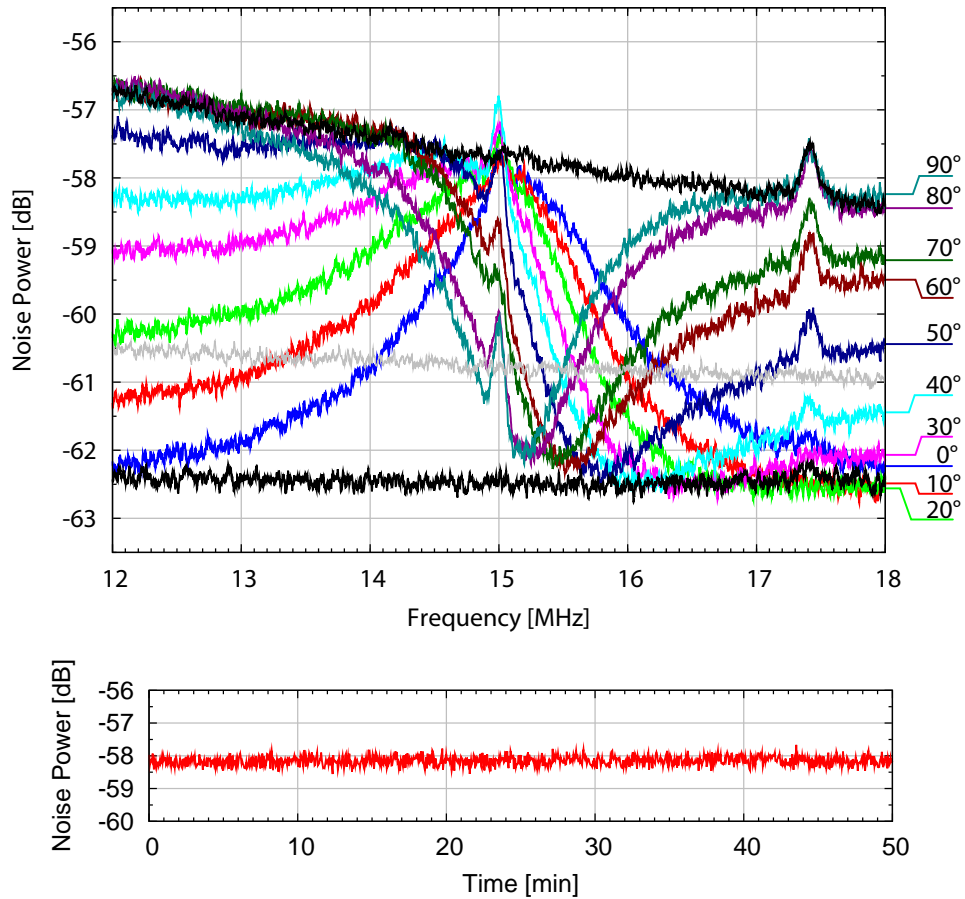


Figure 4.18: Measured noise power spectra of frequency-dependent squeezed light for a filter cavity detuning frequency of +15.15 MHz. The noise power spectra of the vacuum state (gray curve) and of a frequency-independent squeezed state measured in amplitude and phase quadrature (black curves) are illustrated as references. The colored spectra represent a frequency-dependent spectra measured for different quadrature angles. The lower part of the figure shows the long term stability of the setup and the homodyne angle control. Here, the noise power for a homodyne angle of 10° at a frequency of 14.7 MHz is measured for 50 minutes.

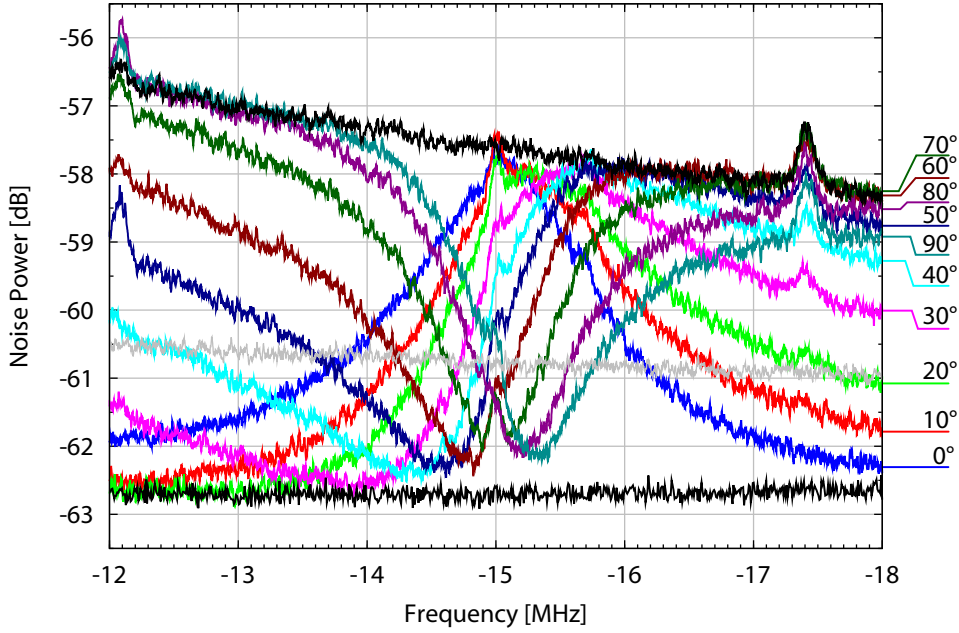


Figure 4.19: Measured noise power spectra of frequency-dependent squeezed light for a filter cavity detuning frequency of -15.15 MHz. The noise power spectra of the vacuum state (gray curve) and of a frequency-independent squeezed state measured in amplitude and phase quadrature (black curves) are illustrated as references. The colored spectra represent a frequency-dependent squeezed state measured for different quadrature angles.

4.4.2 Tomography of frequency-dependent light

For an even more striking demonstration of the frequency-dependent squeezing, one can reconstruct the Wigner function of the produced squeezed state at various sideband frequencies. Figure 4.21 shows the reconstructed Wigner function of the vacuum state and a frequency-dependent squeezed state for a sideband frequency of 14.1 MHz as a contour plot. The latter Wigner function is produced by reflecting the output field of the OPA from the detuned filter cavity locked to a sideband frequency of -15.15 MHz. The reflected field is measured with the homodyne detector and demodulated with the sideband frequency of interest (here 14.1 MHz). The DAQ system transforms the data into a histogram and changes the homodyne angle stepwise from 0° – 180° in 100 equidistant steps. The ensemble of histograms is then transformed into the Wigner function using the inverse Radon transformation. Details of the technique for reconstruction of the Wigner function are given in Section 4.3. The axes of the graphs in Figure 4.21 are scaled such that the standard deviation of the FWHM of the vacuum state is equal to unity. For a better comparison between the two states, an ellipse and a circle are drawn onto the Wigner function of the squeezed state, which represent the contour of the two Wigner functions at a specific height. It is clearly visible that the squeezed state shows quantum correlations between the phase and amplitude quadratures, i.e., squeezing at about 30° . Note that this Wigner function is centered at the origin, implying that no coherent excitation at 14.1 MHz is present. However, the plot does not show a minimum uncertainty

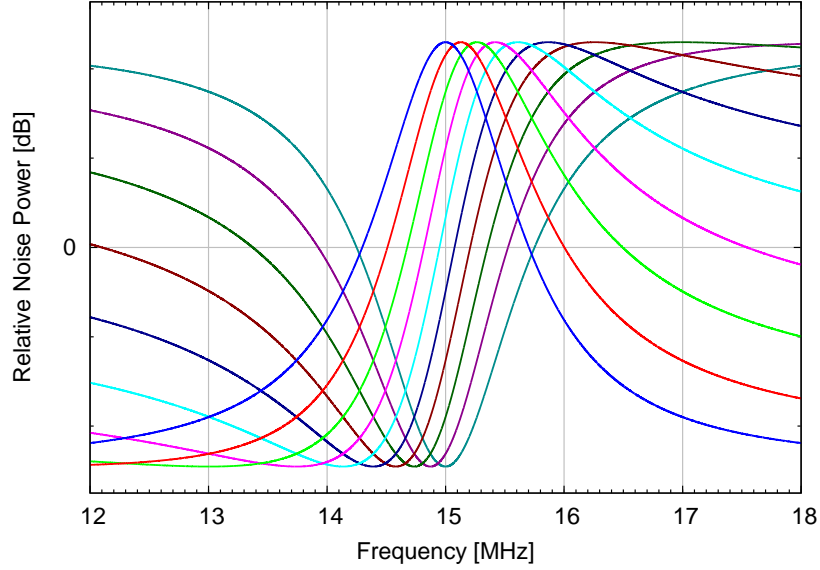


Figure 4.20: Simulated noise power spectra of frequency-dependent squeezed light for a filter cavity detuning frequency of -15.15 MHz. These curves are calculated using Equation 4.14 and can be compared with the spectra from Figure 4.19. Losses and OPA linewidth are not considered.

state as defined by Equation 2.36. Additional noise in the anti-squeezed quadrature is clearly detected. The area of this squeezed state is determined to be a factor of 1.16 larger than the vacuum state, also shown in Figure 4.21. This increased area can be partly attributed to optical losses in the squeezed beam and additional imprinted phase noise.

To see the rotation of the squeezing ellipse in quadrature phase space, the reconstructed Wigner functions at 12 frequencies in the interval between 12–18 MHz are shown in Figure 4.22. For this plot the filter cavity is locked to the negative sideband frequency of $\Omega_c/2\pi = -15.15$ MHz. The sideband frequency of the individual Wigner functions is given in the upper left corner of each plot. Note that the short axis of the squeezing ellipse at a sideband frequency of -12 MHz is almost aligned along the amplitude quadrature. It is clearly visible that the orientation of the ellipse changes with the sideband frequency and shows a clockwise rotation. To get an impression of a three dimensional Wigner function, the ellipse presented in the upper left corner of Figure 4.22 is plotted again. This 3D plot of the Wigner function for the sideband frequency of -12 MHz is shown in Figure 4.23.

If the detuning frequency of the filter cavity is changed to the positive sideband frequency of $+15.15$ MHz, the rotation of the ellipse changes from clockwise to anticlockwise. This behavior is presented in Figure 4.24.

4.4.3 Compensation of the rotation of the squeezing ellipse

To determine the rotation angle of every single Wigner function plotted in Figures 4.22 and 4.24 for a detuning frequency of -15.15 MHz and $+15.15$ MHz respectively, one needs

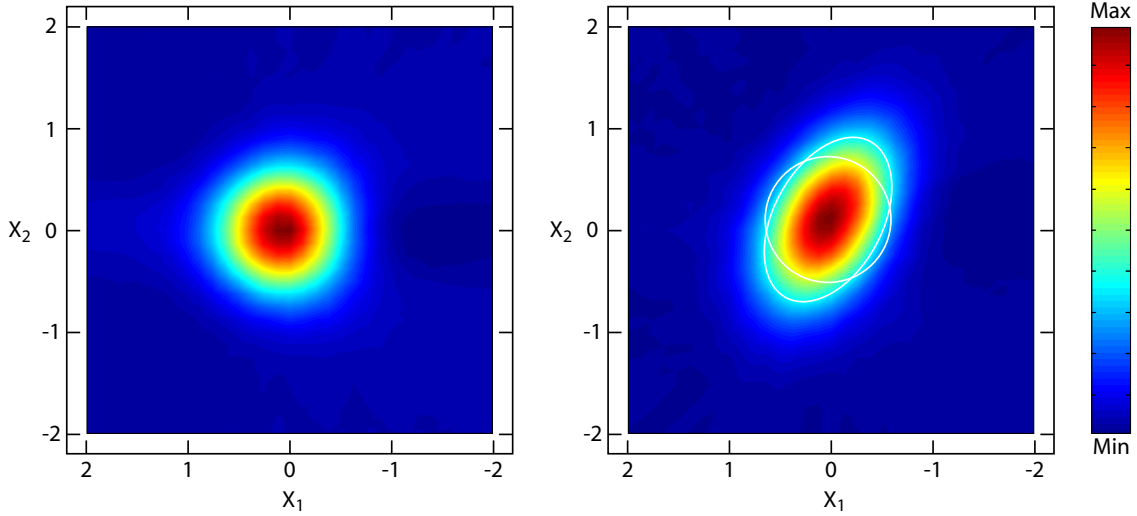


Figure 4.21: Comparison of the reconstructed Wigner functions of the vacuum state and a frequency-dependent squeezed state for a sideband frequency of 14.1 MHz. The figure shows both functions from a bird’s eye view, and the height is encoded based on the color bar on the right-hand side. For a better comparison, an ellipse and a circle are drawn in white onto the Wigner function of the squeezed state, which represent the contour of the two Wigner functions at a specific height.

a reference. Here the reference is given by the phase quadrature. The rotation angles for the individual detuning cases of the filter cavity are plotted in Figure 4.25. In this figure the solid lines represent the results one obtains by using the theory according to Equation 4.15. The theory curves are calculated based on the filter cavity parameters. The experimental data are plotted as points including an error bar. The results for the -15.15 MHz detuning case of the filter cavity is shown in red [curve (a)] and the $+15.15$ MHz detuning case in blue [curve (b)]. Note that the measured values nicely follow the curves predicted by the theory. The difference between the two detuning cases is that the quadrature rotation angle is almost the negative value of the complementary case. Thus, the sum of the data of the two different detuning cases is almost zero as predicted by theory and shown by the magenta curve (c). This is the experimental proof, that two subsequent filter cavities, symmetrically detuned from the carrier frequency ω_0 , like in this case to ± 15.15 MHz, lead to an identical phase shift of the positive and negative sidebands with respect to the carrier. As already seen in Figure 4.10, the rotation of the squeezing quadrature is completely cancelled due to the fact that the phasors at opposite sideband frequencies now all add up in the same quadrature, like in the case of frequency-independent squeezed light. The only difference is the absolute phase of the sidebands, which is irrelevant.

As a consequence, a filter cavity can be used to compensate the effect of a detuned cavity, where the squeezed field gets reflected, like in the case of GEO 600. To achieve this, a filter cavity for GEO 600 has to have the same linewidth and corresponding dispersion as the detuned SRC. In Chapter 5 an experiment using a tabletop dual-recycled Michelson interferometer, like GEO 600 but scaled down by a factor of 1000, will be described. A

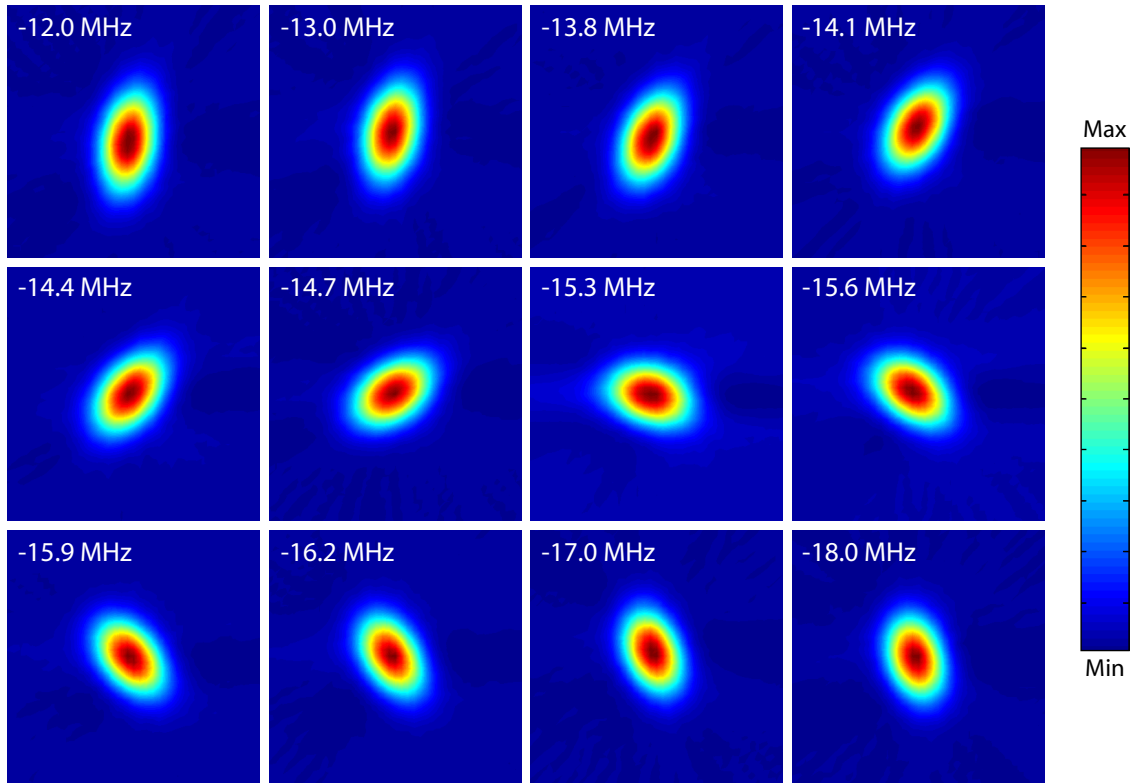


Figure 4.22: Contour plots of the Wigner functions of the frequency-dependent squeezed state for different frequencies. The detuning frequency of the filter cavity is -15.15 MHz. The Wigner functions have been normalized such that the height color encoding is the same for each plot. One can see that the squeezing ellipse is rotating clockwise starting from -12 MHz to -18 MHz.

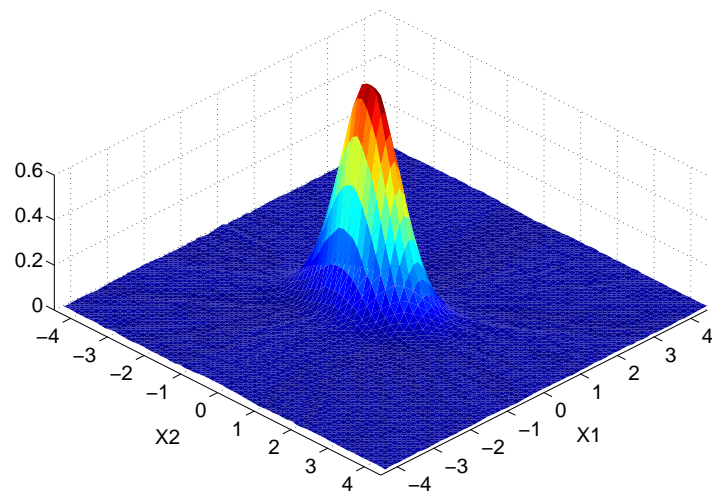


Figure 4.23: The three dimensional Wigner function of the frequency-dependent squeezed state measured at a frequency of 12 MHz and with a filter cavity detuning of -15.15 MHz

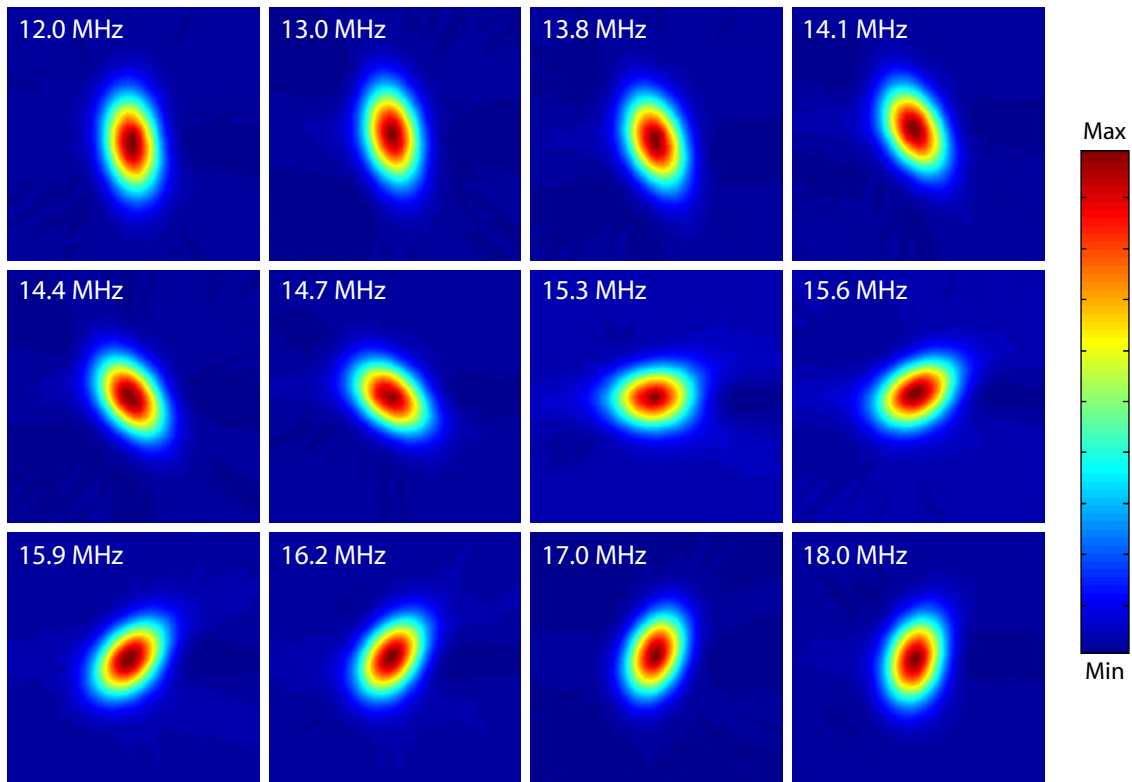


Figure 4.24: Contour plots of the Wigner functions of the frequency-dependent squeezed state for different frequencies. The detuning frequency of the filter cavity is +15.15 MHz. The Wigner functions have been normalized such that the height color encoding is the same for each plot. One can see that the squeezing ellipse is rotating counter clockwise going from low to high sideband frequencies.

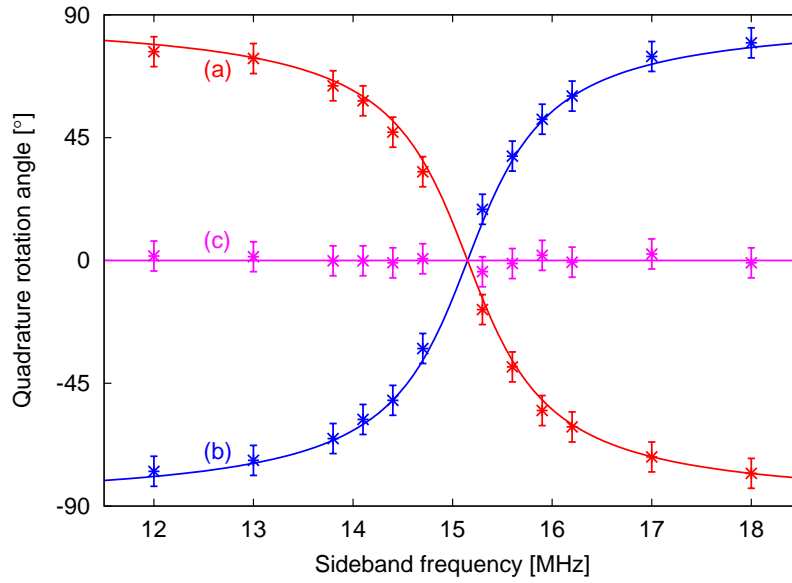


Figure 4.25: Measured rotation angles of the 24 frequency-dependent squeezing ellipses presented in Figures 4.22 and 4.24. The rotation angles for a filter cavity detuning of -15.15 MHz are shown in red [curve (a)] and for a filter cavity detuning of $+15.15$ MHz in blue [curve (b)]. The sum of these two curves is shown in magenta [curve (c)]. The rotation of the quadrature angle can therefore be compensated by reflecting the squeezed light at two detuned cavities with opposite detuning frequencies.

filter cavity is used in this experiment to compensate the rotation of the squeezing ellipse. Chapter 7, where a future upgrade from GEO 600 to the next generation GW detector GEO-HF will be presented, includes a detailed analysis of possible filter cavity topologies that can be used to eliminate the rotation of the squeezing ellipse in GEO-HF.

Chapter 5

Squeezed-light-enhanced dual-recycled Michelson interferometer

This chapter presents the experimental demonstration of a squeezed-light-enhanced dual-recycled Michelson interferometer. In 1981 Caves [Cav81] proposed increasing the sensitivity of an interferometer by using squeezed states of light. In a simple quantum noise limited Michelson interferometer the enhancement using squeezed light is comparable to using a higher laser power (see Section 4.1, Figures 4.2 and 4.3). Either an increase in laser power by a factor of four or a squeezed vacuum, with reduced noise variance by a factor of four, will result in a sensitivity enhancement of the Michelson interferometer by a factor of two.

The technique of power recycling [DHK⁺83] is used in all current Michelson interferometer based gravitational wave (GW) detectors to enhance the circulating light power. In this situation a mirror (the *power-recycling mirror*) is placed between the Michelson interferometer and the laser. In the normal operation mode of a GW detector all light coming from the laser is reflected back by the interferometer, leaving the other port of the Michelson interferometer beam splitter dark; this is the so-called *dark port*. The power recycling mirror reflects all light back to the laser thereby forming a cavity with the interferometer. This leads to an increase in the internal power of the interferometer, enhancing the sensitivity in the shot noise limited frequency range (see Equation 4.1).

Signal recycling was proposed by Meers [Mee88] to raise the sensitivity even further. Here a mirror is placed between the photodetector in the dark port and the Michelson interferometer. This mirror forms a cavity with the interferometer and enhances the signal generated by a gravitational wave by sending the signal sidebands back into the interferometer. The interaction with the end mirror test masses is increased leading to an enhanced signal strength. In contrast to the power-recycling cavity, the signal-recycling cavity is, in most cases, slightly detuned to the carrier frequency to increase the signal sidebands around a specific sideband frequency, e.g. 350 Hz as is the case in Figure 4.2. This resonance frequency can be tuned with the micro position, the so-called *tuning*, of the signal-recycling mirror. Gea-Banacloche and Leuchs [GBL87] have studied the compatibility of power recycling and squeezed field injection, and Chickarmane and Dhurandhar [CD96] have shown the compatibility of signal recycling and squeezed field injection in the shot noise limited area. This analysis has been extended by Harms *et al.* [HCC⁺03] to the radiation pressure dominated frequency range, thus showing

that all three techniques (squeezed field injection, power recycling and signal recycling) can be used to increase the sensitivity of Michelson interferometer based GW detectors simultaneously.

Experimental demonstrations of squeezed-light-enhanced interferometers are rare. A tabletop Mach-Zehnder interferometer using squeezed light [XWK87] was demonstrated in 1987. In the same year Grangier *et al.* [GSYL87] presented their results of a squeezed-light-enhanced polarization interferometer. Later, at least two of the enhancement techniques have been combined to demonstrate viable interferometers. In 1991 Strain and Meers [SM91] demonstrated the first power and signal-recycled Michelson interferometer as a tabletop setup. The combination of power and signal recycling is often called *dual recycling*. Later, Heinzl *et al.* [HSM⁺98] demonstrated a dual-recycled Michelson interferometer in a fully suspended configuration. The first squeezed-light-enhanced power-recycled Michelson interferometer [MSM⁺02] was demonstrated in 2002 with the intention to show the application of squeezed light in GW detection. Chapter 4 presents the basic idea of how squeezed light can be used in a GW detector to enhance its sensitivity. This chapter introduces the fact that formerly frequency-independent squeezed light becomes frequency-dependent after reflection at the detuned signal-recycling cavity. Future gravitational wave detectors such as Advanced LIGO [ADVa] will make use of dual recycling in combination with tuned high finesse arm cavities to increase the light power even further. In such a configuration the signal recycling technique is called *resonant sideband extraction*, because the GW signal has to be extracted from the arm cavities with the signal-extraction mirror. In Advanced LIGO, like in GEO 600, the signal-extraction and signal-recycling cavities are detuned from the carrier frequency. Thus, a filter cavity is needed to compensate for the rotation of the squeezing ellipse (see Chapter 4). The experiment described in the current chapter uses the dual-recycled Michelson interferometer configuration comparable to the one used by GEO 600. In fact, it is similar to GEO 600 only smaller by a factor of 1000. This experiment proves the optical compatibility of all three advanced interferometer techniques described above. Furthermore, it uses a read-out and control scheme, which prevents the frequency range of interest being deteriorated from modulation signals as is the case in the experiment described in the previous chapter (see Figures 4.18 and 4.19). The results of the squeezed-light-enhanced dual-recycled Michelson interferometer have been published in [VCH⁺05] and [VCH⁺06b].

This chapter is divided into four sections. First, the general optical layout of the experiment is described in Section 5.1. Here, the differences with respect to the experiments discussed earlier in this thesis are highlighted. Section 5.2 draws attention to the dual-recycled Michelson interferometer. The optical setup, the generation of error signals, and the lock acquisition will be presented in detail. Section 5.3 presents signal injection into the interferometer using a second laser. In the last section the experimental results are discussed. This includes a detailed loss estimation of the experiment and a prognosis of the allowed losses in GEO 600 to achieve an increase in the sensitivity by a factor of two by using squeezed light.

5.1 Optical layout

A schematic of the experimental optical setup can be seen in Figure 5.1. In principle this is the setup for the generation of frequency-dependent squeezed light, described earlier in Chapter 4, but extended by a dual-recycled Michelson interferometer. A further extension is the use of a second laser source to inject single sideband signals through one of the interferometer's end mirrors.

The main laser used in the experiment is a Nd:YAG laser with an output of 2 W at 1064 nm. The laser beam is split and about 1 W is used for the SHG, to produce the necessary second harmonic pump field for the OPA. The remaining power is passed through a modecleaner (see Section 3.2.2 for details). This ring cavity removes amplitude fluctuations from the beam and stabilizes the beam position. The control of the modecleaner length is achieved via a PDH locking scheme as described in Section 3.2.3. A phase modulation with a frequency of 18 MHz is chosen to derive the needed error signal for the length control of the modecleaner. The required EOM is positioned such that the SHG can also be controlled with a PDH locking scheme with the same frequency. The former control scheme of the SHG, based internal modulation has been abandoned (see Section 3.3.4). The beam that passes through the modecleaner is divided into several beams, each serving a different goal. About 50 mW are used as local oscillator and guided directly to the homodyne detector. The remaining light is phase modulated with 15 MHz. This phase modulation is used later for the power-recycling cavity control. For the OPA cavity length control a fraction of 100 mW is separated from this beam. This seed field has been increased compared to the previous experiments, because the newly used OPA crystal has a much better HR coating on its back surface, compared with the crystals used the OPAs in Chapters 3 and 4. Details on the new OPA can be found in Section 5.1.1. The remaining light available for the filter cavity and Michelson interferometer is passed again through an EOM with a modulation frequency of 134.4 MHz. This phase modulation is used to derive the error signals for the filter cavity, the differential mode of the Michelson interferometer and for the signal-recycling cavity. The overall power used for the filter cavity control is 30 mW and the complete Michelson interferometer needs 120 mW. Details on the control schemes of the filter cavity and the Michelson interferometer can be found in Sections 5.1.2 and 5.2, respectively. A Faraday isolator is used between the 134.4 MHz EOM, the filter cavity and the Michelson interferometer to circumvent any problems based on the back-reflected fields from the filter cavity or Michelson interferometer to the modecleaner. The second laser is phase locked to the main laser. Thus, a tiny fraction from the main laser is overlapped with the signal laser beam. The beat signal is sensed by a photodetector that is used to derive an error signal. The PZT of the signal laser is actuated to control its frequency. Details of the phase-locked loop (PLL) and the signal laser beam are given in Section 5.3.

The OPA generates a frequency-independent squeezed field. This is passed through a Faraday isolator, which avoids the OPA being seeded from any back-reflected light. A quarter-wave plate transforms the initial s-polarized beam into a circular polarized beam, before it is mode matched to the filter cavity. From this side the filter cavity is an overcoupled cavity and the squeezing gets reflected at the detuned locked filter cavity with only small losses. The detuning frequency of the filter cavity is chosen to be

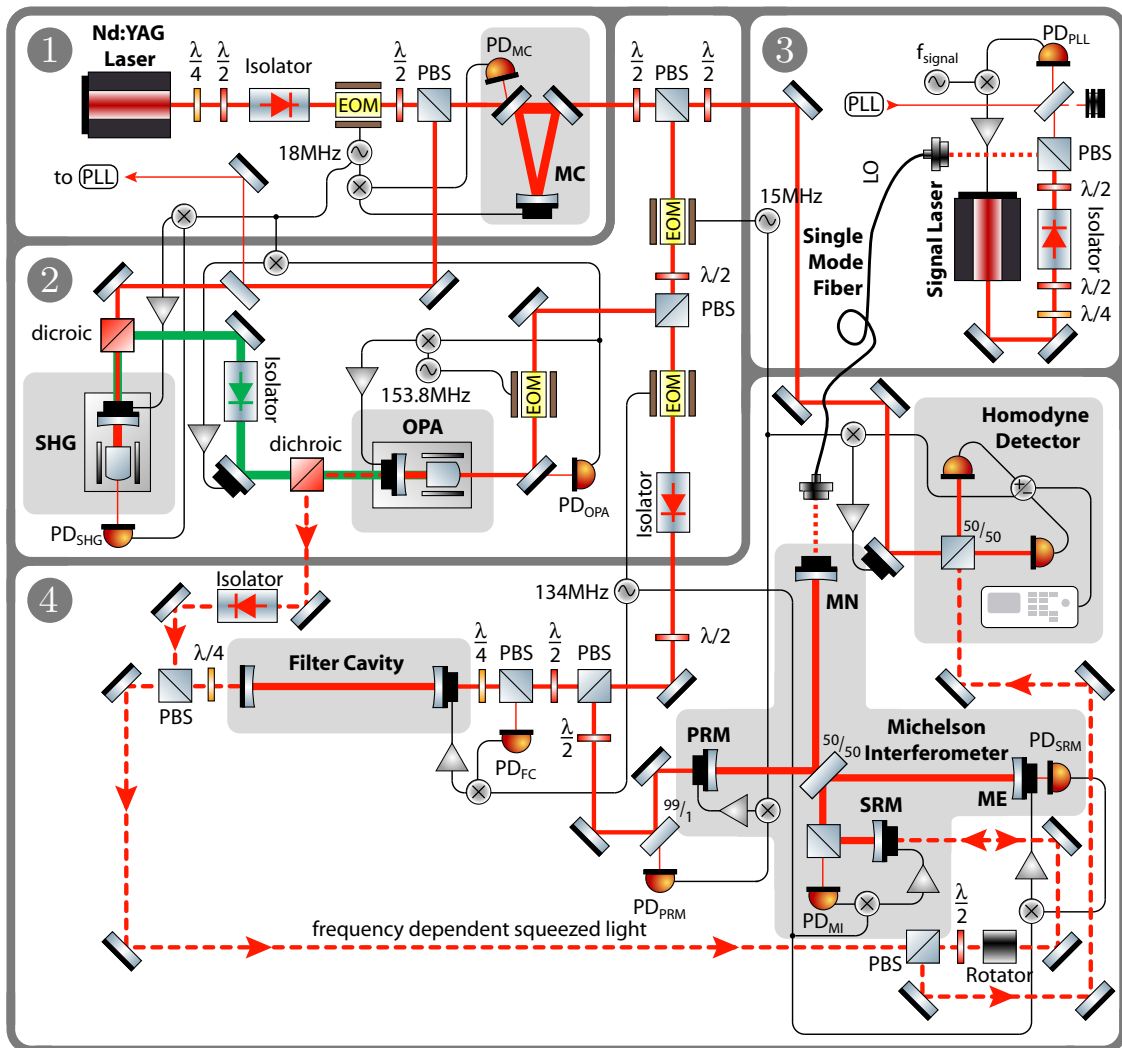


Figure 5.1: Schematic of the optical layout of the squeezed-light-enhanced dual-recycled Michelson interferometer experiment. The layout is divided into four sections. The first section is the laser preparation stage and contains the main Nd:YAG laser and the mode cleaner. The second stage contains the two nonlinear cavities. The SHG produces the required harmonic pump field to generate the squeezing in the OPA. The signal laser is contained in the third section. This is phase locked to the main laser and runs on a different but tunable laser frequency. This second laser field is used to measure the SNR improvements and the signal transfer function of the dual-recycled Michelson interferometer. This interferometer and the corresponding filter cavity are located in the fourth section of the optical layout. The squeezed field generated inside the OPA is first reflected at the filter cavity before it is reflected at the signal-recycling cavity. A Faraday rotator is used to guide this field into the homodyne detector. EOM: electro-optical modulator; SHG: second harmonic generator; OPA: optical parametric amplifier; MC: mode cleaner; PBS: polarizing beam splitter; LO: local oscillator; PRM: power-recycling mirror; SRM: signal-recycling mirror; MN: north end mirror; ME: east end mirror.

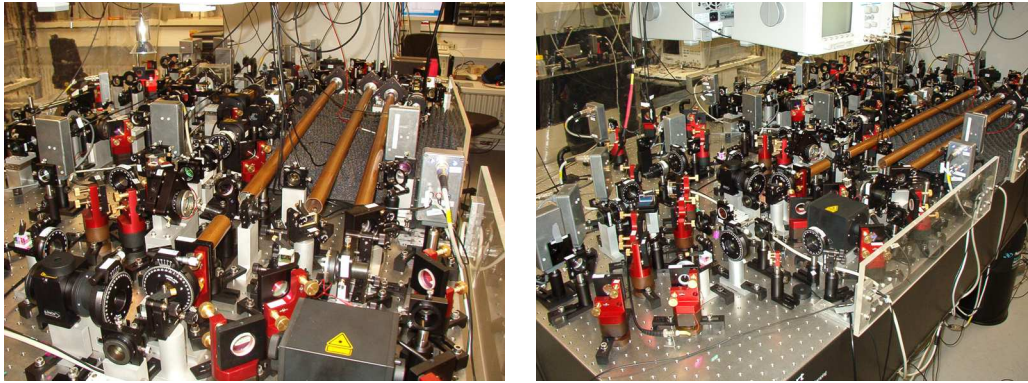


Figure 5.2: Two photographs of the optical table containing the squeezed-light-enhanced dual-recycled Michelson interferometer experiment. The left-hand picture is taken from the direction of the south port. On the lower end one can see the Faraday rotator that is used to guide the reflected squeezed field from the signal-recycling cavity to the homodyne detector. In the center of the picture, one can see three copper tubes. These mark from left to right the filter cavity and the interferometer’s north and east arm. On the lower end of the north arm one can identify the interferometer’s beam splitter, whereas at the lower end of the east arm mirror one can see the folding mirror. The right-hand picture shows the experiment in total. On the left border one can identify the two tilted homodyne photodetectors.

-10 MHz with respect to the carrier frequency. The back-reflected squeezed field from the filter cavity is frequency-dependent now (see Section 4.1). This frequency-dependent squeezed field is passed through a faraday rotator before it is mode matched into the signal-recycling cavity of the dual-recycled Michelson interferometer. A half-wave plate ensures that the squeezed field is s-polarized before it enters the signal-recycling cavity. The signal-recycling cavity is detuned to a frequency of $+10$ MHz with respect to the carrier frequency. From Section 4.4.3 we know that the detuning frequency with the opposite sign compared to the filter cavity detuning frequency, now cancels the frequency dependence of the squeezed field. The back-reflected squeezed field from the signal-recycling cavity passes the Faraday rotator again and is guided to the homodyne detector. Details on the homodyne detector can be found in Section 5.1.3. The complete setup of the experiment can be seen in the photos in Figure 5.2.

The following subsections discuss in detail the changes to the OPA, filter cavity and the homodyne detector in comparison to the former experiments. The new components of the setup, the dual-recycled Michelson interferometer and the signal laser including the PLL, are described in Sections 5.2 and 5.3.

5.1.1 OPA

The OPA used for this experiment is based on an intermediate step between the MK I and the MK II design described in Section 3.3.3.2. The cavity design is hemilithic, meaning the $\text{MgO}:\text{LiNbO}_3$ back surface forms one end mirror and a separate outcoupling mirror is used as the second end mirror of the cavity. This outcoupling mirror is located in a separate

six-axis mirror mount¹. This separation into two parts—on the one hand the outcoupling mirror mount and on the other the nonlinear crystal housed in the oven—is based on the MK I design. The new part, taken from the MK II design is the heating system. The former resistor-based heating system has been replaced by two high temperature compatible peltier elements. These peltier elements allow active heating and cooling of the crystal. They are located close to the crystal as well as the NTC sensor measuring the actual temperature. The relocation of the NTC sensor in combination with the peltier elements allows a much faster temperature feedback, which leads to an overall improvement of the conversion stability of the OPA. The MK II design of the oven is described in more detail in Section 3.3.3.2.

The crystal of the OPA is also changed compared to the experiments presented in in Chapters 3 and 4. The most important change is the increase of the MgO doping from 5% to 7%. This affects the phase matching temperature, which dropped to about 60°C. The crystal dimensions are $2 \times 6.5 \times 2.5$ mm (length \times width \times depth) with respect to the orientation shown in Figure 3.14. The flat surface is anti-reflection (AR) coated for both wavelength's used with the corresponding power reflectivities of $R_{532\text{ nm}} < 0.2\%$ and $R_{1064\text{ nm}} < 0.05\%$. The crystal's back surface has a radius of curvature RoC=8 mm. It has a high reflective (HR) coating for both wavelengths with specified power reflectivities of $R_{532\text{ nm}} < 99.90\%$ and $R_{1064\text{ nm}} < 99.97 \pm 0.02\%$. It turns out, that the HR coating of the crystal's back surface for 1064 nm is higher than the desired specifications. From separate transmission measurements and the measured finesse values, the power reflectivity is found to be approximately $R_{1064\text{ nm}} < 99.996\%$. Compared with the specified value, the transmission is reduced by a factor of ten. This made it much more difficult to generate a reasonable error signal for the cavity length via the reflected seed field. Hence, the seed field power has to be increased to about 100 mW. The outcoupling mirror has a radius of curvature of RoC=25 mm and is separated from the crystal's flat surface by about 23 mm. It uses an HR coating for 1064 nm ($R_{1064\text{ nm}} = 96.7\%$) to form a cavity with a finesse of about $\mathcal{F} = 130$. From these values a free spectral range of 4 GHz and a linewidth of 23.5 MHz can be calculated. The coating for 532 nm is anti-reflective and has a power reflectivity of $R_{532\text{ nm}} < 0.2\%$ which ensures that the harmonic pump field only double passes the OPA cavity.

The control scheme of the OPA is shown in Figure 5.3, where an EOM imprints a phase modulation on the seed field at a frequency of 153.8 MHz. This enables the use of a PDH locking scheme for the OPA cavity length. The reflected seed field from the cavity is detected with a photodiode (PD_{cav}). The error signal is generated in a mixer and evaluated and transformed by a servo, before it is passed through an HV-amplifier and fed back to the outcoupling mirror's PZT. The relative phase between the fundamental seed and the harmonic pump field determines the quadrature angle of the squeezing quadrature. This has to be stabilized as well. The required error signal is derived by using the phase modulation sidebands which are imprinted on the harmonic pump field (see Figure 5.1). These phase modulation sidebands are transformed into an amplitude modulation of the generated fundamental field. This field is sensed on the rear side of the OPA cavity by a separate photodiode (PD_{phase}). The error signal is generated the same

¹manufacturer: Thorlabs; type: K6X

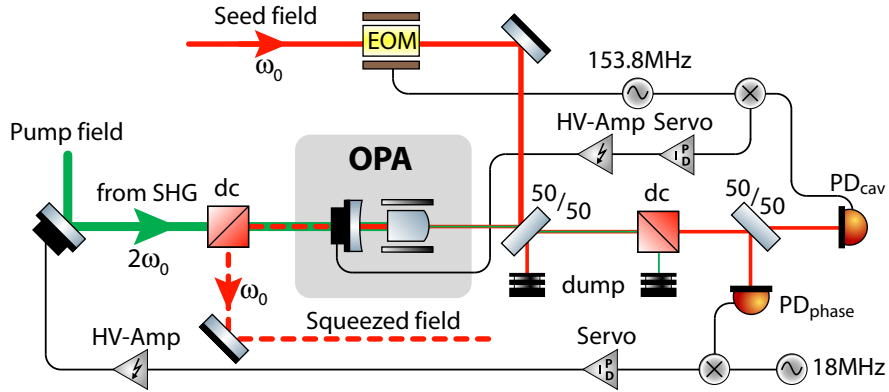


Figure 5.3: Layout of the OPA's control scheme. The seed field is phase modulated at 153.8 MHz with an EOM and coupled into the OPA through the back surface of the nonlinear crystal. From the other side the harmonic pump field is coupled through the outcoupling mirror into the OPA. This harmonic pump field carries phase modulation sidebands at 18 MHz. The field leaving the OPA through the crystal's back surface is separated by a 50/50 beam splitter from the incoming seed field. Another beam splitter is used to detect this field with two photodetectors. One is used to generate the needed error signal for the cavity length, whereas the other is needed to obtain an error signal for the relative phase between the harmonic pump field and the fundamental intra-cavity field. This determines the squeezing angle of the generated squeezed field.

way as described above and fed back to a PZT-mounted mirror in the beam path of the harmonic pump field.

5.1.2 Filter cavity

The filter cavity is used in this experiment to transform the initially frequency-independent squeezed light into frequency-dependent light (see Sections 4.1.4 and 4.1.3 or details). A schematic of the optical setup and the control scheme is presented in Figure 5.4. The filter cavity is a linear cavity with a length of $L = 1.205$ m. This length is chosen to match the filter cavity to the length of the signal-recycling cavity. The resulting free spectral range (FSR) is $f_{\text{FSR}} = 124.4$ MHz. The mirror reflectivities are chosen to be $R_1 = 90\%$ and $R_2 = 99.92\%$ such that the filter cavity is overcoupled looking from the side of the squeezed field. These are the same reflectivities used in the signal-recycling cavity to ensure that both cavities have the same physical properties. The control beam gets phase modulated with a frequency of $f_m = 134.4$ MHz. It passes a quarter-wave plate which turns the initially p-polarized control beam into a circularly polarized beam. The transmitted beam passes a quarter-wave plate behind the filter cavity again and is then guided to the OPA. To ensure that this control field for the filter cavity does not seed the OPA from this side, a Faraday isolator is placed between the OPA and the filter cavity. The back-reflected field at the filter cavity passes the first quarter-wave plate again and is thereby separated from the incoming beam with a polarizing beam splitter (PBS) before being detected with a photodiode (PD_{FC}). A demodulation of the photocurrent with the modulation frequency f_m results in an error signal. This is evaluated by a servo, passed through a HV-amplifier and fed back to the PZT-mounted cavity mirror. The special

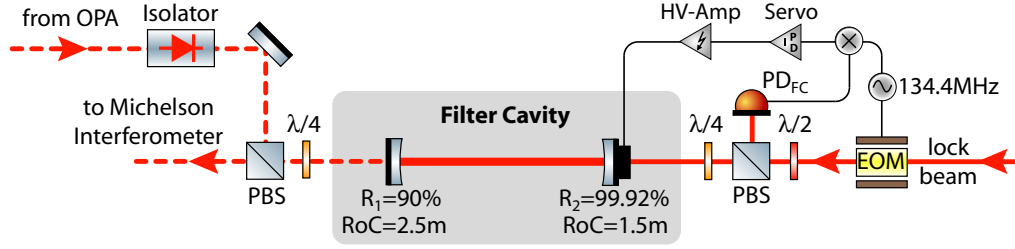


Figure 5.4: Layout of the filter cavity’s control scheme. The filter cavity is composed of two spherical mirrors. Its length control is achieved with the lock beam coming from the right. This beam is phase modulated with a frequency of 134.4 MHz. This frequency allowed locking the cavity to a sideband frequency of ± 10 MHz beside the carrier frequency due to the fact that the free spectral range is 124.4 MHz. Another feature of this control scheme is that no modulation peaks are visible in spectra around 10 MHz. The error signal was generated by detecting the reflected beam from the filter cavity. The separation between the incoming and outgoing beam was accomplished by a combination of a PBS and a quarter-wave plate. On the other side of the filter cavity such a combination of a PBS and a quarter-wave plate was used to reflect the initially frequency-independent squeezed field at the filter cavity and guide it towards the Michelson interferometer. A Faraday isolator between the filter cavity and the OPA was used to avoid any transmitted light from the locking beam seeding the OPA from this side.

feature of this control scheme is that the modulation frequency is larger than the FSR of the filter cavity. In principle this results in the same error signal as if the frequency $f_m = 10$ MHz has been chosen. The advantage of the used locking scheme is that the desired detection band of 5–15 MHz is not deteriorated by a 10 MHz modulation peak, however it is still possible to stabilize the filter cavity at the carrier frequency or at a sideband frequency $\pm f_m$. Figure 5.5 compares the measured error signal with a simulation made with the program FINESSE [Fre]. The measurement reveals the same error signal as predicted by the simulation. In the measured data a different transverse mode other than the TEM_{00} mode is present, which shows the non-optimal mode matching of the control beam into the cavity. This other mode can be neglected because it is reflected directly at the filter cavity and does not disturb the experiment. The more important mode matching is that of the squeezed beam into the filter cavity from the other side. This is measured to be better than 95%, which contributes directly to the losses of the squeezed field. Looking at losses to the squeezed beam in the area concerned with the filter cavity, one has to consider the Faraday isolator between the OPA and the filter cavity. This component caused a transmission loss of 6% to the squeezed beam. Another loss source is the transmission of the squeezed field through the filter cavity. Although the cavity is strongly overcoupled, the transmission losses are calculated to be 3%.

The filter cavity is normally locked to a sideband frequency of $-f_m$, which corresponds to a strong phase shift of the reflected field around a sideband frequency of -10 MHz. The reflection of the initially frequency-independent squeezed field at the detuned filter cavity makes the squeezed field frequency-dependent before it is guided to the signal-recycling mirror of the dual-recycled Michelson interferometer.

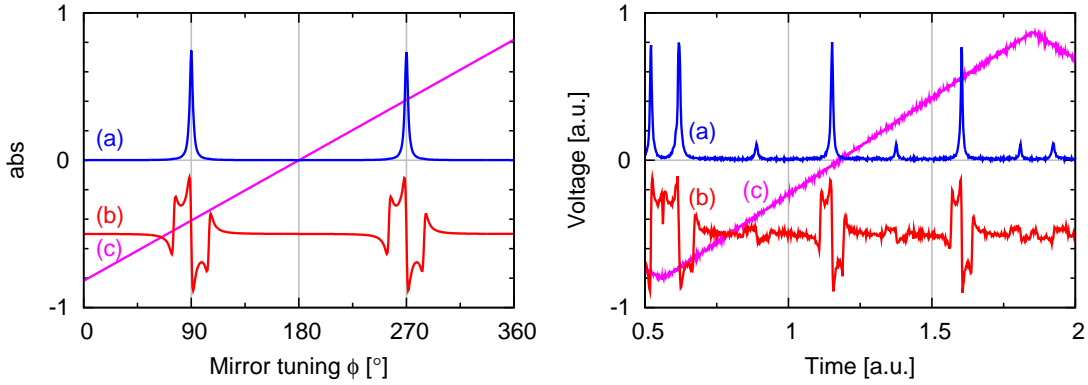


Figure 5.5: Comparison of the simulated (left) and measured (right) transmission and error signal of the filter cavity. The measured transmission of the filter cavity [blue curve (a)] shows that the mode matching of the locking beam into the filter cavity is not optimal. Nevertheless, the error signal [red curve (b)] does match the simulated signal and provided a nice starting point for a stable control. The ramp applied to the PZT of one of the filter cavity’s mirrors is displayed as the magenta curve (c).

5.1.3 Homodyne detector

The homodyne detector used in this experiment is composed of two electronically matched photodetectors. The electronic circuit can be found in Appendix C.4; the transfer function of these photodetectors is shown in Figure 5.6. The bandwidth of the photodetectors is approximately 45 MHz. The photodiodes used in these detectors are Epitaxx ETX1000 with a diameter of 1 mm. They have a quantum efficiency of $93 \pm 3\%$, and are tilted to the brewster angle with respect to the incoming beam, and the maximally detectable light power of each detector is 50 mW. The reason for this high detectable power is that the homodyne photodetectors are also used for aligning the dual-recycled Michelson interferometer. The maximally used power for the Michelson interferometer in s-polarization is 100 mW, which corresponds with the limit of the photodetectors (see Section 5.2 for details). The lack of photodetector sensitivity makes the use of 50 mW as local oscillator power inevitable for the measurements performed in order to achieve a reasonable signal to dark noise ratio. For the alignment of the homodyne visibility, the OPA is locked without the harmonic pump. The filter cavity and the signal-recycling cavity are blocked so that the beam coming from the OPA got reflected at the cavity mirrors without interacting with the cavities. This beam is overlapped with a local oscillator beam of the same intensity and the resulting interference fringes are maximized. The achievable homodyne visibility is about 97.5%, which corresponds to a homodyne mode matching efficiency of 95%. The control of the homodyne detector angle is achieved with the same method as described in Section 3.4.1 and Figure 3.26. The only difference is that a modulation frequency of 18 MHz present on the squeezed field is used to control the homodyne detection angle.

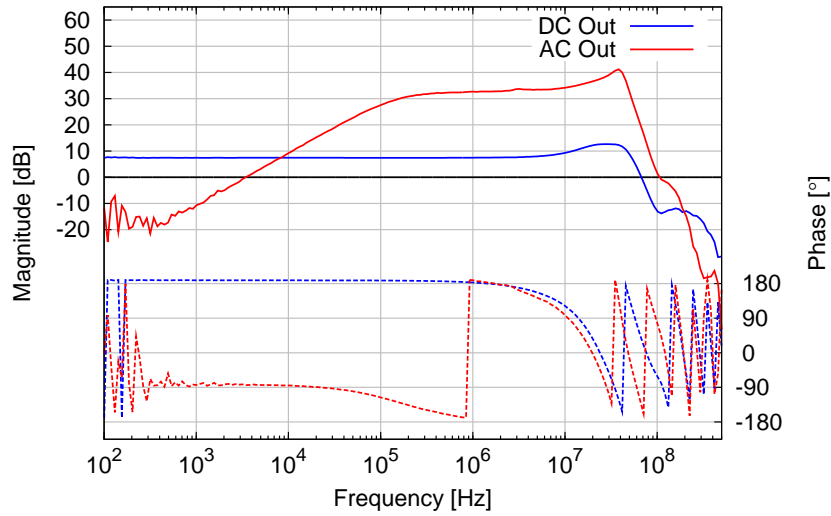


Figure 5.6: Transfer function of one of the homodyne detector photodiodes. The solid red and blue curves show the magnitude of the DC and AC output of the photodiode. The dashed curves with the same color show the corresponding phases. The DC output is in principle located directly behind the transimpedance amplifier. The AC output is a high pass filtered and amplified version of the DC output. The bandwidth of the homodyne detector is measured to be about 45 MHz. The schematics of the photodetectors can be found in Appendix C.4.

5.2 The dual-recycled Michelson interferometer

The optical layout of the dual-recycled Michelson interferometer is displayed in Figure 5.7. Its parameters are selected in such a way that the interferometer fits easily on an optical table with a dimension of $1.2 \times 2.4 \text{ m}^2$, together with the optics related to production and detection of squeezed light. However the development of a locking scheme for the dual-recycled Michelson interferometer becomes easier with longer optical path length inside the interferometer. The longer the arm length of the interferometer, the lower the FSR of the power-recycling and signal-recycling cavities. The desire not to have any modulation peaks in the detection band from 5–15 MHz makes it indispensable to use modulation frequencies shifted by at least one FSR with respect to the carrier frequency. Hence, a tradeoff between these two incompatibilities had to be made. Consequently, an arm length of 1 m for the Michelson interferometer is chosen.

The control method of the Michelson interferometer is based on phase-modulation sidebands imprinted on the incoming beam by an EOM. This type of modulation for the control is often called Schnupp modulation [Sch88]. It requires an arm length difference of the interferometer such that the relative phase of the light field returning from the arms of the interferometer depend on the frequency of the light. As a result, even if the south port of the interferometer is dark for the carrier frequency, it can be bright for the phase modulation frequency. Hence, the modulation sidebands can sense the position of the signal-recycling mirror or the information about the dark port condition can be send into the south port of the interferometer. The difference in arm length is called *Schnupp asymmetry*. Figure 5.8 shows the frequency-dependent transmission of a

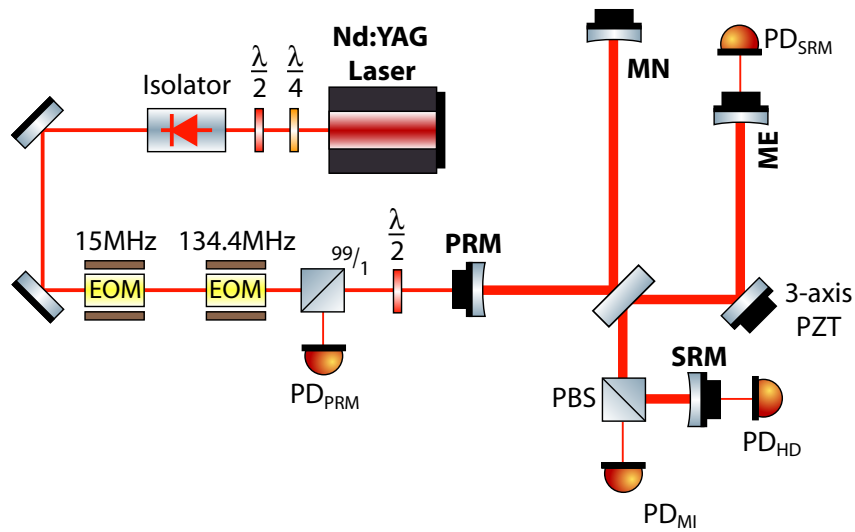


Figure 5.7: Schematic of the optical layout of the dual-recycled Michelson interferometer. Two EOM's are used to provide the phase modulation sidebands needed to control the three degrees of freedom of the dual-recycled Michelson interferometer: the length of the power-recycling cavity, the length of the signal-recycling cavity, and the differential arm length of the interferometer. A folding mirror in the east arm is used to co-align the two interferometer arms to fit the interferometer on the optical table. A PBS is used in the south port of the interferometer to separate the two orthogonal polarization modes. The s-polarization is resonant inside the signal-recycling cavity, whereas the p-polarization was used to generate an error signal for the differential arm length of the interferometer independent of the signal-recycling mirror position. The four photodetectors displayed in the schematic are used to align and lock the dual-recycled Michelson interferometer. EOM: electro-optical modulator; PBS: polarizing beam splitter; PRM: power-recycling mirror; SRM: signal-recycling mirror; MN: north end mirror; ME: east end mirror.

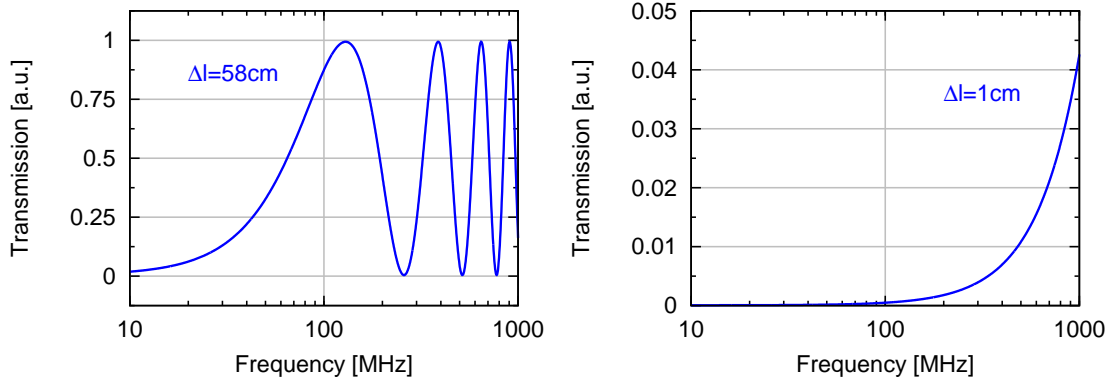


Figure 5.8: Comparison of the frequency-dependent transmission from the input of the Michelson interferometer into the south port for different Schnupp asymmetries of the interferometer arms. The left-hand figure shows the resulting transmission into the south port of the interferometer for an arm length difference of the two interferometer arms, the *Schnupp asymmetry*, of 58 cm. Note, that for small sideband frequencies the south port is dark. With rising sideband frequency the transmission rises and reaches unity at frequencies around 130 MHz. The figure on the right-hand side shows the same plot for a Schnupp asymmetry of 1 cm. One can see that the transmission around 130 MHz is the order of 10^{-3} . The optimal Schnupp asymmetry for the control scheme would have been 58 cm, in which case the modulation sidebands of 134.4 MHz would resonate optimally in the signal-recycling cavity. However, a Schnupp asymmetry of about 1 cm is chosen to optimize the mode overlap of the beams propagating in the arms on the Michelson interferometer’s beam splitter, although the transmission of the 134.4 MHz modulation sidebands is much worse compared to the optimal case.

light field injected into the interferometer at the south port. The difference between the two plots is a different Schnupp asymmetry. In the left plot the Schnupp asymmetry is chosen to be 58 cm which results in a very good transmission from the entrance of the interferometer into the south port for frequencies around 130 MHz. The plot on the right-hand side uses a Schnupp asymmetry of only 1 cm. One can see that the transmission in the same frequency range is reduced largely. The first maximum of the transmission in this case is found at a frequency of 7.5×10^9 Hz. The transmission in the frequency range of 130 MHz is the order of 10^{-3} . Nevertheless, a Schnupp asymmetry in the order of 1 cm is selected to maximize the mode overlap on the interferometer beam splitter of the two beams returning from the arms. A larger Schnupp asymmetry would lower the Michelson interferometer fringe visibility and result in a non-dark south port.

The power-recycling and signal-recycling cavities have the same length. A distance of 0.2 m between each recycling mirror and the Michelson interferometer beam splitter fixes the total length of the recycling cavities to about 1.205 m. The resulting FSR is then calculated to be 124.4 MHz. The selection of recycling mirror reflectivities depends on the frequency range of interest for the latter measurements. The desired signal recycling frequency is 10 MHz. Together with the constraint that the OPA starts producing squeezed states above a sideband frequency of 3.5 MHz, the frequency range from 5–15 MHz is chosen. To see the full effects of the signal-recycling cavity in the signal transfer function, the linewidth of the signal-recycling cavity should be about 2 MHz. The end mirror

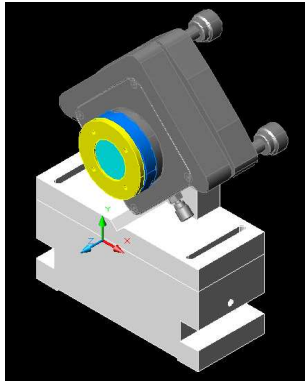


Figure 5.9: CAD model of the six-axis mirror mounts with the embedded PZT to actuate the longitudinal position of the interferometer mirrors. The basic mirror mount is a K6X made by Thorlabs. A custom-made brass counterweight is attached to this mirror mount. The mirror and the PZT are embedded into this counterweight and this stack is compressed by an aluminum cap. Increasing the tension can be used to shift the first PZT resonance to higher frequencies.

reflectivity is supposed to be highly reflective but should also allow the transmitted fraction to be large enough for monitoring the interferometer conditions and for generation of an error signal. Consequently, the interferometer end mirror reflectivity is selected to be 99.92% and the reflectivity of the two recycling mirrors is 90%. This results in a linewidth of 2.1 MHz and a finesse of 59 for the power-recycling and signal-recycling cavities. The radius of curvature (RoC) of the mirrors are selected such that the cavity waist would lie in the arms but closer to the beam splitter than to the end mirrors. As a result, the radii of curvature are chosen to be: $\text{RoC}_{\text{end}} = 1.5 \text{ m}$ for the end mirrors and $\text{RoC}_{\text{recycling}} = 2 \text{ m}$ for the recycling mirrors. The arising waist has a radius of approximately $450 \mu\text{m}$. All interferometer mirrors are housed in six-axis mirror mounts with a custom-made inlay. This inlay is made out of brass and acts as a counterweight for the embedded PZT². A CAD diagram of this mirror mount and the included PZT is presented in Figure 5.9.

Figure 5.7 shows a PBS placed into the south port of the interferometer. A combination of three polarizing beam splitters is used to achieve a high suppression of p-polarized light reaching the signal-recycling mirror. By using the PBS the p-polarized mode can be detected with a separate photodiode; this polarization does not interact with the signal-recycling mirror. This is important for the locking scheme as we will see in Section 5.2.2. The power ratio between the s- and p-polarization mode could be adjusted with a half-wave plate in front of the Michelson interferometer and is chosen to be 100mW in s-polarization and 20 mW in the p-polarization mode.

Figures 5.7 and 5.2 also show that the classical orientation of the two interferometer arms with a 90° adjacent angle is not used due to limited space on the optical table. Instead, the east arm of the interferometer has been folded such that the north and east arm are orientated in parallel to each other. The folding mirror is placed in a three-axis PZT enhanced mirror mount³. This mirror mount houses three PZT's that can be used

²Manufacturer: Piezomechanik, Type: HPSt 500/15-8/5

³Manufacturer: Thorlabs, Type: KC1-PZ/M

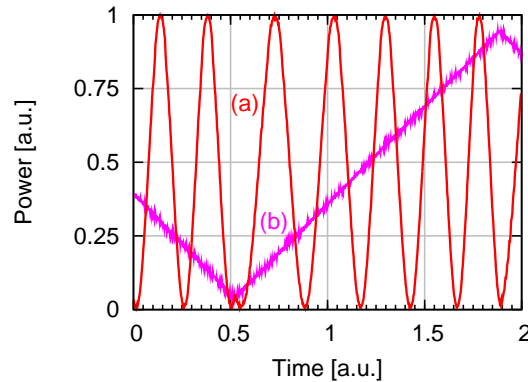


Figure 5.10: Measured visibility of a simple Michelson interferometer. Curve (a) shows the intensity on one of the homodyne detector photodiodes, while a ramp [curve (b)] is applied to one of the end mirrors PZT, changing the differential arm length of the interferometer.

for fine adjustment of the Michelson interferometer’s fringe visibility with high accuracy. The alignment of the dual-recycled Michelson interferometer is described in the next section. Afterwards, we will focus on the generation of the error signals for the three degrees of freedom of the interferometer.

5.2.1 The alignment of the squeezed field into the filter cavity and Michelson interferometer

Alignment of the experiment is not automated by any auto-alignment control and has to be maintained manually on a daily basis. The main goal of the alignment is not only to have an optimally adjusted dual-recycled Michelson interferometer, but also involves the alignment of the mode matching of the squeezed field into the filter cavity, signal-recycling cavity, and into the homodyne detector. Therefore the interferometer has to be mode matched to the filter cavity as well as the homodyne detector. The challenge here is not to misalign already aligned elements while working on a different mode matching or alignment.

Alignment starts with a simple Michelson interferometer without any recycling. Hence, the power- and signal recycling mirrors have to be removed. Tilting these mirrors is not sufficient because of the tiny beam displacement caused in transmission of a tilted glass plate. The end mirrors of the simple Michelson interferometer are moved differentially by applying a ramp to the two end mirror PZTs. The resulting Michelson fringes are checked with one of the homodyne photodetectors. The coarse alignment of the arms is achieved by adjusting the two six-axis end mirror mounts⁴. For fine adjustments the folding mirror mount in the east arm is used. This folding mirror is a three-axis PZT enhanced mirror mount⁵, which allows an adjustment by applying a voltage to the PZTs. A three-axis PZT controller is used to manually align the Michelson interferometer fringe visibility remotely and achieved a maximally value of 99.9%, see Figure 5.10 as an example of a measured

⁴Manufacturer: Thorlabs, Type: K6X

⁵Manufacturer: Thorlabs, Type: KC1-PZ/M

Michelson interferometer fringe visibility. Multiple apertures are used in the incoming beam path from the modecleaner and also in the beam path to the homodyne detector to ensure that the alignment does not drift from day to day into a specific direction. After the alignment of the simple Michelson interferometer, the power-recycling mirror is integrated into the setup. The power-recycling cavity alignment is obtained by holding the differential arm length of the interferometer such that the dark fringe condition is fulfilled while ramping the position of the power-recycling mirror. Without deteriorating the alignment of the interferometer fringe visibility, the power-recycling mirror is the only mirror that may be adjusted. Hence, the same six-axis mirror mount, as for the end mirrors with the custom-made inlay including a PZT for longitudinal position changes of the mirror, is used as shown in Figure 5.9. The mode matching quality of the incoming beam into the power-recycling cavity can be seen in Figure 5.11. Despite the TEM_{00} mode there is a tiny fraction of one other transverse mode remaining.

The next step is the alignment of the signal laser. The optical layout of its injection into the interferometer and more details are presented in Section 5.3. For the alignment of the signal injection, the main input beam of the Michelson interferometer is blocked. Now the only input into the interferometer is the signal laser entering through the north end mirror of the interferometer. The power-recycling mirror is ramped and the differential arm length is adjusted to keep the interferometer on the dark fringe condition. A part of the light inside the power-recycling cavity is then transmitted onto the photodiode PD_{PRM} (see Figure 5.7), which is normally used for locking and control of the power-recycling cavity. Due to the fact that the signal laser has to be transmitted through three mirrors, of which two have a reflectivity of more than 99%, the power of the signal laser has to be increased during the alignment to about 100 mW to see a nominal signal on the photodiode. Two lenses and a steering mirror set in the beam path of the signal laser in front of the north end mirror are used to match the mode of the incoming laser beam to the mode of the interferometer.

Now that we have a fully aligned power-recycled Michelson interferometer, this has to be matched to the filter cavity. The reasoning behind this is that if the squeezed beam is mode matched to the filter cavity, and the power-recycled Michelson interferometer is matched to the filter cavity, then the squeezed beam is also matched to the power-recycled Michelson interferometer. To align the Michelson interferometer to the filter cavity, the interferometer has to be locked to a point where some power is emitted through the normally dark south port. For this reason the interferometer can be locked with the DC signal of PD_{MI} (see Figure 5.7) to a point such that the output power of the interferometer into the south port is 10 mW. The filter cavity control beam is blocked and the mode matching of the interferometer output beam is controlled with photodiode PD_{FC} (see Figure 5.1). The mode matching of the interferometer beam into the filter cavity can be optimized to a value of 98.3% with some steering mirrors in between. Afterwards the filter cavity control beam is matched into the aligned filter cavity from the other side. To match the outgoing beam of the OPA into the filter cavity, the OPA is locked to amplification, which resulted in a beam power of a few mW. This beam is then mode matched to the filter cavity with steering mirrors and lenses in the beam path between the OPA and the filter cavity. The quality of the mode overlap is controlled with PD_{FC} ; hence the orientation of the quarter-wave plate on the side where the OPA beam enters

the filter cavity has to be changed. After the successful alignment of the squeezed beam to the filter cavity with a mode matching better than 95%, this wave plate has to be turned to its original setting. Here, it is very important to control the angle of the quarter-wave plate with the transmitted filter cavity control beam. Only if the alignment is optimal, the transmitted filter cavity control beam is not guided towards the Michelson interferometer and is also not guided towards the OPA after passing the Faraday isolator. In the first case if the filter cavity control beam is guided towards the interferometer it would be superimposed with the squeezed field, thereby diminishing the maximum amount of squeezing achievable. In the second case if the filter cavity control field enters the OPA from the backside this would result in a deteriorated squeezing performance as well. For this reason the Faraday isolator removes all the parts of the filter cavity control beam from the critical beam paths.

The squeezed beam is now aligned to the filter cavity and into the power-recycled Michelson interferometer. What remains is the integration of the signal-recycling mirror. Its alignment is achieved with the outgoing OPA beam locked to amplification. The beam path between the power-recycling mirror and the beam splitter of the interferometer is blocked, transforming the interferometer into a power-recycled interferometer from the other side. A highly sensitive photodiode is used in transmission of the east end arm mirror to check the alignment quality. The only element which is able to be used for the alignment was the signal-recycling mirror mount itself. Hence, again the six-axis mirror mount with the embedded PZT for longitudinal position control is used (Figure 5.9). The mode matching efficiency of the squeezed beam into the signal-recycling cavity was measured to be 95%.

Finally the squeezed beam has to be overlapped with the local oscillator beam on the homodyne beam splitter. Thus, the OPA is locked without the pump and the filter and signal-recycling cavity are blocked. Then the beam coming from the OPA is guided into homodyne detector. A steering mirror set and a pair of lenses in the local oscillator path are used to maximize the homodyne visibility up to 95%. The whole experiment is then completely aligned and measurements could be taken.

5.2.2 Generation of error signals for the dual-recycled Michelson interferometer

The generation of error signals is always a crucial part of operating such a complex device as a dual-recycled Michelson interferometer. In total there are three degrees of freedom to be controlled: the interferometer's differential arm length, and the length of the power-recycling and signal-recycling cavities. The problem is to generate three linearly independent error signals. For a good guideline for generation of linearly independent error signals, the reader is referred to [Thü04].

Initially, it was planned to use only Schnupp modulation sidebands for the control of the dual-recycled Michelson interferometer, meaning phase modulation sideband imprinted on the control beam before it enters the interferometer. In total two modulation frequencies were needed to generate the three individual error signals. In Figure 5.7 one can see that two EOM's are used to generate phase modulation sidebands on the interferometer control beam with frequencies of 15 MHz and 134.4 MHz. The first plan of the

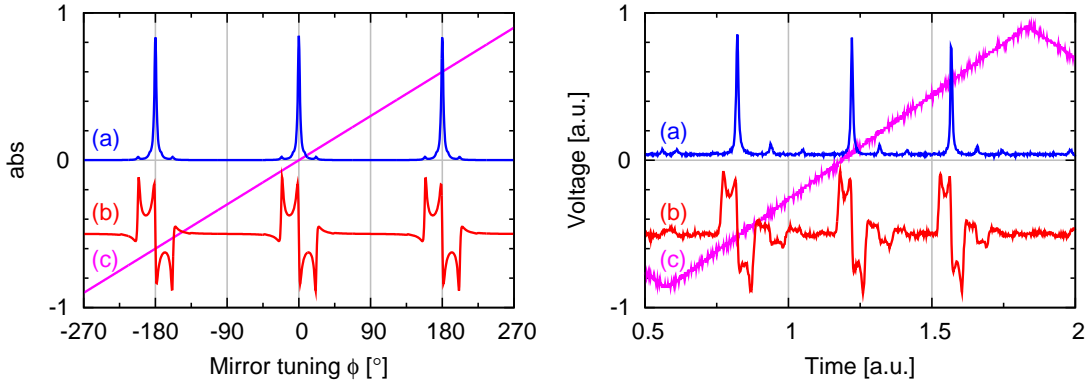


Figure 5.11: Comparison of the simulated transmission and error signal of the power-recycling cavity with the real ones. The figure on the left shows the simulated transmission [blue curve (a)] and error signal [red curve (b)] of the power-recycling cavity. The figure on the right shows the measured signals. One can see a very good agreement between the two. The ramp applied to the PZT of the power-recycling mirror is displayed as the magenta curve (c).

interferometer control included a third modulation frequency of 124.4 MHz for the control of the differential arm length. This frequency and the needed EOM were discarded due to the fact that the generated error signal was strongly dependent on the position of the signal-recycling mirror and also was too small to enable a stable control. The only solution to enhance this error signal would have been an increase in the Schnupp asymmetry of the interferometer arms. The resulting increase in the minimum dark port power due to the mode mismatch between the two arms did not allow good measurements. Consequently another control scheme based on a different polarization mode was chosen and is explained later in this section.

The first error signal to be generated is that for the power-recycling cavity. If the differential arm length is at its operating point then the south port of the interferometer is dark and the control beam entering the interferometer is reflected back to the power-recycling mirror. In this situation the power-recycling cavity, formed by the power-recycling mirror and the Michelson interferometer, can be estimated with a normal linear cavity. Hence, a standard PDH control can be used to stabilize the length of the power-recycling cavity. The 15 MHz modulation sidebands are sensed in reflection with a photodiode (see PD_{PRM} in Figure 5.7). The resulting error signal is compared to that predicted by theory in Figure 5.11. Note, that all simulated data are generated with the frequency domain interferometer simulation software FINESSE [Fre]. Both plots in Figure 5.11 show a nice PHD type error signal with steep slopes at the resonance frequency and around the modulation frequency. This error signal is used to lock the power-recycling cavity length to the laser's carrier frequency. To see that this generated error signal is almost independent of the position of the interferometer's end mirror, a surface plot of the error signal is presented in Figure 5.12. The x-axis shows the tuning of the power-recycling mirror, the y-axis the tuning of the east end arm mirror (ME). The operation point is shown in the center of the plot at the mirror tunings: $\phi_{\text{PRM}} = 0^\circ$ and $\phi_{\text{ME}} = 90^\circ$. Note, that for every east end arm mirror position a nice error signal for the position of the power-recycling

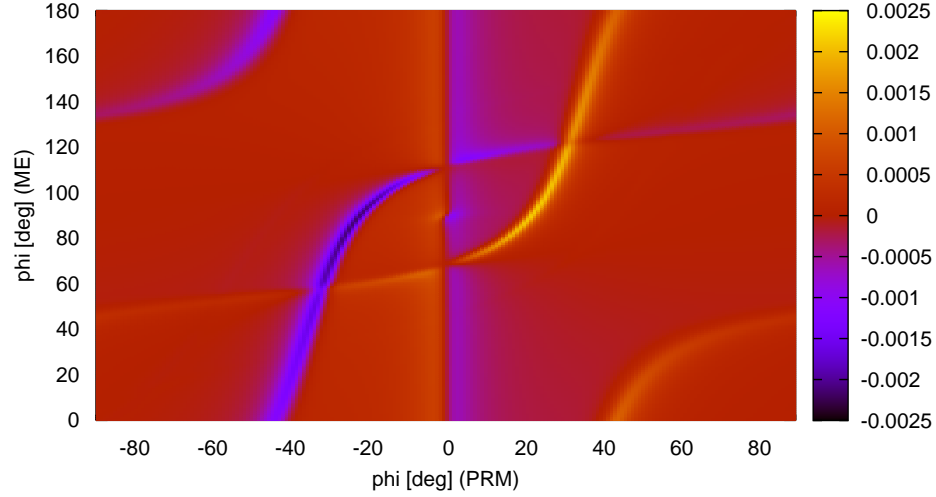


Figure 5.12: Surface plot of the power-recycling cavity error signal versus the tuning of the power-recycling mirror and the east end arm mirror. This shows the error signal near the operating point of the power-recycling mirror at a tuning of $\phi_{\text{PRM}} = 0^\circ$ and $\phi_{\text{ME}} = 90^\circ$. This error signal is almost independent of the differential arm length of the Michelson interferometer due to the fact that the sign change around $\phi_{\text{PRM}} = 0^\circ$ is present for every tuning of the east end arm mirror ϕ_{ME} .

mirror at $\phi_{\text{PRM}} = 0^\circ$ can be found. Figure 5.13 shows the coupling of the signal-recycling mirror (SRM) position and the generated power-recycling cavity error signal. The operation point is found again in the middle of the plot ($\phi_{\text{PRM}} = 0^\circ$ and $\phi_{\text{SRM}} = 90^\circ$). Here, one can see that there is absolutely no coupling between the two. The reason for this is that the interferometer is on its operation point, where the dark port condition is fulfilled. Hence, there is no light in the south port, which could interact with the signal-recycling mirror.

The following describes the error signal for the length control of the signal-recycling cavity. The goal for the signal-recycling cavity is to lock it to a sideband frequency of ± 10 MHz either side of the carrier frequency. This is because the filter cavity is also locked to a sideband frequency of ∓ 10 MHz either side of carrier frequency, but on the other side of the carrier to assure that the squeezed light reflected at both of the cavities is frequency-independent again. Section 4.4.3 gives details of the compensation of the squeezing ellipse rotation. To generate the error signal, a modulation frequency of 134.4 MHz is used. This frequency is exactly 10 MHz larger than the FSR of the signal-recycling cavity. Therefore, the generated error signal is the same as if a modulation frequency of 10 MHz has been used. The difference is that by using the modulation frequency shifted by one FSR, one can guarantee that no modulation spikes will be present in a measured spectra around 10 MHz. This is a big advantage because the desired measurement will be in a frequency range of 5–15 MHz. On the other hand the electronics have to work at these

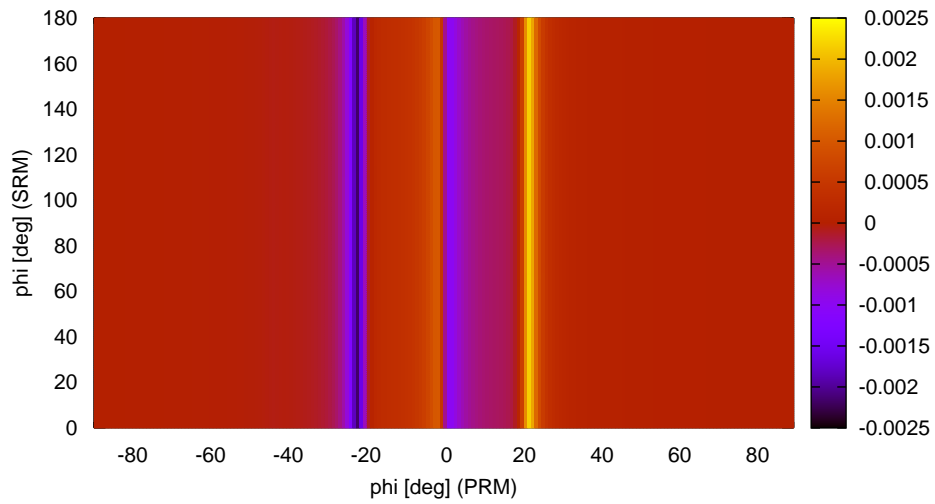


Figure 5.13: Surface plot of the power-recycling cavity error signal versus the tuning of the power-recycling mirror and the signal-recycling mirror. One can clearly see that the error signal is independent of the signal-recycling mirror tuning ϕ_{SRM} . This is a consequence of the fact that the Michelson interferometer is locked to a dark fringe. Hence, no light is propagating to the south port, which would sense the position of the signal-recycling mirror.

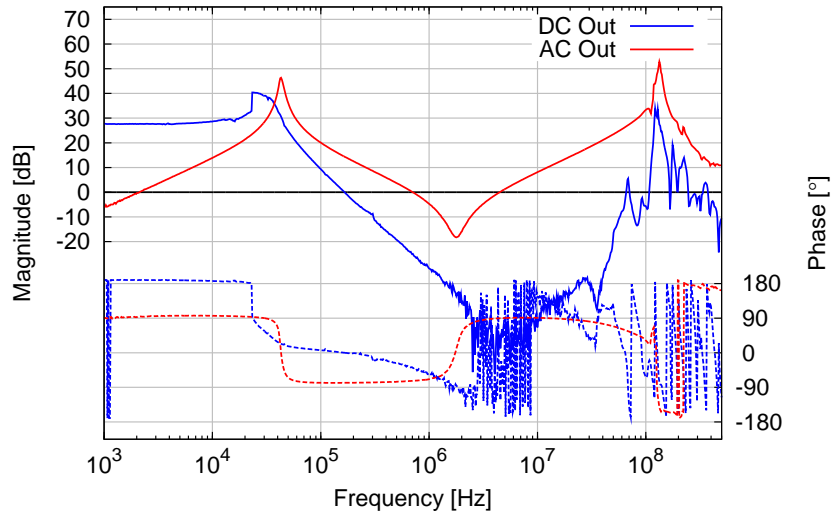


Figure 5.14: Transfer function of a resonant photodiode optimized for a frequency of 134.4 MHz. The solid blue and red curves show the magnitude of the DC and the AC output of the photodiode. The dashed curves with the same color show the corresponding phases. One can see that the bandwidth of the DC output is very low. The AC output shows two strong resonances one at a frequency of 40 kHz and one at 134.4 MHz. The schematics of the photodetectors can be found in Appendix C.5.

high frequencies. Consequently all photodiodes used to detect the modulation frequency of 134.4 MHz are resonant photodiodes. An example for the transfer function of such a photodiode can be found in Figure 5.14. The Schnupp asymmetry of the arms makes sure that a fraction of the 134.4 MHz sidebands is deviated into the south port of the interferometer (Figure 5.8). These sidebands sense the position of the signal-recycling mirror and are back-reflected into the interferometer. The resonant photodiode (PD_{SRM} in Figure 5.7) behind the east arm mirror detects a fraction of the light propagating in the interferometer arms. Demodulating the photocurrent with the modulation frequency of 134.4 MHz results in the error signal for the signal-recycling cavity. This error signal is compared to the simulated one in Figure 5.15. The error signal is the red curve (b). The correct position of the signal-recycling mirror can be found in the measured data in the time range of 0.25–0.4 a.u. This position can be distinguished from the others by looking at the power in the interferometer arms [blue curve (a)] and at the dark port power [green curve (d)]. While the signal-recycling cavity length is swept over the carrier frequency, the power in the interferometer’s arms decreases and the dark port power simultaneously rises only by a small amount, which is almost invisible in the measured data. The two steep slopes in the error signal, separated by approximately $\pm 8^\circ$ from the resonance of the carrier frequency at 90° , are used to stabilize the signal-recycling cavity to one of the desired ± 10 MHz sidebands. The coupling of the differential arm length into the error signal of the signal-recycling cavity is presented in Figure 5.16. Here, one can see two straight lines at a signal-recycling mirror tuning of about $\phi_{\text{SRM}} = 82^\circ$ and $\phi_{\text{SRM}} = 98^\circ$ which correspond to the sideband frequencies of ± 10 MHz. Note, that if the

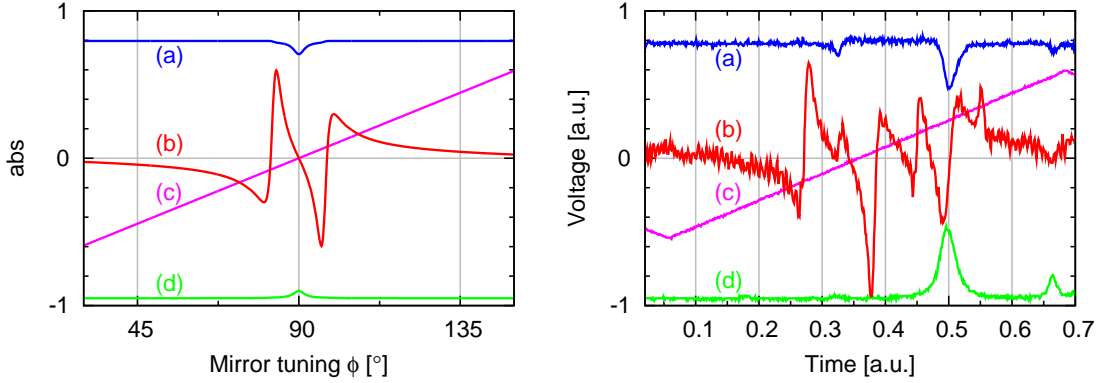


Figure 5.15: Comparison of the simulated (left) and measured (right) error signal of the signal-recycling cavity. The intra-cavity power of the signal-recycling cavity is given by curve (a). In comparison one can see that in the real measurement a higher order transverse mode is also present around a time position of 0.5 a.u. This wrong transverse mode provokes a false error signal which is much smaller than the true error signal located in the time range between 0.27 and 0.4 in curve (b). Looking at the light power in the dark port [curve (d)] one can easily distinguish between the two modes. Only at the correct position is the dark fringe condition satisfied. The two steep slopes of the true error signal are used to lock the signal-recycling cavity to a sideband frequency of ± 10 MHz. Curve (c) shows the ramp applied to the signal-recycling mirror's PZT. Note, that the individual signals have been resized.

derivation of the operating point of the east end arm mirror (ME) becomes too large, the sign flip at $\phi_{\text{SRM}} = 82^\circ$ and $\phi_{\text{SRM}} = 98^\circ$ vanishes and the signal-recycling cavity can no longer be stabilized to its nominal operation point. Hence, it is mandatory to lock the differential arm length first. Afterwards, the signal-recycling cavity can be locked to one of the ± 10 MHz sidebands. Looking at the coupling between the power-recycling mirror position and the error signal for the signal-recycling cavity in Figure 5.17, one sees almost the same situation as before. The position of the power-recycling mirror is essential and a usable signal recycling error signal can only be generated in a range of 0.5° of the power-recycling mirror tuning. Again it is mandatory to lock the power-recycling cavity length to its operation point before the signal-recycling cavity can be locked at all.

The third error signal that needs to be generated is that for the differential arm length of the interferometer. This error signal was also generated with the frontal phase modulation at a frequency of 134.4 MHz applied to the interferometer control beam. As mentioned earlier error signal used primarily was small and showed a large coupling to the signal-recycling mirror position. Therefore the final error signal was decoupled from the signal-recycling mirror by using an orthogonal polarization mode. In Figure 5.7 one can see that polarizing beam splitter (PBS) is placed in between the interferometer beam splitter and the signal-recycling mirror. In fact this PBS was a combination of three polarizing beam splitters to achieve a higher suppression of the two polarization modes. The s-polarized light in the south port of the interferometer is guided by the PBS to the SRM, whereas the p-polarization mode is detected by the photodetector PD_{MI} . Figure 5.18 shows a comparison of the simulated and the measured error signal.

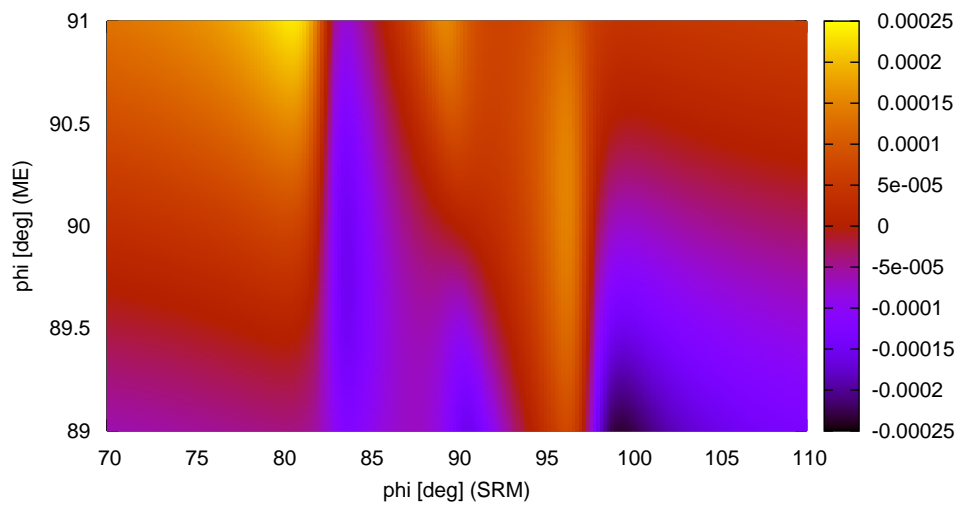


Figure 5.16: Surface plot of the signal-recycling cavity error signal versus the tuning of the signal-recycling mirror and the east end arm mirror. Note, that the error signal near the operation point of the signal-recycling mirror is at a tuning of $\phi_{\text{PRM}} = 90^\circ$ and $\phi_{\text{ME}} = 90^\circ$. This error signal is strongly dependent on the differential arm length of the Michelson interferometer. Hence, the differential arm length has to be locked to a dark fringe before a reasonable error signal for the signal-recycling cavity can be generated. Then this can be used to lock the signal-recycling cavity to a detuning frequency of ± 10 MHz.

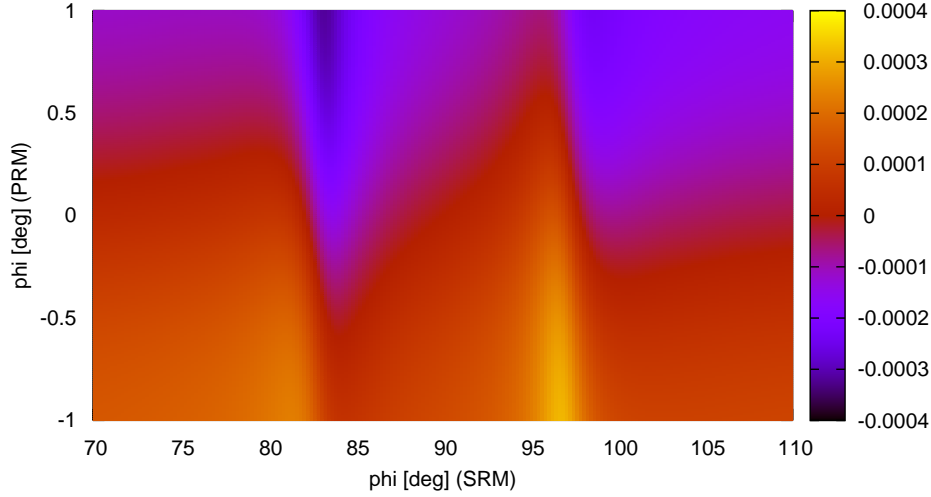


Figure 5.17: Surface plot of the signal-recycling cavity error signal versus the tuning of the signal recycling and power recycling mirrors. One can clearly see that the error signal depends strongly on the power-recycling mirror tuning ϕ_{PRM} . Hence, the power-recycling cavity has to be locked to the correct position before the signal-recycling cavity can be locked.

In the measured data the power in the south port of the interferometer for the two polarization modes are given by curve (c) (s-polarization) and curve (d) (p-polarization). Both signals look almost identical despite the fact they are shifted on the x-axis. This displacement corresponds to unequal differential arm lengths of the interferometer for the two polarization modes. This displacement corresponds to a different resonance frequency for the two polarization modes in the interferometer, which can be explained by the birefringence of the AR coating of the interferometer beam splitter or the HR coating of the folding mirror in the east arm of the interferometer. Generating the error signal by detecting the p-polarization mode together with a small offset applied to the error signal allows stable control of the dark port condition for the s-polarization mode. The error signal is fed back differentially to both end mirrors of the interferometer. The power distribution between the two orthogonal polarization modes is adjusted with a half-wave plate located in front of the power-recycling mirror. The ratio between s- and p-polarization is 100mW to 20mW.

Now that we can generate error signals for all three degrees of freedom of the dual-recycled Michelson interferometer, we will concentrate on the lock acquisition of the interferometer in the next subsection.

5.2.3 Lock acquisition of the dual-recycled Michelson interferometer

We know that the error signals of the differential arm length and of the signal-recycling cavity length are not independent of the other degrees of freedom (see Section 5.2.2).

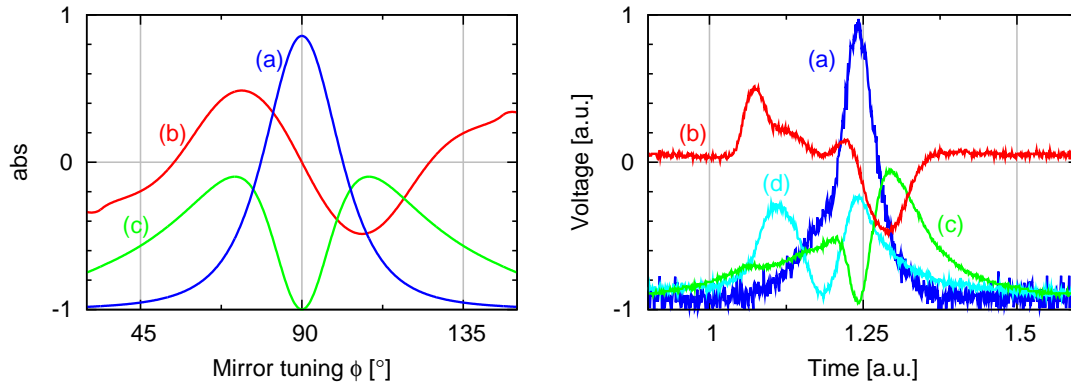


Figure 5.18: Comparison of the simulated (left) and the measured (right) error signal of the differential arm length of the Michelson interferometer. The error signal [curve (b)] is generated by the p-polarized mode, whose power is given by curve (d). This error signal can be used with a slight offset to lock the differential arm length of the interferometer to the dark port condition for the s-polarized mode [curve (c)]. The power in the interferometer arms is given by trace (a). Note, that the individual signals have been resized.

Hence the lock acquisition must be hierarchic, meaning that individual degrees of freedom have to be locked carefully one after the other. The error signal for the power-recycling cavity is the most robust, making this degree of freedom a good candidate with which to start the lock acquisition. The differential arm length has to be manually adjusted such that the dark port condition is fulfilled, this results in the biggest power buildup in the power-recycling cavity. Ramping the longitudinal position of the power-recycling mirror reveals the point where the carrier is resonant in the power-recycling cavity and the control loop for the length of the power-recycling cavity can be closed. Now that the power-recycling cavity is locked, the differential arm length has to be stabilized. As we know from Figure 5.12, the power recycling lock is stable over a large range of the differential arm length, allowing the interferometer end mirror to be ramped differentially. Figure 5.18 has been measured in such a manner. Now the phase of the Michelson differential error signal can be adjusted to the correct value and the control loop can be closed. In this phase of the lock acquisition, the dark port can be adjusted. First the error signal offset can be changed to the optimal value, then one can use the three-axis PZT mount of the folding mirror to optimize the mode overlap of the beams from the two interferometer arms, thereby minimizing the power in the dark port.

Now that we have a power-recycled Michelson interferometer, all that remains to be done is to lock the signal-recycling cavity length. Due to the fact that the signal-recycling mirror position couples into the Michelson interferometer differential arm error signal, the ramp applied to the signal-recycling mirror PZT has to be very small and slow. This way it is possible to scan the position of the signal-recycling mirror (Figure 5.15) without losing the lock of the power-recycled Michelson interferometer. Now the phase of the error signal can be adjusted and the decision can be made as to which sideband the signal-recycling cavity shall be locked. By closing this last control loop the dual-recycled Michelson interferometer is fully locked. The lock status of the interferometer is diagnosed

by various monitoring photodetectors as well as by monitoring the shape of the output mode from the interferometer's dark port.

5.3 Injecting signals into the interferometer

The idea of the experiment described in this chapter is not only to prove that the rotation of the squeezing ellipse—caused by the reflection at the detuned signal-recycling cavity—can be compensated by the filter cavity, but also to demonstrate the first squeezed-light-enhanced dual-recycled Michelson interferometer. Hence, it is required to measure the transfer function of the interferometer and to show an increase of the signal-to-noise ratio (SNR) due to the lowered noise floor by using squeezed light. There are different techniques to inject signals into the interferometer and measure its transfer function. The most easiest method to implement, because all needed components are already integrated into the setup, is signal generation via the PZT's of the end mirrors. A modulation signal applied differentially to these end mirrors would result in an amplitude modulation at the dark port. Then this would be detectable with the homodyne detector. The problem with this method is signal strength calibration. Normally, PZTs only show a linear transfer function in the kHz regime, and in the desired frequency range of 5–15 MHz the transfer function of a PZT becomes strongly nonlinear, which makes accurate calibration difficult. Hence, the use of the PZT to measure the signal transfer function of the dual-recycled Michelson interferometer has been discarded.

The second idea has been to use an EOM in each interferometer arm; their flat transfer function would make a calibration relatively simple. A modulation signal can be applied to the EOM's such that the arm length is changed differentially with a specific frequency in the range of 5–15 MHz. This would create an amplitude modulated field leaving the dark port and the homodyne detector could be used to measure the transfer function of the Michelson interferometer. The problem with this solution is the EOM in the each interferometer arm. They are additional optical components in the beam path, which could cause mode distortion due to inhomogeneities in the material, subsequently causing a non-optimal fringe visibility of the interferometer. Optical losses introduced by the EOM's are also a problem for the squeezing enhanced performance of the dual-recycled Michelson interferometer. On one hand the losses would result in a broader linewidth which would not fit to the filter cavity such that the rotation of the squeezing ellipse would not be cancelled optimally. On the other hand losses in the arms degrade the amount of squeezing at the optical resonance frequency. In this frequency range, the squeezing propagates through the interferometer and losses bring the squeezed vacuum noise level closer to the (unsqueezed) vacuum noise level. Hence, this option has been discarded as well.

The final way to inject signals into the interferometer with the goal of measuring the signal transfer function of the interferometer and the improved SNR when using squeezed light, is to use a second laser to inject single sidebands through one of the interferometer end mirrors. This second laser, called the signal laser, is shown in Figure 5.1. The idea of this solution is based on [dVSM02]. The signal laser is phase locked to the main laser; the PLL is shown in Figure 5.19. The main laser is overlapped with the signal laser on a

50/50 beam splitter. Due to the fact that these two lasers generally do not have the same carrier frequencies ($\nu_0 \neq \nu_1$), the two output fields of the beam splitter show an amplitude modulation. This amplitude modulation corresponds to the frequency difference of the main and signal laser frequencies ($\nu_0 - \nu_1$). A photodiode senses the optical field in one beam splitter output port and the amplitude modulation of the light field is transformed into an amplitude modulated photocurrent. If one uses an electrical mixer and combines this photocurrent with an external modulation with the desired modulation frequency of the injected signal ν_{mod} , one finds in principle in the output of the mixer the difference frequency ν_{diff} between the actual and the desired modulation frequency. By actuating the signal laser's internal PZT to shift its carrier frequency, ν_1 , one can zero the modulation frequency difference ν_{diff} , and the control loop can be closed. This control loop allows a step-wise change of the desired modulation frequency ν_{mod} by 10kHz without losing lock. This is fundamental for the latter measurement of the signal transfer function. Now that the phase lock between the two lasers is established, a fraction of the signal laser is coupled into a single mode polarization-maintaining fiber. This is necessary because the signal laser does not fit onto the same table as the rest of the experiment. The output of the fiber is then mode matched into the interferometer. The optimization of the mode matching is done as an intermediate step of the Michelson interferometer alignment. The signal-recycling mirror is not integrated into the setup and the main interferometer beam is blocked before entering the interferometer. The power-recycling mirror is ramped and the differential arm length is manually set to resonance. Hence, the mode matching efficiency can be measured with the photodiode normally used for locking the power-recycling cavity. Mode matching of the signal laser to the Michelson interferometer is not critical and a mode matching efficiency of about 90% is sufficient. After alignment a combination of a half-wave plate and a PBS are used to attenuate the signal laser beam. This is followed by two gray filters which have individual transmittances of only 1%. This strong attenuation of the signal laser field is necessary to achieve a signal to noise ratio at the signal recycling resonance frequency of only 15 dB. Without the attenuation the whole homodyne detector is saturating, thereby not allowing a reasonable measurement. Using only a single sideband for generating signals inside the interferometer is basically different from a phase modulation imprinted by a gravitational wave. However, in a vacuum noise limited signal-recycled interferometer with a detuning frequency larger than the signal-recycling cavity bandwidth, only one signal sideband is propagating inside the signal-recycling cavity, whereas the other sideband is suppressed greatly, see [SHSD04]. Hence a single sideband is sufficient to characterize the signal transfer function of the dual-recycled interferometer.

As an example of successful injection of signal sidebands into the power-recycled Michelson interferometer, the signal transfer function in the range 4.5–14.5 MHz is displayed in Figure 5.20. The signal transfer function (shown as a magenta curve) is measured with the signal laser's single sideband injection method. The power-recycled Michelson interferometer is fully locked during this measurement. For the measurement, the desired modulation frequency, ν_{mod} , is changed manually in steps of 10 kHz over the frequency range of the displayed measurement. The spectrum analyzer is run in the max hold mode to measure only the maximum amount of power at a given frequency. The increase in the SNR is also visible in Figure 5.20. As references the vacuum noise and

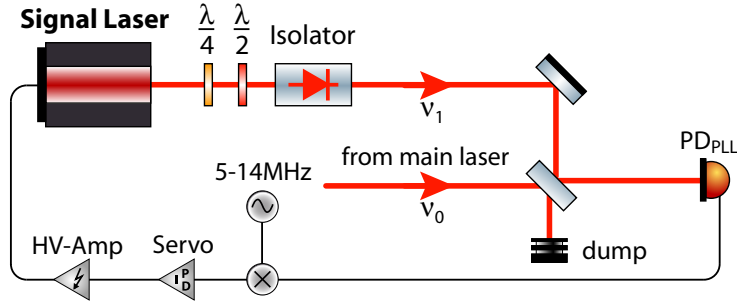


Figure 5.19: Layout of the control scheme of the phase-locked loop (PLL) of the two lasers. Both lasers are overlapped on a 50/50 beam splitter. One output of the beam splitter is detected with a photodiode, which senses an amplitude modulation of $\nu_0 - \nu_1$. The resulting photocurrent is mixed with an external modulation of the desired modulation frequency, ν_{mod} . Now the resulting current contains the modulation frequency difference, ν_{diff} , between the actual and desired modulation frequencies. This frequency difference can be adjusted to zero with the signal laser PZT and the PLL can be closed.

squeezed vacuum noise without injected signals are given by the solid red and blue curves. The dashed curves with the same colors correspond to the vacuum and squeezed vacuum noises with injected signals. In these traces one can see ten signal peaks with a frequency spacing of 1 MHz in the range 5–14 MHz. These curves are ten individually measured curves artificially merged together to see overall ten signals in one trace. One can see that the SNR of the squeezed-light-enhanced measurement is approximately 2 dB larger compared to normal interferometer performance since the vacuum noise level has been lowered.

5.4 Experimental results

Now that we have seen that the dual-recycled Michelson interferometer can be fully locked in all three degrees of freedom and how the signal injection can be achieved, we can present the results of the squeezed-light-enhanced dual-recycled Michelson interferometer. Note that all measurements presented here are at least 5 dB above the detection dark noise which has been removed from the measured data. The harmonic pump double passing the nonlinear crystal of the OPA provided a classical gain of five. The relative phase between the harmonic pump and the fundamental field inside the OPA cavity is locked to deamplification so that a dim broadband amplitude squeezed beam of about $92 \mu\text{W}$ is generated at a wavelength of 1064 nm. While the filter cavity and the signal-recycling cavity are blocked, the dim amplitude squeezed beam is guided towards the homodyne detector. Together with the vacuum noise, this frequency-independent squeezed field is measured by the homodyne detector as a reference in the amplitude quadrature. The local oscillator power used in the homodyne detector for all measurements presented is measured to be 50 mW. The resulting spectra are shown in Figure 5.21. Due to a slight difference in the transfer functions of the homodyne photodiodes used, the vacuum and the squeezed vacuum noise spectra are not flat and rise for higher frequencies. After measurement of these frequency-independent references, the filter cavity is locked to a

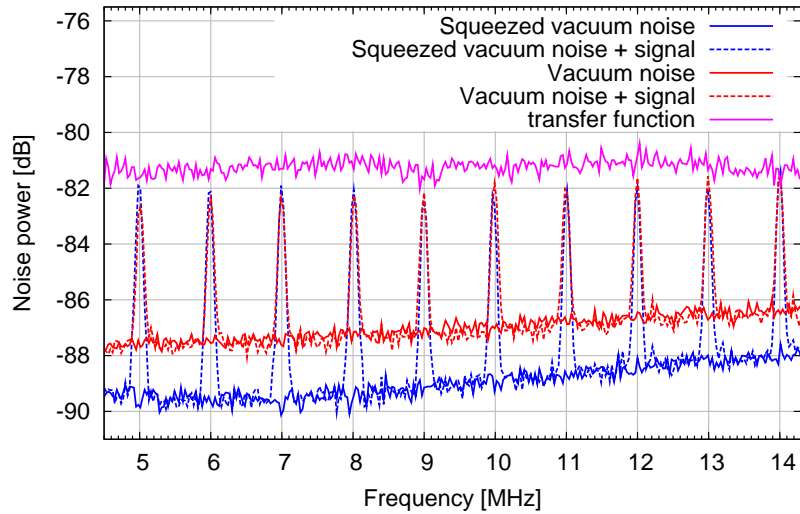


Figure 5.20: Signal transfer function of the power-recycled Michelson interferometer. The vacuum noise (solid red curve) and the squeezed vacuum noise (solid blue curve) are displayed as references. The corresponding dashed curves in the same color represent the vacuum noise and squeezed vacuum noise with ten injected signals. Each of these curves is artificially merged together from ten individual measurements. One can see that the maxima of the signal peaks follow the signal transfer function of the power-recycled Michelson interferometer (solid magenta curve). The improvement in the SNR by using squeezed field injection is measured to be about 2 dB in this case.

sideband frequency of -10 MHz, whereas the signal-recycling cavity is still blocked. Then the amplitude squeezed field which gets reflected at the detuned locked filter cavity is measured by the homodyne detector. Figure 5.21 shows the vacuum (red curve) and frequency-independent squeezed noise (blue curve) in comparison to the resulting spectrum of the frequency-dependent squeezed field back-reflected from the filter cavity (green curve). One can see the effect of the rotating ellipse (see Section 4.4). At low frequencies the spectrum is amplitude squeezed but turns into phase quadrature squeezing at the resonance frequency of 10 MHz. As a result, the measured spectrum in the amplitude quadrature shows a large amount of anti-squeezing. At higher frequencies the frequency-dependent field turns back into an amplitude squeezed state. Blocking the filter cavity while the dual-recycled Michelson interferometer is fully locked with a signal-recycling cavity detuned to a sideband frequency of +10 MHz results in the magenta curve in Figure 5.21. Now that the dim amplitude squeezed field is only reflected at the detuned signal-recycling cavity, the resulting spectrum looks almost identical to previous case. This shows that the effect to the measured data of the detuning frequencies with different leading sign is the same, although the effect looks different in the sideband picture (see Figure 4.9). If the dim amplitude squeezed field is reflected at the detuned locked filter cavity and at the detuned locked signal-recycling cavity, the effects should compensate and the measured result should be the same as the measured squeezed field reference. In Figure 5.21, the cyan colored curve shows the result of the dim amplitude squeezed field reflected first at the filter cavity and afterwards at the signal-recycling cavity. In

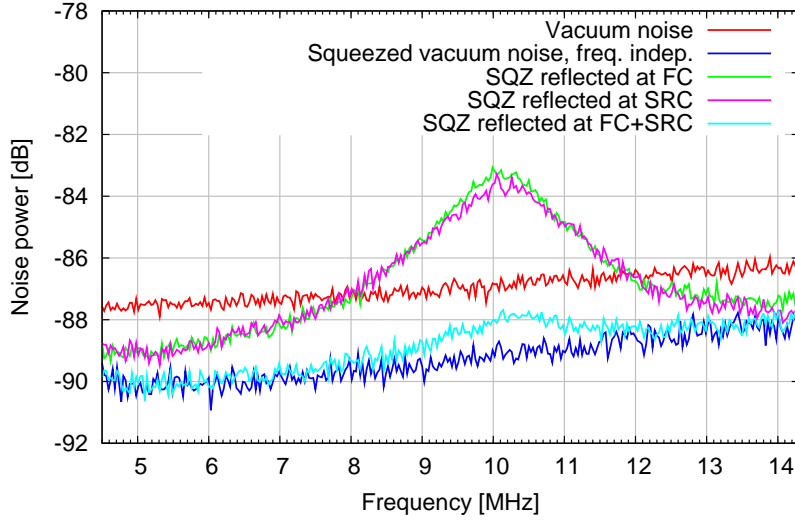


Figure 5.21: Amplitude quadrature noise spectra measured with the homodyne detector to see the effects of the filter and signal-recycling cavities on the formerly frequency-independent squeezing produced by the OPA. As references, the vacuum noise and squeezed vacuum noise are given by the red and blue curves, respectively. If the squeezed field is only reflected at the filter cavity or at the signal-recycling cavity before it is measured with the homodyne detector, one obtains the green and the magenta curves. Both are almost identical. One can see amplitude squeezing at low and high frequencies, whereas around the detuning frequency of 10 MHz only the anti-squeezing is visible due to the rotation of the squeezing ellipse. If the squeezed field is reflected at both the filter cavity and the signal-recycling cavity this results in the cyan curve, which shows a broadband improvement, compared to the vacuum noise level. Only around the detuning frequency the resulting curve differs from the squeezed vacuum noise curve. This can be explained by the intra-cavity losses due to the PBS in the signal-recycling cavity. This loss deteriorates the squeezing performance only in the region where the squeezing leaks into the cavity. As a result the cyan curve proves that the rotation of the ellipse, due to the signal-recycling cavity, can be compensated by prior reflection at the filter cavity.

comparison to the squeezed reference field, one can see that for low and high frequencies the curves are identical. Around the resonance frequency of the filter cavity and signal-recycling cavity, the squeezing is deteriorated. This is due to the fact that for frequencies within the linewidth of the cavity the squeezed field propagates through the cavity and is not directly reflected at the cavity mirror. Therefore all losses inside the cavity will affect the amount of squeezing (see Equation 2.74). The intra-cavity losses of the filter cavity are low and can be neglected. On the contrary, the signal-recycling cavity contained three polarizing beam splitters in the south port, the main beam splitter of the interferometer, and the folding mirror; all these components together have a total loss of about 1.1%. Together with a signal-recycling cavity finesse of $\mathcal{F}_{\text{SRC}} = 59$ the resulting total loss for the squeezing is 48%. This degrades an initial squeezing of about -2.5 dB into a resulting squeezing of -1.1 dB, which corresponds to the effect visible in Figure 5.21.

Figure 5.22 shows almost the same plots as Figure 5.21. Here, the difference is that the two curves, where the dim amplitude squeezed field is only reflected at either the filter

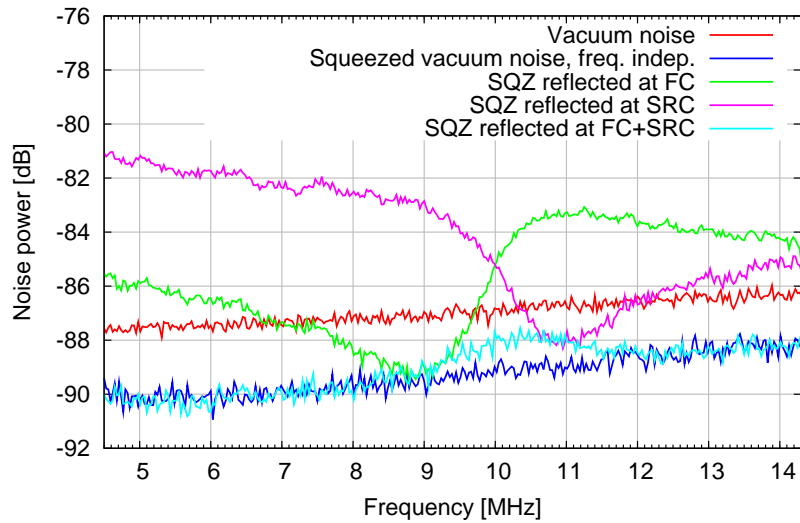


Figure 5.22: Noise spectra measured with the homodyne detector to observe the effects of the filter and signal-recycling cavities on the formerly frequency-independent squeezing produced by the OPA. This figure shows almost the same result as Figure 5.21, except the curves where the squeezed light is either reflected at the filter cavity (green curve) or at the signal-recycling cavity (magenta curve) are different. To measure these two, the offset of the homodyne error signal is changed such that the measured noise is in a slightly different quadrature than the amplitude quadrature. One can clearly see that each of the curves touches the curve measured by reflecting the squeezed field at both the filter and signal-recycling cavities, at a different frequency. This behavior has already been seen in Section 4.4.

cavity or at the signal-recycling cavity, are measured in a different quadrature. One can see that the optimal squeezing improved frequency is slightly to one side the detuning frequency. This behavior has already been discussed in Section 4.4.

To measure the signal transfer function, the signal laser was used to inject signals into the dual-recycled Michelson interferometer as described in Section 5.3. The idea is to measure the signal transfer function of the dual-recycled Michelson interferometer as well as to demonstrate the increasing SNR by replacing the ordinary vacuum noise—which couples into the interferometer through the dark port—with a squeezed vacuum state. Figure 5.23 shows the results of these measurements. The vacuum noise and frequency-independent squeezed vacuum noise are given as references (solid red and blue curves, respectively). The corresponding curves with the injected signals are the dashed red and blue curves. Each of these represents an artificially merged trace of ten individual measurements with injected signals in the range between 5–14 MHz equally separated by 1 MHz. One can easily see that the SNR is increased by the amount of squeezing. At a frequency of 5 MHz this increase in the SNR corresponds to 2.8 dB, which degrades to about 2 dB at 14 MHz by going to higher frequencies. This degradation of the squeezing performance is due to the limited linewidth of the OPA cavity of 23.5 MHz. This limitation could be removed by lowering the reflectivity of the outcoupling mirror, which would need an increase in the harmonic pump power of the OPA. More details on how one could increase the amount of squeezing are given in Section 2.11. The magenta curve

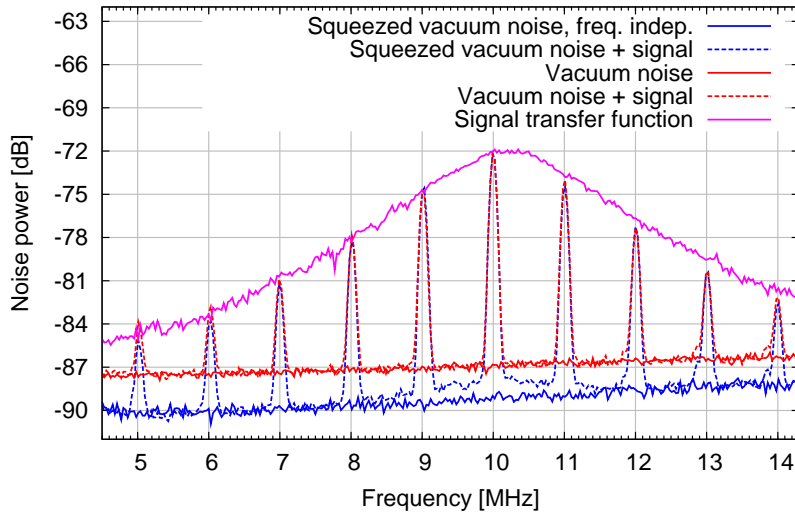


Figure 5.23: Measured signal transfer function of the dual-recycled Michelson interferometer together with the clear demonstration of the increased SNR of the squeezed-light-enhanced dual-recycled Michelson interferometer. The vacuum noise (solid red curve) and the squeezed vacuum noise (solid blue curve) are displayed as references. The dashed curves with the same color show the corresponding vacuum and squeezed vacuum noise curves including ten injected signals. Each of these curves has been artificially merged together by ten individual measurements containing one signal. One can see that the SNR ratio is improved around 5 MHz by 2.8 dB. This improvement degrades at higher frequencies due to the limited linewidth of the OPA cavity of 23.5 MHz. The maxima of the signal peaks follow nicely the measured signal transfer function of the dual-recycled Michelson interferometer (magenta curve).

displayed in Figure 5.23 shows the signal transfer function of the dual-recycled Michelson interferometer. This is measured by using the max hold function of the spectrum analyzer. Hence, the frequency of the injected signals can be changed slowly until the maxima of the individual signals composed the signal transfer function in the desired frequency range. One can see a nice resonance structure induced by the detuned signal-recycling cavity. The maximum of the signal transfer function lies in the region of 10 MHz. Compared to 4.5 MHz the signal strength at 10 MHz is increased by about 12 dB.

In conclusion, this experiment is the first realization of an experiment using power recycling, signal recycling and squeezed light to achieve a broadband increase in the sensitivity of a Michelson interferometer. This broadband non-classical noise suppression can only be achieved by the use of a separate filter cavity, which compensated the effect of the detuned signal-recycling cavity that normally would have caused a rotation of the squeezing ellipse (see Chapter 4). The optical layout of the experiment is directly applicable to large scale gravitational wave detectors, which utilize signal recycling (such as GEO 600 [GEO]) and can lead to an improvement in the vacuum noise limited regime. The planned second generation detector Advanced LIGO [ADVA] will use resonant sideband extraction and can also be enhanced by the use of squeezed light if the filter cavity resonance structure is matched to the signal-extraction cavity. Advanced LIGO and other future generation detectors will use such large laser powers that the radiation pressure

noise (see Equation 4.2) can become dominant in the low-frequency regime. Additional filter cavities are needed then to achieve a broadband enhancement in this radiation pressure dominated area [KLM⁺01, PC02, HCC⁺03]. The application of squeezed light for enhancing a large scale gravitational wave detector demands that the frequency range in which the squeezing is produced to cover the gravitational wave detection band of 10 Hz–10 kHz. Recent experiments [MGB⁺04, VCH⁺06a] have shown good results of squeezing in the gravitational wave frequency regime. The generation of low-frequency squeezing will also be discussed in Chapter 6 of this thesis. Finally the improvement in a large scale gravitational wave detector should be a factor of two in sensitivity. This corresponds to measured -6 dB of squeezing at the detector. Including only 17% losses this corresponds to a production of -10 dB in the OPA cavity. A detailed analysis of the loss estimation of the presented tabletop experiment is described in the following subsection in comparison with loss estimation for a large scale interferometer.

5.4.1 Loss estimation

This section analyzes the losses of the described tabletop squeezed-light-enhanced dual-recycled Michelson interferometer in detail. From this analysis the maximum affordable losses for a large gravitational wave detector are estimated. In the case of the squeezed-light-enhanced dual-recycled Michelson interferometer presented in this chapter, we start at the OPA cavity, which has an escape efficiency (see Equation 2.94) of 90%. On the way to the filter cavity the squeezed field passes the Faraday isolator, which has a measured transmission efficiency of 94%. The mode matching efficiency of the squeezed field into the filter cavity is only 95%. On the way to the signal-recycling cavity, whose mode matching is measured to have an efficiency of 95%, a Faraday rotator is double passed with an transmission efficiency of 97%. The overlap between the local oscillator and the squeezed beam on the homodyne beam splitter provokes a maximum homodyne visibility of $\xi = 97.5\%$, which results in a homodyne efficiency of $\xi^2 = 95\%$. The last loss in this list is the limited quantum efficiency of the individual photodiodes, which is $93 \pm 3\%$. All these efficiencies are collated in Table 5.1. The overall efficiency of the squeezed field is then 65%. Using this together with the achieved SNR improvement at 6 MHz in Figure 5.23 of 2.8 dB, one can calculate the amount of squeezing inside the OPA. One finds that about 5.7 dB of squeezing is produced inside the OPA. How these individual losses degrade the initial squeezing to the measured value can also be seen in Figure 5.24. As mentioned before, the degradation of the squeezing amount to higher frequencies is due to the limited linewidth of the OPA cavity of 23.5 MHz. Another frequency-dependent loss mechanism is the additional loss around the detuning frequency. As we have already discussed, this is mainly induced by the three polarizing beam splitters which are integrated into the south port of the dual-recycled Michelson interferometer. They are needed for the control scheme of the interferometer. In a large scale interferometer these losses are much lower and will be neglected in the following.

To achieve an improvement in the sensitivity of GEO 600 by a factor of two, one needs to detect 6 dB of squeezing. Such a nonclassical noise suppression has been achieved before in a simple squeezing experiment at the GW detector's laser wavelength of 1064 nm. In [LRB⁺99] 7 dB of squeezing has been measured. Taking the losses of this experiment

OPA escape efficiency:	ρ	90%
Transmission efficiency of the Faraday isolator (single pass)	η_{FI}	94%
Transmission efficiency of the Faraday rotator (double pass)	η_{FR}	97%
Mode matching efficiency to the filter cavity:	mm_{FC}	95%
Mode matching efficiency to the signal-recycling cavity:	mm_{SRC}	95%
Homodyne efficiency	ξ^2	95%
Quantum efficiency of the photodiodes:	η_{PD}	93%
Overall efficiency:		65%

Table 5.1: List of the individual efficiencies applied to the squeezed field from its generation until its detection for the dual-recycled Michelson interferometer experiment

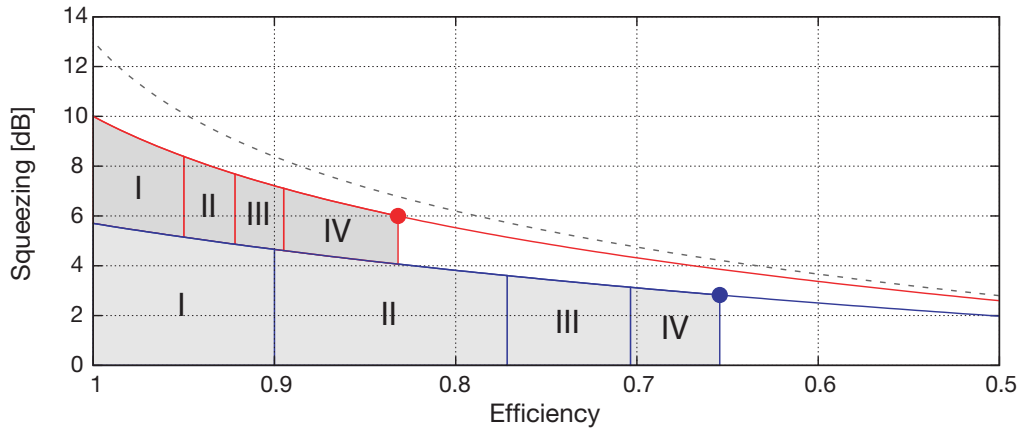


Figure 5.24: Measured squeezing strength versus detection efficiency for three different examples. The lower blue curve corresponds to the dual-recycled Michelson interferometer experiment described in this chapter. The red curve shows the result for the discussed case of GEO 600 with 17% overall losses turning an initial squeezing of 10 dB into a measured 6 dB. The dashed gray curve shows the dependency of an initial squeezing of 13 dB. The shaded areas labelled with Roman numerals correspond to different components causing losses: (I) escape efficiency of the OPA; (II) losses due to mode matching; (III) transmission losses due to Faraday isolators/rotators; (IV) quantum efficiencies of the photodiodes.

into account, one can recalculate that the squeezing inside the used OPO is indeed at least 10 dB. Hence, we will assume in the following that we can produce 10 dB inside the OPA, which may only be degraded to 6 dB. This limits the overall loss to 17%. To reach this goal, the following efficiencies of the individual loss components and mechanisms have to be achieved. Compared to the tabletop experiment described in this chapter, the outcoupling efficiency of the OPA has to be increased to a value of 95%. This is achievable by lowering the outcoupling mirror's reflectivity of the existing OPA to 93%. To obtain the same amount of squeezing, the harmonic pump power has to be increased quadratically with respect to the outcoupling mirrors' transmissivity in return. The next big loss sources in the experiment are the single pass through the Faraday isolator and the double pass through the Faraday rotator. Both are made from terbium gallium garnet crystals, which have a transmission loss of $0.5\% \text{ cm}^{-1}$. The main differences between the isolator and the rotator are the quantity and quality of polarizing beam splitters (PBSs) used. The isolator uses two PBSs with an off-the-shelf anti-reflection (AR) coating, whereas the rotator uses only one PBS with a custom-made AR coating. The rotator also allows an optimization of the magnetic field. The main losses of the Faraday rotator are therefore the off-the-shelf anti-reflection (AR) coating of the terbium gallium garnet crystal. If one optimizes all the described elements concerning the isolator and the rotator, an overall loss of the three passes through the isolators/rotators of 3% should be possible. The next loss sources we have to discuss are the individual mode matching efficiencies into the filter cavity and the signal-recycling cavity. In the case of GEO 600, a suspended triangular cavity with an optical round trip length of 1200 m can be used as a filter cavity (see Chapter 7 for the optical integration into the existing vacuum system). The much longer Rayleigh range compared to the filter cavity used in the tabletop experiment should result in a more easily adjustable mode matching. Nevertheless, large mode matching optics with a high homogeneity are needed. However, the lack of intra-cavity components and the low circulating light power could result in a mode matching efficiency of 99%, taking the experience with current GW detectors into account. Presumably the mode matching into the signal-recycling cavity will be more challenging due to the high circulating light power. This results in a thermal lens of the interferometer's beam splitter, which can reduce the Gaussian beam profile quality. As a consequence the mode matching efficiency into the signal-recycling cavity should be lower than that for the filter cavity. However, it is planned to use thermal compensation schemes [WAA⁺04] that could also lead to a mode matching efficiency of 99% of the signal-recycling cavity. The previously discussed frequency-dependent loss acts on the squeezing only in the frequency range around the detuning frequency of the signal-recycling cavity. This is due to the intra-cavity loss acting on the squeezing while it is propagating through the signal-recycling cavity. As mentioned before the main losses in the tabletop experiment are due to the PBSs, which are not present in any large scale GW detector. Although the intra-cavity losses of the signal-recycling cavity are not negligible, this loss is still acting mostly at the detuning frequency. Hence, only the improvement at the resonance frequency is degraded but the neighboring frequencies would still profit from the squeezing, providing an improved detection bandwidth. Assuming that a homodyne readout would be used in the advanced detectors, the signal beam coming out of the interferometer has to be mode matched with a strong local oscillator beam on a 50/50 beam splitter. The reflected field from the AR

coating of the interferometer's beam splitter could be used as a local oscillator. This would have a similar mode shape compared to the signal beam which would result in an increased mode matching efficiency. A value of 99% should be achievable. Finally the quantum efficiency of the photodiodes has to be taken into account. The photodiodes used in the tabletop experiment are currently the best available photodiodes for 1064 nm and have a quantum efficiency of $93 \pm 3\%$. Here we assume that this quantum efficiency can be reached for high power photodiodes, because in a large scale interferometer the photodetectors are required to detect a power of about 1 W. The described loss budget described so far is displayed in Figure 5.24. As one can see an overall efficiency of 83% is possible, which would degrade an initial squeezing of 10 dB to 6 dB.

Following the above analysis of the loss budget on the squeezed field in a large scale GW detector, it seems feasible to achieve an overall improvement of the sensitivity by a factor of two. This presumes that 10 dB of squeezing can be produced inside an OPA and an overall loss of only 17% is affecting the squeezed field on its way to detection.

Chapter 6

Coherent control of broadband vacuum squeezing

This chapter represents the published article [CVDS07] containing the newly developed locking scheme for the optical parametric oscillator (OPO) cavity and the squeezing results achieved in the low-frequency band from 10 Hz–10 kHz. These results were obtained in collaboration with H. Vahlbruch who will present a detailed analysis of the experiment in his thesis [Vah]. The experiment described here uses the experience gained from an earlier experiment which also aimed at the generation of low-frequency squeezing [SVF⁺04]. An optical subtraction method was used in the previous experiment to cancel the technical noise at low frequencies. A description of the optical subtraction scheme used in the former experiment is given in Appendix D. The newly developed locking scheme does not require any optical subtraction to achieve a squeezed quantum noise performance at low frequencies. The new experiment consequently avoids superimposing any technical noise onto the squeezed beam. Hence, a solely vacuum seeded OPO was used to generate low-frequency squeezed vacuum, which was stably controlled with the newly developed locking scheme.

6.1 Abstract

We present the observation of optical fields carrying squeezed vacuum states at side-band frequencies from 10 Hz to above 35 MHz. The field was generated with type-I optical parametric oscillation below threshold at 1064 nm. A coherent, unbalanced classical modulation field at 40 MHz enabled the generation of error signals for stable phase control of the squeezed vacuum field with respect to a strong local oscillator. Broadband squeezing of approximately -4 dB was measured with balanced homodyne detection. The spectrum of the squeezed field allows a quantum noise reduction of ground-based gravitational wave detectors over their full detection band, regardless of whether homodyne readout or radio-frequency heterodyne readout is used.

6.2 Introduction

Quantum noise is one of the limiting noise sources in laser interferometers and appears as an uncertainty of the light field's quadratures, which carry the signal of the interfer-

ometric measurement. For coherent laser radiation the quantum noise is minimal, and symmetrically distributed among pairs of noncommuting field quadratures. The finite, non-zero value of this so-called vacuum noise is a manifestation of Heisenberg's uncertainty relation (HUR). However, for certain nonclassical states of light the quantum noise can be asymmetrically distributed among field quadratures, such as amplitude and phase quadratures. In the case of squeezed states [Wal83], the quantum noise of one quadrature is reduced below vacuum noise, whereas the quantum noise in the orthogonal quadrature is increased without violating the HUR. Since an interferometer measures a certain, single quadrature of the field, an appropriately squeezed field can improve the signal-to-noise ratio in a quantum noise limited interferometer.

The application of squeezed states in laser interferometers was first proposed by Caves [Cav81] in 1981. Motivated by the challenging effort at the direct observation of gravitational waves [Tho83], Caves suggested injecting squeezed vacuum states of light into the dark signal port of interferometric gravitational wave detectors. The goal of that proposal was the reduction of the vacuum noise of the interferometer's readout laser beam, which is often called shot noise. Two years later Unruh [Unr83] realized that squeezed light can be used to correlate interferometer shot noise and radiation pressure noise (back-action noise) in such a way that the so-called standard quantum limit can be broken, and a quantum nondemolition measurement on the mirror test mass position can be performed. For an overview we refer the reader to Ref. [KLM⁺01]. The theoretical analysis of Harms *et al.* [HCC⁺03] further motivated research on squeezed states. They found that advanced interferometer recycling techniques [Mee88] that also aim for an improvement of the signal-to-shot-noise ratio are also fully compatible with squeezed-field injection.

The first observation of squeezed states was done by Slusher *et al.* [SHY⁺85] in 1985. Since then different techniques for the generation of squeezed light have evolved. One of the most successful approaches to squeezed-light generation is optical parametric oscillation (OPO). Hence common materials like MgO:LiNbO₃ can be used to produce broadband squeezing at the carrier wavelength of today's gravitational wave (GW) detectors (1064 nm). In the future, various recycling techniques as well as the most powerful single-mode lasers available will be used to reduce the quantum noise in GW detectors. It is generally expected that the interferometer sensitivities will be limited by shot noise in the upper audio band and by radiation pressure noise in the lower audio band [Sho03]. At intermediate frequencies, both quantum noise and thermal noise [BGV99] are expected to dominate the overall noise floor. Therefore squeezing of quantum noise indeed offers a further increase of GW detector sensitivities.

Gravitational wave detectors require a broadband squeezed field in the detection band from about 10 Hz to 10 kHz. If a radio-frequency (rf) heterodyne readout is used, squeezing in the band of 10 kHz around twice the rf-phase modulation frequency is also required [GBL87]. Furthermore, GW detectors utilize recycling cavities, implying that the orientation of the squeezing ellipse needs to be designed for every sideband frequency. The transformation from frequency-independent squeezing to optimized frequency-dependent squeezing can be performed by optical filter cavities, as proposed in [KLM⁺01] and demonstrated in [CVH⁺05]. The combination of squeezed-field injection and optimized orientations of squeezing ellipses, as well as power recycling and signal recycling of interferometers, has been demonstrated in [VCH⁺05, VCH⁺06b]. Squeezed states at audio

frequencies have been demonstrated recently [MGB⁺04, MMG⁺05, VCH⁺06a].

Applications of squeezed states generally require active phase control with respect to the local oscillator field of the readout scheme. Controlling the squeezed fields is indeed the basic problem for squeezed-field applications in GW detectors. Common control schemes rely on the injection of a weak, phase-modulated seed field at the carrier frequency into the OPO, thereby turning the device into an optical parametric amplifier (OPA). It has been shown that even the lowest carrier powers introduce too large amounts of classical laser noise at audio frequencies, and squeezing can no longer be achieved [MGB⁺04]. On the other hand, phase modulation sidebands are not present in a pure vacuum field. For this reason a coherent control field could not be created in [MGB⁺04] for either the squeezed-field carrier frequency or the relationship between the squeezed quadrature angle and local oscillator. The quadrature angle was locked instead using so-called noise locking, whose stability was found to be significantly less than what can be achieved with coherent modulation locking [MMG⁺05] as used in GW interferometers.

In this paper we report on the generation and coherent control of broadband squeezing from subaudio frequencies up to radio frequencies. The coherent control scheme that was first used in [VCH⁺06a] is presented in detail.

6.3 Control scheme

All current interferometric gravitational wave detectors are Michelson interferometers operating close to a dark fringe at the signal output port. The optical field at the output port consists of a local oscillator field that beats with modulation sideband fields at frequencies Ω_s generated by gravitational waves and (quantum) noise. In homodyne detection, the local oscillator has the same optical frequency ω_0 as the main interferometer laser field. In heterodyne detection the local oscillator consists of a combination of upper and lower modulation sideband fields at frequencies $\omega_0 \pm \omega_m$. Both detection schemes provide eigenvalues of the time-dependent quadrature operator $\hat{q}_\theta(\Omega_s, \Delta\Omega, t)$, where $\Delta\Omega$ is the resolution bandwidth (RBW) and θ the quadrature angle. The angle θ might be chosen to select the quadrature with the optimum signal-to-noise ratio. In the following we will refer to the amplitude quadrature ($\theta = 0$) and the phase quadrature ($\theta = 90^\circ$) with the subscripts 1 and 2. For vacuum fields, the variances of the quadrature operators are typically normalized to unity and the Heisenberg uncertainty relation sets the following lower bound for the product of the quadrature variances:

$$\Delta^2 \hat{q}_1(\Omega_s, \Delta\Omega, t) \times \Delta^2 \hat{q}_2(\Omega_s, \Delta\Omega, t) \geq 1. \quad (6.1)$$

For a broadband amplitude-squeezed field, $\Delta^2 \hat{q}_1(\Omega_s, \Delta\Omega, t)$ is always below the unity vacuum noise reference for all sideband frequencies within the squeezing band. The HUR requires that in this case $\Delta^2 \hat{q}_2(\Omega_s, \Delta\Omega, t)$ is greater than unity by a factor of at least the inverse of the squeezed quadrature variance. A squeezed vacuum field is said to be pure if, for all sideband frequencies in a certain band, the equals sign holds in Eq. (6.1). If a pure, squeezed vacuum field senses optical loss due to absorption or scattering, the squeezed field gets mixed with the (ordinary) vacuum field. In that case the equals sign

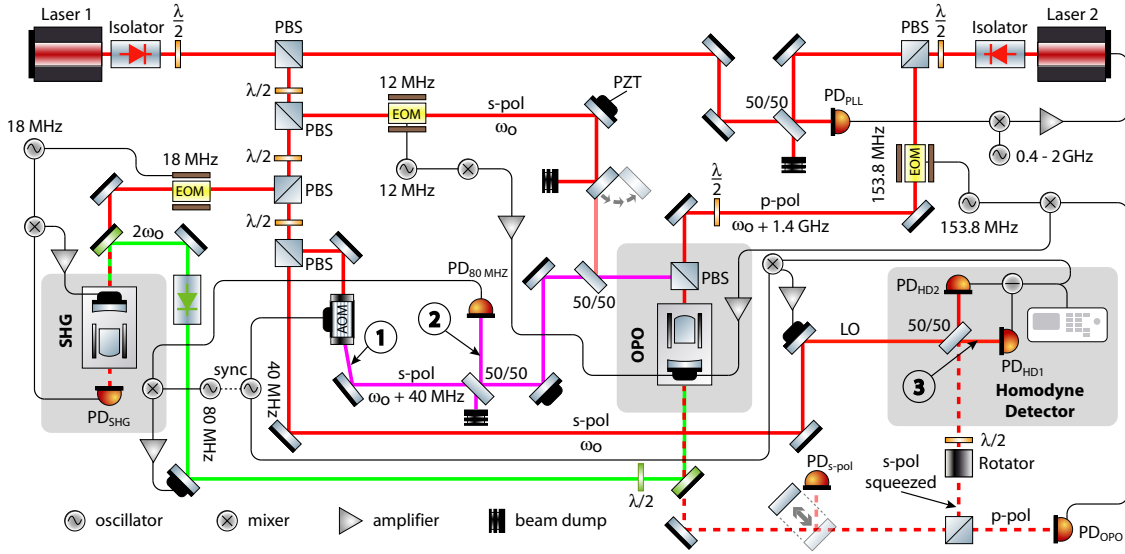


Figure 6.1: Schematic of the experiment. Generation and full coherent control of a broadband squeezed vacuum field at 1064 nm was achieved utilizing two independent but phase-locked laser sources. Laser 1 provided the main carrier frequency of homodyning local oscillator (ω_0). It also provided the quadrature control field (QCF), which was frequency shifted through an acousto-optical modulator (AOM), and the optical parametric oscillator (OPO) pump field, which was produced through second harmonic generation (SHG). Laser 2 provided another frequency-shifted control field for locking the OPO cavity length. PBS: polarizing beam splitter; DC: dichroic mirror; LO: local oscillator, PD: photodiode; EOM: electro-optical modulator, PZT: piezoelectric transducer.

in Eq. (6.1) is no longer realized; however, we still speak of a squeezed vacuum field or just vacuum squeezing.

For the application of a squeezed vacuum field in an interferometer, the squeezed quadrature needs to be matched to the interferometer readout quadrature. To achieve this goal the OPO cavity needs to be length controlled to resonate for the carrier frequency ω_0 . Furthermore, the wave front of the second-harmonic OPO pump field has to be phase controlled with respect to the interferometer readout field. Note that the phase of the OPO pump field determines the phase of the squeezed field. Both control requirements mentioned can easily be realized if a radio-frequency phase-modulated field at carrier frequency, that is sent through the OPO cavity, can be utilized. If such a field cannot be applied, for example because its noise prevents the observation of squeezed states, coherent control is much more difficult to achieve. In this section we discuss in detail the coherent control scheme that was first used in [VCH⁺06a].

Our scheme uses control fields that are coherent with the squeezed field without interfering with it. The latter ensures that noise from the control fields does not deteriorate the nonclassical performance of the squeezed field. Altogether two coherent control fields are required. Both are frequency shifted against the carrier frequency ω_0 . A coherent, frequency-shifted field can be generated by an independent but phase-locked laser source or by an acousto-optical modulator (AOM) acting on a tapped laser beam from the

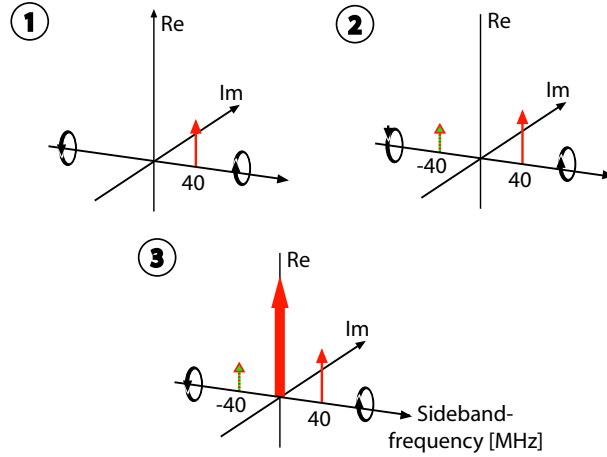


Figure 6.2: Complex optical field amplitudes at three different locations in the experiment, which are marked in Figure 6.1.

same source. The first frequency-shifted control field enables length control of the OPO cavity. It carries radio-frequency phase modulation sidebands, is orthogonally polarized with respect to the squeezed vacuum field, and is injected into the OPO cavity. The frequency shift should exactly compensate the birefringence of the nonlinear crystal such that both control field and squeezed field simultaneously resonate in the OPO cavity. The frequency shift as well as the orthogonal polarization prevents the interference of the squeezed vacuum field and the control field.

The control of the quadrature angle of the squeezed vacuum with respect to a local oscillator or an interferometer carrier field is more challenging. This request is achieved by the second control field (quadrature control field, QCF) which is also injected into the OPO cavity. This field does sense the OPO nonlinearity but is frequency shifted against the vacuum squeezed mode. The QCF allows the generation of two individual error signals for two different servo control loops. The first error signal is used to control the relative phase between the QCF and the OPO pump field. The second error signal is used to control the relative phase between the OPO pump field and the local oscillator field of the interferometer, or rather the homodyne detector. The combination of both error signals provides the means to stabilize the quadrature of the squeezed vacuum field with respect to a local oscillator.

In the following we show that the required error signals can be gathered from the QCF leaving the OPO cavity, and from the interference of the QCF with the local oscillator field at the homodyne detector. We label those two error signals $S_{\text{err}}^{\text{QCF-P}}$ and $S_{\text{err}}^{\text{QCF-LO}}$, respectively, and first derive an expression for the parametrically amplified quadrature control field QCF. Before parametric amplification the QCF at optical frequency $\omega_0 + \Omega$ represents a single sideband field with respect to the carrier frequency ω_0 (see ① in Figs. 6.1 and 6.2). In the following we describe this field by the real-valued amplitude α_Ω . The expectation values of the annihilation operators of the upper and lower sideband fields at frequencies $\omega_0 \pm \Omega$ may then be written as follows:

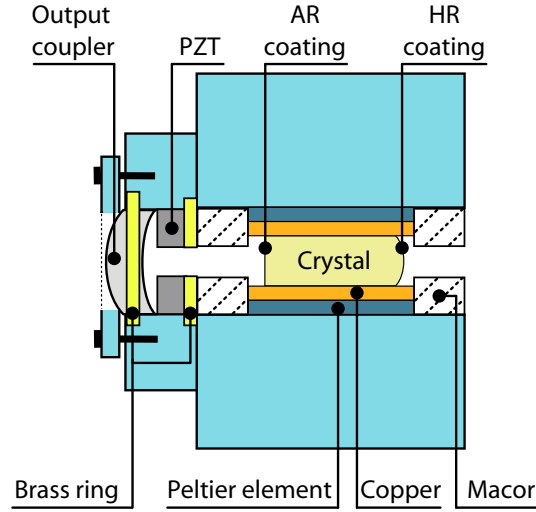


Figure 6.3: Cut through the squeezed-light source. The hemilithic cavity is formed by the highly reflection-coated crystal back surface and an outcoupling mirror. The inside of the oven consists of two Peltier elements which are used to actively stabilize the temperature of the crystal. The thermal contact to the crystal is done via copper plates. To thermally shield the crystal from outside, Macor blocks are used. These have two small drillings on the optical axis for the laser beam. The temperature sensor is embedded into the copper plates. A stack made out of a brass ring, a PZT, the outcoupling mirror, and a Viton ring is clamped together with an aluminum cap. This stack is bolted onto the oven to have a rigid cavity.

$$\langle \hat{a}_+ \rangle \equiv \langle \hat{a}(\omega_0 + \Omega) \rangle = \alpha_\Omega, \quad \langle \hat{a}_- \rangle \equiv \langle \hat{a}(\omega_0 - \Omega) \rangle = 0. \quad (6.2)$$

The quadrature amplitudes [CS85] are given by

$$\hat{a}_1 = \frac{1}{\sqrt{2}}(\hat{a}_+ + \hat{a}_-^\dagger), \quad \hat{a}_2 = \frac{1}{i\sqrt{2}}(\hat{a}_+ - \hat{a}_-^\dagger). \quad (6.3)$$

Here all quantities are defined for discrete frequencies. This simplifies our description and is reasonable because the bandwidth of the error signals is small compared to Ω .

The OPO acts on these quadrature amplitudes in different ways. If it amplifies the phase quadrature then it deamplifies the amplitude quadrature, and vice versa. Mathematically, this effect of amplification and deamplification of the quadratures $\bar{\mathbf{a}} = \begin{pmatrix} \hat{a}_1 \\ \hat{a}_2 \end{pmatrix}$

can be described with the use of the squeezing operator

$$S(r, \phi) = \exp \left[r \left(\hat{a}_+ \hat{a}_- e^{-2i\phi} - \hat{a}_+^\dagger \hat{a}_-^\dagger e^{2i\phi} \right) \right] \quad (6.4)$$

with squeezing factor r and squeezing angle ϕ [CS85]. The resulting squeezed quadrature vector $\bar{\mathbf{b}}$ is given by:

$$\begin{aligned} \bar{\mathbf{b}} &= \begin{pmatrix} \hat{b}_1(\Omega) \\ \hat{b}_2(\Omega) \end{pmatrix} = S(r, \phi) \bar{\mathbf{a}} S^\dagger(r, \phi) \\ &= \begin{pmatrix} \cosh(r) + \sinh(r) \cos(2\phi) & \sinh(r) \sin(2\phi) \\ \sinh(r) \sin(2\phi) & \cosh(r) - \sinh(r) \cos(2\phi) \end{pmatrix} \bar{\mathbf{a}}. \end{aligned} \quad (6.5)$$

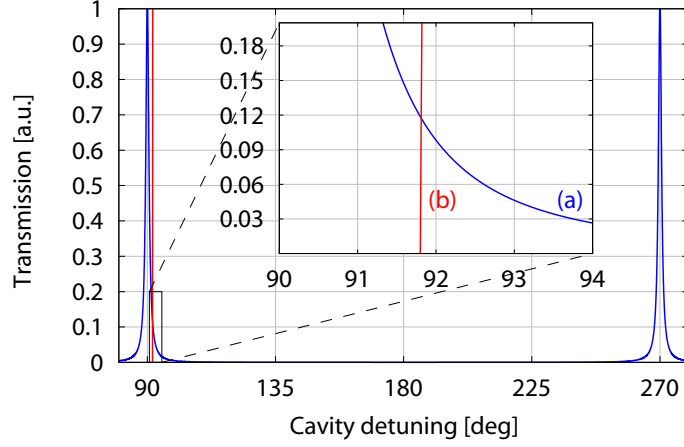


Figure 6.4: Theoretical OPO cavity transmission [curve (a)] versus cavity detuning (peak normalized to unity). The cavity linewidth is 29.8 MHz. The 40 MHz frequency offset from the carrier frequency of the AOM—producing the QCF—is marked with the plumb line [curve (b)].

The expectation values of the new squeezed quadrature amplitudes $\hat{b}_1(\Omega)$ and $\hat{b}_2(\Omega)$ take the following form

$$\begin{aligned}\langle \hat{b}_1(\Omega) \rangle &= -\frac{i\alpha\Omega}{\sqrt{2}} S_{2\phi} \sinh(r) + \frac{\alpha\Omega}{\sqrt{2}} [\cosh(r) + C_{2\phi} \sinh(r)] , \\ \langle \hat{b}_2(\Omega) \rangle &= \frac{\alpha\Omega}{\sqrt{2}} S_{2\phi} \sinh(r) - \frac{i\alpha\Omega}{\sqrt{2}} [\cosh(r) - C_{2\phi} \sinh(r)] .\end{aligned}\quad (6.6)$$

To derive the corresponding electrical field

$$E^{\text{QCF}}(t) \propto \langle \hat{b}^{(+)}(t) + \hat{b}^{(-)}(t) \rangle \quad (6.7)$$

with

$$\hat{b}^{(\pm)}(t) \equiv \frac{1}{2} [\hat{b}_1(t) \pm i\hat{b}_2(t)] e^{\mp i\omega_0 t} \quad (6.8)$$

we need the Fourier transformations of $\hat{b}_1(\Omega)$ and $\hat{b}_2(\Omega)$. Since we consider a single frequency we obtain

$$\begin{aligned}\hat{b}_1(t) &= \hat{b}_1(\Omega)e^{-i\Omega t} + \hat{b}_1^*(\Omega)e^{i\Omega t} , \\ \hat{b}_2(t) &= \hat{b}_2(\Omega)e^{-i\Omega t} + \hat{b}_2^*(\Omega)e^{i\Omega t} .\end{aligned}\quad (6.9)$$

By choosing $\exp(r) = \sqrt{g}$ we simplify our expression and find for the outgoing QCF from the OPO

$$E^{\text{QCF}}(t) \propto \frac{1+g}{\sqrt{2g}} \alpha\Omega \cos(\omega_0 t + \Omega t) - \frac{1-g}{\sqrt{2g}} \alpha\Omega \cos(\omega_0 t - \Omega t - 2\phi) . \quad (6.10)$$

This is the desired expression for the parametrically amplified QCF, and forms the basis for the following derivation of the two error signals $S_{\text{err}}^{\text{QCF-P}}$ and $S_{\text{err}}^{\text{QCF-LO}}$. One can easily

see in Eq. (6.10) that $E^{\text{QCF}}(t)$ is composed of two sidebands that are equally separated by Ω from the carrier frequency ω_0 . This is also illustrated in the sideband scheme ② in Figure 6.2. The quadrature where these two sidebands beat with each other can be chosen using the squeezing angle ϕ . If one uses a squeezing angle of $\phi = 0$ the following electrical field is found:

$$E^{\text{QCF}}(t)_{\phi=0} \propto \frac{1}{\sqrt{2}} \left(\sqrt{g} \cos(\Omega t) - i \frac{1}{\sqrt{g}} \sin(\Omega t) \right) \times a_{\Omega}(\Omega) e^{-i\omega_0 t} + \text{c.c.}, \quad (6.11)$$

which has also been provided in [VCH⁺06a].

Detection of the outgoing field $E^{\text{QCF}}(t)$ from the OPO with a single photodiode results in the following photocurrent:

$$I^{\text{QCF}} \propto \frac{\alpha_{\Omega}^2}{2g} [(1+g) \cos(\omega_0 t + \Omega t) - (1-g) \cos(\omega_0 t - \Omega t - 2\phi)]^2. \quad (6.12)$$

Demodulating I^{QCF} with frequency 2Ω and subsequent low-pass filtering provide the error signal $S_{\text{err}}^{\text{QCF-P}}$ for the relative phase between the second-harmonic pump field and the QCF, given in terms of the squeezing angle ϕ

With an appropriate demodulation phase one obtains the sinusoidal error signal

$$S_{\text{err}}^{\text{QCF-P}} \propto \frac{(-1+g^2) \alpha^2 \sin(2\phi)}{4g}. \quad (6.13)$$

Now that we are able to stabilize ϕ with respect to the QCF, the first step to a complete coherent control of a squeezed vacuum generated by an OPO is satisfied.

In a second step the phase Φ between the second-harmonic pump field and the local oscillator needs to be controlled. The error signal $S_{\text{err}}^{\text{QCF-LO}}$ is generated from the difference current of the two homodyne photodiodes PD_{HD1,2}. Overlapping the local oscillator field $E^{\text{LO}} \propto \alpha^{\text{LO}} e^{-i\omega_0 t} e^{-i\Phi} + \text{c.c.}$ with the outgoing QCF $E^{\text{QCF}}(t)$ from the OPO at the LO homodyne beam splitter results in two homodyne detector fields E^{HD1} and E^{HD2} which are individually detected with a single photodiode. The complex field amplitudes of one of the homodyne detector fields can be seen graphically in Figure 6.2,③. Mathematically they are given by

$$\begin{aligned} E^{\text{HD1}} &= \frac{1}{\sqrt{2}} [E^{\text{LO}} + E^{\text{QCF}}(t)] \\ &\propto \frac{1}{\sqrt{2}} \left[\alpha^{\text{LO}} e^{-i(\omega_0 t + \Phi)} + \left(\frac{1+g}{\sqrt{2g}} \alpha_{\Omega} \cos(\omega_0 t + \Omega t) \right. \right. \\ &\quad \left. \left. - \frac{1-g}{\sqrt{2g}} \alpha_{\Omega} \cos(\omega_0 t - \Omega t - 2\phi) \right) \right] + \text{c.c.} \end{aligned} \quad (6.14)$$

$$\begin{aligned} E^{\text{HD2}} &= \frac{1}{\sqrt{2}} [E^{\text{LO}} - E^{\text{QCF}}(t)] \\ &\propto \frac{1}{\sqrt{2}} \left[\alpha^{\text{LO}} e^{-i(\omega_0 t + \Phi)} - \left(\frac{1+g}{\sqrt{2g}} \alpha_{\Omega} \cos(\omega_0 t + \Omega t) \right. \right. \\ &\quad \left. \left. - \frac{1-g}{\sqrt{2g}} \alpha_{\Omega} \cos(\omega_0 t - \Omega t - 2\phi) \right) \right] + \text{c.c.} \end{aligned} \quad (6.15)$$

The difference current I_{diff} of the induced photocurrents $I^{\text{HD1,2}} = |E^{\text{HD1,2}}|^2$ is then given by

$$\begin{aligned} I_{\text{diff}} &\propto \frac{4\sqrt{2}\alpha^{\text{LO}}\alpha_{\Omega}\cos(\Phi + \omega_0 t)}{\sqrt{g}} \\ &\times \left[(1+g)\cos(\omega_0 t + \Omega t) - (1-g)\cos(\omega_0 t - \Omega t - 2\phi) \right] \\ &\propto \frac{2\sqrt{2}\alpha^{\text{LO}}\alpha_{\Omega}(-1+g)}{\sqrt{g}} \times \cos(\Omega t + 2\phi + \Phi), \end{aligned}$$

where Eq. (6.16) is the difference of the photocurrents after low-pass filtering. The demodulation of I_{diff} with Ω and again low-pass filtering results in the error signal $S_{\text{err}}^{\text{QCF-LO}}$ for the relative phase Φ between the second-harmonic pump and the local oscillator

$$S_{\text{err}}^{\text{QCF-LO}} \propto \frac{\sqrt{2}\alpha^{\text{LO}}\alpha_{\Omega}(-1+g)}{\sqrt{g}} \sin(2\phi + \Phi). \quad (6.16)$$

This error signal depends not only on the relative phase between the second-harmonic pump and the local oscillator Φ , but also on the squeezing angle ϕ . However, it becomes clear that the combination of both error signals according to Eqs. (6.13) and (6.16) enables full coherent control of the squeezed vacuum generated by an OPO with respect to the local oscillator of a downstream experiment.

6.4 Experimental setup and results

Figure 6.1 shows the schematic of our experimental setup that was used to demonstrate coherently controlled broadband vacuum squeezing. Altogether two independent, but phase-locked laser sources (lasers 1 and 2) were utilized. Both were monolithic nonplanar neodymium-doped yttrium aluminum garnet (Nd:YAG) ring laser of 2 and 1.2 W single-mode output powers at 1064 nm, respectively. Approximately 1.4 W of laser 1 was used to pump a second-harmonic-generation (SHG) cavity. The design of the SHG cavity was the same as for our OPO cavity. The two differed only in the reflectivities of the outcoupling mirrors.

A detailed sketch of our SHG and OPO cavity design and mounting is shown in Figure 6.3. We used a hemilithic layout which was formed by an outcoupling mirror and a highly reflection-coated crystal back surface. The oven was made of an aluminum surrounding that houses the crystal and the Peltier elements and served as a heat sink. The outcoupling mirror together with the piezoelectric transducer (PZT) and a Viton ring formed a stack that was clamped together with an aluminum cap. This stack was located in an aluminum plate that was bolted onto the aluminum surrounding of the oven. Macor blocks were used to thermally shield the crystal from outside. The Macor blocks had two small holes on the optical axis for the laser beam. A servo loop was used for active temperature stabilization of the crystal. The required temperature sensor was embedded into the copper plates and the servo feedback was put on the peltier elements. The OPO as well as the SHG crystal were made from 7% doped $\text{MgO}:\text{LiNbO}_3$ and had the

dimensions $2.5 \times 5 \times 6.5 \text{ mm}^3$. The curved back surface of the crystals had a high-reflection coating ($R=99.96\%$) whereas the flat surface had an antireflection coating ($R < 0.05\%$) for both wavelengths. The cavities had a free spectral range of approximately 4 GHz. The crystals were mounted into the ovens in such a way that s -polarized fields could sense the nonlinearity

The SHG used an outcoupling mirror with power reflectivities of $R_{1064 \text{ nm}} = 92\%$ and $R_{532 \text{ nm}} < 4\%$. The cavity length was controlled using the Pound-Drever-Hall (PDH) locking scheme with a phase modulation at a sideband frequency of 18 MHz. The generated second-harmonic field had a power of up to 500 mW.

The OPO cavity utilized an outcoupling mirror with power reflectivities of $R_{1064 \text{ nm}} = 95.6\%$ and $R_{532 \text{ nm}} = 20\%$. This resulted in a linewidth of 28.9 MHz at 1064 nm (see Figure 6.4). For the OPO or OPA two different control loops for stabilizing the cavity length were set up. The first cavity length control loop was used during alignment of our experiment. It utilized a resonant s -polarized seed beam that carried phase modulation sidebands at a frequency of 12 MHz for a PDH locking scheme. The error signal could be generated using either the sum of the homodyne detectors or an additional detector placed in transmission of the OPA (see Figure 6.1). The latter detector was also used to determine the frequency offset between the s - and p -polarized laser beams inside the OPA or OPO. The error signal was fed back to the PZT-mounted output coupler. The second cavity length control loop was used for the generation of squeezed vacuum states at low frequencies, since the first control loop introduced too much noise at low frequencies (see Sec. 6.3). This control was realized with a p -polarized field generated by the second monolithic nonplanar Nd:YAG ring laser (laser 2). Due to the birefringence of the MgO:LiNbO₃ crystal the TEM₀₀'s of the OPO cavity for s - and p -polarization are not degenerate. To ensure that both polarizations resonate simultaneously in the cavity we shifted the frequency of the p -polarized field. We determined the frequency shift to be about 1.4 GHz. The frequency offset was controlled via a phase-locked loop (PLL) that could be operated from nearly DC up to 2 GHz with a bandwidth of several kilohertz. The error point of the PLL was fed back to the PZT of the second laser. Phase modulation sidebands at a frequency of 153.8 MHz were imprinted onto the p -polarized field, which was then injected through the back surface of the OPO crystal. The transmitted part was spatially separated from the s -polarized squeezed vacuum with a polarizing beam splitter (PBS) and detected by the photodetector. A PDH locking technique was used to generate an error signal which was fed back to the PZT of the OPO cavity.

Following our proposal described above we utilized a second coherent but frequency-shifted control field for the phase control of the squeezed vacuum field, detuned by Ω with respect to the main carrier frequency (ω_0 , laser 1) by an AOM [see Eq. (6.3) & ① in Figs. 6.1 and 6.2]. The frequency of the AOM was $\Omega/2\pi = 40 \text{ MHz}$. This frequency-shifted s -polarized infrared QCF (440 μW) was also injected into the OPO cavity through the crystal's back surface. It therefore had to be spatially overlapped with the p -polarized locking beam using a 50/50 beam splitter. To eliminate technical noise below 1 kHz in the homodyne spectra, the zero order of the AOM had to be blocked carefully. If only small fractions of this non-frequency-shifted field leaked into the cavity, the squeezing spectrum was spoiled by the large technical noise in the low-frequency regime.

Figure 6.4 shows that only 11.5% of the QCF was coupled into the cavity. This 11.5%

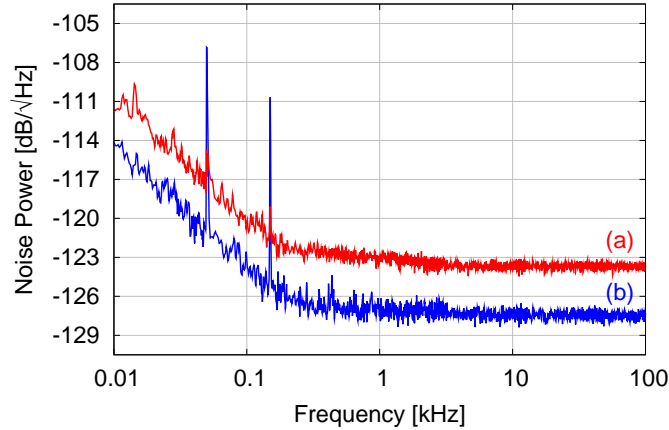


Figure 6.5: Measured quantum noise spectra at sideband frequencies $\Omega_s/2\pi$: (a) shot noise and (b) squeezed noise with $88 \mu\text{W}$ local oscillator power. All traces are pieced together from five fast Fourier transform frequency windows: 10–50 Hz, 50–200 Hz, 200–800 Hz, 800–3.2 kHz, and 3.2–10 kHz. Each point is the averaged rms value of 100, 100, 400, 400, and 800 measurements in the respective ranges. The RBWs of the five windows were 250 mHz, 1 Hz, 2 Hz, 4 Hz, and 16 Hz, respectively.

interacted with the pump field inside the cavity, its quadratures were parametrically amplified and deamplified, and an additional sideband at -40 MHz [see Eq. (6.10)] was generated. This outgoing QCF from the OPO then consisted of two sidebands, each separated by 40 MHz from the carrier frequency ω (see ② in Figs. 6.1 and 6.2). The error signal could be obtained by detecting the outgoing QCF from the OPO and demodulating the photocurrent at 80 MHz as illustrated in the sideband scheme in Figs. 6.1 and 6.2. By feeding back the error signal to a PZT-mounted mirror in the path of the second-harmonic pump field, stable control of ϕ was realized [see Eq. (6.13)]. The error signal for controlling the homodyne angle Φ [see Eq. (6.16)] was derived at the homodyne detector. The difference of the two photodiode currents was demodulated with a frequency of 40 MHz . The output of this servo loop was fed back to a PZT-mounted mirror in the local oscillator path.

The homodyne detector was built from a p -polarization-optimized 50/50 beam splitter and two electronically and optically matched photodetectors based on Epitaxx ETX500 photodiodes. The angular orientation of the photodiodes was optimized to achieve the maximum power to optimize the detection efficiency. We used two different pairs of matched photodetectors: one was optimized for the low-frequency regime whereas the other pair was optimized for high bandwidth. In all measured spectra shown here the electronic noise of the detection system was subtracted from the measured data.

The low-frequency-optimized homodyne photodiode pair permits the measurement of the low-frequency spectrum of the OPO (see Figure 6.5) in the detection bandwidth of GW interferometers and above up to 100 kHz . For these low-frequency measurements we used a nominal local oscillator power of $88 \mu\text{W}$. The resulting shot noise limit of the homodyne detection system is shown as curve (a) in Figure 6.5, whereas the squeezed quantum noise is shown in curve (b). During the measurement period of approximately

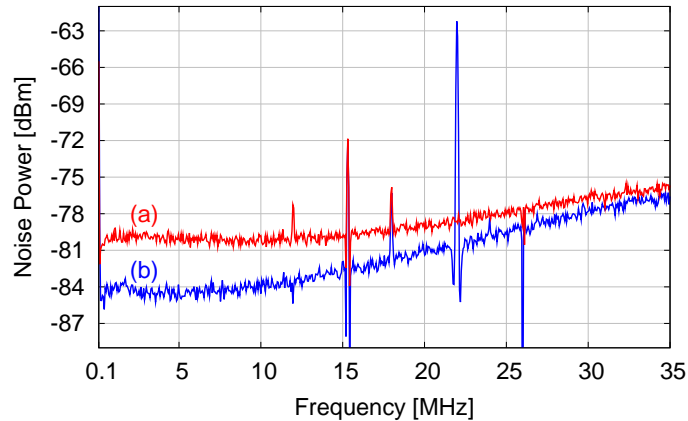


Figure 6.6: Measured quantum noise spectra: (a) shot noise and (b) squeezed noise with 8.9 mW local oscillator power. The spikes at 15.5, 22, and 26 MHz are results from the dark noise correction of modulation peaks due to other electronic fields.

1.5 h the complete experiment including the OPO with all its related control loops, was controlled stably in all degrees of freedom. For the measurements in Figure 6.5 a parametric gain of 10 was used, which was obtained using 60 mW of the second-harmonic pump field. The propagation losses of the squeezed vacuum were dominated by the Faraday rotator passthrough efficiency of only 95%. The mode matching efficiency between the local oscillator and the squeezed field was measured to be 94.3%. Altogether this allowed us to measure 4 dB squeezing over the complete detection band of ground-based GW interferometers.

The OPO squeezing spectrum from 100 kHz to 35 MHz is shown in Figure 6.6. Curve (a) shows the shot noise limit of the homodyne detector, while the squeezing spectrum is shown in curve (b). Both traces take the dark noise into account. These measurements were done with the high-bandwidth-optimized homodyne detector using a local oscillator power of 8.9 mW. The resulting shot noise showed a nonwhite behavior above 10 MHz. This stemmed from small deviations in the transfer functions of the two homodyne photodetectors used. One can see that up to 10 MHz we observed at least 4 dB of squeezing, peaking around 5 MHz with up to 4.95 dB of squeezing (see Figure 6.7). At higher frequencies the squeezing degraded to approximately 1 dB due to the linewidth of the OPO cavity. Lowering the finesse of the OPO would open up the high-frequency regime for a better squeezing performance, but higher pump powers would be needed to produce the same amount of squeezing.

The two individual measurements show that we have produced 4 dB of squeezing over more than six decades from 10 Hz up to 10 MHz.

6.5 Application to gravitational wave detectors

In [VCH⁺06a] a broadband squeezed vacuum field was applied to a simple Michelson interferometer. A nonclassical signal-to-shot-noise improvement was observed using balanced homodyne detection. However, real gravitational wave Michelson interferometers

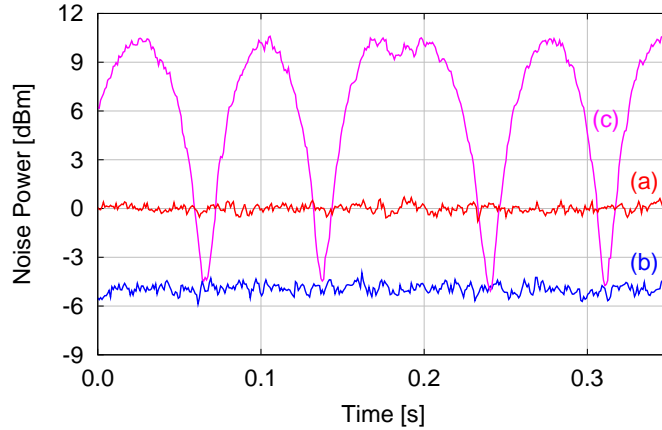


Figure 6.7: Time series of shot noise [curve (a)], squeezed noise with locked local oscillator phase [curve (b)] and squeezed noise with scanned local oscillator phase [curve (c)] at $\Omega_s/2\pi = 5$ MHz sideband frequency. A nonclassical noise suppression of about 5.0 ± 0.1 dB is demonstrated. The dark noise has been subtracted.

are much more complex. Here we discuss two aspects that are important when coherently controlled broadband squeezed vacuum fields are applied to signal-recycled gravitational wave detectors with heterodyne readout.

In an application to a gravitational wave detector, the quadrature control field, here shifted in frequency by $\Omega/2\pi = 40$ MHz, will enter the interferometer from the dark port together with the squeezed field [Cav81, SHSD04]. The best choice for the QCF frequency is such that it is offresonant with respect to the signal-recycling cavity (SRC). In this case the QCF is basically reflected from the SRC, which minimizes possible disturbances to other interferometer control loops. A generally rather important interferometer control field stabilizes the Michelson interferometer on a defined differential arm length to provide the desired dark signal port condition. In GEO 600 this control field operates at a sideband frequency of 14.9 MHz and is photoelectrically detected in the dark port. Obviously, the QCF frequency Ω should also provide a sufficiently large offset from that frequency of 14.9 MHz. Our choice of $\Omega/2\pi = 40$ MHz is therefore rather practical in the case of GEO 600.

Another aspect is the compatibility of the squeezed vacuum field demonstrated here and the heterodyne detection scheme that is currently used in all gravitational wave detectors, namely GEO 600 [AC04, HtL06], LIGO [AAD⁺92, AC04], TAMA 300 [AtTC01], and VIRGO [AAA⁺04]. Gea-Banacloche and Leuchs [GBL87] have shown that an interferometer with heterodyne readout requires squeezing in the band of expected gravitational wave signals (Ω_s) and also squeezing around twice the heterodyne frequency ($2\omega_m \pm \Omega_s$). This is because the noise at $\omega_m \pm \Omega_s$ contains vacuum noise contributions from $2\omega_m \pm \Omega_s$. It was later shown that these results are still valid for detuned signal-recycled interferometers [CDR⁺98].

The realization that broadband squeezing up to $2\omega_m \pm \Omega_s$ is needed to gain the full sensitivity enhancement from squeezing leads to the question as to where one should inject the squeezed vacuum field. Figure 6.8 shows a schematic of GEO 600. In normal

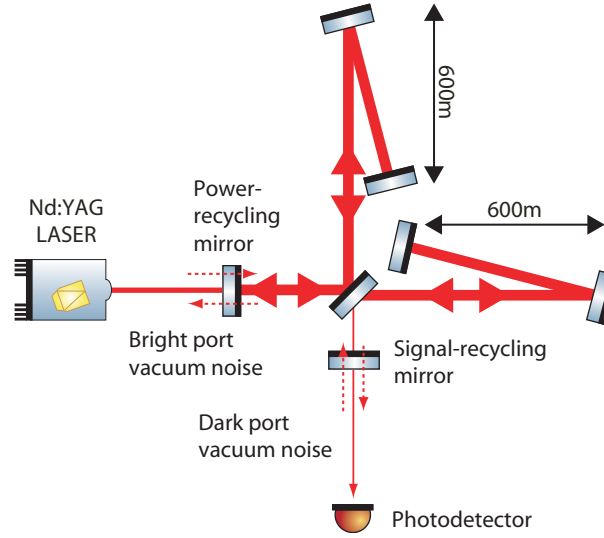


Figure 6.8: Simplified schematic of the gravitational wave detector GEO 600. The dashed arrows represent the relevant vacuum fields entering and leaving the interferometer if optical loss inside the interferometer can be neglected. Generally, the squeezed vacuum states need to be injected into the interferometer in such a way that they constructively interfere in the dark signal output port for all relevant frequencies.

operation the interferometer behaves like an almost perfect mirror for the carrier light entering from the bright port and for vacuum fluctuations entering from the dark port. Due to a small, but macroscopic, difference of the two arm lengths, which is needed for the Schnupp modulation [Sch88], the reflectivity of this mirror is frequency dependent. Thus, the amplitude reflectivity $r(\omega)$ changes at different sideband frequencies, relative to the carrier frequency. The decision as to which interferometer port the squeezed states will be injected into, is therefore dependent on the sideband frequency.

We can distinguish between three different cases. First, the interferometer has high reflectivities in the two interesting frequency regions: $r(\Omega_s) \approx r(2\omega_m \pm \Omega_s) \approx 1$. If so, we can inject the squeezed states at all frequencies from the dark port. These will then be perfectly reflected and we obtain the full improvement from the squeezing.

The second case is that we have a high reflectivity at the signal frequency Ω_s but high transmission at frequency $2\omega_m \pm \Omega_s$, $r(\Omega_s) \approx 1$; $r(2\omega_m \pm \Omega_s) \approx 0$. If we still injected all the squeezed states from the dark port, we would lose the squeezing at $2\omega_m \pm \Omega_s$, which results in a less sensitive interferometer. To solve this problem one might split the squeezed-light field in frequency space e.g. use a filter cavity. We then obtain a field that carries the low-frequency squeezing around Ω_s and a second field that is squeezed around frequencies $2\omega_m \pm \Omega_s$. The low-frequency squeezed field is injected through the dark port, whereas the second one has to be injected through the bright port together with the carrier field. This will then give the optimal performance increase one expects from using squeezed light. Instead of using a filter cavity, one might employ two independent sources of squeezed states with optimized nonclassical noise suppression in the audio and rf bands, respectively. The third case is that the interferometer reflectivity is still high at the signal

frequencies, $r(\Omega_s) \approx 1$, but has an intermediate reflectivity, $0 < r(2\omega_m \pm \Omega_s) < 1$, near twice the modulation frequency. In this case the power fraction of $r(2\omega_m \pm \Omega_s)^2$ has to be tapped off the high-frequency part of the squeezed field. This fraction has to be injected into the interferometer's bright port, whereas the remaining fraction is injected into the dark port, together with 100% of the low-frequency part of the squeezed field. In this way the squeezed field at high frequencies senses a Mach-Zehnder-type configuration and constructively interferes in the interferometer's (dark) signal port. Again the broadband squeezed field is optimally employed for a nonclassical sensitivity improvement of a gravitational wave detector with heterodyne readout. We note that in all these three cases one has to use frequency-dependent squeezed fields to compensate the phase shifts from the reflection at a detuned cavity [HCC⁺03, CVH⁺05].

GEO 600 currently uses a heterodyne frequency of 14.9 MHz. The reflectivity of the interferometer at this frequency is approximately 96% in power. Consider now a broadband vacuum squeezed field of 6 dB nonclassical noise suppression from 10 Hz up to 30 MHz injected into GEO 600's dark port. Neglecting optical losses inside the interferometer, the squeezed states at gravitational wave signal frequencies are perfectly reflected. Those at twice the heterodyne frequency sense 4% loss, and their nonclassical noise suppression degrades from 6 to about 5.5 dB, which is still a useful value. Hence the injection of the complete broadband vacuum squeezed field into the dark port seems to be a reasonable approach in the case of GEO 600.

6.6 Conclusion

We have reported on a control scheme for phase locking of squeezed vacuum fields, generated by optical parametric oscillation, to a local oscillator of a downstream experiment or of a homodyne detector. Our scheme utilized two frequency-shifted control fields that allowed us to control the length of the OPO cavity as well as the angle of the squeezed-field quadrature. This control scheme allowed stable generation and observation of broadband squeezed fields covering more than six decades from 10 Hz to about 35 MHz. We discussed the application of our control scheme and the broadband squeezed field generated for GEO 600, as an example for a large-scale gravitational wave detector. We found that such a squeezed field injected into the signal dark port can improve GEO 600's sensitivity beyond its shot noise limit, even if the current heterodyne readout is used.

Chapter 7

The potential of a squeezed-vacuum-enhanced GEO-HF

Currently the German-British collaboration GEO is running the GW detector GEO 600, which is close to reaching its design sensitivity (see Figure 7.1). In recent years GEO 600 has operated together with the LIGO detectors [AAD⁺92] in an international network of interferometers searching for gravitational waves. As soon as VIRGO [BFV⁺90] reaches its design sensitivity it will join this international network. All three projects plan to upgrade their GW detectors in the near future. The successor of GEO 600 is GEO-HF [WAA⁺06], which is currently planned to go online in 2010. Due to the limited infrastructure of GEO 600 the upgrade is planned in small sequential steps, which will be tested individually in prototypes first. Currently GEO 600 can compete with the longer interferometers of LIGO and VIRGO, because of signal-recycling [Mee88] (see Chapter 5). This gives the GEO team the flexibility of tuning the peak sensitivity of the detector to different frequencies.

Next generation detectors such as Advanced LIGO [Gia05, ADVa], Advanced VIRGO [ADVb] and LCGT [KtLC06] have an enormous advantage compared to GEO 600 in the low frequency range due to their long interferometer arms. Thus, there exist no plans for GEO 600 to match one of the other next generation detectors broadband sensitivities. The strategy of GEO-HF is to operate as a high-frequency detector in the kilohertz region to look for sources such as normal modes in neutron stars [Kok04] or quasi-normal modes in black holes. Hence, the upgrade will concentrate on lowering the limiting noise sources at high frequencies, shot noise and thermal noise. The latter is also responsible for the fact that GEO-HF cannot compete with other next generation detectors in the low frequency range. Nevertheless, the future plans for GEO-HF foresee that it can work together with the other detectors in a so-called network operation mode. Here, the signal recycling is tuned to optimize the low frequency performance and reach sensitivities comparable to LIGO and VIRGO. The network mode is important for GEO-HF to stay compatible with the frequency range of the other international GW wave detectors. Therefore it is a constraint that the low frequency performance is not deteriorated by the upgrade from GEO 600 to GEO-HF.

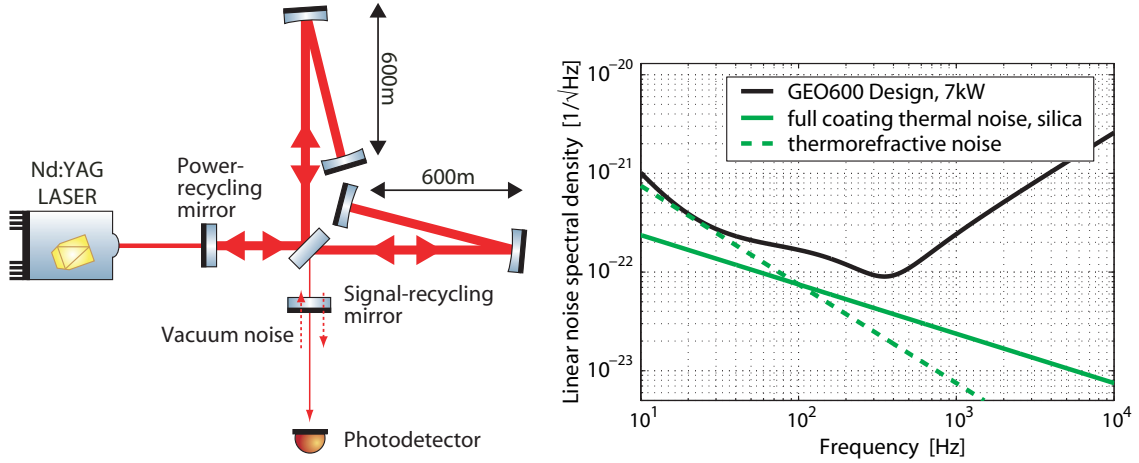


Figure 7.1: Schematic of the optical layout of GEO 600 and its quantum noise limited design strain sensitivity. The two limiting thermal noises are displayed as reference. Note, that the thermal noise will change if the main optics of the interferometer are exchanged.

7.1 The upgrade: From GEO to GEO-HF

The GEO-HF detector will be based on the current GEO 600 infrastructure. In fact even if one wants to increase the arm length, a river is prohibiting this. The optical scheme of the GEO 600 detector is presented in Figure 7.1. Since no major changes to the optical layout are planned in the upgrade, this figure also corresponds to the GEO-HF layout.

GEO 600 is a Michelson interferometer with an effective arm length of 1200m. The arms are folded once to fit into the 600m long vacuum tubes. The weight of each end mirror test mass is 5.6 kg. The laser source is a Nd:YAG laser with a wavelength of 1064nm and an output power of up to 12W. GEO 600 is currently the only GW detector that uses not only power recycling [DHK⁺83] but also signal recycling [Mee88]. The basic idea of power recycling is to send the light back into the interferometer that would normally propagate back to the laser. The regular working condition of the interferometer is to establish a dark port at the unused beam splitter port. Hence, all the light entering the interferometer leaves the interferometer via the same path. By placing the power-recycling mirror between the laser and the interferometer all the light is sent back into the interferometer and the circulating light power inside the interferometer increases. The power reflectivity of GEO 600's power-recycling mirror is $R_{\text{PRM}} = 99.9$, which results in a power recycling factor of approximately 1000. The sensitivity in the shot noise limited regime is therefore enhanced by a factor of 100, whereas the sensitivity is lower by a factor of 100 in the radiation pressure dominated area. Details of the power scaling of the quantum noise limited sensitivity of a Michelson interferometer based GW detector are discussed earlier in Chapter 4 (Figure 4.2). Signal recycling uses a mirror in the dark port to send the GW induced signal sidebands back into the interferometer. The repeated interaction with the end mirror test masses enhances the signal sidebands. Normally the signal-recycling cavity is slightly detuned from the carrier frequency to enhance the GW in a certain frequency range. The enhancement of the signal leads to an increased sensitivity.

Currently, the signal recycling detuning frequency of the GW detector GEO 600 is chosen to be 350 Hz, which can be changed easily by adjusting the microscopic position of the signal-recycling mirror.

Lowering the noise in the high-frequency regime

As mentioned before the limiting noise sources in the high-frequency range are shot noise and thermal noise. The thermal noise can be separated into different sources; the three largest being coating thermal noise [CCF⁺04], substrate thermal noise [LT00], and thermorefractive noise [BV01]. The first two result in a displacement of the mirror surface, whereas the thermorefractive noise causes fluctuations in the index of refraction and is therefore important for transmissive optics, such as the beam splitter. Here, GEO-HF has disadvantages compared to the other GW detectors, which use arm cavities to have large energies stored in the arms and still low power in the main beam splitter. The substrate thermal noise depends on the mechanical quality factor Q of the mirror substrates. New results from experiments [APF⁺04] and calculations [PAB⁺05] show that the Q -factor of the fused silica substrate used in GEO 600 has a least factor of ten higher Q -factor than assumed before. Hence, the substrate thermal noise is much smaller than the other two thermal noises and is not included in the following analysis. The coating thermal noise is the most dominant in the high-frequency range. It originates inside the alternating layers of the coating due to the non-homogeneity of the layer material and the layer connections. Note, all three noise sources are only material dependent and do not change with the power used inside the interferometer. The only way to change the coating thermal and thermorefractive noise is to change the main optics of the interferometer. Recent measurements [HABT⁺07] show that coating thermal noise can be improved by doping the Ta_2O_5 with TiO_2 . A different approach is to change the layer thickness to reduce the total amount of Ta_2O_5 , which mainly causes the coating thermal noise. A change of the main optics is not an easy task. All mirrors have to be suspended again and it would take at least several months to implement the new substrates into the vacuum system. Therefore it is currently planned not to change the main optics. Only if the development of new coatings and materials has advanced much further and if the achievable result is worth the amount of time and funds an exchange would be considered. However, the benefits could also lead to an increase in the sensitivity in the low frequency range, while the signal recycling parameters can be optimized to the network operation mode as well as to the high-frequency mode.

The aim in GEO-HF is to lower the limiting shot noise contributions. There exist three different methods that can be used to achieve this goal. All three methods will be discussed in the following.

Increasing the circulating laser power

To begin with, one can increase the circulating light power inside the interferometer. It is planned to add an amplifier in the current laser system, which can deliver of up to 200 W [WDF⁺06].

The aim is to increase the circulating light power by a factor of 10 compared to the

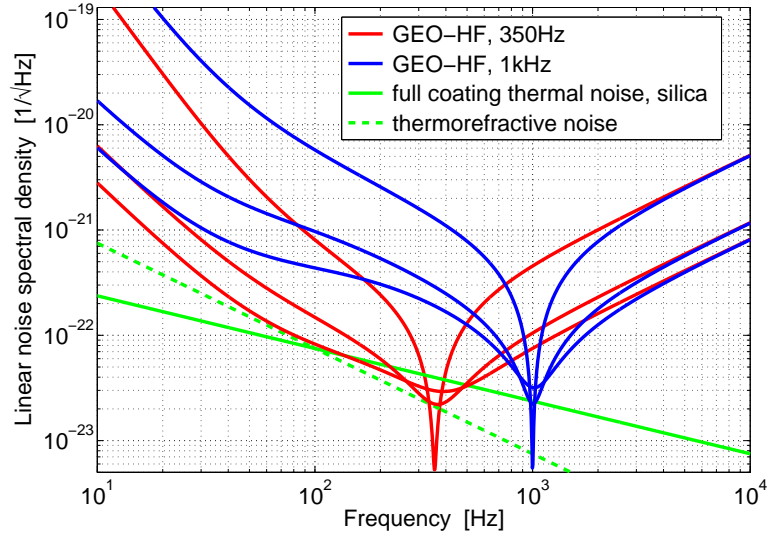


Figure 7.2: Strain sensitivities for different signal recycling factors ($R_{\text{SRM}} = 98.05\%$, $R_{\text{SRM}} = 99.05\%$ and $R_{\text{SRM}} = 99.95\%$ and two different signal recycling resonance frequencies [350 Hz (red curves) and 1 kHz (blue curves)]. The limiting thermal noises are given by the green curves.

current GEO 600 design, resulting in a decreased shot noise by a factor of $\sqrt{10}$. The total power inside the interferometer is then 70 kW, which will be assumed in the simulation presented in Section 7.2.

The higher circulating laser power results in a stronger thermal lens in the beam splitter, which causes a mode mismatch of the beams in the two interferometer arms. Hence, the dark-fringe contrast is deteriorated by an unacceptable amount. Currently, GEO 600 uses ring heaters [WAA⁺04] to compensate the thermal lens. In GEO-HF the level of aberration is much higher and it is currently not clear if the ring heater can still compensate the effects. A more sophisticated solution, based on a scanning CO₂ laser, has to be developed and tested in the prototypes before it can be installed into GEO-HF.

Changing the signal recycling parameters

The shot noise level and its characteristics can also be changed with the signal-recycling cavity. On one hand a change of the signal recycling factor results in a changing bandwidth of the signal recycling resonance. On the other hand the microscopic tuning of the signal-recycling mirror position can be freely adjusted, which results in a change of the signal-recycling cavity's resonance frequency. Both behaviors are displayed in Figure 7.2. Here, the quantum noise limited sensitivity of GEO-HF for two different signal recycling resonance frequencies and three different signal recycling factors is shown.

An increase in the signal recycling factor results in an improved sensitivity in a small frequency range, whereas a lower signal recycling factor can be used for a broadband enhancement with reduced peak sensitivity. The signal recycling factor changes with the reflectivity of the signal-recycling mirror. Hence, it cannot be changed while the detector

is running. The vacuum system has to be opened to switch from one signal-recycling mirror to a different one. Thus, a tradeoff is needed between the maximum sensitivity in the high frequency range and a sensitivity in the network operation mode which closely matches the LIGO or VIRGO curve. Figure 7.2 shows that an increase of the signal recycling factor makes almost no sense in combination with a power increase. The current signal-recycling mirror reflectivity $R = 98.05\%$ would already result in a clearly thermal noise limited sensitivity in the network mode with a detuning frequency of 350 Hz. Even for a detuning of 1 kHz the sensitivity gets very close to thermal noise with the current signal recycling factor. A potential solution is to use an etalon as a signal-recycling mirror thereby enabling easy adjustment of the signal recycling factor [Hil03]. A change in the longitudinal length of the etalon, e.g. caused by thermal heating, would result in a change of the effective reflectivity. Hence, an adjustment of the signal recycling factor could be achieved quite easily. However, before the signal-recycling mirror would be exchanged by an etalon, detailed tests would have to be performed in one of the prototypes first.

The microscopic tuning of the signal-recycling mirror can be used to shape the shot noise limited sensitivity. In Figure 7.2 three different signal recycling factors are given for two different signal recycling tunings, 350 Hz and 1 kHz. Because the tuning is given by the microscopic position of the signal-recycling mirror, this is easily changed during the operation of the interferometer. The tuning can be changed continuously in a frequency range from about 250 Hz up to several kilohertz, thereby allowing smooth changes of the shot noise characteristics in the higher frequency range. As described later it can also be quite useful to switch from detuned signal recycling to tuned signal recycling.

Squeezed-light enhancement

A completely different way to enhance the shot noise limited sensitivity of a GW detector is to use squeezed vacuum (see Chapter 6) to replace the ordinary vacuum fluctuations entering the interferometer through its dark port. A Faraday rotator has to be incorporated into the dark port of the interferometer for injection of the squeezed state. As seen in Chapter 4, the reflection of initially frequency-independent squeezed vacuum at the detuned signal-recycling cavity results in frequency-dependent squeezed light and the sensitivity can only be enhanced in a small frequency range (see Figure 4.6). To compensate the effects of the signal-recycling cavity, a filter cavity is needed (details in Chapter 5). The initial frequency-dependent squeezed vacuum is first reflected at the filter cavity before it is injected into the signal-recycling cavity. The resulting sensitivity is improved by the square root of the squeezing strength over the full shot noise limited range.

In the following section the potential improvements to GEO-HF's sensitivity using squeezed-vacuum injection are simulated and discussed.

7.2 Possible increase in GEO-HF's sensitivity due to squeezed vacuum

In this section simulations of GEO-HF's sensitivity are presented and discussed. The MATLAB code is based on the input-output formalism and includes radiation pressure

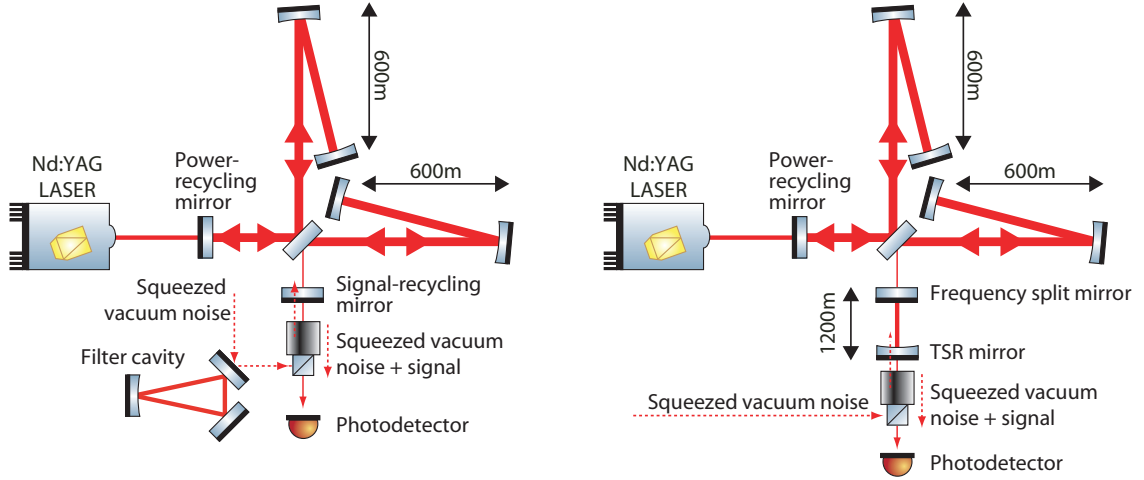


Figure 7.3: Schematic of the potential optical layouts of GEO-HF. The left-hand figure shows the dual-recycled Michelson interferometer configuration with squeezed-vacuum injection. To gain a broadband improvement in the shot noise limited regime a filter cavity has to be incorporated, as well as the required Faraday rotator. The right-hand figure displays the optical layout of the twin-signal recycling (TSR) configuration, which uses an additional cavity in the dark port instead of the signal-recycling mirror.

noise. Details of the formalism can be found in [Har06]. The calculated sensitivities only include radiation pressure noise and shot noise. All other noises are not included in the model. Because GEO-HF will be used as a high-frequency GW detector, the optical spring [HCC⁺03] is suppressed in the simulations by tuning the signal-recycling cavity to the sideband, where the optical spring is damped instead of resonantly enhanced. In all simulated sensitivities presented in this section the two dominating thermal noises—coating thermal noise and thermorefractive noise—of the actual main optics are given as references. They are not included in the calculation of the sensitivity since a reduction in thermal noise is still possible by changing the main optics of the interferometer.

Additional optics are needed to enhance GEO-HF’s sensitivity by using squeezed vacuum. The Faraday rotator in the dark port for injection of the squeezed vacuum is the first of such optics. Additionally, a filter cavity has to be implemented which cancels the rotation of the squeezing ellipse due to reflection at the detuned signal-recycling cavity. Recently, a new interferometer topology called twin-signal recycling (TSR) has been suggested by Thüring [TSLD07]. TSR uses a linear cavity instead of a signal-recycling mirror, thereby forming a three-mirror cavity [Thü04] together with the Michelson interferometer. Such a three-mirror cavity has a resonance doublet and the two resonances are separated by the frequency ν_{split} . If this resonance doublet is chosen to be symmetrically around the carrier frequency ν_0 the TSR interferometer acts almost like a detuned signal-recycled Michelson interferometer with a detuning frequency of $\nu_{\text{split}}/2$. The difference with respect to the signal recycling configuration is the TSR configuration recycles both GW induced signal sidebands, which results in a direct sensitivity improvement by a factor of two. The other interesting feature of the TSR configuration is that it does not need an additional filter cavity in combination with squeezed vacuum. Because of its

double resonance feature the squeezed vacuum does not become frequency-dependent on reflection. The drawback of the TSR configuration is implementation into the vacuum system. If one analyzes the parameters of such a configuration, one realizes the length of the additional cavity in the dark port is 1200 m. Details on the possible implementation of the TSR configuration and of a filter cavity are discussed in Section 7.3. The schematics of the optical layouts of a squeezed-vacuum-enhanced GEO-HF detector using detuned signal recycling of TSR are displayed in Figure 7.3.

Currently, the upgrade to GEO-HF includes a power increase by a factor of ten and a concentration on the high-frequency range. Additionally, presuming that a source for generating the squeezed vacuum produces 10 dB of squeezing such that with a total loss of 17%, 6 dB will be detected by the photodetector, then an improvement of the shot noise limited sensitivity by a factor of two would be possible (see Section 5.4.1). Starting with these facts and not changing the current signal recycling factor, one obtains the sensitivity given in Figure 7.4. This figure compares the two different modes of operation—the network mode (upper graph) and the high-frequency mode (lower graph). The design sensitivity of GEO 600 is given by the black curve. For simulation of the network mode, a detuning of the signal-recycling cavity of 350 Hz is chosen. The power increase by a factor of ten results in the red curve. This sensitivity is already thermal noise limited between 150–500 Hz. With additional 6 dB squeezing, one obtains the blue curve, which is limited by the thermal noise between 25–800 Hz. For frequencies above 800 Hz its sensitivity is a factor of two below the non-squeezed-vacuum-enhanced sensitivity. The high-frequency mode is simulated by detuning the signal-recycling cavity to 1 kHz. The non-squeezed-vacuum-enhanced sensitivity (red curve) reaches almost the thermal noise at 1 kHz. The squeezed-vacuum-enhanced sensitivity (blue curve) has a peak sensitivity of $\dot{h} = 1.6 \times 10^{-23}$ at 1 kHz, which is limited by the coating thermal noise around 1 kHz. As a consequence such a design of the signal-recycling cavity is not favorable.

If the actual signal recycling reflectivity is reduced from $R_{\text{SRM}} = 98.05\%$ to $R_{\text{SRM}} = 88\%$ and the detuning frequency is increased to 1 kHz, one obtains the results presented in Figure 7.5. The differences of the detuned signal recycling configuration between the network mode and the high-frequency mode are most significant in the high-frequency range. The changes in the mid-frequency range are quite small. To summarize, the non-squeezed-vacuum-enhanced sensitivity is limited by thermal noise only in a small frequency range, whereas the squeezed-vacuum-enhanced sensitivity is limited by thermal noise below frequencies of 600–800 Hz and shows the expected improvement by a factor of two in the higher frequency range.

Another feature, also visible in the sensitivity of this configuration, is the lack of improvement by squeezed-vacuum injection in the radiation pressure dominated low-frequency regime. Moreover, in the network mode, the sensitivity with the squeezed vacuum in the radiation pressure dominated frequency range is worse than the normal sensitivity. For an improvement in this frequency range a second filter cavity is needed to compensate the radiation pressure effects [KLM⁺01]. Because the limiting noise source of GEO-HF in this frequency range will be seismic noise, this behavior will not be analyzed or discussed any further.

Figure 7.5 also comprises the results of the TSR configuration in the two possible operation modes of the GW detector. Note, that this comparison is purely theoretical,

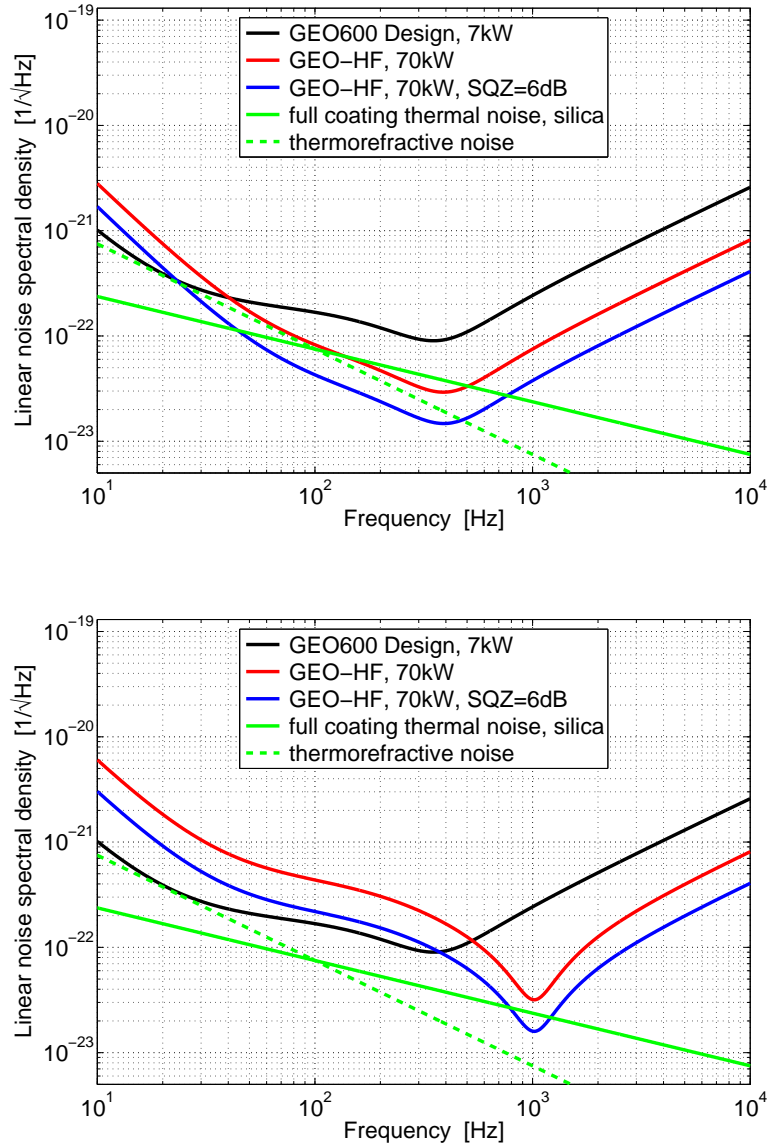


Figure 7.4: Comparison of GEO-HF’s quantum noise limited strain sensitivities in the two different operation modes for a detuned signal recycling configuration with $R_{\text{SRM}} = 98.05\%$. As a reference the actual GEO 600 design sensitivity is given by the black curve. A power increase by a factor of ten leads directly to the non-squeezed-vacuum-enhanced sensitivity (red curve) and the 6 dB squeezed-vacuum-enhanced sensitivity (blue curve) of GEO-HF. As one can see even the non-squeezed-vacuum-enhanced sensitivity in the network operation mode (upper graph) is limited by thermal noise. The high-frequency operation mode uses a detuning of 1 kHz and the results are comprised in the lower graph. Here, the squeezed-vacuum-enhanced sensitivity is limited by thermal noise near the resonance frequency.

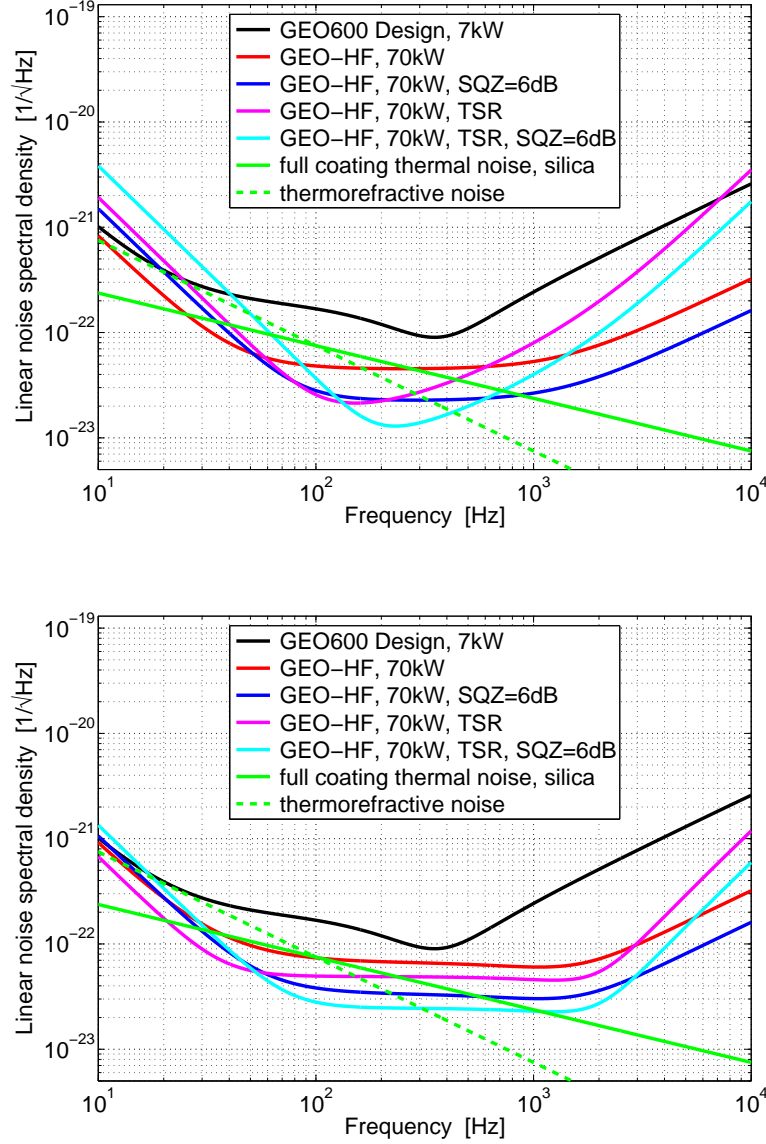


Figure 7.5: Comparison of GEO-HF's quantum noise limited strain sensitivities in the two different operation modes for a detuned signal recycling configuration with $R_{\text{SRM}} = 88\%$ and for the TSR configuration. As a reference the actual GEO 600 design sensitivity is given by the black curve. The network operation mode is displayed in the upper graph, which can be compared directly to the high-frequency operation mode given by the lower graph. As one can see the TSR configuration performs less well than the detuned signal recycling configuration in the network operation mode if the limiting thermal noise is taken into account. But in the high-frequency operation mode it performs better than the detuned signal recycling configuration below 3 kHz but worse above.

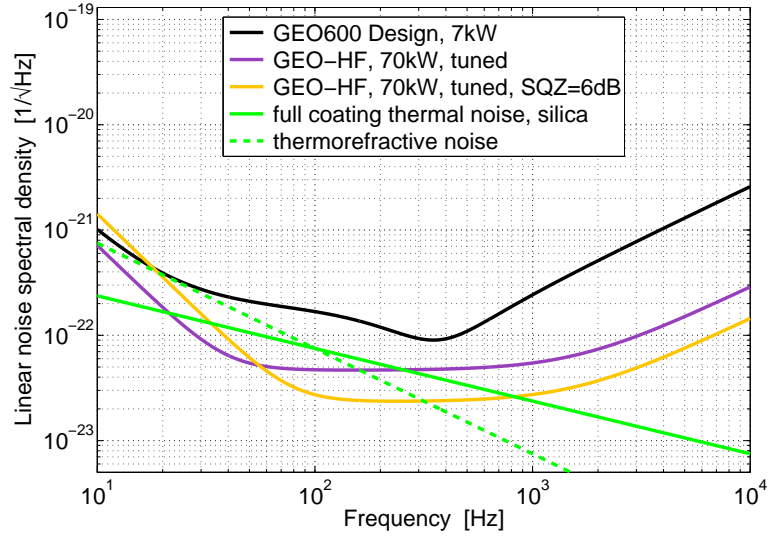


Figure 7.6: GEO-HF’s quantum noise limited strain sensitivities for a tuned signal recycling configuration with $R_{\text{SRM}} = 80\%$. Such a configuration has a large bandwidth but still a very good peak sensitivity. Because this configuration lacks the tuning feature, the displayed result applies to the network operation mode as well as to the high-frequency operation mode.

because the required tuning feature to get from one detector mode into the other is missing or at least complicated to achieve. To tune the resonance frequency the reflectivity of the split-frequency mirror¹ of the TSR cavity has to be changed. This can only be achieved by changing the mirror, which is not practical or one has to use an etalon as a split-frequency mirror. Using the etalon turns the initial three mirror cavity in principle into a four mirror cavity. Nevertheless, it is worth investigating the performance of this configuration in the two different operation modes. Comparing the two results of the TSR configuration, one realizes that the network mode is worse than the high-frequency mode. The improvements in the network mode around the resonance frequency are limited completely by the thermal noise and even at all other frequencies the performance is worse compared with the TSR sensitivity in the high-frequency operation mode. This is because the TSR configuration has a cavity pole of second order, therefore the sensitivity above the resonance frequency falls off much faster than the detuned signal recycling configuration.

Comparing the results of the TSR configuration with the ones of the detuned signal recycling configuration, one sees that the TSR configuration can only compete in the high-frequency operation mode. In the mid-frequency range its sensitivity is slightly better than that of the detuned signal recycling configuration. Above 3 kHz the TSR configuration performs worse because of the second order cavity pole.

It turns out that there is a third good configuration for GEO-HF: the tuned signal recycling configuration. Compared to the detuned signal recycling configuration, the tuned one has its resonance at the carrier frequency. The advantage of the tuned configuration

¹The split-frequency mirror is the TSR cavity mirror, located more closely to the beam splitter of the Michelson interferometer.

is the recycling of both GW induced signal sidebands. This doubles the signal and leads to an increase in sensitivity by a factor of two. Moreover, the tuned signal recycling configuration does not need a filter cavity for the preparation of the injected squeezed vacuum. Hence, a tuned signal recycling configuration is much easier to establish, no additional optics or changes to the optical layout are needed. This simplicity makes it very attractive as a potential configuration used in GEO-HF. However, the tuned configuration lacks the tuning feature. It is not possible to switch between the two desired operation modes. To reach a comparable sensitivity as the two prior discussed configurations, the reflectivity of the signal-recycling mirror has to be reduced to $R_{\text{SRM}} = 80\%$. The resulting sensitivity with and without squeezing is presented in Figure 7.6. One sees the achievable sensitivity without squeezing is limited by thermal noise below 250 Hz, whereas the squeezing-enhanced sensitivity is limited below 900 Hz. A direct comparison between the tuned signal recycling, detuned dual recycling and the TSR configurations is displayed in Figure 7.7. For a clear view only the squeezed-vacuum-enhanced sensitivities are shown. The tuned configuration is as good as the detuned case in the network mode and even better in the high-frequency mode. This is a remarkable result, although the detuned case allows an optimization to a specific frequency it cannot beat the tuned signal recycling configuration. Comparing the TSR configuration with the tuned signal recycling configuration, one sees that the peak sensitivity of the TSR configuration in the network mode is better but the peak sensitivity is still largely limited by the thermal noise. The bandwidth of the tuned signal recycling configuration is much broader, which gives it a big advantage. In the high-frequency operation mode the differences are small. The TSR configuration performs a little bit better between 1 kHz and 3 kHz, but slightly worse for larger frequencies.

In summary, all three possible configurations show almost identical results. Every configuration has its own advantages and disadvantages. Before concluding which configuration would be the best to use in GEO-HF, a detailed analysis of the implementation of the additional required optics and its parameters is presented in the next section.

7.3 Parameters and implementation of the required additional optics

The main challenge for the detuned signal recycling configuration will be the implementation of the required filter cavity into the current vacuum system. The same applies to the 1200 m long linear cavity needed for the TSR configuration. Hence, the parameters of the cavities and their implementation into the existing infrastructure will be discussed in this section. A schematic of the optical layout and the vacuum system is given in Figure 7.8. The laser system consists of a master and an injection-locked slave system delivering up to 12 W at a wavelength of 1064 nm. This laser beam is stabilized and its TEM_{00} mode filtered by two suspended modecleaner ring cavities, housed in the vacuum system directly in front of the dual recycled Michelson interferometer. The power-recycling mirror and the signal-recycling mirror are placed very close to the interferometer's beam splitter. The distance is measured to be about 1.1 m. The interferometer arms are folded in the vertical plane. The folding mirrors (MFN and MFE) are placed in a 600 m distant vac-

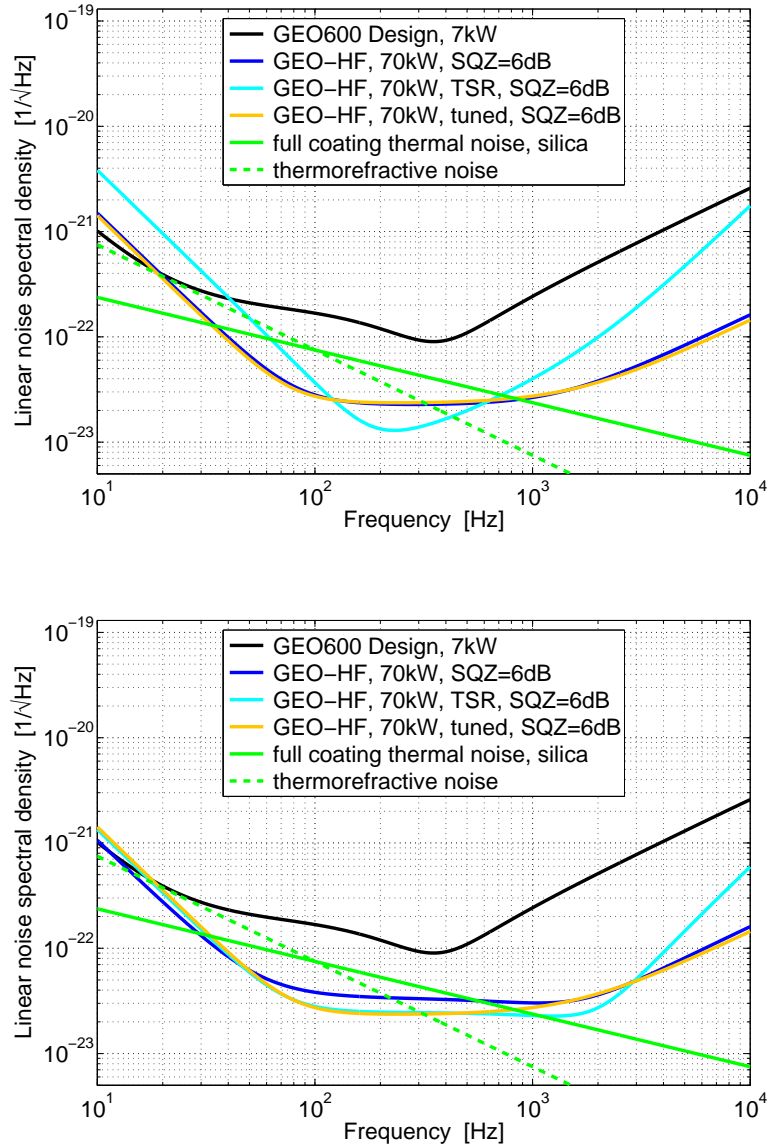


Figure 7.7: Comparison of GEO-HF’s quantum noise limited strain sensitivities in the two different operation modes for a detuned signal recycling configuration with $R_{\text{SRM}} = 88\%$, for the TSR configuration and for the tuned signal recycling configuration with $R_{\text{SRM}} = 80\%$. As a reference the current GEO 600 design sensitivity is given by the black curve. The network operation mode is displayed in the upper graph, which can be compared directly to the high-frequency operation mode given by the lower graph. One sees that the tuned signal recycling configuration competes with the other two configurations.

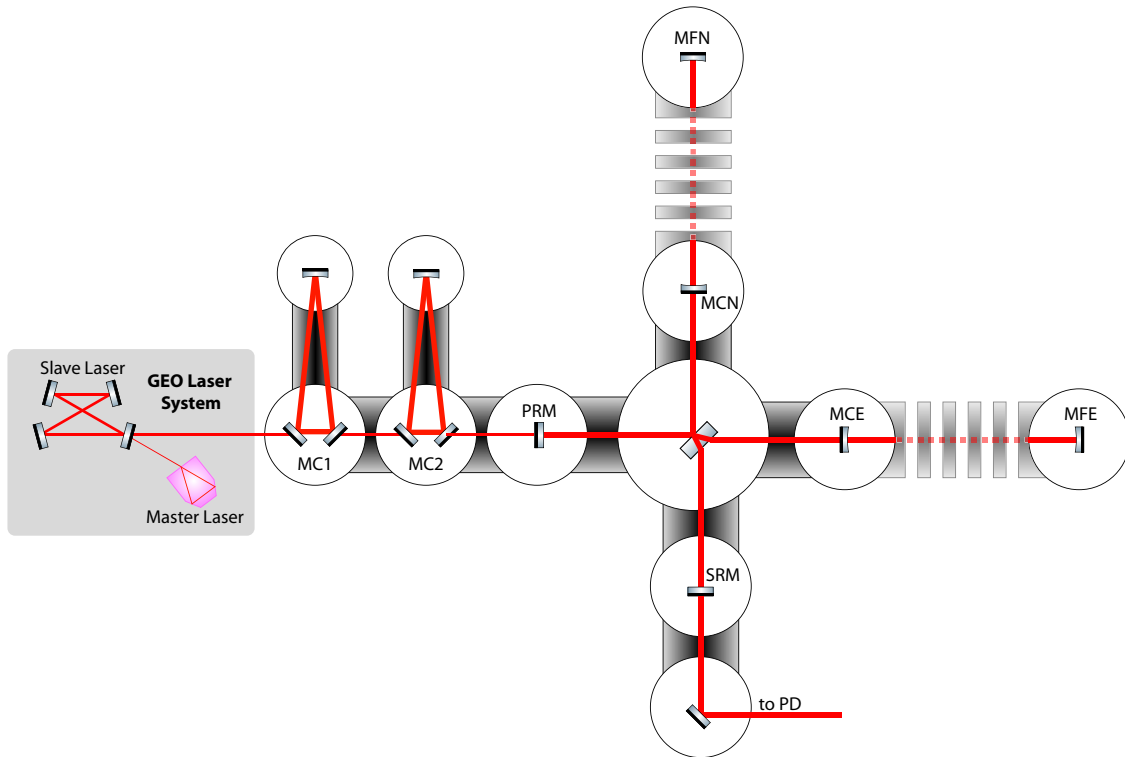


Figure 7.8: Schematic of the optical layout and the corresponding vacuum system of the current GEO 600 gravitational wave detector. The laser system is composed of a master and an injection-locked slave system that can deliver of up to 12 W at a wavelength of 1064 nm. Two suspended modecleaners in the vacuum system are used to stabilize the beam and supply a pure TEM_{00} mode for the dual recycled Michelson interferometer. The folding mirrors (MFN and MFE) are separated from the beam splitter by 600 m. These folding mirrors send the light back through the arm to the central mirrors (MCN and MCE). From here the light is reflected back to the folding mirrors and then to the beam splitter. Folding of the arms results in an effective arm length of 1200 m.

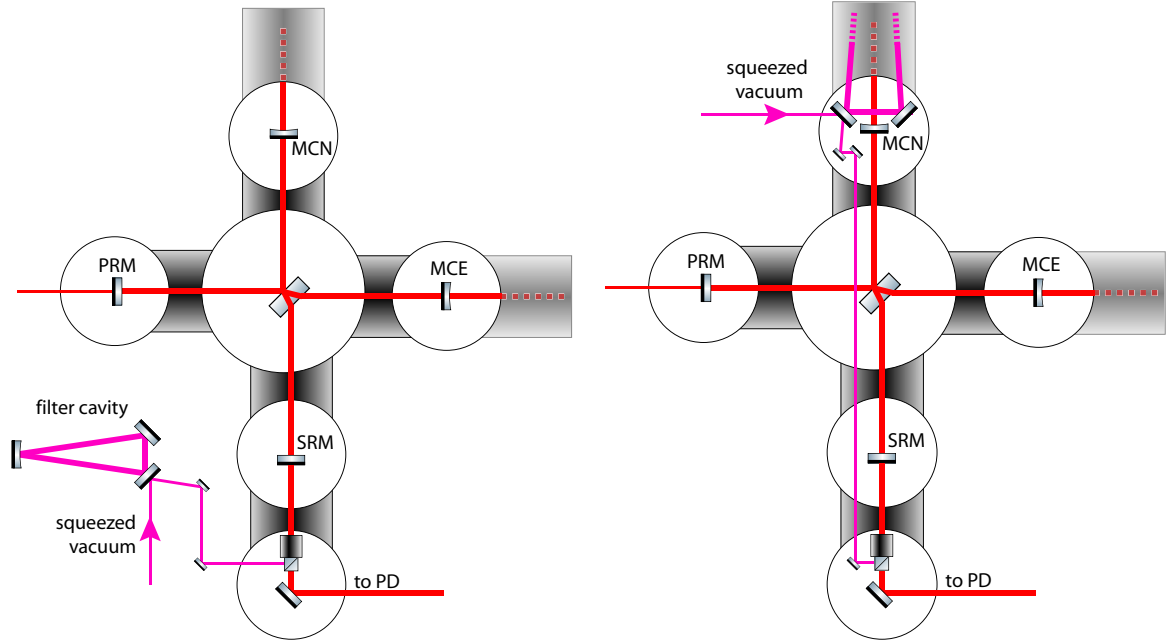


Figure 7.9: Schematic of the optical layout and the vacuum system for implementation of a short (left) or a long filter cavity (right) into the current infrastructure. To easily distinguish between the squeezed vacuum and the interferometer beams their colors are different.

uum tank and from here the laser beam is guided to the central end mirrors (MCN and MCE). The beam is reflected upon itself and propagates back to the folding mirror and hence to the beam splitter. The detection of a GW signal is made with photodetector placed in the south arm behind the signal-recycling mirror outside the vacuum system.

7.3.1 A short filter cavity

The first configuration to be analyzed is the use of a short filter cavity in combination with a detuned signal recycling Michelson interferometer. In the following, a reflectivity of the signal-recycling mirror of $R_{\text{SRM}} = 88\%$ is assumed as it is used in the simulation presented in Figure 7.5. The important parameters of the signal-recycling cavity are: length $L = 1200$ m, finesse $\mathcal{F} \approx 49$, free-spectral range $\text{FSR} \approx 125$ kHz and linewidth $\Delta\nu = 2.56$ kHz. To compensate the rotation of the squeezing ellipse, the filter cavity needs to match the linewidth under all circumstances. A short ring-shaped filter cavity with an optical length of 8 m can easily be incorporated into the current infrastructure of the detector (see Figure 7.9). Additionally, a Faraday rotator is needed to inject the squeezed vacuum into the interferometer. To match the linewidth of the signal-recycling cavity, the short filter cavity needs an input coupling mirror with a transmissivity of $T_{\text{coupler}} = 310$ ppm and a loss of 10 ppm. The other two mirrors of the ring-shaped filter cavity have to have a transmissivity of 50 ppm and a loss of 5 ppm. These specifications are high and very close to the limit currently achievable with the best optics and coatings. The finesse of this 8 m long suspended cavity is $\mathcal{F} \approx 14600$. Hence, the lock acquisition

would be hard to achieve. It seems an 8 m long filter cavity is not the optimal solution in terms of optics quality and lock acquisition.

7.3.2 A long filter cavity

A different option is to integrate a ring-shaped filter cavity into the northern interferometer arm (Figure 7.9). The squeezed vacuum has to be injected into the vacuum tank housing the northern central mirror (MCN) and the two mirrors of the filter cavity. The northern folding mirror (MFN) can be used as well as the third mirror for the filter cavity. This would simplify the integration of the new optics. The squeezed vacuum is reflected at the filter cavity and guided south through the vacuum system to the Faraday rotator, which injects the squeezed vacuum into the interferometer. On its way south the most problematic areas are the beam splitter tank and a gate valve used for sealing the signal-recycling mirror from the rest of the vacuum system.

The long round-trip length of 1200 m allows the use of more moderate optics parameters, assuming the results presented in Figure 7.5. The input coupling mirror of the filter cavity has a reflectivity of $R_{\text{coupler}} = 93.8\%$ and a total loss of 0.1%. The other two mirrors of the ring-shaped filter cavity have a transmissivity of 150 ppm and a loss of 10 ppm. These specifications are the same as for the current folding mirrors. The finesse of the 1200 m long filter cavity is $\mathcal{F} \approx 98$, which is only about a third of the actual signal recycling finesse used in GEO 600. Hence, the lock acquisition and control of this filter cavity should be much easier. The biggest concerns about the long filter cavity are the installation of the mirrors and guiding the squeezed vacuum through the vacuum systems. However, if one wants to use a detuned signal recycling configuration in combination with squeezed-vacuum injection, the 1200 m long filter cavity is stringently required.

7.3.3 Twin-signal-recycling cavity

A further alternative is to change the optical layout of GEO-HF from a detuned signal recycling Michelson interferometer to a TSR Michelson interferometer. As suggested in [TSLD07], an additional 1200 m long linear cavity in the dark port of the interferometer would replace the signal-recycling mirror. The two cavity mirrors are the split-frequency mirror (MSPLIT) and the twin-signal-recycling mirror (MTSR). A potential layout of the implementation of the TSR cavity into the existing vacuum system is presented in Figure 7.10. Note that the former signal-recycling mirror is replaced by the MSPLIT. The light leaving the interferometer is then guided to the northern folding mirror, which sends the light to the MTSR housed near the MCE. From here the light propagates southwards to the photodetector. On its way, the light passes a Faraday rotator needed for injection of the squeezed vacuum. The integration of this 1200 m long linear TSR cavity is hard to establish due to the complex and long beam path through almost the entire vacuum system.

The optic parameters are moderate. If one assumes the results presented in Figure 7.5, the reflectivity of MTSR is $R_{\text{MTSR}} = 80\%$ with a loss of 0.1%. As mentioned earlier the reflectivity of MSPLIT determines the split frequency and thereby the detuning frequency. Hence, the reflectivity changes with the desired operation mode of the GW detector.

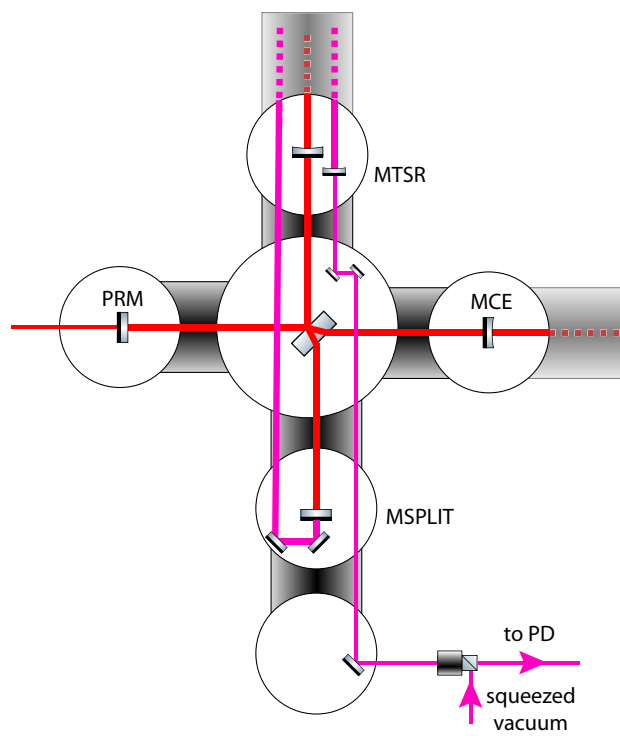


Figure 7.10: Schematic of the optical layout and the vacuum system for integration of a TSR configuration into the current infrastructure

The network operation mode with a detuning of 350 Hz needs a MSPLIT reflectivity of $R_{\text{MSPLIT}} = 99.88\%$ and the high-frequency operation mode demands a reflectivity of $R_{\text{MSPLIT}} = 98.99\%$. The deviation of the reflectivities of the MSPLIT for the two operation modes is small and a tiny aberration from the desired reflectivity of the mirror would cause a change in the detuning frequency. The lacking feature of an easy change of the resonance frequency during the operation of the interferometer is the obstacle of the TSR configuration.

7.4 Conclusion

The three possible optical configurations have their own advantages and disadvantages.

The TSR configuration in the high-frequency operation mode shows the best sensitivity in the mid frequency range, which is mostly covered by thermal noise. At high frequencies its sensitivity decreases much faster than the other configurations (Figure 7.7). The implementation into the existing infrastructure is comparably complex to a 1200 m long filter cavity, but the biggest problem is the lack of the ability to change the detuning frequency easily.

The detuned signal recycling configuration is only practicable with the 1200 m long filter cavity. The integration of the filter cavity into the setup is a challenging task, but can be achieved. The sensitivity is comparable to the other configurations and the tuning feature allows an easy change of the resonance frequency even to higher frequencies than 1 kHz.

The easiest configuration in terms of implementation into the current infrastructure is the tuned signal recycling configuration. The only additional optic required is the Faraday isolator. No filter cavity is needed to achieve a broadband improvement in the shot noise limited frequency range by squeezed-light injection. To achieve a high bandwidth of the signal-recycling cavity the signal-recycling mirror has to be exchanged, which has to be done in the other two configurations as well. The performance of this configuration in the high-frequency operation mode is almost the same as for detuned signal recycling. In the network operation mode it offers the best sensitivity taking thermal noise into account.

In conclusion, the tuned signal recycling configuration seems to be the best choice. Only if the tuning feature is needed, one should aim for the detuned signal recycling configuration. The TSR configuration could be better than the detuned Michelson interferometer configuration if and only if the split-frequency mirror is exchanged with another linear cavity. This would change the TSR from a three mirror cavity to four mirror cavity, which would allow a tuning of the resonance frequency. It seems that more prototype testing is required until a final decision for the optical configuration of GEO-HF can be made.

Appendix A

Matlab scripts

A.1 The reconstruction of the Wigner function from the measured data

Before the reconstruction of the Wigner function can be obtained the measured data has to be stored with the DAQ system. Note that the file format of the stored data looks like the following:

```
%START
# in bin 1, angle=180°*1/Nangle
# in bin 2, angle=180°*1/Nangle
.
. until total numbers of bins = Nbin reached
.
# in bin=Nbin, for angle=180°*1/Nangle
# in bin 1, for angle=180°*2/Nangle
# in bin 2, for angle=180°*2/Nangle
.
. until total numbers of bins = Nbin reached
.
# in bin=Nbin, for angle=180°*2/Nangle
.
. until total step number Nangle for the angles is reached
.
# in bin=Nbin, for the angle=180°*Nangle/Nangle
%END
```

This file format was chosen by B. Hage, who was responsible for the development of the DAQ system.

The MATLAB code for the reconstruction of the Wigner function from these measured data file is given by:

```
name=importdata('VaK15M.txt');
% import the measured histograms of the vacuum state
%name=importdata('L14M1.txt');
```

```

% import measured histograms of the squeezed state;
Nangle=102; % number of measured histograms between 0-180° + 2
Nbin=100; % number of bins
Spalte=1; % column of interest
for k=1:Nangle for l=1:Nbin pname(l,k)=name(l+Nbin*(k-1),Spalte);
end; end;
% store data from file into the matrix pname
wname=iradon(pname,180/Nangle,0.9); %inverse radon transformation of pname

sigm=(4.669+4.785)/2; % standard deviation of the vacuum state,
%this is derived by
%typing in the console:
%fit((1:length(wname))',(wname(length(wname)/2,:))', 'gauss1')
%-> c is vacuums-sigma in one quadrature oder
%fit((1:length(wname))',(wname(:,length(wname)/2))', 'gauss1')
%-> c is vacuums-sigma a quadrature 90° to the first one

eins=2*sqrt(log(2))*(sigm); % normalization factor
%% START normalization to satisfy that the integrated wigner function = 1
% summe=sum(sum(wname));
% dingel=dingel*eins*eins/summe;
%% END normalization to satisfy that the integrated wigner function = 1

%%% START normalization to a min value of 0 and a max value of 1
% This is useful to compare different plots against each other
tmp=wname-(min(min(wname))); mywigner=tmp/(max(max(tmp)));
null=length(mywigner)/2; %axis scaling factor
%%% END normalization

%%% Start plotting a surface plot
scrsz = get(0,'ScreenSize'); % get screen size
figure('Position',[10 40 scrsz(3)/1.3 scrsz(4)/1.2])
% set plot window size
surface(mywigner','FaceColor','interp','LineStyle','none');
set(gcf,'Renderer','painters'); grid on view(0,90)
XLim([null-2*eins null+2*eins]) YLim([null-2*eins null+2*eins])
axis square; colorbar set(gca,'XTick',[null-5*eins null-4*eins
null-3*eins null-2*eins null-eins null null+eins null+2*eins
null+3*eins null+4*eins null+5*eins]);
set(gca,'XTickLabel',{'-5','-4','-3','-2','-1','0','1','2','3','4','5'});
set(gca,'YTick',[null-5*eins null-4*eins null-3*eins null-2*eins
null-eins null null+eins null+2*eins null+3*eins null+4*eins
null+5*eins]);
set(gca,'YTickLabel',{'-5','-4','-3','-2','-1','0','1','2','3','4','5'});

```


A.2 Calculation of GEO-HF's quantum noise limited sensitivity

In this section the basic MATLAB code is presented to calculate the quantum noise limited sensitivity of GEO-HF with and without squeezed input. This code is based on the input-output formalism and includes radiation pressure effects details can be found in [Har02]. The code was developed by J. Harms and has been slightly modified to fit the needs of this simulation.

```
clear;
%physical constants
c=299792458; hbar=1.054e-34;
%Calculation of SQZ-Input at GEO-MultiCav parameters
m=5.6;           % mirror mass
Lsr1=1200;      % length of the arms
Pin=70;         % input power
Parm=500*Pin;   % power in arms due to PRC
o=1.77e15;      % angular laser frequency
rend=1;         % end mirror reflectivity
rsr1=sqrt(0.8805); % signal recycling mirror reflectivity
tend=sqrt(1-rend^2); % end mirror transmissivity
tsr1=sqrt(1-rsr1^2); % signal recycling transmissivity
phisr1=-(2*pi*1000*Lsr1/c); % detuning phase for 350 Hz

% Frequency range of interest from 10^fmin to 10^fmax
fmin=0; fmax=4;
steps=2000;     % number of frequency bins

% Variable initialization
Ein=[1 0; 0 1]; % Unity matrix
data=[]; thermal=[];

for f=logspace(fmin,fmax,2000) % begin of calculation
ctn=0.75e-21./f^0.5; % coating thermal noise
trtn=0.75e-20./f; % thermorefractive noise
thermal=[thermal; [ctn trtn]];
h=sqrt(20*hbar/m/Lsr1^2/(2*pi*f)^2); %S QL für GEO600
K=4*Parm*o/(m/5)/c^2/(2*pi*f)^2; % optomechanical coupling
KM=[1 0;-K 1]; % coupling matrix
Psr1=[cos(phisr1) -sin(phisr1); sin(phisr1)
      cos(phisr1)]*exp(i*2*pi*f*Lsr1/c); % Propagation matrix
r=0.690775527898; % squeezing value for 6dB squeezing
sphi=pi/10*9.5; % squeezing angle
SQ=[cosh(r)+sinh(r)*cos(2*sphi), sinh(r)*sin(2*sphi);
    sinh(r)*sin(2*sphi) cosh(r)-sinh(r)*cos(2*sphi)];
%Squeezing matrix
```

```

% enhancement in Cav-Sr1
Insr1=tsr1*inv(Ein-rsr1*rend*Psr1*KM*Psr1);
RHOSr1=(rsr1*Ein-rend*Psr1*KM*Psr1)*inv(Ein-rsr1*rend*Psr1*KM*Psr1);

% Rotation of noise transfer in quadrature: multiply RHOSr1 with (0,1)
% and take arctan(y/x)
Rotrefp=RHOSr1*[0;1];
Rotrefanglep=atan((Rotrefp(2))/(Rotrefp(1)))/pi*180;
Rotsig=Insr1*[0;1];
Rotsigangle=atan((Rotsig(2))/(Rotsig(1)))/pi*180;

% optimum squeezing angle
T11=RHOSr1(1,1); T12=RHOSr1(1,2); T21=RHOSr1(2,1);
T22=RHOSr1(2,2);

% determining the noise quadrature rotation w/o optimal Squeezing
RHOWos=(rsr1*Ein-rend*Psr1*Psr1)*inv(Ein-rsr1*rend*Psr1*Psr1);
RHOnoise=RHOWos*[1;0]; ANGwos=atan((RHOnoise(2))/(RHOnoise(1)));

% RHO für squeezing
RHOSqz=RHOSr1*SQ;

% signal transfer through the interferometer
sig=sqrt(1)*Insr1*Psr1*rend*KM*[0;1]*sqrt(2*K)/h;

% determining the optimal homodyne detection angle (see Harms PRD 68
Tsym=RHOSr1*transpose(conj(RHOSr1));
Ssym=1/2*(sig*transpose(conj(sig))+conj(sig)*transpose(sig));
Q11=Ssym(1,1)*(Tsym(1,2)+Tsym(2,1))-Tsym(1,1)*(Ssym(1,2)+Ssym(2,1));
Q12=Ssym(1,1)*Tsym(2,2)-Tsym(1,1)*Ssym(2,2);
Q22=Tsym(2,2)*(Ssym(1,2)+Ssym(2,1))-Ssym(2,2)*(Tsym(1,2)+Tsym(2,1));
Q=[Q11 Q12; Q12 Q22]; zetaopt=-acot(1/Q11*(sqrt(-det(Q))+Q12));

% Phase quadrature without squeezing
zeta=pi/2.; % homodyne angle
noiseoutphs=[cos(zeta)
sin(zeta)]*1/2*(RHOSr1*transpose(conj(RHOSr1))+conj(RHOSr1)
*(transpose(RHOSr1)))*[cos(zeta);sin(zeta)];
sigoutphs=[cos(zeta)
sin(zeta)]*1/2*(sig*transpose(conj(sig))+conj(sig)*transpose(sig))
*[cos(zeta);sin(zeta)];
NtoSphs=sqrt(noiseoutphs/sigoutphs);
lambdaoptphs=atan(-(T11*cos(zeta)+T21*sin(zeta))/(T12*cos(zeta)
+T22*sin(zeta)));

```

```

% Amplitude quadrature without squeezing
zeta=0.; noiseoutamp=[cos(zeta)
sin(zeta)]*1/2*(RH0sr1*transpose(conj(RH0sr1))+conj(RH0sr1)
*(transpose(RH0sr1)))*[cos(zeta);sin(zeta)];
sigoutamp=[cos(zeta)
sin(zeta)]*1/2*(sig*transpose(conj(sig))+conj(sig)*transpose(sig))
*[cos(zeta);sin(zeta)];
NtoSamp=sqrt(noiseoutamp/sigoutamp);
lambdaoptamp=atan(-(T11*cos(zeta)+T21*sin(zeta))/(T12*cos(zeta)
+T22*sin(zeta)));

% variational readout without squeezing
zeta=zetaopt; noiseoutvar=[cos(zeta)
sin(zeta)]*1/2*(RH0sr1*transpose(conj(RH0sr1))+conj(RH0sr1)
*(transpose(RH0sr1)))*[cos(zeta);sin(zeta)];
sigoutvar=[cos(zeta)
sin(zeta)]*1/2*(sig*transpose(conj(sig))+conj(sig)*transpose(sig))
*[cos(zeta);sin(zeta)];
NtoSvar=sqrt(noiseoutvar/sigoutvar);
lambdaoptvar=atan(-(T11*cos(zeta)+T21*sin(zeta))/(T12*cos(zeta)
+T22*sin(zeta)));

%%%%%%%%%%%%%%%%%%%%%%%%%%%%%%%%%%%%%%%%%%%%%%%%%%%%%%%%%%%%%%%%%%%%%%%% SQUEEZED INPUT %%%%%%%%%%%%%%%
% Squeezing matrix
r=0.690775527898; % squeezing value for 6dB squeezing
sphi=pi/2*1*0.7; % squeezing angle
SQ=[cosh(r)+sinh(r)*cos(2*sphi), sinh(r)*sin(2*sphi);
sinh(r)*sin(2*sphi) cosh(r)-sinh(r)*cos(2*sphi)];
RH0sqz=RH0sr1*SQ;

% Phase quadrature with squeezing
zeta=pi/2.; noiseoutsqzphs=[cos(zeta)
sin(zeta)]*1/2*(RH0sqz*transpose(conj(RH0sqz))+conj(RH0sqz)
*(transpose(RH0sqz)))*[cos(zeta);sin(zeta)];
sigoutsqzphs=[cos(zeta)
sin(zeta)]*1/2*(sig*transpose(conj(sig))+conj(sig)*transpose(sig))
*[cos(zeta);sin(zeta)];
NtoSphssqz=sqrt(noiseoutsqzphs/sigoutsqzphs);

% Amplitude quadrature with squeezing
zeta=0.; noiseoutsqzamp=[cos(zeta)
sin(zeta)]*1/2*(RH0sqz*transpose(conj(RH0sqz))+conj(RH0sqz)
*(transpose(RH0sqz)))*[cos(zeta);sin(zeta)];
sigoutsqzamp=[cos(zeta)

```

```

sin(zeta)]*1/2*(sig*transpose(conj(sig))+conj(sig)*transpose(sig))
    *[cos(zeta);sin(zeta)];
NtoSampsqz=sqrt(noiseoutsqzamp/sigoutsqzamp);

% squeezed variational with squeezing
zeta=zetaopt; sphi=lambdaptvar; SQ=[cosh(r)+sinh(r)*cos(2*sphi),
sinh(r)*sin(2*sphi); sinh(r)*sin(2*sphi)
cosh(r)-sinh(r)*cos(2*sphi)]; RHOsqz=RHOsr1*SQ;
noiseoutsqzvar=[cos(zeta)
sin(zeta)]*1/2*(RHOsqz*transpose(conj(RHOsqz))+conj(RHOsqz)
    *(transpose(RHOsqz)))*[cos(zeta);sin(zeta)];
sigoutsqzvar=[cos(zeta)
sin(zeta)]*1/2*(sig*transpose(conj(sig))+conj(sig)*transpose(sig))
    *[cos(zeta);sin(zeta)];
NtoSsqzvar=sqrt(noiseoutsqzvar/sigoutsqzvar);

% fully frequency-dependent sqz for amplitude quadrature
r=0.690775527898; % squeezing value for 6dB squeezing
sphi=lambdaptamp; SQ=[cosh(r)+sinh(r)*cos(2*sphi),
sinh(r)*sin(2*sphi); sinh(r)*sin(2*sphi)
cosh(r)-sinh(r)*cos(2*sphi)]; RHOsqz=RHOsr1*SQ; zeta=0.;
noiseoutsqzamp=[cos(zeta)
sin(zeta)]*1/2*(RHOsqz*transpose(conj(RHOsqz))+conj(RHOsqz)
    *(transpose(RHOsqz)))*[cos(zeta);sin(zeta)];
sigoutsqzamp=[cos(zeta)
sin(zeta)]*1/2*(sig*transpose(conj(sig))+conj(sig)*transpose(sig))
    *[cos(zeta);sin(zeta)];
NtoSampsqzfd=sqrt(noiseoutsqzamp/sigoutsqzamp);

% just one filter cavity for phase quad with squeezing
r=0.690775527898; % squeezing value for 6dB squeezing
lambdaptphs=-ANGwos; sphi=lambdaptphs;
SQ=[cosh(r)+sinh(r)*cos(2*sphi), sinh(r)*sin(2*sphi);
sinh(r)*sin(2*sphi) cosh(r)-sinh(r)*cos(2*sphi)];
RHOsqz=RHOsr1*SQ; zeta=pi/2.; noiseoutphs1filt=[cos(zeta)
sin(zeta)]*1/2*(RHOsqz*transpose(conj(RHOsqz))+conj(RHOsqz)
    *(transpose(RHOsqz)))*[cos(zeta);sin(zeta)];
sigoutphs1filt=[cos(zeta)
sin(zeta)]*1/2*(sig*transpose(conj(sig))+conj(sig)*transpose(sig))
    *[cos(zeta);sin(zeta)];
NtoSphs1filt=sqrt(noiseoutphs1filt/sigoutphs1filt);

data=[data; [NtoSphs NtoSphssqz NtoSphs1filt]]; end;

%%%%%%%%%% plotting the results %%%%%%%%%%%

```

```

scrsz = get(0,'ScreenSize');
%%% 4:3 resolution with FS 20 and width 0.75
figure('Position',[10 40 scrsz(3)/1.3 scrsz(4)/1.2])
%%% 16:9 resolution with FS 16 and width 0.9
%figure('Position',[10 40 scrsz(3)/1.3 scrsz(4)/1.5]) % 16:9 Auflösung
set(gcf,'DefaultLineLineWidth',0.15);
set(gcf,'DefaultAxesLineWidth',0.75);
set(0,'DefaultAxesFontSize',20); x=logspace(fmin,fmax,2000);
loglog (x,data(:,1),'r','LineWidth',3); % GEO-HF without squeezing
hold on;
loglog (x,data(:,3),'b','LineWidth',3); % GEO-HF with 6dB squeezing
loglog (x,thermal(:,1),'g','Linewidth',3); % coating silica thermal noise
loglog (x,thermal(:,2),'g--','Linewidth',3); % thermorefractive noise
legend(' GEO600 Design, 7kW', ' full coating thermal noise, silica',
      ' thermorefractive noise','Location','North') % Legend Figure 1
axis([10 10000 5.*10^(-24) 1.3*10^(-19)]); xlabel('Frequency
[Hz]'); ylabel('Linear noise spectral density [1/\surdHz]'); grid
on;

```

Appendix B

Control loop basics and optimizations

This chapter presents how a servo is optimized for controlling a physical system to its nominal operating point. Diverse scripts and programs are described in the following which are used to during the optimization procedure. In the second section an easy way on measuring the open-loop transfer function of the control loop is presented.

B.1 Optimizing a servo controller

The aim in building a servo controlled loop is to stabilize a physical system to a specific state. To achieve the best results the used servo has to be matched to the physical system. In this section the optimization procedure is described in detail.

Imagine a cavity which length has to be stabilized to match its resonance frequency to the laser frequency. Normally a PZT-mounted mirror is used to change the cavity length by an electrical signal. Due to the fact that the PZT and the mirror mount have specific resonances which depend on their physical properties, an individual servo has to be designed to achieve the best performance. This normally means a servo with high unity gain frequency as well as a large low-frequency gain, while the resonance of the PZT and the mirror mount must not be excited.

The optimization process starts with the measurement of the transfer function of the physical system. A schematic of this measurement process is shown in Figure B.1. The idea behind a transfer function is to measure the reaction of the system to an injected disturbance. Thus, while the cavity is locked and the system is in its nominal operating point, a signal S is injected into the the loop by a summing amplifier behind the servo. This signal propagates through the loop and is measured at point M in front of the servo. To eliminate the effects of the servo used in the loop, a reference signal R containing the injected signal and the normal control signal, which holds the cavity length on resonance, is also measured. By measuring M/R the transfer function of the system composed of the HV-amplifier, the PZT-mounted mirror and the photodiode can be revealed. An example of such a measurement is displayed in Figure B.2. This transfer function shows a large PZT resonance around 60 kHz. On the other hand the servo has to be designed in such a way that the resonance is suppressed below unity gain with a low-pass filter. On the other hand, the gain at low frequencies has to be enlarged with electronic integrator circuits. The boundary condition of the open loop gain at the unity gain frequency is the phase margin. A rule of thumb is to have at least 35° of phase margin at the unity

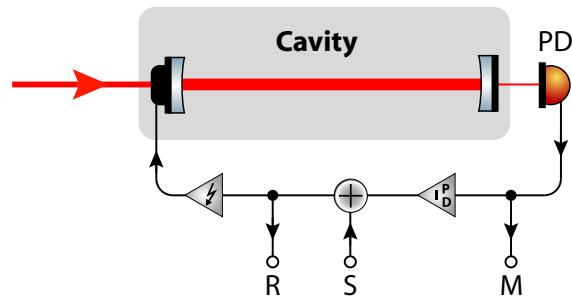


Figure B.1: Schematic of measuring a transfer function of a PZT actuated cavity. A signal S is added to the output of the servo. This signal S disturbs the locked cavity, which results in an amplitude change of the transmitted light field sensed by the photodiode. This disturbance is then measured at the point M . A network analyzer is normally used to inject signals over a predefined frequency range. To distinguish between the injected signal S and the normal servo signal that is needed to hold the cavity on resonance, a reference measurement is performed at point R , so that the network analyzer performs a normalized measurement by calculating M/R .

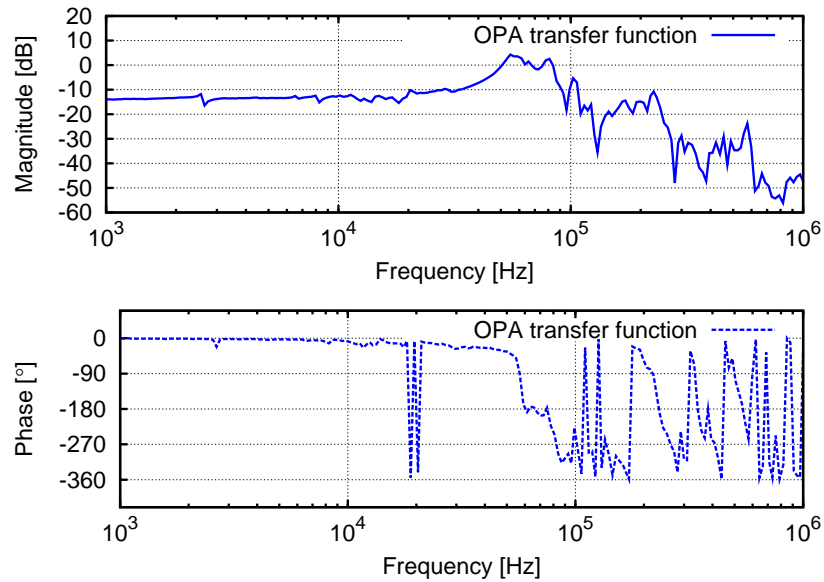


Figure B.2: Measured transfer function of the OPA cavity. The measurement was achieved with the technique described in Figure B.1. A large PZT resonance is visible around 60 kHz, which has to be suppressed by the servo.

gain frequency to build a stable control loop. It is worth noting that, at frequencies where the gain is higher than unity the phase lag can be substantially higher than 180° without leading to a system instability. Details on control theory and stability criterions can be found in [AC00]. A good way of finding reasonable values for the low-pass and integrator corner frequency is using gnuplot and multiply the low-pass and integrator transfer functions directly to the measured OPA cavity transfer function. This is done e.g. by the following gnuplot file.

```

reset
set term windows
set data style lines
set function style lines
set angles degrees
set logscale x
set xlabel 'Frequenz [Hz]'
set xtics 1,10,1e6
set mxtics 10
set ytics nomirror
set style line 1 lt 1 lw 2 pt 3 ps 0.5 linecolor rgb "blue"
set style line 2 lt 2 lw 2 pt 3 ps 0.5 linecolor rgb "blue"
set style line 3 lt 1 lw 2 pt 3 ps 0.5 linecolor rgb "red"
set style line 4 lt 2 lw 2 pt 3 ps 0.5 linecolor rgb "red"
set grid xtics y2tics layerdefault back lw 1
set grid xtics ytics layerdefault back lw 1
i=sqrt(-1)
set format x "10^%L"

pole1(x,f)=1/(1+{0,1}*x/f) # simple pole
zero1(x,f)=(1+{0,1}*x/f) # simple zero
pole2(x,f,q)=1/(1+{0,1}*x/(f*q)-x**2/f**2) # pole with Q
zero2(x,f,q)=(1+{0,1}*x/(f*q)-x**2/f**2) # zero with Q
servo(x)=pole1(x,1)*zero1(x,20000)*pole1(x,1)*zero1(x,2000)
          *pole2(x,25e3,0.7674)
          # combined Servo transfer function including
          # low-pass filter at 25kHz
mag(x)=20*log10(abs(servo(x)))+150
phase(x)=arg(servo(x))

set xrange[100:1000000]
set key
set size 1,1
set origin 0,0
set multiplot
set size 1,0.5
set origin 0,0.5

```

```
set ylabel 'Magnitude [dB]'
set yrange[-60:60]
set ytics 20
plot 'newopa.txt' u:($1):($2+mag($1)) ls 1 title "open
                                loop transfer function",\
      (mag(x)) ls 3 title "servo transfer function"

set size 1,0.5
set origin 0,0
set ylabel 'Phase [{/Symbol \260}]'
set yrange[-430:150]
set ytics 90
plot 'newopa.txt' u:($1):(int($3+phase($1)-180)%360) ls 2
                                title "open-loop transfer function",\
      int(phase(x))%360 ls 4 title "servo transfer function"
unset multiplot
```

The OPA cavity transfer function data points are stored in the file “newopa.txt”. The servo designed in this example uses a second order low-pass filter with a corner frequency of 25 kHz to suppress the PZT resonance. Two integrators located at 2 kHz and 20 kHz increase the low-frequency gain. The resulting servo transfer function and the open loop gain transfer function, which is the combination of the measured OPA cavity transfer function (Figure B.2) and the servo transfer function are presented in Figure B.3. The potential unity gain frequency is about 10 kHz. In this region the gain of the open-loop transfer function is higher compared to the resonance of the PZT and a phase margin of about 80° is available.

Now that suitable parameters for a servo have been determined, the circuit parameters for the low-pass filter and the two integrators are needed. The analog circuit simulation program LISO from G. Heinzel is used to simulate the behavior of the servo. The simulation file for the servo transfer function looks like the following:

```
# filename servo.fil
##### Servo
#Integrator no.1
pole 100
zero 20k
#Differentiator not used
#zero 35k
#pole 500k
#Integrator no.2
pole 100
zero 2k

#Low-pass filter
pole 25.0k 0.7674
```

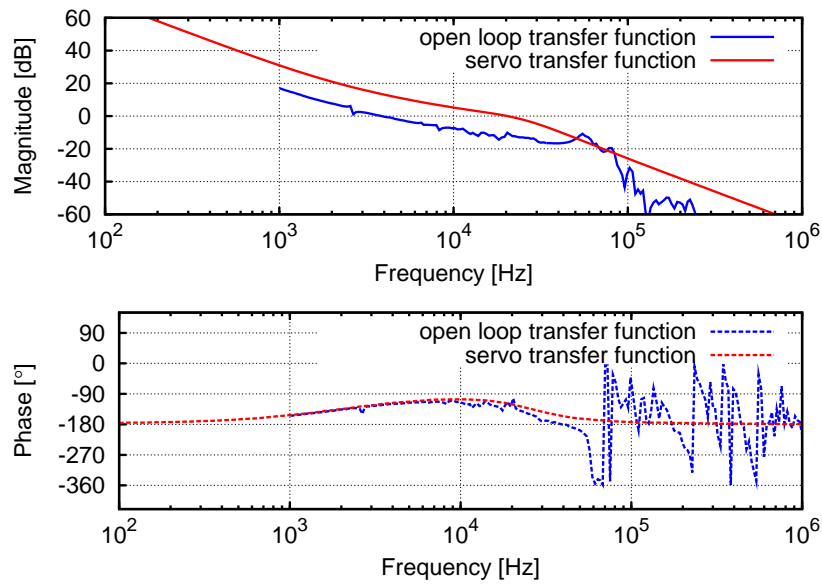


Figure B.3: Bode plot of the open loop transfer function and servo transfer function of the OPA

```
# proportional gain adjustment
#factor 200      # factor for only one integrator
factor 4000     # factor for two integrators with
                # and without low-pass filter
freq log 10 1000k 1000
```

The file contains a simulation of two integrators, each made by a pole and a zero, and the low-pass filter with corner frequency of 25 kHz. LISO is calculating the transfer function of the servo from this input file. Now we need an input file, which contains the circuit layout of the servo such that LISO can calculate the needed values for the resistors and capacitors. The servo circuit containing the two integrators and the low-pass filter is given by the following file.

```
# filename servo-circuit.fil
uinput n1      # input
r ra 1f n1 nain
##### I und D
#D            # not used here
#r r1a 116.10144 nain n1a ### fitted
r r2a 1.8017317k nain opam ### fitted
#c c1a 2.2n n1a opam ### fitted
#I
r r3a 360.35168k opam opao ### fitted
r r4a 1.8017317k opam n2a ### fitted
```

```
c c2a 4.4n n2a opao ### fitted
#r rtest1 1f n2a opao

op opa op27 gnd opam opao

##### I und D
r rb 1f opao nbin

#D          # not used here
#r r1b 106.64549 nbin n1b ### fitted
r r2b 1.1099431k nbin opbm ### fitted
#c c1b 2.2n n1b opbm ### fitted
#I
r r3b 22.22863k opbm opbo ### fitted
r r4b 1.1099431k opbm n2b ### fitted
c c2b 68n n2b opbo ### fitted
#r rtest 1f n2b opbo

op opb op27 gnd opbm opbo

##### LP
r rd 1f opbo ndin

r r1d 4.1969449k ndin n1d ### fitted
r r2d 4.1886188k n1d opd  ### fitted
c c1d 2.2n n1d opdo ### fitted
c c2d 1n opd  GND ### fitted

op opd op27 opd  opdo opdo

uoutput opdo
#factor -2.7391298k ### fitted
factor -1      ### fitted

#param factor 1u 1M

## D-Fit
#param r1c 1 1M
#param r2c 1 1M
#sparam r4c

## I-Fit
param r2b 1 1M
sparam r4b
param r3b 1 1M
```

```
param c2b 1f 1m

#param c1b 1f 1m

## LP-Fit
#param r1d 1 1M
#param r2d 1 1M
#param c1d 1f 1m
#param c2d 1f 1m

freq log 10 100k 1000
fit servo.out dbdeg rel
```

The fit of the servo values can only be achieved in an iterative way because of the large parameter space. Hence, one starts with the “servo.fil”, to generate a servo transfer function which contains only the first integrator. It is important to adjust the proportional gain (factor) to match the high-frequency gain to 0 dB. Only this satisfies that the simulated integrator circuit is not attenuating the processed signal. In the case of one activated integrator, the needed factor is 200.

The next step is to run the “servo-circuit.fil” file. This file contains the electric circuit of two combined integrator/differentiator circuits and a low-pass filter. At first one starts with the simulation of a single integrator, the differentiator is not needed and resistor “r1a” and the capacitor “c1a” are commented. The proportional gain of the circuit, defined by “factor” has to be set to -1 , due to using an inverting amplifier as integrator circuit. The output of the simulated circuit has to be set to the first OP-amplifier output “opao”. Afterwards the four lines of the integrator fit routine have to be un-commented and LISO can process this simulated circuit input file. LISO will try to fit the values of “r2a, r3a, r4a and c2a” and rewrite the new values into the input file. Usually LISO fits values with an arbitrary precision. Hence, the resulting capacitor values are not available and one has to choose manually a capacitor in the range of the fitted value and re-run LISO with this capacitor value being fixed. Most of the time the resistor values are easily found by combining two resistors in a serial or parallel circuit.

Now that the first integrator values have been fixed, the procedure starts again, now with the circuit made out of two integrators. The “servo.fil” file has to be run with a factor of 4000 to gain the simulated servo transfer function with two integrators. In the “servo-circuit.fil” the factor has to be changed to one and the simulated circuit output has to be set to the second OP-amplifier output “opbo”. Before the calculation can be started the names of the components to fit have to be changed from rXa to rXb and from cXa to cXb, where X is the number of the relevant component. Now the optimization can be performed as described before.

After both integrators circuits have been fitted, the procedure have to be repeated for the low pass filter. At the end all values for the circuit are known and the servo can be optimized with this values.

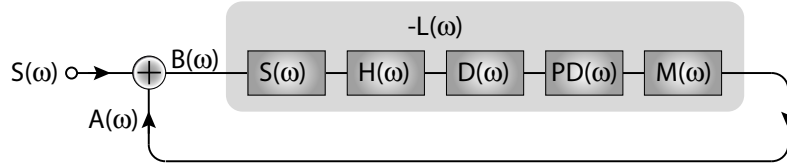


Figure B.4: Schematic of a control loop with integrated summing amplifier to measure the open loop gain transfer function $L(\omega)$. A signal S is injected into the loop and the response of the loop to this disturbance is measured at two different positions A and B inside the loop. The open loop gain is then given by the ratio of $-A/B$.

B.2 Measuring an open-loop transfer function

The open loop gain $L(\omega)$ determines the performance of a control loop by showing how good disturbances at specific frequencies are suppressed inside the loop, for details see [AC00]. Therefore it is crucial to have access to the open loop gain. In Figure B.4 the open loop gain $L(\omega)$ is a combination of the servo's transfer function $S(\omega)$, the HV-amplifier's transfer function $H(\omega)$, the device's transfer function $D(\omega)$ (e.g. a cavity), the photodiode's transfer function $PD(\omega)$, and the mixer's transfer function $M(\omega)$. Ideally one could measure $L(\omega)$ by opening the loop, injecting a sine wave at the input B , measure the corresponding mixer output at point A and taking their ratio by using a network analyzer. A sweep of the sine wave's frequency would result in the desired open-loop transfer function. The problem with this kind of direct measurement is the free-running output can be outside the sensor range, while the loop is open. Hence, no useful signal can be detected. Moreover, the gain of the loop may be large enough to drive the actuator into saturation, such that no change of the actual state can be measured by the sensor.

An effective way of accessing the open-loop transfer function is via an indirect measurement while the loop is closed [Hei95]. Figure B.4 shows that the following relations are valid

$$B(\omega) = S(\omega) + A(\omega) \quad (\text{B.1})$$

$$A(\omega) = -L(\omega) \cdot B(\omega) = -L(\omega) \cdot [S(\omega) + A(\omega)]. \quad (\text{B.2})$$

From this follows directly the open-loop transfer function

$$L(\omega) = \frac{-A(\omega)}{B(\omega)}, \quad (\text{B.3})$$

which can be measured easily with a network analyzer.

An example of an open-loop transfer function measured by this method is displayed in Figure B.5.

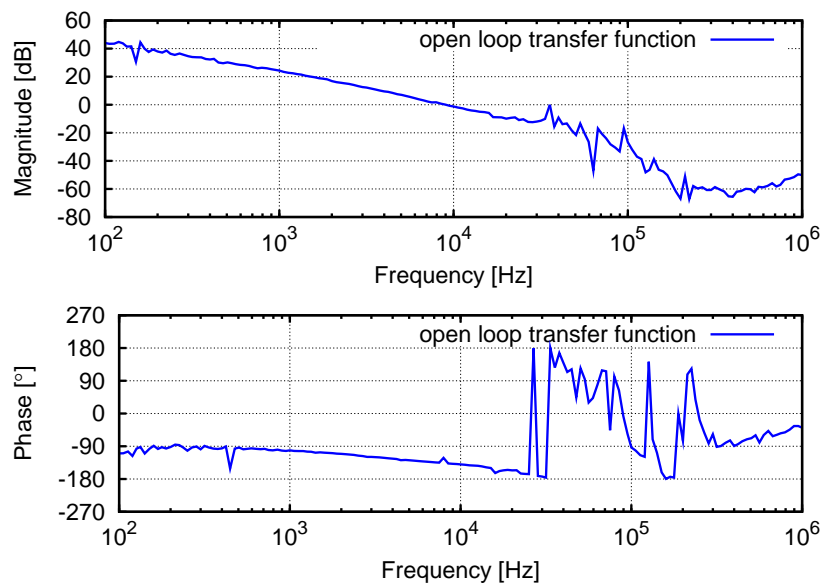


Figure B.5: Measured open loop transfer function of the SHG cavity control loop. The unity gain frequency is about 10 kHz.

Appendix C

Electronics

C.1 Temperature controller

The circuit diagram of the temperature controller used for stabilizing the temperature of crystals inside the SHG, OPA and OPO ovens are displayed in Figures C.1 and C.2. This temperature controller was designed by H. Vahlbruch.

C.2 HV amplifier

The schematics of the high voltage amplifier are presented in Figures C.3–C.6.

C.3 Modecleaner servo

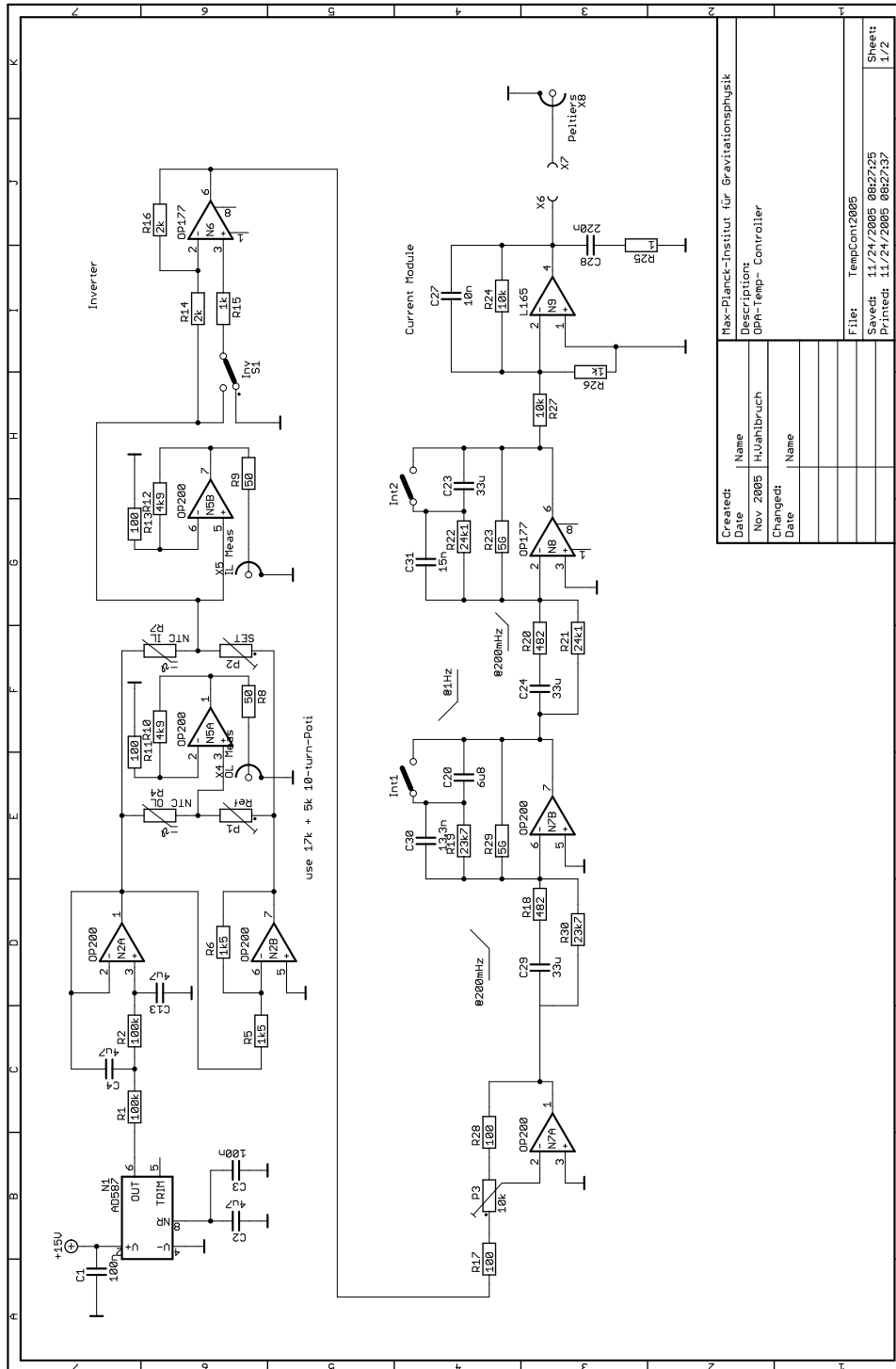
The circuit diagram of the generic servo that has been used for most of the control loops is presented in Figures C.7 and C.8. For simplicity, the power supply circuits are not shown. The electronic layout of the servo was designed by H. Vahlbruch. This servo presented here has to be adapted to the individual control loop. The best way to do this is to measure a transfer function of the loop and calculate the best servo to that loop with the procedure presented in Section B.1.

C.4 Homodyne photodiode

The circuit diagram of the homodyne photodiodes is shown in Figure C.9. These photodiodes have been designed by B. Hage.

C.5 Resonant photodiode

The circuit diagram of a resonant photodiode can be found in Figure C.10. These photodiode design has been developed by B. Hage.



Created:	Name
Date	HUJahrbruch
Description	OPA-Temp- Controller
Changed:	Name
Date	
File:	TempCon12005
Saved:	11/24/2005 08:22:25
Printed:	11/24/2005 08:27:37
	Sheet
	1/2

Figure C.1: Circuit diagram of temperature controller used for stabilizing the temperature of the SHG, OPA and OPO ovens. Part 1/2

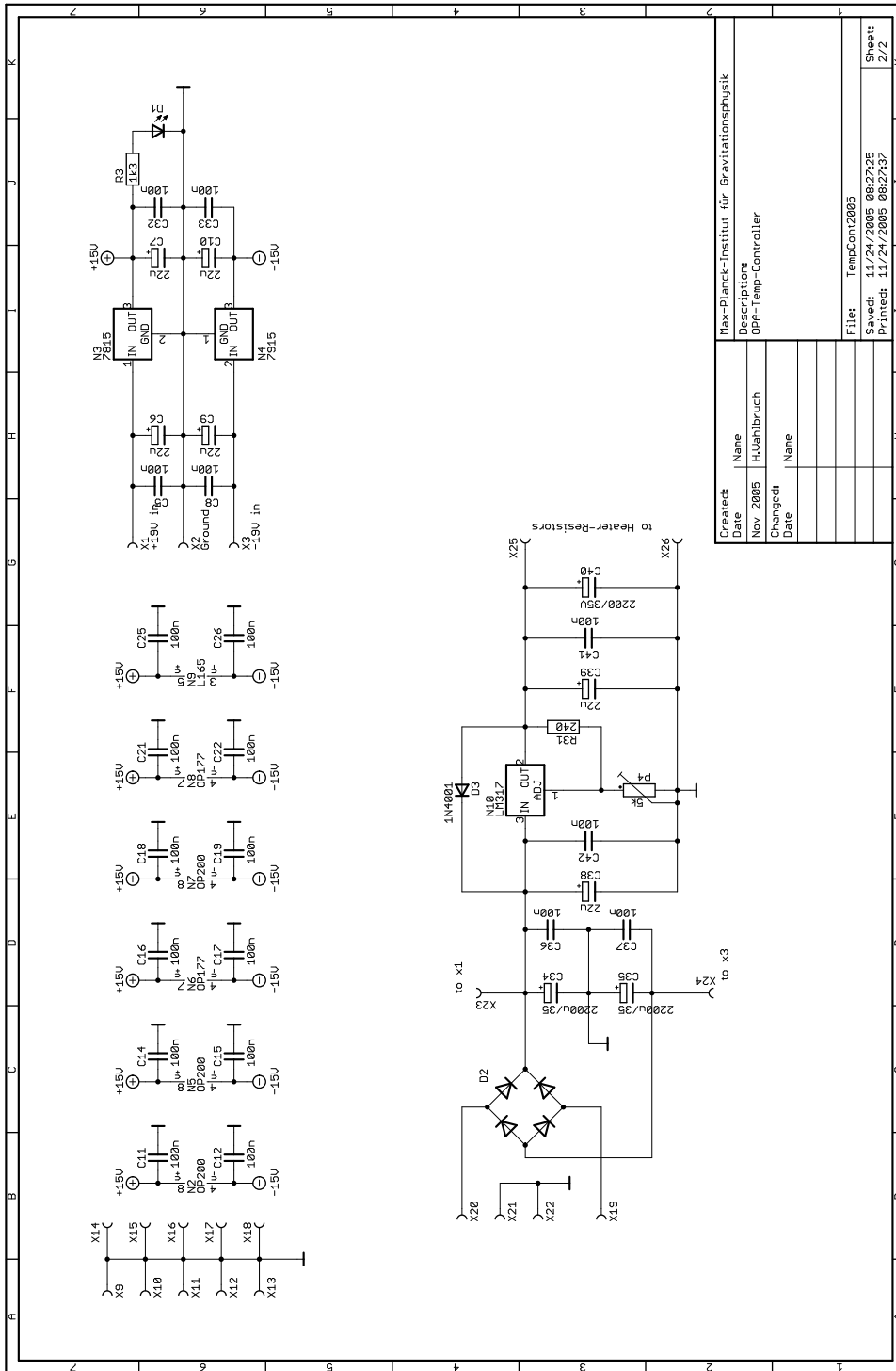


Figure C.2: Circuit diagram of temperature controller used for stabilizing the temperature of the SHG, OPA and OPO ovens. Part 2/2

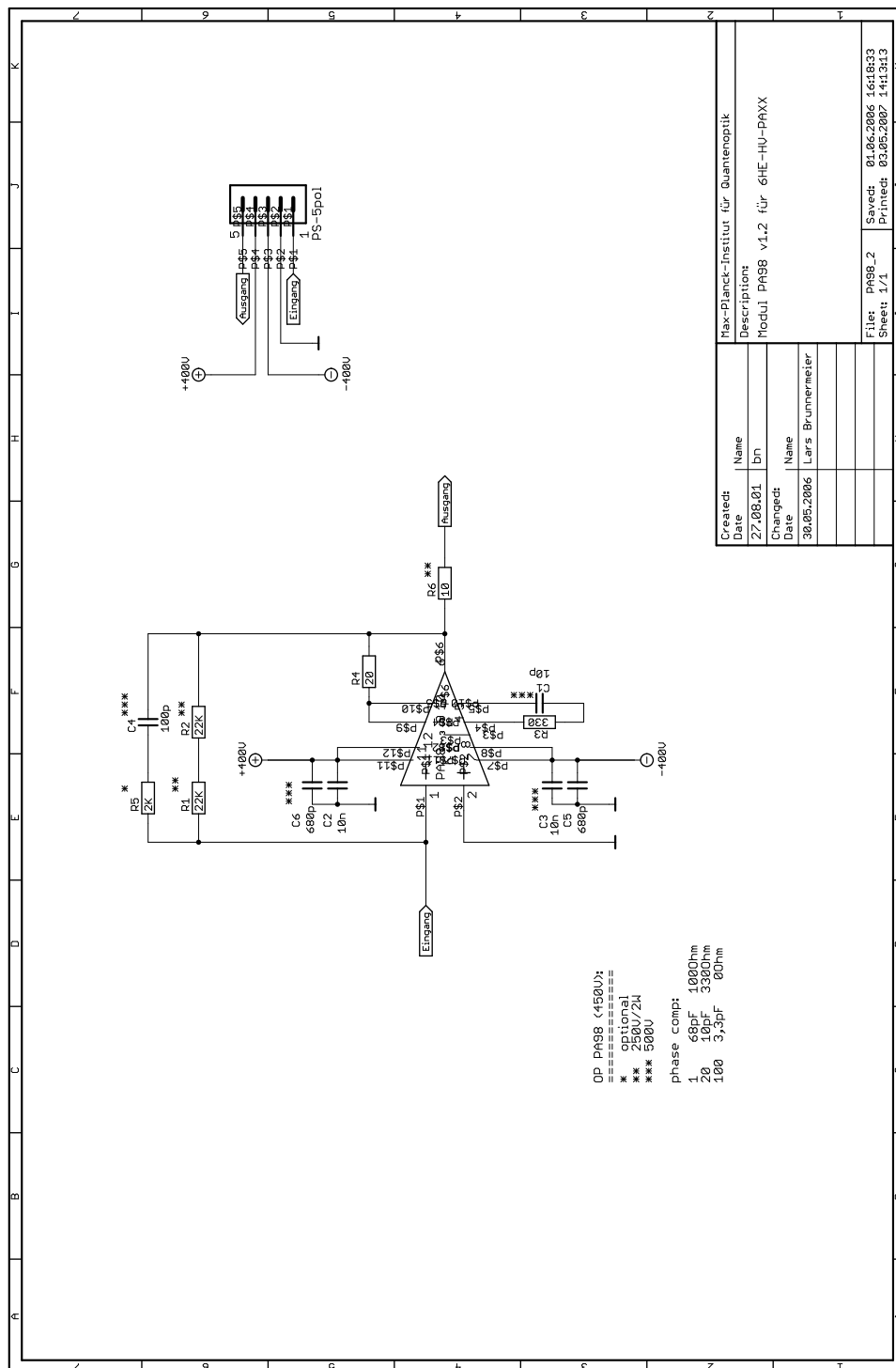


Figure C.3: Circuit diagram of the HV amplifier. Part 1/4

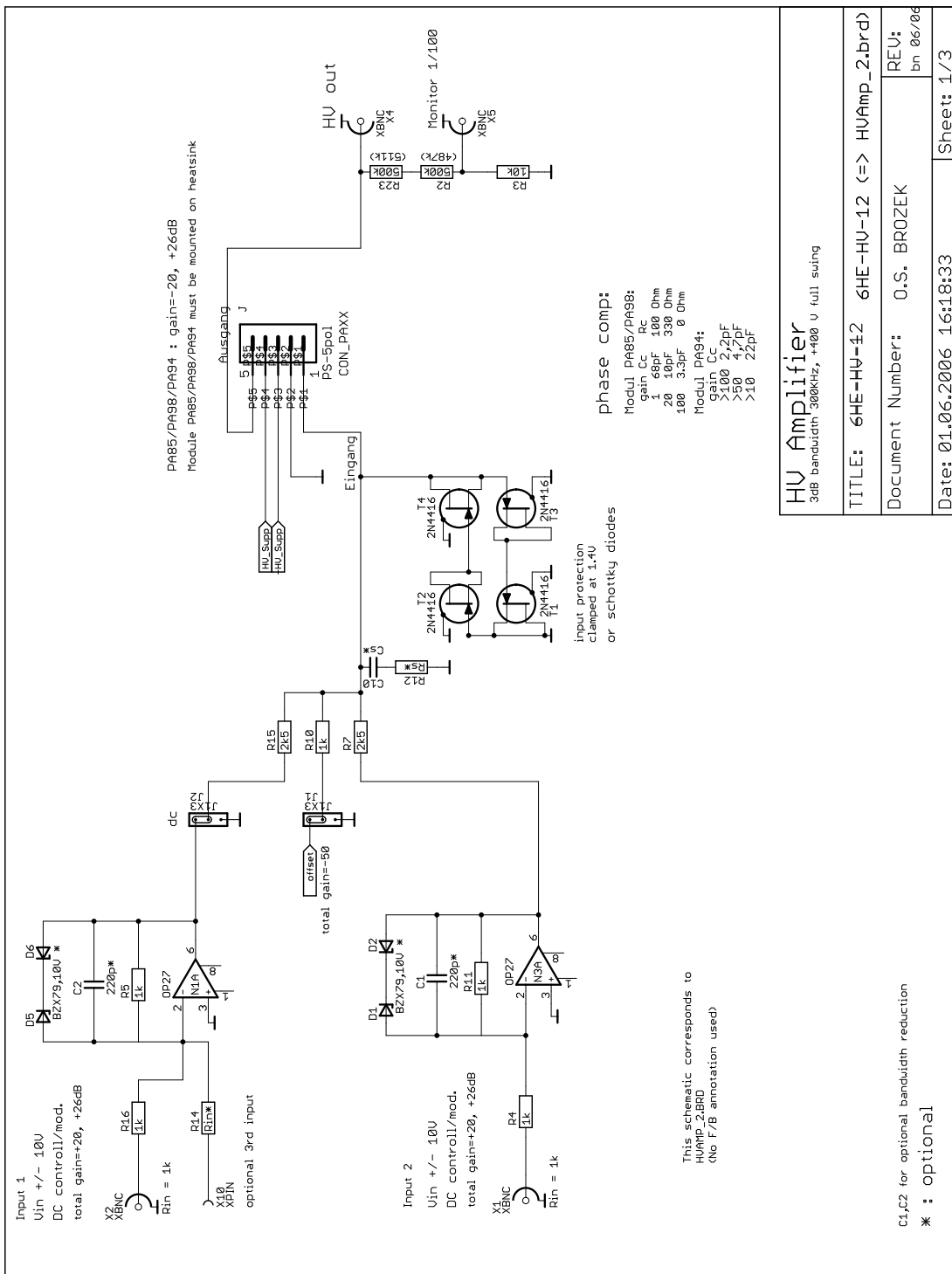


Figure C.4: Circuit diagram of the HV amplifier. Part 2/4

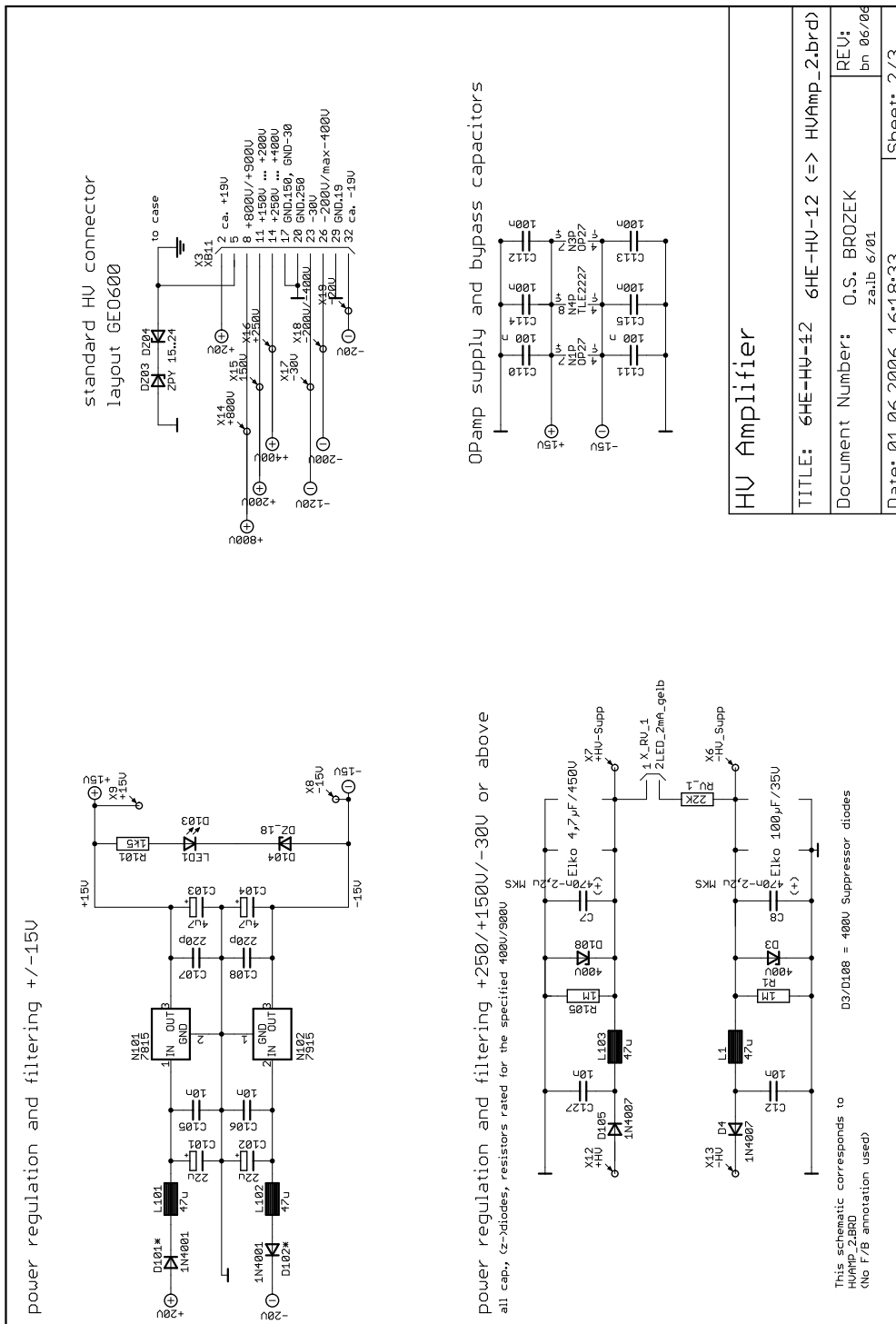


Figure C.5: Circuit diagram of the HV amplifier. Part 3/4

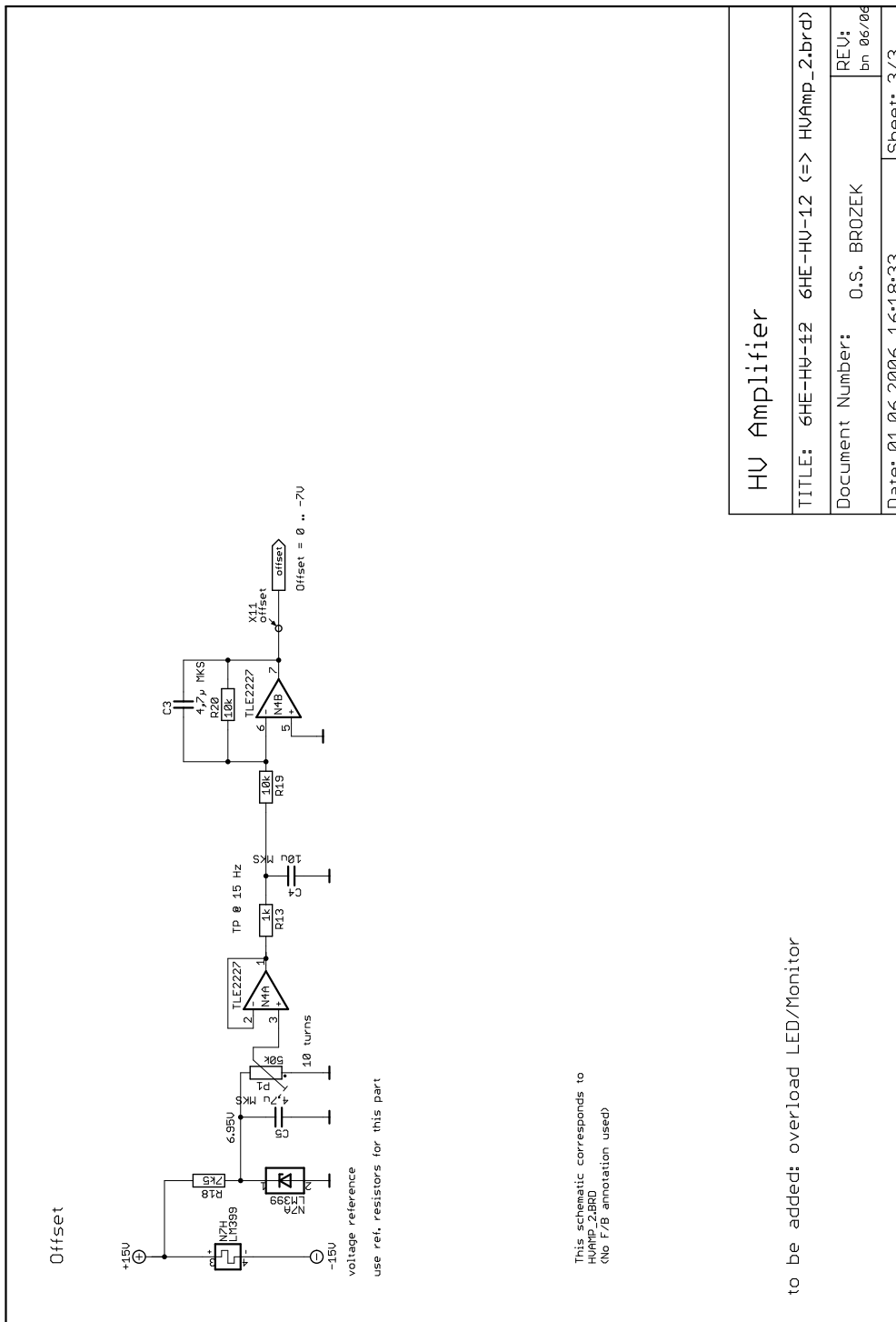


Figure C.6: Circuit diagram of the HV amplifier. Part 4/4

HV Amplifier	
TITLE: 6HE-HV-12 6HE-HV-12 (=> HVAmp_2.brd)	
Document Number:	0.S. BROZEK
REV:	bn 06/06
Date: 01.06.2006 16:18:33	Sheet: 3/3

to be added: overload LED/Monitor

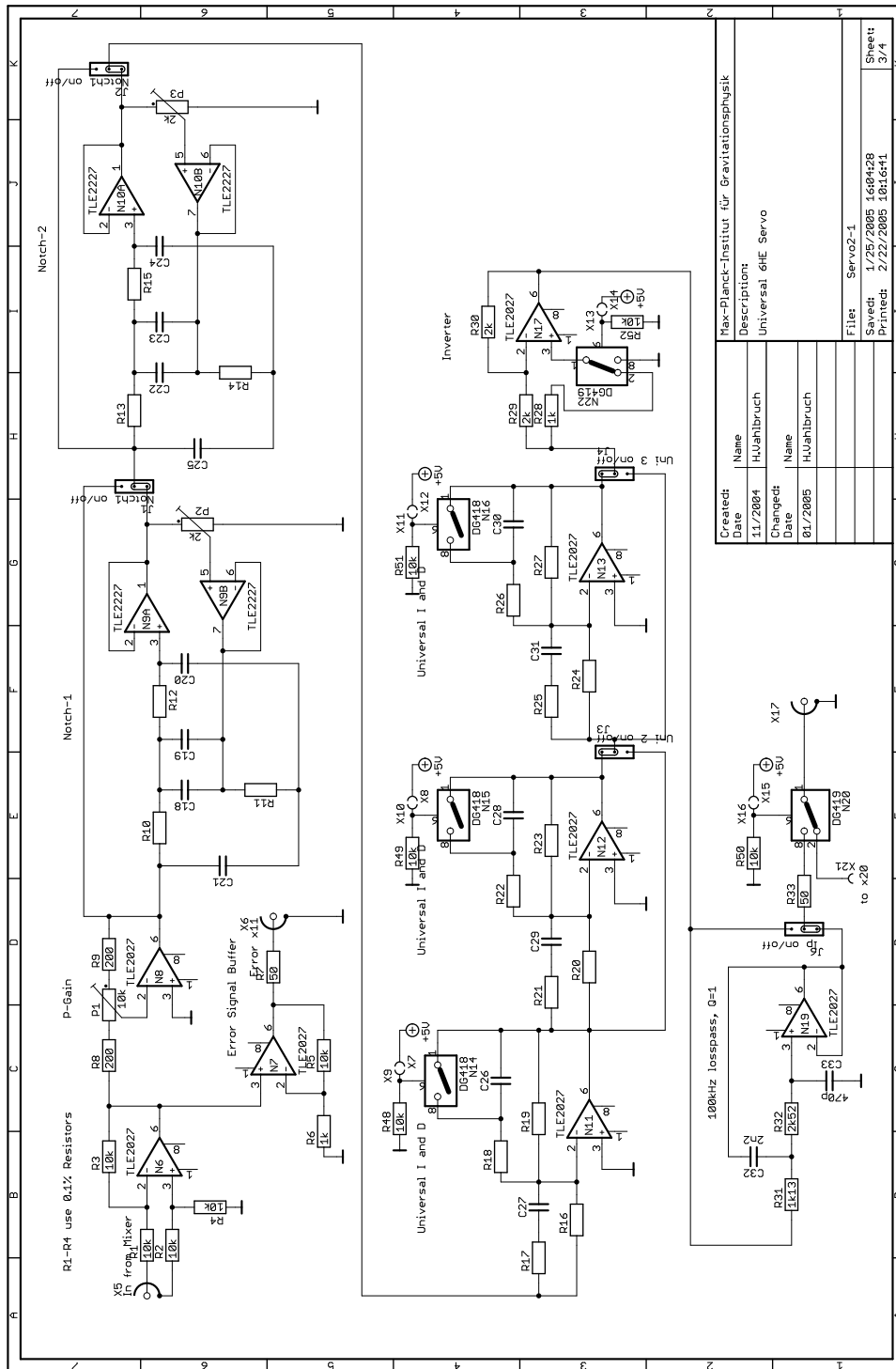


Figure C.7: Circuit diagram of generic servo layout. Part 1/2

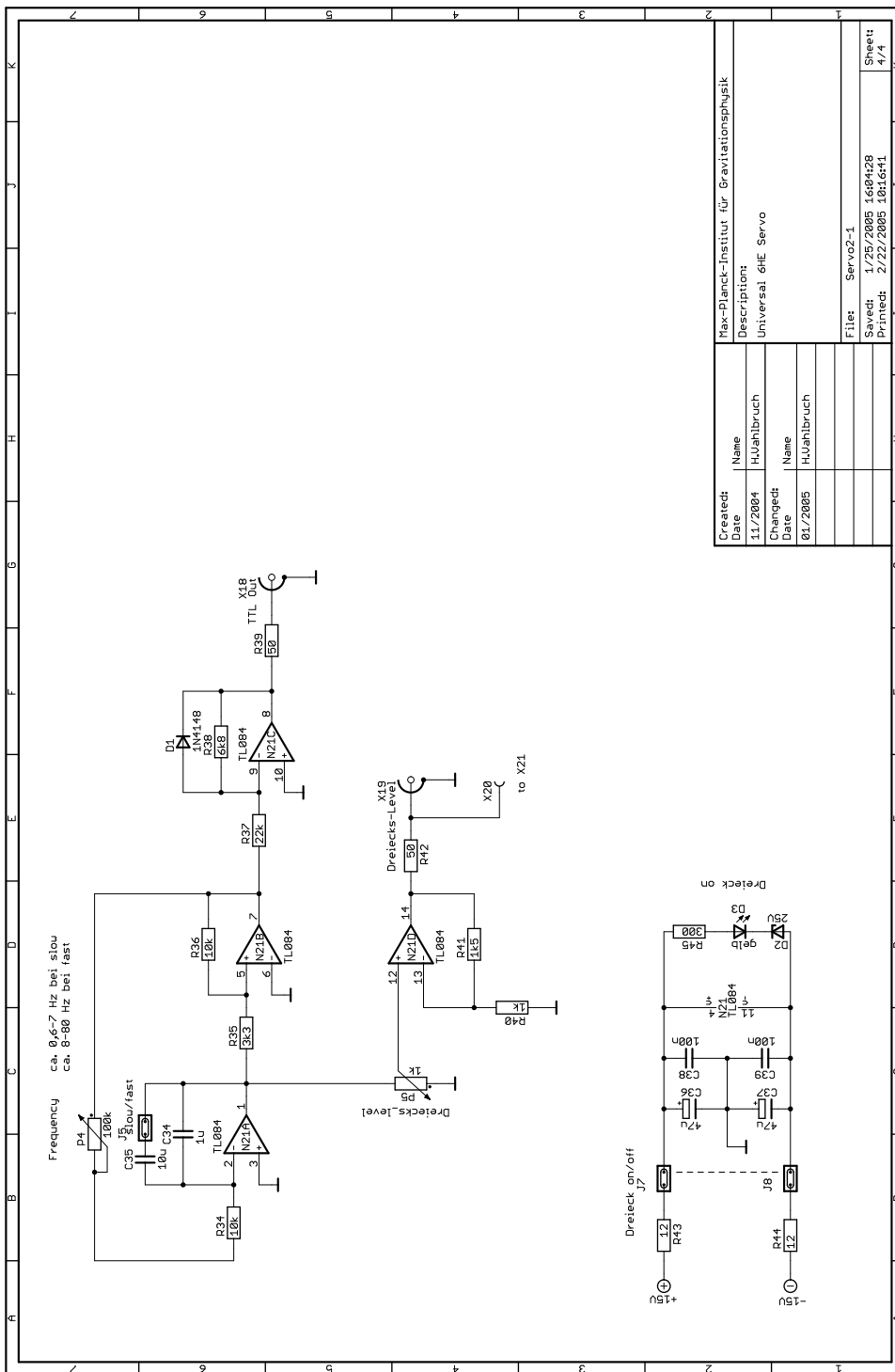


Figure C.8: Circuit diagram of generic servo layout. Part 2/2

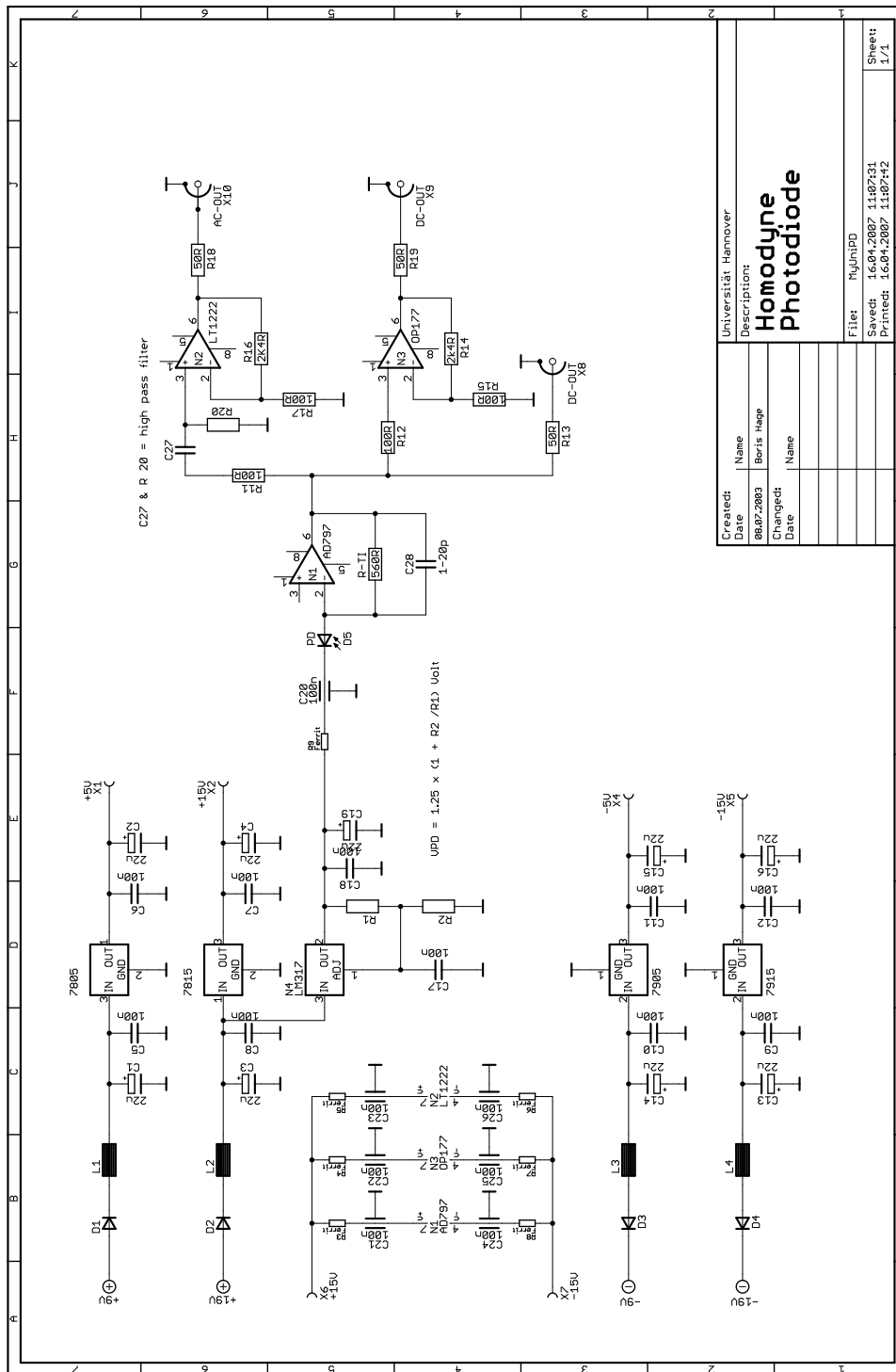
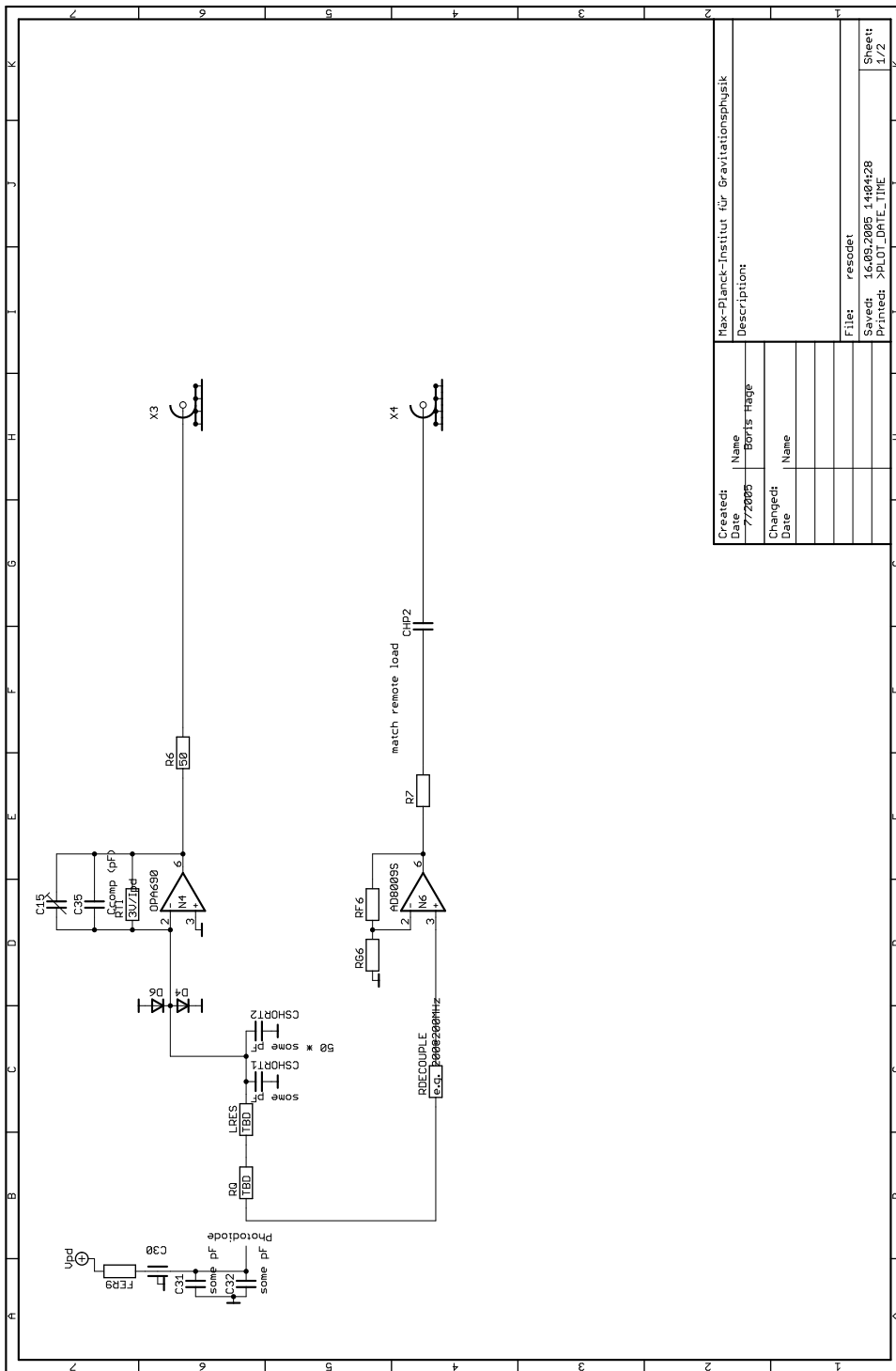


Figure C.9: Circuit diagram of the homodyne photodiode



Created Date	Name	Max-Planck-Institut für Gravitationsphysik
7/7/2005	Boris Häge	Description
Changed Date	Name	
		File: resodet
		Saved: 16.09.2005, 14:04:28
		Printed: >PLOT_DATE_TIME
		Sheet: 1/2

Figure C.10: Circuit diagram of a resonant photodiode

Appendix D

Origin of technical noise in the squeezed field

The technical noise below 3.5 MHz originates from the classical seed field entering the OPA cavity through the backside. Its source are mainly the laser relaxation oscillation and amplitude noise of the pump light [HRH⁺97]. The seed field is partially transmitted through the OPA and its noise characteristics are superimposed with the squeezed vacuum produced by the OPA. The seed field is needed for two reasons. First it is used for the length control of the OPA cavity (see Sec 3.3.5.1). Secondly it carries phase modulation sidebands that are also partially transmitted through the cavity which allow a stable control of the homodyne detection angle (see Section 3.4.1).

In Figure D.1 the attenuation of the transmitted power through the cavity is presented. The attenuation of the noise transmitted through the OPA cavity is 14.5 dB. Knowing this and looking at a typical squeezing spectra (Figures 3.27 and 3.29), one realizes that the technical noise in the squeezing spectrum is still up to 20 dB above the vacuum noise level.

Subtraction of optical signals

One idea to get rid of the technical noise is to use a separate bright coherent laser beam and overlap it with the weak squeezed beam. This idea was used in [SVF⁺04] to produce squeezed states down to sideband frequencies of 80 kHz. The two overlapped beams both originate from the same laser source. Hence, the experiment is in principle a Mach-Zehnder Interferometer with independently adjustable beam splitter reflectivities ϵ_1 and ϵ_2 (Figure D.2). To show the common mode noise cancellation first one has to derive the amplitude quadrature operator $\tilde{X}_{1,\text{out}}$ in frequency space. The amplitude noise from the laser source $\tilde{X}_{1,\text{src}}$ and vacuum fluctuations entering lossy ports of the setup ($\tilde{X}_{1,\text{vac}}, \tilde{X}_{1,\text{loss}}, \tilde{X}_{1,\text{oc}}$) are only considered in the following calculation. A bright coherent state represented by the quadrature operator $\tilde{X}_{1,\text{src}}$ encounters the beam splitter with reflectivity ϵ_1 that couples in the vacuum fluctuations through the unused beam splitter port. The resulting outgoing fields are given by

$$\begin{aligned}\tilde{X}_{1,\text{ic}} &= \sqrt{\epsilon_1}\tilde{X}_{1,\text{vac}} + \sqrt{1-\epsilon_1}\tilde{X}_{1,\text{src}} \\ \tilde{X}_{1,\text{ref}} &= \sqrt{1-\epsilon_1}\tilde{X}_{1,\text{vac}} - \sqrt{\epsilon_1}\tilde{X}_{1,\text{src}}.\end{aligned}\tag{D.1}$$

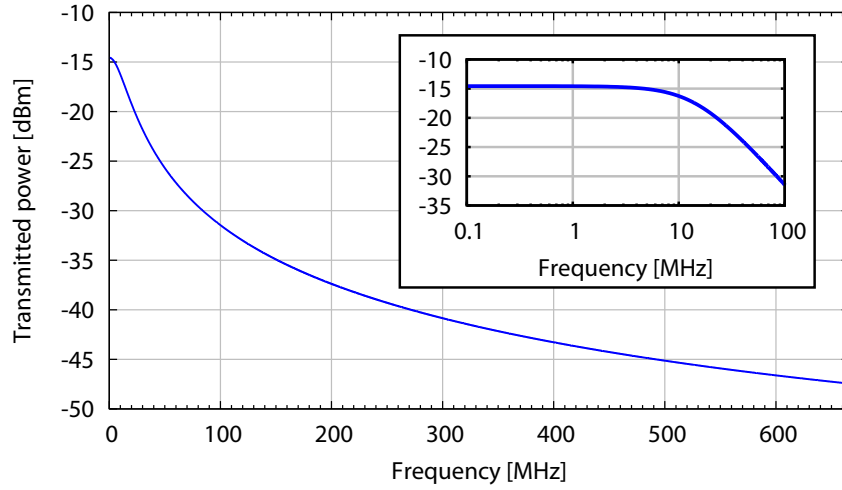


Figure D.1: Frequency dependence of the transmitted power of a field entering the OPA cavity through the backside of the crystal. The inlay displays a zoomed plot of the low-frequency regime. The transmission losses are almost constant below 10 MHz with an attenuation of -14.5 dB.

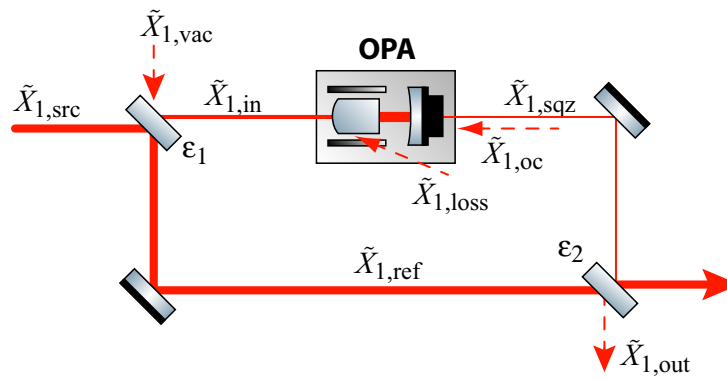


Figure D.2: Schematic of the experimental setup for the suppression of the technical noise below 3.5 MHz

The field $\tilde{X}_{1,\text{ic}}$ is used as a seed field for the OPA. The OPA acts in a way as it is described in Section 3.3.2 to produce an amplitude quadrature squeezed beam in transmission. Following the treatment of optical parametric amplification (Section 3.3.2), the amplitude quadrature of the outgoing field $\tilde{X}_{1,\text{sqz}}$ is given by

$$\tilde{X}_{1,\text{sqz}}(\Omega) = \frac{2\sqrt{\kappa_{\text{ic}}\kappa_{\text{oc}}}\tilde{X}_{1,\text{ic}} + (2\kappa_{\text{ic}} - i\Omega - \kappa + g)\delta\tilde{X}_{1,\text{oc}} + 2\sqrt{\kappa_{\text{oc}}\kappa_{\text{loss}}}\delta\tilde{X}_{1,\text{loss}}}{i\Omega + \kappa - g}, \quad (\text{D.2})$$

where κ_{m1} , κ_{m2} and κ_{loss} are the input, output and loss coupling rates, respectively, for the OPA cavity with the total decay rate $\kappa = \kappa_{\text{m1}} + \kappa_{\text{m2}} + \kappa_{\text{loss}}$. Moreover the operators $\tilde{X}_{1,\text{oc}}$ and $\tilde{X}_{1,\text{loss}}$ are both purely representing vacuum fluctuations that are coupled in from the output coupler or by losses. The reference beam $\tilde{X}_{1,\text{ref}}$ is given a phase shift ϕ before being interfered with the squeezed beam $\tilde{X}_{1,\text{sqz}}$ on the second beam splitter with reflectivity ϵ_2 . The output of the second beam splitter is then described by

$$\tilde{X}_{1,\text{out}} = \sqrt{\epsilon_2}\tilde{X}_{1,\text{sqz}} + \sqrt{1 - \epsilon_2}\tilde{X}_{1,\text{ref}}e^{-i\phi}. \quad (\text{D.3})$$

Using this together with Equation D.2 results in

$$\begin{aligned} \tilde{X}_{1,\text{out}} = & \left\{ \left[\sqrt{(1 - \epsilon_1)\epsilon_2}2\sqrt{\kappa_{\text{oc}}\kappa_{\text{oc}}} - \sqrt{(1 - \epsilon_2)\epsilon_1} (i\Omega + \kappa - g) e^{-i\phi} \right] \tilde{X}_{1,\text{src}} \right. \\ & + \left[\sqrt{\epsilon_1\epsilon_2}2\sqrt{\kappa_{\text{ic}}\kappa_{\text{oc}}} + \sqrt{(1 - \epsilon_1)(1 - \epsilon_2)} (i\Omega + \kappa - g) e^{-i\phi} \right] \tilde{X}_{1,\text{vac}} \\ & + [\sqrt{\epsilon_2} (2\sqrt{\kappa_{\text{oc}}\kappa_{\text{loss}}})] \tilde{X}_{1,\text{oc}} \\ & \left. + [\sqrt{\epsilon_2}2\sqrt{\kappa_{\text{loss}}\kappa_{\text{oc}}}] \tilde{X}_{1,\text{loss}} \right\} \cdot \frac{1}{i\Omega + \kappa - g}. \end{aligned} \quad (\text{D.4})$$

The value of the relative phase ϕ from the reference beam to the squeezed output of the OPA is set to zero to satisfy a complete cancelation of the coherent amplitude at the chosen output port. The noise spectrum of the output field may be calculated using $V_{1,\text{out}}(\Omega) = \langle \tilde{X}_{1,\text{out}}^2 \rangle - \langle \tilde{X}_{1,\text{out}} \rangle^2$. In the following it is assumed that all involved vacuum fields are uncorrelated among themselves and its variances can be set so $V_{1,\text{vac}} = V_{1,\text{oc}} = V_{1,\text{loss}} = 1$. Assuming further that sideband frequencies of interest are within the linewidth of the cavity the approximation $\Omega \ll \kappa$ can be used. Then the laser source contributions to the output field can be completely removed if the following relation between the two beam splitters is satisfied

$$\epsilon_1 = \left(1 + \frac{\epsilon_2}{1 - \epsilon_2} \frac{4\kappa_{\text{ic}}\kappa_{\text{oc}}/\kappa^2}{(1 - g/\kappa)^2} \right)^{-1}. \quad (\text{D.5})$$

This condition can be interpreted as ϵ_1 compensating for the classical OPA gain in order to achieve perfect interference visibility. Experimentally this condition is easily realized by matching the intensities of the squeezed beam with the reference beam—scaled with $1 - \epsilon_2$ —at the second beam splitter. If the condition in Equation D.5 is satisfied the detected variance by the homodyne detector simplifies to

$$V_{1,\text{out}} = 1 + \epsilon_2\eta_{\text{esc}} \frac{4\frac{g}{\kappa}}{\left(1 - \frac{g}{\kappa}\right)^2}, \quad (\text{D.6})$$

with the escape efficiency $\eta_{\text{esc}} = \kappa_{\text{oc}}/\kappa$. From the above equation of a squeezed vacuum results that the reflectivity of the second beam splitter ϵ_2 should be close to unity to minimize the losses of the squeezing. In the experiment described in [SVF⁺04] the second beam splitter has a reflectivity of 99% the resulting 1% loss for the squeezed beam is small compared to the overall loss of such an squeezing experiment. Comparing the discovered variance of the squeezed vacuum output of the second beam splitter with a seeded OPA output (Equation 3.25) reveals that Equation D.6 is identical if the OPA is seeded only with a vacuum noise limited input combined with a detection loss of $1 - \epsilon_2$.

Appendix E

Transfer function of Fabry-Perot cavity

The transfer function of a linear Fabry-Perot cavity (Figure E.1) is derived in this chapter. In the following it is assumed that the cavity mirrors are lossless. These can be modelled with transfer matrix of the beam splitter given by Equation 2.67 with the mirrors individual amplitude reflectivity r and amplitude transmissivity t . As a result one obtains the mirror transfer matrix

$$M = \begin{pmatrix} r & it \\ it & r \end{pmatrix}. \quad (\text{E.1})$$

The relation between the light fields—coupling with the two cavity mirrors m_1 and m_2 shown in Figure E.1—are given by

$$\begin{pmatrix} a_{\text{refl}} \\ a_1 \end{pmatrix} = \begin{pmatrix} r_1 & it_1 \\ it_1 & r_1 \end{pmatrix} \begin{pmatrix} a_{\text{in}} \\ a'_2 \end{pmatrix} \quad (\text{E.2})$$

$$\begin{pmatrix} a_2 \\ a_{\text{trans}} \end{pmatrix} = \begin{pmatrix} r_2 & it_2 \\ it_2 & r_2 \end{pmatrix} \begin{pmatrix} a'_1 \\ 0 \end{pmatrix}. \quad (\text{E.3})$$

Here the individual fields correspond to: the incoming field a_{in} , the transmitted field a_{trans} , the reflected field a_{refl} , and the intra-cavity fields a_1, a'_1, a_2 and a'_2 . The propagation of the fields inside the cavity are described by

$$a'_1 = a_1 e^{ikL} \quad (\text{E.4})$$

$$a'_2 = a_2 e^{ikL}, \quad (\text{E.5})$$

where k corresponds to the wave number $k = 2\pi/\lambda$ and L is the geometrical length of the cavity. From Equations E.2–E.5 together with abbreviation

$$d = \frac{1}{1 - r_1 r_2 e^{2ikL}} \quad (\text{E.6})$$

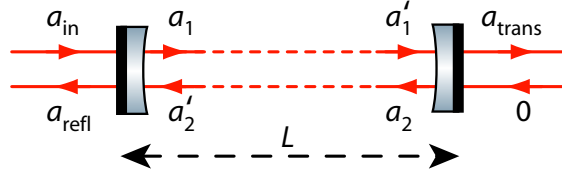


Figure E.1: Light field amplitudes at a Fabry-Perot cavity

the following relations for the field amplitudes can be derived:

$$a_1 = i d t_1 a_{in} \quad (\text{E.7})$$

$$a_1' = i d t_1 a_{in} e^{ikL} \quad (\text{E.8})$$

$$a_2 = i d t_1 r_2 a_{in} \quad (\text{E.9})$$

$$a_2' = i d t_1 r_2 a_{in} e^{ikL} \quad (\text{E.10})$$

$$a_{trans} = -d t_1 t_2 a_{in} e^{ikL} \quad (\text{E.11})$$

$$a_{refl} = r_1 a_{in} - d t_1^2 r_2 a_{in} e^{2ikL} \quad (\text{E.12})$$

$$= (r_1 - r_2 e^{2ikL}) d a_{in}. \quad (\text{E.13})$$

Therefore, the amplitude transfer functions in transmission and reflection of the Fabry-Perot cavity are given by the ratios

$$\tau = \frac{a_{trans}}{a_{in}} = \frac{-t_1 t_2 e^{ikL}}{1 - r_1 r_2 e^{2ikL}} \quad (\text{E.14})$$

$$(\text{E.15})$$

$$\rho = \frac{a_{refl}}{a_{in}} = \frac{r_1 - r_2 e^{2ikL}}{1 - r_1 r_2 e^{2ikL}}. \quad (\text{E.16})$$

These equations have been used in Figures 3.15, 4.25, 6.4, and D.1 to simulate the properties of a Fabry-Perot cavity and calculate the power reflectivity, power transmissivity or the frequency-dependent phase change that has to be applied to the field in reflection and transmission.

Bibliography

- [AAA⁺04] F. Acernese, P. Amico, N. Arnaud, D. Babusci, R. Barillé, F. Barone, L. Barsotti, M. Barsuglia, F. Beauville, M. A. Bizouard, C. Boccara, F. Bondu, L. Bosi, C. Bradaschia, L. Bracci, S. Braccini, A. Brillet, V. Brisson, L. Brocco, D. Buskulic, G. Calamai, E. Calloni, E. Campagna, F. Cavalier, G. Cella, E. Chassande-Mottin, F. Cleva, T. Cokelaer, G. Conforto, C. Corda, J.-P. Coulon, E. Cuoco, V. Dattilo, M. Davier, R. De Rosa, L. Di Fiore, A. Di Virgilio, B. Dujardin, A. Eleuteri, D. Enard, I. Ferrante, F. Fidecaro, I. Fiori, R. Flaminio, J.-D. Fournier, S. Frasca, F. Frasconi, L. Gammaitoni, A. Gennai, A. Giazotto, G. Giordano, G. Guidi, H. Heitmann, P. Hello, P. Heusse, L. Holloway, S. Kreckelberg, P. La Penna, V. Lorette, M. Loupias, G. Losurdo, J.-M. Mackowski, E. Majorana, C. N. Man, F. Marion, F. Martelli, A. Masserot, L. Massonnet, M. Mazzoni, L. Milano, J. Moreau, F. Moreau, N. Morgado, F. Mornet, B. Mours, J. Pacheco, A. Pai, C. Palomba, F. Paoletti, R. Passaquieti, D. Passuello, B. Perriola, L. Pinard, R. Poggiani, M. Punturo, P. Puppò, K. Qipiani, J. Ramonet, P. Rapagnani, V. Reita, A. Remillieux, F. Ricci, I. Ricciardi, G. Russo, S. Solimeno, R. Stanga, A. Toncelli, M. Tonelli, E. Tournefier, F. Travasso, H. Trinquet, M. Varvella, D. Verkindt, F. Vetrano, O. Veziant, A. Viceré, J.-Y. Vinet, H. Vocca, and M. Yvert. Status of VIRGO. *Classical and Quantum Gravity*, 21:S385, 2004. 173
- [AAB⁺05] S. Anza, M. Armano, E. Balaguer, M. Benedetti, C. Boatella, P. Bosetti, D. Bortoluzzi, N. Brandt, C. Braxmaier, M. Caldwell, L. Carbone, A. Cavalleri, A. Ciccolella, I. Cristofolini, M. Cruise, M. Da Lio, K. Danzmann, D. Desiderio, R. Dolesi, N. Dunbar, W. Fichter, C. Garcia, E. Garcia-Berro, A. F. Garcia Marin, R. Gerndt, A. Gianolio, D. Giardini, R. Gruenagel, A. Hammesfahr, G. Heinzl, J. Hough, D. Hoyland, M. Hueller, O. Jennrich, U. Johann, S. Kemble, C. Killow, D. Kolbe, M. Landgraf, A. Lobo, V. Lorizzo, D. Mance, K. Middleton, F. Nappo, M. Nofrarias, G. Racca, J. Ramos, D. Robertson, M. Sallusti, M. Sandford, J. Sanjuan, P. Sarra, A. Selig, D. Shaul, D. Smart, M. Smit, L. Stagnaro, T. Sumner, C. Tirabassi, S. Tobin, S. Vitale, V. Wand, H. Ward, W. J. Weber, and P. Zweifel. The LTP experiment on the LISA Pathfinder mission. *Classical and Quantum Gravity*, 22(10):S125–S138, 2005. 6
- [AAB⁺06] O. D. Aguiar, L. A. Andrade, J. J. Barroso, F. Bortoli, L. A. Carneiro, P. J. Castro, C. A. Costa, K. M. F. Costa, J. C. N. de Araujo, A. U. de Lucena,

- W. de Paula, E. C. de Rey Neto, S. T. de Souza, A. C. Fauth, C. Frajuca, G. Frossati, S. R. Furtado, N. S. Magalhães, R. M. Marinho Jr, J. L. Melo, O. D. Miranda, N. F. Oliveira Jr, K. L. Ribeiro, C. Stellati, W. F. Velloso Jr, and J. Weber. The Brazilian gravitational wave detector Mario Schenberg: status report. *Classical and Quantum Gravity*, 23(8):S239–S244, 2006. 3
- [AAD⁺92] A. Abramovici, W. E. Althouse, R. W. P. Drever, Y. Gürsel, S. Kawamura, F. J. Raab, D. Shoemaker, L. Sievers, R. E. Spero, K. S. Thorne, R. E. Vogt, R. Weiss, S. E. Whitcomb, and M. E. Zucker. LIGO: The Laser Interferometer Gravitational-Wave Observatory. *Quarterly Progress Report*, 256:325–333, 1992. 5, 173, 177
- [ABB⁺06] P. Astone, R. Ballantini, D. Babusci, M. Bassan, P. Carelli, G. Cavallari, F. Cavanna, A. Chincarini, E. Coccia, C. Cosmelli, S. D’Antonio, F. Durbath, V. Fafone, S. Foffa, G. Gemme, G. Giordano, M. Maggiore, A. Marini, Y. Minenkov, I. Modena, G. Modestino, A. Moleti, G. P. Murtas, A. Pai, O. Palamara, G. V. Pallottino, R. Parodi, G. Piano Mortari, G. Pizzella, L. Quintieri, A. Rocchi, F. Ronga, R. Sturani, R. Terenzi, G. Torrioli, R. Vaccarone, G. Vandoni, and M. Visco. Status report on the EXPLORER and NAUTILUS detectors and the present science run. *Classical and Quantum Gravity*, 23(8):S57–S62, 2006. 3
- [AC00] A. Abramovici and J. Chapsky. *Feedback Control Systems - A Fast-Track Guide for Scientists and Engineers*. Kluwer Academic Publishers, 2000. 205, 210
- [AC04] B. Abbott and The LIGO Scientific Collaboration. Detector description and performance for the first coincidence observations between LIGO and GEO. *Nuclear Instruments and Methods in Physics Research Section A*, 517:154, 2004. 173
- [AD05] P. Aufmuth and K. Danzmann. Gravitational wave detectors. *New Journal of Physics*, 7:202, 2005. 1, 3, 7
- [Adh05] R. Adhikari. Enhanced LIGO. LIGO internal document G060433-00-I, 2005. 5
- [ADVa] Advanced LIGO. <http://www.ligo.caltech.edu/advLIGO/>. 5, 126, 155, 177
- [ADVb] Advanced VIRGO. <http://wwwcascina.virgo.infn.it/advirgo/>. 5, 177
- [APF⁺04] A. Ageev, B. C. Palmer, A. De Felice, S. D. Penn, and P. R. Saulson. Very high quality factor measured in annealed fused silica. *Classical and Quantum Gravity*, 21(16):3887–3892, 2004. 179
- [ATF06] T. Aoki, G. Takahashi, and A. Furusawa. Squeezing at 946nm with periodically-poled KTiOPO4. *Opt. Exp.*, 14:6930–6935, 2006. 46

-
- [AtTC01] M. Ando and the TAMA Collaboration. Stable Operation of a 300-m Laser Interferometer with Sufficient Sensitivity to Detect Gravitational-Wave Events within Our Galaxy. *Phys. Rev. Lett.*, 86:3950, 2001. 173
- [BC02] A. Buonanno and Y. Chen. Signal recycled laser-interferometer gravitational-wave detectors as optical springs. *Phys. Rev. D*, 65:042001, 2002. 8, 96
- [BFV⁺90] C. Bradaschia, R. Del Fabbro, A. Di Virgilio, A. Giazotto, H. Kautzky, V. Montelatici, D. Passuello, A. Brillet, O. Cregut, P. Hello, C. N. Man, P. T. Manh, A. Marraud, D. Shoemaker, J. Y. Vinet and F. Barone, L. Di Fiore, L. Milano, G. Russo, J. M. Aguirregabiria, H. Bel, J. P. Duruisseau, G. Le Denmat, Ph. Tournenc, M. Capozzi, M. Longo, M. Lops, I. Pinto, G. Rotoli, T. Damour, S. Bonazzola, J. A. Marck, Y. Gourghoulon, L. E. Holloway, F. Fuligni, V. Iafolla, and G. Natale. The VIRGO Project: A wide band antenna for gravitational wave detection. *Nucl. Instrum. Methods A*, 289(3):518–525, 1990. 5, 177
- [BGV99] V. B. Braginsky, M. L. Gorodetsky, and S. P. Vyatchanin. Thermodynamical fluctuations and photo-thermal shot noise in gravitational wave antennae. *Phys. Lett. A*, 264:1–10, 1999. 7, 162
- [Bla00] E. D. Black. An introduction to Pound-Drever-Hall laser frequency stabilization. *Am. J. Phys.*, 69:79, 2000. 62
- [Boy92] R. W. Boyd. *Nonlinear Optics*. Academic Press, 1992. 65, 66, 67
- [BR03] H.-A. Bachor and T. C. Ralph. *A Guide to Experiments in Quantum Optics*. Wiley-VCH, 2003. 17, 25, 26, 28, 31, 68
- [Bre98] G. Breitenbach. *Quantum state reconstruction of classical and nonclassical light and a cryogenic opto-mechanical sensor for high-precision interferometry*. PhD thesis, Universität Konstanz, 1998. 112
- [Buc01] B. C. Buchler. *Electro-optic Control of Quantum Measurements*. PhD thesis, Australian National University, 2001. 68, 70, 72
- [BV01] V. B. Braginsky and S. P. Vyatchanin. Frequency fluctuations of nonlinear origin in self-sustained optical oscillators. *Physics Letters A*, 279:154–162, 2001. 7, 179
- [Cav81] C. M. Caves. Quantum-mechanical noise in an interferometer. *Phys. Rev. D*, 23:1693, 1981. 93, 96, 125, 162, 173
- [CCF⁺04] D. R. M. Crooks, G. Cagnoli, M. M. Fejer, A. Gretarsson, G. Harry, J. Hough, N. Nakagawa, S. Penn, R. Route, S. Rowan, and P. H. Sneddon. Experimental measurements of coating mechanical loss factors. *Classical and Quantum Gravity*, 21(5):S1059–S1065, 2004. 7, 179

- [CD96] V. Chickarmane and S. V. Dhurandhar. Performance of a dual recycled interferometer with squeezed light. *Phys. Rev. A*, 54:786, 1996. 125
- [CDR⁺98] V. Chickarmane, S. V. Dhurandhar, T. C. Ralph, M. Gray, and H.-A. Bachor. Squeezed light in a frontal-phase-modulated signal-recycled interferometer. *Phys. Rev. A*, 57:3898, 1998. 173
- [Col04] H. Collins. *Gravity's Shadow*. University Of Chicago Press, 2004. 3
- [CS85] C. M. Caves and B. L. Schumaker. New formalism for two-photon quantum optics. I. Quadrature phases and squeezed states. *Phys. Rev. A*, 31:3068, 1985. 101, 166
- [CT02] C. Cutler and K. S. Thorne. An overview of gravitational wave sources. In N. Bishop and S. D. Maharaj, editors, *General Relativity and Gravitation, Proceedings of the 16th International Conference*, pages 72–111. World Scientific, 2002. 1
- [CVDS07] S. Chelkowski, H. Vahlbruch, K. Danzmann, and R. Schnabel. Coherent control of broadband vacuum squeezing. *Phys. Rev. A*, 75:043814, 2007. Copyright (2007) by the American Physical Society. 161
- [CVH⁺05] S. Chelkowski, H. Vahlbruch, B. Hage, A. Franzen, N. Lastzka, K. Danzmann, and R. Schnabel. Experimental characterization of frequency-dependent squeezed light. *Phys. Rev. A*, 71:013806, 2005. 93, 162, 175
- [DHK⁺83] R. W. P. Drever, J. L. Hall, F. V. Kowalski, J. Hough, G. M. Ford, A. J. Munley, and H. Ward. Quantum Optics, Experimental Gravitation, and Measurement Theory. pages 503–514. Plenum, New York, 1983. 8, 94, 125, 178
- [Don99] S. Donati. *Photodetectors: Devices, Circuits and Applications*. Prentice Hall, 1999.
- [dVSM02] G. de Vine, D. A. Shaddock, and D. E. McClelland. Variable reflectivity signal mirrors and signal response measurements. *Class. Quantum Grav.*, 19:1561, 2002. 149
- [dWBB⁺06] A. de Waard, M. Bassan, Y. Benzaim, V. Fafone, J. Flokstra, G. Frossati, L. Gottardi, C. T. Herbschleb, A. Karbalai-Sadegh, K. Kuit, H. van der Mark, Y. Minenkov, J. B. R. Oonk, G. V. Pallottino, J. Pleikies, A. Rocchi, O. Usenko, and M. Visco. Preparing for science run 1 of MiniGRAIL. *Classical and Quantum Gravity*, 23(8):S79–S84, 2006. 3
- [Ein16] A. Einstein. Approximative integration of the field equations of gravitation. *Sitzungsber. Preuss. Akad. Wiss. Berlin*, page 688, 1916. 1
- [Ein18] A. Einstein. On gravitational waves. *Sitzungsber. Preuss. Akad. Wiss. Berlin*, page 154, 1918. 1

-
- [ENKB91] R. C. Eckhardt, C. D. Nabors, W. J. Kozlovsky, and R. L. Byer. Optical parametric oscillator frequency tuning and control. *J. Opt. Soc. Am. B*, 8:646, 1991. 67
- [FH05] É. É. Flanagan and S. A. Hughes. The basics of gravitational wave theory. *New Journal of Physics*, 7:204, 2005. 1
- [FHPW61] P. A. Franken, A. E. Hill, C. W. Peters, and G. Weinreich. Generation of Optical Harmonics. *Phys. Rev. Lett.*, 7:118, 1961. 64
- [Fra04] A. Franzen. Erzeugung von gequetschtem Licht für die Gravitationswellen-Astronomie. Diplomarbeit, Universität Hannover, 2004. 57
- [Fre] A. Freise. Finesse – Frequency domain INterfERometer Simulation SofTwarE. <http://www.rzg.mpg.de/adf/>. 132, 141
- [Fre03] A. Freise. *The Next Generation of Interferometry: Multi-Frequency Optical Modelling, Control Concepts and Implementation*. PhD thesis, Universität Hannover, 2003. 94
- [Fri05] P. Fritschel. DC Readout for Advanced LIGO. LIGO internal document G030460-00-R, 2005. 5
- [GBL87] J. Gea-Banacloche and G. Leuchs. Squeezed states for interferometric gravitational-wave detectors. *J. Mod. Opt.*, 34:793–811, 1987. 93, 125, 162, 173
- [GC85] C. W. Gardiner and M. J. Collett. Input and output in damped quantum systems: Quantum stochastic differential equations and the master equation. *Phys. Rev. A*, 31:3761–3774, 1985. 70
- [GC04] A. Giazotto and G. Cella. Some considerations about future interferometric GW detectors. *Classical and Quantum Gravity*, 21(5):S1183–S1190, 2004. 5
- [GEO] The GEO 600 gravitational wave detector. <http://geo600.aei.mpg.de/>. 94, 155
- [Gia05] J. A. Giaime. The Advanced LIGO detector. Talk at the Amaldi 6 Conference, LIGO internal document LIGO-G050315-00-D, 2005. 5, 177
- [Goß04] S. Goßler. *The suspension systems of the interferometric gravitational-wave detector GEO 600*. PhD thesis, Universität Hannover, 2004. 7, 94
- [God06] K. Goda. Optimum Choice of Nonlinear Crystals toward Higher Levels of Squeezing at 1064 nm. 2006. 74
- [GP63] M. E. Gertsenshtein and V. I. Pustovoit. On the detection of low frequency gravitational waves. *Soviet Physical Journal of Experimental and Theoretical Physics*, 16:433–435, 1963. 3

- [Gro03] H. Grote. *Making it Work: Second Generation Interferometry in GEO 600!* PhD thesis, Universität Hannover, 2003. 94
- [GSYL87] P. Grangier, R. E. Slusher, B. Yurke, and A. LaPorta. Squeezed-light-enhanced polarization interferometer. *Phys. Rev. Lett.*, 59(19):2153–2156, Nov 1987. 126
- [HABT⁺07] G. M. Harry, M. R. Abernathy, A. E. Becerra-Toledo, H. Armandula, E. Black, K. Dooley, M. Eichenfield, C. Nwabugwu, A. Villar, D. R. M. Crooks, G. Cagnoli, J. Hough, C. R. How, I. MacLaren, P. Murray, S. Reid, S. Rowan, P. H. Sneddon, M. M. Fejer, R. Route, S. D. Penn, P. Ganau, J.-M. Mackowski, Ch. Michel, L. Pinard, and A. Remillieux. Titania-doped tantala/silica coatings for gravitational-wave detection. *Classical and Quantum Gravity*, 24(2):405–415, 2007. 179
- [Hag04] B. Hage. Quantentomographische Charakterisierung gequetschter Zustände. Diplomarbeit, Universität Hannover, 2004. 109, 112, 115
- [Hak70] H. Haken. *Light and Matter I c Band 25, Teil 2 of Handbuch der Physik.* Springer, 1970. 70
- [Har02] J. Harms. Quantum Noise in the Laser-Interferometer Gravitational-Wave Detector GEO 600. Diplomarbeit, Universität Hannover, 2002. 102, 197
- [Har06] J. Harms. *The Detection of Gravitational Waves.* PhD thesis, Universität Hannover, 2006. 26, 182
- [HCC⁺03] J. Harms, Y. Chen, S. Chelkowski, A. Franzen, H. Vahlbruch, K. Danzmann, and R. Schnabel. Squeezed-input, optical-spring, signal-recycled gravitational-wave detectors. *Phys. Rev. D*, 68:042001, 2003. 93, 96, 97, 125, 156, 162, 175, 182
- [HDG⁺02] I. S. Heng, E. Daw, J. Giaime, W. O. Hamilton, M. P. McHugh, and W. W. Johnson. Allegro: noise performance and the ongoing search for gravitational waves. *Classical and Quantum Gravity*, 19(7):1889–1895, 2002. 3
- [Hei27] W. Heisenberg. Über den anschaulichen Inhalt der quantentheoretischen Kinematik und Mechanik. *Zeitschrift für Physik*, 43:172–198, 1927. 18
- [Hei95] G. Heinzel. Resonant Sideband Extraction – Neuartige Interferometrie für Gravitationswellendetektoren. Diplomarbeit, Universität Hannover, 1995. 210
- [Her80] G. T. Herman. *Image Reconstruction from Projections: The Fundamentals of Computerized Tomography.* Academic Press, New York, 1980. 109, 112
- [Hil03] S. Hild. Thermisch durchstimmbares Signal-Recycling für den Gravitationswellendetektor GEO 600. Diplomarbeit, Universität Hannover, 2003. 181

- [HRH⁺97] C. C. Harb, T. C. Ralph, E. H. Huntington, D. E. McClelland, H.-A. Bachor, and I. Freitag. Intensity-noise dependence of Nd:YAG lasers on their diode-laser pump source. *J. Opt. Soc. Am. B*, 14:2936, 1997. 60, 225
- [HSM⁺98] G. Heinzl, K. A. Strain, J. Mizuno, K. D. Skeldon, B. Willke, W. Winkler, R. Schilling, A. Rüdiger, and K. Danzmann. Experimental Demonstration of a Suspended Dual Recycling Interferometer for Gravitational Wave Detection. *Phys. Rev. Lett.*, 81(25):5493–5496, 1998. 126
- [HT75] R. A. Hulse and J. H. Taylor. Discovery of a pulsar in a binary system. *Astrophys. J.*, 195:L51, 1975. 2
- [HtL06] S. Hild and the LSC. The status of GEO 600. *Class. Quantum Grav.*, 23:S643–S651, 2006. 5, 173
- [Hul94] R. A. Hulse. The discovery of the binary pulsar. *Rev. Mod. Phys.*, 66(3):699–710, Jul 1994. 2
- [JR90] M. T. Jaekel and S. Reynaud. Quantum Limits in Interferometric Measurements. *Europhys. Lett.*, 13:301, 1990. 93, 96
- [KL66] H. Kogelnik and T. Li. Laser Beams and Resonators. *Proceedings of the IEEE*, 54:1312–1329, 1966. 29
- [KLM⁺01] H. J. Kimble, Y. Levin, A. B. Matsko, K. S. Thorne, and S. P. Vyatchanin. Conversion of conventional gravitational-wave interferometers into quantum nondemolition interferometers by modifying their input and/or output optics. *Phys. Rev. D*, 65:022002, 2001. 10, 98, 99, 105, 156, 162, 183
- [Kok04] K. D. Kokkotas. High-frequency sources of gravitational waves. *Classical and Quantum Gravity*, 21(5):S501–S507, 2004. 177
- [KS89] A. C. Kak and M. Slaney. *Principles of Computerized Tomographic Imaging*. I.E.E.E.Press, 1989. 109
- [KtLC06] K. Kazuaki and the LCGT Collaboration. The status of LCGT. *Classical and Quantum Gravity*, 23(8):S215–S221, 2006. 5, 6, 7, 177
- [Lam98] P. K. Lam. *Applications of Quantum Electro-Optic Control and Squeezed Light*. PhD thesis, Australian National University, 1998. 22, 34
- [LBD⁺86] J. Livas, R. Benford, D. Dewey, A. Jeffries, P. Saulson, D. Shoemaker, and R. Weiss. The MIT gravitational wave detector. In R. Ruffini, editor, *Proceedings of the Fourth Marcel Grossmann Meeting on General Relativity*, pages 591–597. Elsevier Science Ltd, 1986. 5
- [Leo97] U. Leonhardt. *Measuring the Quantum State of Light*. Cambridge University Press, 1997. 109
- [LIS] LISA–Laser Interferometer Space Antenna. <http://lisa.jpl.nasa.gov/>. 6

- [LIS05] *Proceedings of the 5th international LISA symposium and the 38th ESLAB symposium*, volume 22. *Class. Quant. Grav.*, 2005. 6
- [LMR⁺87] G. Leuchs, K. Maischberger, A. Rüdiger, R. Schilling, L. Schnupp, and W. Winkler. Proposal for the Construction of a Large Laser Interferometer for the Measurement of Gravitational Waves. *Quarterly Progress Report*, 131, 1987. 5
- [LRB⁺99] P. K. Lam, T. C. Ralph, B. C. Buchler, D. E. McClelland, and H.-A. Bachor. Optimization and transfer of vacuum squeezing from an optical parametric oscillator. *J. Opt. B.*, 1:469, 1999. 46, 156
- [LT00] Y. T. Liu and K. S. Thorne. Thermoelastic noise and homogeneous thermal noise in finite sized gravitational-wave test masses. *Phys. Rev. D*, 62(12):122002, Nov 2000. 7, 179
- [Mal06] M. Malec. *Commissioning of advanced, dual-recycled gravitational-wave detectors: simulations of complex optical systems guided by the phasor picture*. PhD thesis, Universität Hannover, 2006. 35
- [Mee88] B. J. Meers. Recycling in laser-interferometric gravitational-wave detectors. *Phys. Rev. D*, 38:2317, 1988. 9, 93, 94, 125, 162, 177, 178
- [MGB⁺04] K. McKenzie, N. Grosse, W. P. Bowen, S. E. Whitcomb, M. B. Gray, D. E. McClelland, and P. K. Lam. Squeezing in the Audio Gravitational-Wave Detection Band. *Phys. Rev. Lett.*, 93:161105, 2004. 156, 163
- [MGG⁺06] K. McKenzie, M. B. Gray, S. Goßler, P. K. Lam, and D. E. McClelland. Squeezed state generation for interferometric gravitational-wave detection. *Class. Quantum Grav.*, 23:S245–S250, 2006.
- [Miz95] J. Mizuno. *Comparison of optical configurations for laser-interferometric gravitational-wave detectors*. PhD thesis, Universität Hannover, 1995. 94
- [MMF71] G. E. Moss, L. R. Miller, and R. L. Forward. Photon-noise-limited laser transducer for gravitational antenna. *Appl. Opt.*, 10:2495–2498, 1971. 4
- [MMG⁺05] K. McKenzie, E. E. Mikhailov, K. Goda, P. K. Lam, N. Grosse, M. B. Gray, N. Mavalvala, and D. E. McClelland. Quantum noise locking. *J. Opt. B*, 7:S421–S428, 2005. 163
- [MSM⁺02] K. McKenzie, D. A. Shaddock, D. E. McClelland, B. C. Buchler, and P. K. Lam. Experimental Demonstration of a Squeezing-Enhanced Power-Recycled Michelson Interferometer for Gravitational Wave Detection. *Phys. Rev. Lett.*, 88:231102, 2002. 126
- [MtTc02] A. Masaki and the TAMA collaboration. Current status of TAMA. *Classical and Quantum Gravity*, 19(7):1409–1419, 2002. 5

-
- [MTW73] C. Misner, K. S. Thorne, and J. A. Wheeler. *Gravitation*. W. H. Freeman, 1973. 1
- [MUY⁺04] S. Miyoki, T. Uchiyama, K. Yamamoto, H. Hayakawa, K. Kasahara, H. Ishit-suka, M. Ohashi, K. Kuroda, D. Tatsumi, S. Telada, M. Ando, T. Tomaru, T. Suzuki, N. Sato, T. Haruyama, Y. Higashi, Y. Saito, A. Yamamoto, T. Shintomi, A. Araya, S. Takemoto, T. Higashi, H. Momose, J. Akamatsu, and W. Morii. Status of the CLIO project. *Classical and Quantum Gravity*, 21(5):S1173–S1181, 2004. 6
- [NHK⁺86] G. P. Newton, J. Hough, G. A. Kerr, B. J. Meers, N. A. Robertson, H. Ward, J. B. Mangan, and S. Hoggan. Some improvements to the Glasgow gravitational wave detector. In R. Ruffini, editor, *Proceedings of the Fourth Marcel Grossmann Meeting on General Relativity*, pages 599–604. Elsevier Science Ltd, 1986. 5
- [PAB⁺05] S. D. Penn, A. Ageev, D. Busby, G. M. Harry, A. M. Gretarsson, K. Numata, and Ph. Willems. Frequency and surface dependence of the mechanical loss in fused silica. *arXiv*, gr-qc:0507097v1, 2005. 179
- [PC02] P. Purdue and Y. Chen. Practical speed meter designs for quantum nonde-molition gravitational-wave interferometers. *Phys. Rev. D*, 66(12):122004, Dec 2002. 156
- [PCK92] E. S. Polzik, J. Carri, and H. J. Kimble. Atomic Spectroscopy with Squeezed Light for Sensitivity Beyond the Vacuum-State Limit. *Appl. Phys. B*, 44:279–290, 1992. 46
- [PCW93] A. F. Pace, M. J. Collett, and D. F. Walls. Quantum limits in interferometric detection of gravitational radiation. *Phys. Rev. A*, 47:3173, 1993. 93
- [Pun05] M. Punturo. Virgo: Plans for the Next Future. LIGO internal document G060332-00, 2005. 5
- [Que03] V. M. Quetschke. *Korrelationen von Rauschquellen bei Nd:YAG Lasersys-temen*. PhD thesis, Universität Hannover, 2003. 62
- [Rad17] J. Radon. Berichte über die Verhandlungen der Königlich-Sächsichen Gesellschaft der Wissenschaften zu Leipzig. *Mathematisch-Physische Klasse*, 69:262, 1917. 112
- [RHC05] S. Rowan, J. Hough, and D. R. M. Crooks. Thermal noise and material issues for gravitational wave detectors. *Physics Letters A*, 347:25–32, 2005. 7
- [Sau94] P. R. Saulson. *Fundamentals of Interferometric Gravitational Wave Detec-tors*. World Scientific Publishing, 1994. 8

- [Sch88] L. Schnupp. Talk at the European Collaboration Meeting on Interferometric Detection of Gravitational Waves, Sorrento). LIGO internal document G060332-00, 1988. 134, 174
- [Sch02] B. F. Schutz. *Gravity from the ground up*. Cambridge University Press, 2002. 1
- [Sha49] C. E. Shannon. Communication in the Presence of Noise. *Proceedings of the IRE*, 37:10.21, 1949. reprinted in Proceedings of the IEEE, Vol. 86, No. 2, February 1998 447. 26
- [Sho03] D. Shoemaker. Ground-based interferometric gravitational-wave detectors in the LISA epoch. *Classical and Quantum Gravity*, 20:S11, 2003. 162
- [SHSD04] R. Schnabel, J. Harms, K. A. Strain, and K. Danzmann. Squeezed light for the interferometric detection of high-frequency gravitational waves. *Class. Quantum Grav.*, 21:S1045, 2004. 93, 150, 173
- [SHY⁺85] R. E. Slusher, L. W. Hollberg, B. Yurke, J. C. Mertz, and J. F. Valley. Observation of Squeezed States Generated by Four-Wave Mixing in an Optical Cavity. *Phys. Rev. Lett.*, 55(22):2409–2412, Nov 1985. 10, 162
- [Sie86] A. E. Siegman. *Lasers*. University Science Books,U.S., 1986. 74
- [SM91] K. A. Strain and B. J. Meers. Experimental demonstration of dual recycling for interferometric gravitational-wave detectors. *Phys. Rev. Lett.*, 66(11):1391–1394, 1991. 126
- [Spe86] R. Spero. The Caltech laser-interferometric gravitational wave detector. In R. Ruffini, editor, *Proceedings of the Fourth Marcel Grossmann Meeting on General Relativity*, pages 615–620. Elsevier Science Ltd, 1986. 5
- [SSM⁺96] K. Schneider, S. Schiller, J. Mlynek, M. Bode, and I. Freitag. 1.1- μ m single-frequency 532-nm radiation by second-harmonic generation of a miniature nd-yag ring laser. *Opt. Lett.*, 21:1999, 1996. 65
- [SSS⁺88] D. Shoemaker, R. Schilling, L. Schnupp, W. Winkler, K. Maischberger, and A. Rüdiger. Noise behavior of the Garching 30-meter prototype gravitational-wave detector. *Phys. Rev. D*, 38(2):423–432, Jul 1988. 5
- [SVF⁺04] R. Schnabel, H. Vahlbruch, A. Franzen, S. Chelkowski, N. Grosse, H.-A. Bachor, W. P. Bowen, P. K. Lam, and K. Danzmann. Squeezed light at sideband frequencies below 100 kHz from a single OPA. *Opt. Comm.*, 240:185–190, 2004. 161, 225, 228
- [Tay94] J. H. Taylor. Binary pulsars and relativistic gravity. *Rev. Mod. Phys.*, 66(3):711–719, Jul 1994. 2
- [Thü04] A. Thüring. Lineare mehrfach Spiegel-Resonatoren für Gravitationswellendetektoren. Diplomarbeit, Universität Hannover, 2004. 140, 182

-
- [Tho83] K. S. Thorne. Gravitational Radiation. In S. W. Hawking and W. Israel, editors, *300 Years of Gravitation*, page 330. Cambridge University Press, Cambridge, England, 1983. 1, 162
- [TSLD07] A. Thüring, R. Schnabel, H. Lück, and K. Danzmann. Detuned Twin-Signal-Recycling for ultrahigh-precision interferometers. *Opt. Lett.*, 32:985, 2007. 182, 191
- [Ueh97] N. Uehara. Ring Mode Cleaner for the Initial LIGO 10 Watt Laser - Internal LIGO Report. Stanford University, Stanford, California, 1997. 61
- [Unr83] W. G. Unruh. Quantum Optics, Experimental Gravitation, and Measurement Theory. page 647. Plenum, New York, 1983. 162
- [Vah] H. Vahlbruch. *in preparation*. PhD thesis. 161
- [Vah04] H. Vahlbruch. Gequetschtes Licht bei kleinen Seitenbandfrequenzen. Diplomarbeit, Universität Hannover, 2004. 57
- [VCH⁺05] H. Vahlbruch, S. Chelkowski, B. Hage, A. Franzen, K. Danzmann, and R. Schnabel. Demonstration of a Squeezed-Light-Enhanced Power- and Signal-Recycled Michelson Interferometer. *Phys. Rev. Lett.*, 95:211102, 2005. 126, 162
- [VCH⁺06a] H. Vahlbruch, S. Chelkowski, B. Hage, A. Franzen, K. Danzmann, and R. Schnabel. Coherent Control of Vacuum Squeezing in the Gravitational-Wave Detection Band. *Phys. Rev. Lett.*, 97:011101, 2006. 156, 163, 164, 168, 172
- [VCH⁺06b] H. Vahlbruch, S. Chelkowski, B. Hage, A. Franzen, K. Danzmann, and R. Schnabel. Squeezed-field injection for gravitational wave interferometers. *Class. Quantum Grav.*, 23:S251–S257, 2006. 126, 162
- [VftAC06] A. Vinante and (for the AURIGA Collaboration). Present performance and future upgrades of the AURIGA capacitive readout. *Classical and Quantum Gravity*, 23(8):S103–S110, 2006. 3
- [WAA⁺04] B. Willke, P. Aufmuth, C. Aulbert, S. Babak, R. Balasubramanian, B. W. Barr, S. Berukoff, G. Cagnoli, C. A. Cantley, M. M. Casey, S. Chelkowski, D. Churches, C. N. Colacino, D. R. M. Crooks, C. Cutler, K. Danzmann, R. Davies, R. J. Dupuis, E. Elliffe, C. Fallnich, A. Freise, S. Goßler, A. Grant, H. Grote, S. Grunewald, J. Harms, G. Heinzl, I. S. Heng, A. Hepstonstall, M. Heurs, M. Hewitson, S. Hild, J. Hough, R. Ingley, Y. Itoh, O. Jennrich, R. Jones, S. H. Hutter, K. Kawabe, C. Killow, K. Kötter, B. Krishnan, V. Leonhardt, H. Lück, B. Machenschalk, M. Malec, R. A. Mercer, C. Messenger, S. Mohanty, K. Mossavi, S. Mukherjee, S. Nagano, G. P. Newton, M. A. Papa, M. Perreux-Lloyd, M. Pitkin, M. V. Plissi, V. Quetschke, V. Re, S. Reid, L. Ribichini, D. I. Robertson, N. A. Robertson, S. Rowan, A. Rüdiger, B. S. Sathyaprakash, R. Schilling, R. Schnabel, B. F. Schutz, F. Seifert,

- A. M. Sintes, J. R. Smith, P. H. Sneddon, K. A. Strain, I. Taylor, C. I. Torrie, C. Ungarelli, A. Vecchio, H. Ward, U. Weiland, H. Welling, P. Williams, W. Winkler, G. Woan, and I. Zawischa. Status of GEO 600. *Class. Quantum Grav.*, 21:S417–S423, 2004. 158, 180
- [WAA⁺06] B. Willke, P. Ajith, B. Allen, P. Aufmuth, C. Aulbert, S. Babak, R. Balasubramanian, B. W. Barr, S. Berukoff, A. Bunkowski, G. Cagnoli, C. A. Cantley, M. M. Casey, S. Chelkowski, Y. Chen, D. Churches, T. Cokelaer, C. N. Colacino, D. R. M. Crooks, C. Cutler, K. Danzmann, R. J. Dupuis, E. Elliffe, C. Fallnich, A. Franzen, A. Freise, I. Gholami, S. Goßler, A. Grant, H. Grote, S. Grunewald, J. Harms, B. Hage, G. Heinzl, I. S. Heng, A. Hepstonstall, M. Heurs, M. Hewitson, S. Hild, J. Hough, Y. Itoh, G. Jones, R. Jones, S. H. Huttner, K. Kötter, B. Krishnan, P. Kwee, H. Lück, M. Luna, B. Machenschalk, M. Malec, R. A. Mercer, T. Meier, C. Messenger, S. Mohanty, K. Mossavi, S. Mukherjee, P. Murray, G. P. Newton, M. A. Papa, M. Perreux-Lloyd, M. Pitkin, M. V. Plissi, R. Prix, V. Quetschke, V. Re, T. Regimbau, H. Rehbein, S. Reid, L. Ribichini, D. I. Robertson, N. A. Robertson, C. Robinson, J. D. Romano, S. Rowan, A. Rüdiger, B. S. Sathyaprakash, R. Schilling, R. Schnabel, B. F. Schutz, , F. Seifert, A. M. Sintes, J. R. Smith, P. H. Sneddon, K. A. Strain, I. Taylor, R. Taylor, A. Thüring, C. Ungarelli, H. Vahlbruch, A. Vecchio, J. Veitch, H. Ward, U. Weiland, H. Welling, L. Wen, P. Williams, W. Winkler, G. Woan, and R. Zhu. The GEO-HF project. *Class. Quantum Grav.*, 23:S207–S214, 2006. 177
- [Wal83] D. F. Walls. Squeezed states of light. *Nature*, 306:141, 1983. 162
- [WDF⁺06] B. Willke, K. Danzmann, C. Fallnich, M. Frede, M. Heurs, P. King, D. Kracht, P. Kwee, R. Savage, F. Seifert, and R. Wilhelm. Stabilized High Power Laser for Advanced Gravitational Wave Detectors. *Journal of Physics: Conference Series*, 32:270–275, 2006. 179
- [Web69] J. Weber. Evidence for Discovery of Gravitational Radiation. *Phys. Rev. Lett.*, 22(24):1320–1324, Jun 1969. 2
- [Wei72] R. Weiss. Electromagnetically Coupled Broadband Gravitational Antenna. *Quarterly Progress Report*, 105:54, 1972. Research Laboratory of Electronics, MIT. 4
- [Whi97] A. G. White. *Classical and quantum dynamics of optical frequency conversion*. PhD thesis, Australien National University, 1997. 15, 16, 19, 21, 22
- [Wig32] E. P. Wigner. On the Quantum Correction For Thermodynamic Equilibrium. *Phys. Rev.*, 40:749, 1932. 109
- [WM94] D. F. Walls and G. J. Milburn. *Quantum Optics*. Springer-Verlag, 1994. 10, 13, 14, 20, 69, 102

- [XWK87] M. Xiao, L.-A. Wu, and H. J. Kimble. Precision measurement beyond the shot-noise limit. *Phys. Rev. Lett.*, 59(3):278–281, Jul 1987. 126
- [ZGC⁺03] T. C. Zhang, K. W. Goh, C. W. Chou, P. Lodahl, and H. J. Kimble. Quantum teleportation of light beams. *Phys. Rev. A*, 67:033802, 2003. 46, 52

Acknowledgements

When I started my doctoral studies in a newly founded group at the Albert-Einstein-Institute the future was wide open and it was exciting to see the progress the squeezing group made in the last years. Being part of that amazing group I have to thank many people who contributed to this work.

First I would like to thank Karsten Danzmann for his general support and guidance. You made this institute one of the most attractive places in the world for researchers in the gravitational wave community. I am glad for being part of it and really enjoyed my time here.

I want to thank Roman Schnabel. You did a great job in establishing the squeezing group and expanding it until today. I enjoyed the time working with you in your group. I am grateful you sent me to Canberra to get in touch with the topic and our Australian colleagues. I really enjoyed my time there.

This work would not have been successful without the help of my squeezing colleagues. I want to thank Alexander, André, Boris, James, Jan, Moritz and Nico. You guys are great and I enjoyed sharing my time with you. I am grateful being part of this team over the last years. Especially I would like to thank Henning. We worked closely together in the last years. I liked sharing the lab with you, discussing the next steps of the experiments, pushing each other to the limit or just having a cup of coffee together. Thanks for all of this.

Furthermore I would like to thank all the people who supported me during my doctoral thesis, but who are not part of this squeezing group: Kirk McKenzie and Nicolai Große for sharing their experiences in quantum optics and the Australian way of living with me. Stefan Goßler for motivating me to join the gravitational wave community. Andreas Freise and Paul Cochrane for their guidance in using FINESSE. André Thüring for convincing me to use Gnuplot. Frank Seifert, Patrick Kwee and Tobias Müller for long and interesting discussions on laser related topics. Gerhardt Heinzl and Hartmut Grote for sharing their knowledge on electronics design with me. Harald Lück, Benno Willke and Stefan Hild for fruitful discussions and for giving me a deeper understanding of GEO 600. Andreas Weidner and Heiko zur Mühlen for their help in building electronics. The workshop crew for their help and patience. Alexander Franzen for developing the symbol library intensively used in this thesis. Oliver Burmeister and Sascha Skorupka for their long, informative but most of all funny stories, which sometimes made life easier. Finally, I thank Jan Harms not only for sharing his immense knowledge with me but also for being a friend.

I thank Tahera Ali, Paul Cochrane, James DiGuglielmo, Alexander Franzen, Stefan Goßler, Boris Hage, Jan Harms, Ben Sheard, Henning Vahlbruch and Kerstin for proof-reading my thesis. Nevertheless, I am responsible for all remaining mistakes.

Finally I would like to thank my family for their support over the last years and especially Kerstin for her love. I am deeply grateful that you are always there for me.

Curriculum vitae

Personal data

Name: Simon Chelkowski
Address: Am Kleinen Felde 4
30167 Hannover
Germany
Date of birth: 28. September 1976
Place of birth: Hannover, Germany
Nationality: German

University studies

2003–present Scientific assistant (wissenschaftlicher Angestellter) at the University of Hannover
2003–present Doctoral studies in Physics, University of Hannover, Max-Planck-Institut für Gravitationsphysik (Albert-Einstein-Institut)
2003 Visit to the Quantum Optics group at the Australian National University for three months
2002 Physik Diplom, *Aufbau eines atomaren Sagnac-Interferometers zur hochauflösenden Rotationsmessung (Setup of an atomic Sagnac-Interferometer for high resolution measurements of rotations)*
1997–2002 Diploma studies in Physics at the University of Hannover and the Institute for Quantum Optics

Community service

1996–1997 Community service at Heimvolkshochschule Springe in lieu of military service

Education

1996 University-entrance exam, German certificate of maturity (Abitur), St. Ursula Gymnasium Hannover
1989–1996 High School (Gymnasium) Hannover
1984–1989 Primary School (Grundschule, Orientierungsstufe) Hannover

Publications

2007

- S. Chelkowski, H. Vahlbruch, K. Danzmann and R. Schnabel: *Coherent control of broadband vacuum squeezing*, Phys. Rev. A, **75**, 043814 (2007)

2006

- B. Abbott and the LSC: *Search for gravitational waves from binary black hole inspirals in LIGO data*, Phys. Rev. D, **73**, 062001 (2006)
- B. Abbott and the LSC: *Joint LIGO and TAMA300 search for gravitational waves from inspiralling neutron star binaries*, Phys. Rev. D, **73**, 102002 (2006)
- H. Vahlbruch, S. Chelkowski, B. Hage, A. Franzen, K. Danzmann and R. Schnabel: *Squeezed-field injection for gravitational wave interferometers*, Class. Quantum Grav., **23**, S251-S257 (2006)
- H. Vahlbruch, S. Chelkowski, B. Hage, A. Franzen, K. Danzmann and R. Schnabel: *Coherent Control of Vacuum Squeezing in the Gravitational-Wave Detection Band*, Phys. Rev. Lett., **97**, 011101 (2006)
- H. Lück and the GEO 600 Team: *Status of the GEO 600 detector*, Class. Quantum Grav., **23**, S71-S78 (2006)
- B. Willke and the GEO 600 Team: *The GEO-HF project Class.*, Quantum Grav., **23**, S207-S214 (2006)

2005

- S. Chelkowski, H. Vahlbruch, B. Hage, A. Franzen, N. Lastzka, K. Danzmann and R. Schnabel: *Experimental characterization of frequency-dependent squeezed light*, Phys. Rev. A, **71**, 013806 (2005)
- H. Vahlbruch, S. Chelkowski, B. Hage, A. Franzen, K. Danzmann and R. Schnabel: *Demonstration of a Squeezed-Light-Enhanced Power- and Signal-Recycled Michelson Interferometer*, Phys. Rev. Lett., **95** 211102 (2005)
- H. Grothe and the GEO 600: *The status of GEO 600*, Class. Quantum Grav., **22**, S193-S198 (2005)
- B. Abbott and the LSC: *Limits on Gravitational-Wave Emission from Selected Pulsars Using LIGO Data*, Phys. Rev. Lett., **94**, 181110 (2005)
- B. Abbott and the LSC: *Search for gravitational waves associated with the gamma ray burst GRB030329 using the LIGO detectors*, Phys. Rev. D, **72**, 042002 (2005)
- B. Abbott and the LSC: *Upper limits on gravitational wave bursts in LIGO's second science run* Phys. Rev. D, **72**, 062001 (2005)

- B. Abbott and the LSC: *Search for gravitational waves from galactic and extra-galactic binary neutron stars* Phys. Rev. D, **72**, 082001 (2005)
- B. Abbott and the LSC: *Search for gravitational waves from primordial black hole binary coalescences in the galactic halo* Phys. Rev. D, **72**, 082002 (2005)
- B. Abbott and the LSC: *First all-sky upper limits from LIGO on the strength of periodic gravitational waves using the Hough transform* Phys. Rev. D, **72**, 102004 (2005)
- B. Abbott and the LSC: *Upper limits from the LIGO and TAMA detectors on the rate of gravitational-wave bursts*, Phys. Rev. D, **72**, 122004 (2005)

2004

- R. Schnabel, H. Vahlbruch, A. Franzen, S. Chelkowski, N. Grosse, H.-A. Bachor, W.P. Bowen and K. Danzmann: *Squeezed light at sideband frequencies below 100 kHz from a single OPA*, Opt. Comm., **240**, 185-190 (2004)
- J. R. Smith and the GEO 600 Team: *Commissioning, characterization and operation of the dual-recycled GEO 600*, Class. Quantum Grav., **21**, S1737-S1745 (2004)
- B. Willke and the GEO 600 Team: *Status of GEO 600*, Class. Quantum Grav., 2004, 21, S417-S423 (2004)

2003

- J. Harms Y. Chen, S. Chelkowski, A. Franzen, H. Vahlbruch, K. Danzmann and R. Schnabel: *Squeezed-input, optical-spring, signal-recycled gravitational-wave detectors*, Phys. Rev. D, **68**, 042001(2003)
- M. Hewitson and the GEO 600 Team: *A report on the status of the GEO 600 gravitational wave detector*, Class. Quantum Grav., **20**, S581-S591 (2003)
- A. M. Sintes and the GEO 600 Team: *Detector characterization in GEO 600*, Class. Quantum Grav., **20**, S731-S739 (2003)